UNIVERSIDAD COMPLUTENSE DE MADRID
FACULTAD DE CIENCIAS FÍSICAS

TESIS DOCTORAL

Architectures based on Ga_2O_3 micro- and nanowires with applications in photonics

Arquitecturas basadas en micro- y nanohilos de Ga_2O_3 con aplicaciones en fotónica

MEMORIA PARA OPTAR AL GRADO DE DOCTOR

PRESENTADA POR

Manuel Alonso Orts

Directores

Bianchi Méndez Martín
Emilio Nogales Díaz

Madrid

© Manuel Alonso Orts, 2020

Departamento de Física de Materiales
Facultad de Ciencias Físicas
Universidad Complutense de Madrid

Architectures based on Ga_2O_3 micro- and nanowires with applications in photonics

Arquitecturas basadas en micro- y nanohilos de Ga_2O_3 con aplicaciones en fotónica

PhD Thesis by:
Manuel Alonso Orts

Supervisors:
Bianchi Méndez Martín
Emilio Nogales Díaz

September, 2020

Nothing in life is to be feared, it is only to be understood.
Now is the time to understand more, so that we may fear less.

Marie Curie

Contents

Contents v

Acknowledgements ix

Abstract xvii

Resumen xxi

List of Acronyms xxv

1 Introduction 1
- 1.1 The dawn of gallium oxide 1
- 1.2 Optical properties of micro- and nanoarchitectures based on gallium oxide 6
- 1.3 State of the art in micro- and nanowire photonics 10
- 1.4 Basic concepts of Fabry-Pérot (FP) cavities 11
- 1.5 Objectives and organization of this PhD thesis 12

2 Experimental methods 15
- 2.1 Fabrication methods 15
  - 2.1.1 Thermal evaporation method. VLS and VS growth mechanisms 15
  - 2.1.2 Study of the growth conditions of the nanostructures . 17
  - 2.1.3 Focused Ion Beam (FIB) instrument 19
- 2.2 Characterization methods 22
  - 2.2.1 Scanning Electron Microscope (SEM) 22
    - 2.2.1.1 Cathodoluminescence (CL) 23
    - 2.2.1.2 Energy-dispersive X-ray Spectroscopy (EDS) 25
    - 2.2.1.3 Electron Backscatter Diffraction (EBSD) . . 27
  - 2.2.2 Transmission Electron Microscopy (TEM) 27

2.2.2.1 Basics of TEM 28
2.2.2.2 Scanning Transmission Electron Microscopy (STEM) 31
2.2.3 Fluorescence Spectroscopy 32
2.2.3.1 Photoluminescence (PL) and PL Excitation (PLE) 33
2.2.3.2 Time-Resolved PL (TRPL) 33
2.2.4 Optical spectroscopies in a confocal microscope 34
2.2.4.1 Micro-PL 36
2.2.4.2 Micro-Raman Spectroscopy 37
2.2.5 X-ray Photoelectron Spectroscopy (XPS) 38

3 Influence of Zn or Ge doping in Ga_2O_3 nanostructures 41
3.1 Synthesis and structural analysis of Ga_2O_3:Zn structures . . . 42
3.2 Optical analysis of Ga_2O_3: Zn structures: CL, PL, PLE and TRPL 45
3.3 Discussion on the luminescence of Ga_2O_3:Zn 53
3.4 Synthesis and electron microscopy analysis of Ga_2O_3:Ge nanostructures 56
3.5 Influence of Ge doping on luminescent and structural properties 64
3.6 Conclusions 69

4 Gallium oxide - Tin oxide nano-heterostructures 71
4.1 Synthesis of Ga_2O_3/SnO_2 heterostructures 72
4.2 Polyhedral shape and fin-like decorated structures 74
4.3 Branched and decorated structures: T-shaped and L-shaped . 78
4.4 Skewer-like (SK) heterostructures 82
4.5 Ga_2O_3-SnO_2 crossed-wire (CW) heterostructures 89
4.6 Discussion on the nanostructures' formation mechanisms . . . 99
4.7 Conclusions 101

5 Ga_2O_3 distributed Bragg reflector optical microcavities 103
5.1 Introduction 103
5.2 State of the art in Ga_2O_3 resonant cavities. Design of the DBR mirrors 104
5.3 FDTD simulations on DBR reflectors 109
5.4 FIB patterning and SEM characterization of the microcavities 113
5.5 Polarized μ-PL characterization of the cavities 114
5.6 Analytical study: Marcatili and Goell models, longitudinal resonance condition 117

5.7 DBR reflectivities. Comparison with simulations 122
5.8 Tailoring the Ga_2O_3:Cr cavity designs 126
5.9 Influence of the laser power on the resonances 132
5.10 Undoped Ga_2O_3 DBR cavities 136
5.11 Conclusions 142

6 Conclusions **145**

A Marcatili and Goell mode calculations **151**

Bibliography **159**

B List of publications related to this PhD thesis **173**

Acknowledgements

Como dijo John F. Kennedy, “we must find time to stop and thank the people who make a difference in our lives”. La tesis doctoral ha sido una etapa muy importante de mi vida que recordaré sobre todo con cariño, y en mis recuerdos aparecerán muchas personas que de una forma u otra me han apoyado durante estos años.

En primer lugar, no hay palabras suficientes para agradecer en su justa medida a mis dos directores de tesis, Emilio Nogales y Bianchi Méndez. Formáis un gran equipo del que he tenido la suerte de formar parte durante estos años. Cuando conocí a Emilio y le pregunté por su investigación, tenía entendido que Bianchi y él trabajaban en algo relacionado con materiales y óptica pero no tenía ni idea de qué era el óxido de galio ni de cómo funcionaba un microscopio electrónico. Desde el primer día, Emilio y Bianchi me embarcaron en su proyecto y me enseñaron todo lo que sabían, tanto en el laboratorio como fuera de él. Gracias por haber guiado mis primeros pasos en el laboratorio y por haber tenido la puerta de vuestros despachos siempre abierta para mí, tanto para dudas y análisis científicos como para resolver trabas burocráticas. También agradezco la oportunidad que me habéis dado de conocer y colaborar con científicos internacionales, lo cual se ha traducido en dos estancias (y media) predoctorales en las que también he aprendido mucho. Y, sobre todo, gracias por haber confiado en mí desde el minuto 0 y por el trato personal tan bueno que habéis tenido conmigo durante todo este tiempo.

También me gustaría incluir en los agradecimientos al resto de miembros (senior) del grupo de Física de Nanomateriales Electrónicos: Ana Cremades, Ana Urbieta, Carlos Díaz-Guerra, David Maestre, Javier Piqueras, Paloma Fernández y Pedro Hidalgo. Con todos vosotros he compartido buenos momentos en el laboratorio, en el despacho, en reuniones de grupo, etc. Desde el principio me acogisteis como parte del FINEgroup y me echasteis

una mano cuando lo necesité. Aunque por ahora mi tiempo en el grupo haya terminado, siempre estaré orgulloso de haber pertenecido a él y espero que nuestros caminos se vuelvan a juntar en el futuro.

Agradezco al Ministerio de Ciencia y Universidades (y a sus infinitos nombres anteriores) por el contrato FPU/01982, que me ha permitido realizar la tesis a tiempo completo durante estos 4 años. Agradezco también a los proyectos MAT 2015-65274-R-FEDER y M-ERA.NET PCIN-2017-106 y RTI2018-097195-B-I00 de los que he formado parte.

Para esta tesis también tengo mucho que agradecer a los dos postdocs del FINEgroup con los que he compartido mucho tiempo, Javi Bartolomé y Belén Sotillo. Gracias por haberme ayudado con tanta motivación siempre que os lo he pedido, tanto en el laboratorio como fuera de él. Javi, como agradecimiento te invitaré a una buena tortilla de patatas sin cebolla. Belén, dejo para ti sola el horno de vacío, espero que se siga portando tan bien. Los dos sois para mí un modelo, tanto científico como personal, para mí. Mucha suerte en vuestro futuro. Pienso que nadie merece más que vosotros llegar a las metas que os habéis propuesto.

En este punto, querría agradecer al mejor técnico de laboratorio que se puede pedir, tanto por sus amplios conocimientos técnicos como por su buen humor y gran disposición a ayudar en todo momento. Gracias por todo, Carlos, si el cielo existiera y tuviera que pensar en alguien que se lo hubiera ganado, tu nombre sería el primero que me vendría a la cabeza.

Decía Richard P. Feynman que "teaching and students keep life going". Me gustaría agradecer al departamento de Física de Materiales, a los técnicos de laboratorio David y Esther y, en especial, al alumnado al que tuve la oportunidad de dar clase, por todos los buenos momentos que pasé y por toda la física que aprendí durante la docencia que he impartido durante estos años de investigador predoctoral. También recuerdo a aquellos profesores que motivaron mi interés por la física durante mis estudios de grado y de máster. Finalmente, quiero agradecer a la Universidad Complutense de Madrid por el curso de oratoria que me ofrecieron tras lograr el segundo puesto en el concurso "tesis en 3 minutos", con el que aprendí algunas técnicas útiles y conocí a gente muy interesante.

During this PhD, I was fortunate to spend some weeks/months at three different institutions: the Univeristy of the Basque Country (UPV-EHU, Spain), the University of Warwick (UK) and the University of Bremen (Germany). In these places, I met several people who played an important role

in some of the results which appear in this thesis, as well as in my scientific learning.

- José María San Juan, María Luisa Nó, muchas gracias por todos los patrones de FIB que habéis realizado para las cavidades DBR que aparecen en el capítulo 5. Durante el tiempo de realización de mi tesis tuvimos una gran comunicación, en la que acogisteis con ilusión nuestras propuestas para mejorar las DBRs, intentando llevar al FIB al máximo de sus posibilidades. Gracias también por recibirme con tanto cariño y enseñarme cómo trabajáis allí durante las dos semanas en las que os visité.
- Ana Sánchez, thank you very much for all your help on the TEM work which is included in this thesis. From the collaboration on the Ga_2O_3-SnO_2 heterostructures to the experimental work we carried out when I stayed at Warwick for two months regarding germanium doped gallium oxide, you showed me your broad knowledge regarding HRTEM and STEM. You were also very welcoming when I arrived at Warwick Uni, along with Richard Beanland and your PhD and Postdoc students. I hope that our paths do not diverge in the future.
- Last but not least, I would like to thank Martin Eickhoff for hosting me during my 3-month short stay at the University of Bremen. Thank you for your esteem towards myself and for your involvement on our present and future work together. From the beginning I felt very much at home in your group; starting with the welcome trip up to the table tennis matches with you and the SSM group members (Christian T, Stephan F., Olga K, ...). I would also like to thank Alexander K. for his detailed introduction to MBE, Christian T. for his determination in the lithography trials and Gerwin C. for his collaboration in the pulsed PL measurements.

I would also like to thank Marco Peres for the work we carried out together at the beginning of my thesis and for his useful tips, as well as Luca Gregoratti for his useful advice in the local XPS measurements carried out in Ga_2O_3-SnO_2 heterostructures.

Volviendo a la UCM, gran parte del tiempo que he pasado en la tesis lo he hecho acompañado de doctorandos y postdocs del departamento de Física de Materiales, junto con personas de otros países que realizaron estancias aquí. Gracias por haber contribuido a formar un entorno agradable en el que realizar mi trabajo. Aunque el agradecimiento va para todos, permitidme

que personalice en algunos de vosotros.

- Gracias a María T., mi compañera de grupo y amiga desde el máster, por todas las buenas conversaciones y los momentos graciosos, tan necesarios mientras trabajamos en el despacho. También por los buenos momentos que pasamos en algunos viajes, como el del Junior Euromat de Budapest.
- Gracias a Belén C., Ali P. y Gregor P. por haberme acogido en el despacho con tanto cariño y por todos los buenos consejos que me disteis en el principio del doctorado. En ese momento me ayudasteis a ir entendiendo lo que significaba estar haciendo una tesis.
- Gracias a Álvaro D. por tantas cosas. Fuiste la primera persona del departamento a quien consideré un gran amigo y, tras todos estos años, quizá seas quien más me ha aportado como persona, e incluso científicamente, con tantas charlas fructíferas sobre la investigación, la física o la divulgación y con muchos planes no relacionados con la ciencia. Ojalá algún día encontremos el espacio y el tiempo en el que podamos llevar a cabo todas esas ideas de las que seguimos hablando hoy en día.
- Gracias a Paloma A. por enseñarme que las primeras (y segundas) impresiones no siempre son las correctas, y que puedes llegar a sentir mucho aprecio por alguien que parecía totalmente distinto a ti. Gracias por tu alegría, por el salseo y por haber organizado tantos viajes, escape rooms, partidos de pádel y demás. Gracias a Marta S. por estar en esos planes y por ser un ejemplo de la importancia de la perseverancia para conseguir tus objetivos.
- Gracias a mis compañeros de despacho Jaime D., Antonio V. y Marina G. Por el tiempo pasado juntos, no solo en despacho, también en el laboratorio, en las terrazas en los partidos de pádel, en los viajes y mucho más. Vielen Dank auch an Rocío A. Espero que todo vuelva a la normalidad pronto y podáis terminar esas tesis, en cuyas defensas os prometo que no haré preguntas al final.

No pueden estar fuera de estos agradecimientos todos los amigos que, aunque no tengan mucha idea sobre los nanohilos de óxido de galio, me han apoyado todo este tiempo y han conseguido que en muchas ocasiones desconectase de mi trabajo y pasase muy buenos ratos con ellos. Me gustaría personalizar en algunos de vosotros:

La primera persona que debe aparecer aquí es Silvia R. Gracias por tantos momentos inolvidables vividos juntos durante estos años, por haber confiado tanto en mí y por haberme apoyado en todo momento. También por mostrarme que se puede sacar un buen trabajo adelante aunque te pongan muchas piedras en el camino.

Justo después tienen que aparecer Mario E. e Irene M. Mario, eres una persona que merece la pena tener cerca siempre. Gracias por tantos planes y viajes juntos, y por arrancarme siempre una sonrisa con tus bromas. Irene, gracias por ser una persona tan directa. Por la música y los juegos de mesa. También por cubrirme en una clase de laboratorio y por haber preparado conmigo con tanta ilusión las clases de problemas para ingenieros geólogos.

Gracias a Magdalena M. por el ministerio, los paseos y las tortillas, a Marina P. por tantos planes ilusionantes que hicimos juntos al principio de la tesis, a Irene B y a Víctor A. por haberme acompañado desde la carrera y por esas comidas tan ricas en el CIEMAT, a Diego L. por su humor estadístico, a Mike R. por esos dúos épicos. Gracias también a Jaime S-F por las llamadas que me recuerdan a mi tiempo en el colegio. Y a Adriana, Ángel, Laura, ... con quienes pude desconectar en salsa cubana. Finalmente, a Beatriz P. por haberme acogido y hecho de guía en Copenhague.

Decía Michael J. Fox que “a family is not an important thing, it’s everything”. Tengo la suerte de que tener una familia que solo me ha dado alegrías y estos últimos párrafos de agradecimiento van hacia ellos.

Gracias a mis tíos por vuestro cariño hacia mí. De nuevo, por no poner demasiados nombres, me vais a permitir que personalice en algunos, aunque os quiera mucho a todos. Dani, gracias por todos los momentos que hemos compartido, sobre todo por los musicales. Gracias a Ángeles por tus guisos imbatibles, por tus bromas con cara seria y por haberme acogido durante mis primeros años en Madrid.

Gracias también a mis primos de Madrid, Jose y Laura, por vuestro apoyo incondicional. Cuando vivimos juntos tuvimos una relación de casi-hermanos que espero que no perdamos nunca. Gracias también a mis primos de Elche, incluida Elena, la más joven de la familia. Tienes una alegría y una curiosidad que te van a hacer llegar muy lejos. Gracias a mi abuela Fina, que ha luchado toda su vida por tener a una familia tan unida como la mía. Gracias por esa felicidad y ese amor hacia los demás y en particular hacia mí. Cuando escribo esto no sé si habrás podido venir a mi defensa, pero tienes que saber que estarás en mis pensamientos en ese momento y también en

cada paso que dé en mi vida.

Finalmente, gracias a mis padres por tantas cosas. Gracias por inculcarme el amor por la física (papá) y por los idiomas (mamá). Por haber pasado tan buenos momentos conmigo y por haberme soportado en los pocos momentos amargos. Por haberme visitado en mis estancias en el extranjero y por haber celebrado conmigo los pequeños pasos que iba dando hasta llegar a este momento. También por estos últimos meses de tesis que hemos pasado en cuarentena juntos. Podría seguir, pero tendría que escribir otra tesis, y con una ya he tenido bastante.

A todos vosotros, y a aquellos que me haya olvidado incluir aquí ¡gracias!

Abstract

Transparent Conductive Oxides (TCOs) are materials which combine a very low absorption in the visible range of the electromagnetic spectrum with a moderate electrical conductivity. Among them, gallium oxide (β-Ga_2O_3) is one of the widest band gap semiconductors (almost 5 eV). Lately, this material is experiencing an exponential increase in its research interest, mainly due to two reasons: the better performance and lower cost of some high power electronic devices of Ga_2O_3 compared to the semiconductor giants SiC and AlN and the recent development of high quantum efficiency Ga_2O_3 deep-ultraviolet (deep-UV) photodetectors.

In parallel, one of the current trends in materials science and technology research is the device size reduction in order to improve their performance. One of the important areas which require size reduction is photonics. This sector is based on the study of light generation, detection and manipulation for optical applications, some aiming to improve the current performance of their electronic counterparts. In this context, this PhD thesis is based on studying and tailoring the optical properties of Ga_2O_3 in the nanoscale to support this material as an attractive candidate in photonics.

In this thesis, we have explored the possibility of incorporating several impurities in Ga_2O_3 micro- and nanostructures by thermal evaporation methods. We have found out that certain dopants can favour 1D, 2D or 3D nanostructured growth with different morphologies. The dopants that have been explored in this thesis are zinc (Zn), germanium (Ge), tin (Sn) and chromium (Cr). Each one has shown to also influence the physical properties of the structures.

Firstly, we incorporated zinc in the crystal structure of Ga_2O_3, as this impurity is a good choice for the analysis of the challenging acceptor doping in this material. The most common morphology of the grown Ga_2O_3:Zn

structures is belt-like. The study of Zn-related energy levels has been carried out by several luminescence techniques, which has led to novel results. Then, the incorporation of Ge in Ga_2O_3 nanostructures was carried out for the first time, bearing in mind that this dopant could result in improved n-type doped Ga_2O_3 devices. The use of metallic gallium in combination with germanium powders at temperatures close to the melting point of Ge was the driving force for the growth of elongated Ga_2O_3:Ge nanostructures. Apart from analyzing the formation mechanism of these structures, we have characterized them by electron microscopy and micro-Raman spectroscopy techniques.

Building from these impurity incorporation studies in Ga_2O_3 nanostructures, we went a step forward and optimized the synthesis parameters in order to achieve novel Ga_2O_3-SnO_2 nanoarchitectures, resulting in complex TCO heterostructures. For example, many Ga_2O_3 nanowires with several polyhedral SnO_2 particles attached to their trunks, called skewer-like (SK) structures, were obtained. Furthermore, novel Ga_2O_3 - SnO_2 crossed-wire (CW) structures were synthesized by including an extra precursor to gallium and tin oxide; chromium oxide. According to the thorough transmission electron microscopy (TEM) analysis carried out in this thesis, the nano-heterojuctions of the SK and CW structures have minimal strain by virtue of the lattice matching of certain atomic planes of Ga_2O_3 and SnO_2. The CW structures have also shown light guiding of the orange emission of the SnO_2 crossed wires, which is complementary to the blue-UV emission of the Ga_2O_3 nanowire axis. These results point out to the possibility of shape engineering different dimensionalities of TCO complex architectures in the nanoscale.

Finally, an additional fabrication process has been carried out in this thesis in order to improve the performance of Ga_2O_3-based optical cavities for photonic applications. We have made periodic patterns in both Cr-doped and unintentionally doped (UID) Ga_2O_3 micro- and nanowires by Focused Ion Beam (FIB) microscopy in order to obtain distributed Bragg reflector (DBR) cavities. This thesis presents the whole process carried out to obtain these optical cavities in detail along with the obtained results. First of all, finite-difference time-domain (FDTD) simulations were performed in order to tune the high-reflectivity bands in the design of the DBR cavities. Secondly, the DBRs were fabricated in the unpatterned micro- and nanowires by FIB. Thirdly, polarized micro-photoluminescence (μ-PL) spectra were measured in the nanopatterned cavities, showing strong modulations either

in the red-NIR or the blue-NUV in Ga_2O_3:Cr or UID Ga_2O_3, respectively. Finally, the polarization-dependent μ-PL results were analyzed analytically and compared to a theoretical model and to the FDTD simulations in order to further understand and assess the performance of these optical devices.

We have obtained promising results: We have largely improved the reflectivity of Cr-doped Ga_2O_3 microcavities up to 80% in the red-NIR range, and we have successfully described their optical modes. The resonances lie in the expected wavelength position in both polarization setups and have a high finesse and a high intensity with respect to the primary luminescence. They show reversible wavelength shifts under different pump laser powers, with applications in temperature sensors. Additionally, we have FIB-patterned UID Ga_2O_3 DBR cavities, which imply a further size reduction due to the possibility to guide their lower emission wavelength. Therefore we have been able to control and switch the emission range and the light confinement in Ga_2O_3 optical devices from the red and near-IR towards the near-UV.

To sum up, in this thesis we have studied the influence of several dopants on the structural and optical properties of complex Ga_2O_3 micro- and nanostructures. The promising results of the Ga_2O_3:Zn tunable light emitters, the Ga_2O_3:Ge elongated nanostructures, the Ga_2O_3 - SnO_2 complex nanoarchitectures and the Ga_2O_3:Cr and UID Ga_2O_3 DBR optical micro- and nanocavities pave the way for the development of photonic devices in the micro- and nanoscale based on Ga_2O_3.

Resumen

Los óxidos conductores transparentes (TCOs, por sus siglas en inglés) son materiales que combinan una baja absorción en el rango visible del espectro electromagnético con una conductividad eléctrica moderada. Perteneciente a la familia de los TCOs, el óxido de galio (β-Ga_2O_3) tiene uno de los mayores band gaps de todos los semiconductores (casi 5 eV). Últimamente, el interés científico sobre este material está aumentando exponencialmente por dos principales motivos: el desarrollo de dispositivos de Ga_2O_3 de alta potencia con mejores capacidades y menor coste que los semiconductores comerciales de este sector (SiC y AlN) y el desarrollo de fotodetectores ultravioleta con gran eficiencia cuántica.

Una de las estrategias más importantes en el desarrollo de nuevos materiales es la reducción del tamaño de los dispositivos para mejorar la eficiencia de los mismos. Una de las áreas en que esta reducción de tamaño posee mayor relevancia es la fotónica. Este sector está basado en el estudio de la generación, la detección y la manipulación de la luz para aplicaciones ópticas, en algunos casos con el objetivo de reemplazar ciertos dispositivos electrónicos. En este contexto, esta Tesis Doctoral está basada en el estudio y la modificación de las propiedades ópticas del Ga_2O_3 en la nanoescala para afianzar el atractivo de este material en el área de la fotónica.

En esta tesis hemos explorado la posibilidad de incorporar distintas impurezas en micro- y nanoestructuras de Ga_2O_3 mediante tratamientos de evaporación térmica. Hemos constatado cómo distintas impurezas introducidas en los tratamientos pueden inducir el crecimiento de nanoestructuras de distinta dimensionalidad, 1D, 2D o 3D, y morfología. Los dopantes que se han estudiado son el cinc (Zn), el germanio (Ge), el estaño (Sn) y el cromo (Cr). Se ha observado que cada una de ellos también afecta a las propiedades físicas de las estructuras.

En primer lugar, hemos estudiado la incorporación del Zn en el Ga_2O_3. Mediante este dopante se puede analizar la influencia de las impurezas aceptoras en este material. Se han obtenido mayoritariamente microbarras de Ga_2O_3:Zn, en las cuales hemos analizado la presencia de nuevos niveles electrónicos debidos al Zn a partir de técnicas de luminiscencia, con resultados novedosos. En segundo lugar, hemos realizado los primeros estudios sobre la incorporación de Ge en el Ga_2O_3, teniendo en cuenta que este dopante podría dar lugar a mejores dispositivos tipo n de Ga_2O_3. El uso del galio metálico en combinación con polvos de germanio a temperaturas cercanas al punto de fusión del Ge fue el catalizador para el crecimiento de nanohilos de Ga_2O_3:Ge. Además de estudiar su proceso de crecimiento, dichas estructuras han sido analizadas mediante microscopía electrónica y micro-espectroscopía Raman.

A partir de los resultados anteriores, hemos dado un paso más en la optimización de los parámetros de crecimiento para obtener nanoarquitecturas de Ga_2O_3 - SnO_2, es decir, nano-heteroestructuras complejas basadas en TCOs. Por ejemplo, se han obtenido muchos nanohilos de Ga_2O_3 recubiertos parcialmente con varias partículas de SnO_2 de morfología poliédrica, los cuales hemos denominado "estructuras tipo brocheta". Por otro lado, mediante la incorporación de un precursor extra, el óxido de cromo, hemos obtenido "estructuras CW", formadas por un hilo central de Ga_2O_3 e hilos cruzados de SnO_2. Mediante microscopía electrónica de transmisión (TEM) hemos estudiado con profundidad tanto las brochetas como las estructuras CW, obteniéndose un buen acoplamiento de red a escala atómica en ambos casos. Además, las estructuras CW presentan guiado de luz en el naranja debido a los hilos cruzados de SnO_2. Esta emisión es complementaria a la azul-UV del hilo central de Ga_2O_3. Estos resultados apuntan a la posibilidad de diseñar arquitecturas complejas de TCOs en la nanoescala.

Finalmente, en esta tesis hemos diseñado un procedimiento adicional de fabricación en cavidades ópticas basadas en Ga_2O_3 para mejorar sus prestaciones para aplicaciones fotónicas. Usando el microscopio de Haz de Iones Focalizado (FIB), hemos tallado patrones periódicos en micro- y nanohilos de Ga_2O_3 sin dopar y dopados con cromo para obtener cavidades basadas en reflectores de Bragg (cavidades DBR). Esta tesis presenta con detalle el proceso completo llevado a cabo para obtener estas cavidades, junto con los resultados principales obtenidos. Se comenzó realizando simulaciones de dominio de tiempo de diferencia finita (FDTD) para sintonizar las bandas de reflexión en el diseño de las cavidades DBR. Con estos datos, se fabri-

caron las DBRs mediante FIB, para posteriormente medir la luminiscencia polarizada de las cavidades. Por último, los resultados de μ-PL polarizado se estudiaron analíticamente, comparando con un modelo analítico y con las simulaciones FDTD para examinar y comprender el comportamiento de estos dispositivos ópticos.

Hemos obtenido resultados prometedores: las cavidades DBR de Ga_2O_3:Cr han aumentado sustancialmente su reflectividad hasta el 80% en el rojo-IR cercano, y hemos descrito sus modos ópticos con éxito. Las resonancias se encuentran en los rangos de longitud de onda deseados en ambas polarizaciones, presentan una alta fineza y tienen una alta intensidad respecto a la luminiscencia no guiada. Adicionalmente, muestran desplazamientos en longitud de onda resonante reversibles mediante la aplicación de distintas densidades de excitación del láser incidente, lo cual tiene aplicaciones en sensores de temperatura. Además, se han tallado de nanohilos no dopados, cuya longitud de onda de emisión es menor. Se ha logrado que estos dispositivos tengan una reflectividad de hasta el 50%. Por tanto, hemos logrado controlar y desplazar el rango de emisión y confinamiento de la luz en cavidades ópticas de Ga_2O_3 desde el rojo-IR cercano hasta el violeta-UV cercano.

En resumen, en esta tesis hemos estudiado la influencia de varios dopantes en las propiedades estructurales y ópticas de micro- y nanoestructuras complejas de Ga_2O_3. Los resultados prometedores de los emisores de luz sintonizables de Ga_2O_3:Zn, las estructuras alargadas de Ga_2O_3:Ge, las nanoarquitecturas complejas de Ga_2O_3 - SnO_2 y las micro- y nanocavidades ópticas DBR de Ga_2O_3:Cr y del material no dopado son un avance importante para el desarrollo de dispositivos fotónicos de Ga_2O_3 en la micro- y nanoescala.

List of Acronyms

ADF annular dark field.

BF bright field.

CL cathodoluminescence.

CW crossed-wire.

DAP donor-acceptor pair.

DBR distributed Bragg reflector.

DF dark field.

ED excitation density.

EDS Energy Dispersive X-ray Spectroscopy.

FDTD finite-difference time-domain.

FFT fast Fourier transform.

FIB Focused Ion Beam.

FP Fabry-Pérot.

FSR free spectral range.

HRTEM High-resolution TEM.

L-NB lollipop nanobelt.

L-NW lollipop nanowire.

LMIS liquid metal ion source.

MP melting point.

NIR near-infrared.

NUV near-ultraviolet.

PL photoluminescence.

PLE PL Excitation.

RT room temperature.

SAED Selected Area Electron Diffraction.

SB stop band.

SEM Secondary Electron Microscope.

SK skewer-like.

STEs self-trapped electrons.

STHs self-trapped holes.

TEM Transmission Electron Microscope.

TRES Time-Resolved Emission Spectroscopy.

UID unintentionally doped.

VLS vapor-liquid-solid.

VS vapor-solid.

WG waveguide.

XPS X-ray Photoelectron Spectroscopy.

Chapter 1

Introduction

1.1 The dawn of gallium oxide

Transparent Conductive Oxides (TCOs) are a family of materials which combine a high transparency in the visible range (over 80%) with a rather high electrical conductivity (up to 10^3 S/cm). This is due to their large band gap (> 3 eV) and the presence of intrinsic donor or acceptor defects such as oxygen vacancies or cation vacancies, respectively, which provide free carriers to the semiconductors. Examples of TCOs are ZnO, SnO_2 or Ga_2O_3, as well as ternary compounds like indium tin oxide (ITO). They have become an important family for applications in many fields, ranging from selective chemical sensors [1, 2] to highly efficient solar cells [3].

Monoclinic β-Ga_2O_3 is the most thermodynamically stable phase of gallium oxide. It hereinafter will be referred to as Ga_2O_3. Ga_2O_3 is one of the TCOs which possess a wider band gap: it is reported to be, both experimentally and by first principle calculations, around 4.8 eV at room temperature (RT). There is a general consensus that Ga_2O_3's band gap is a direct one, although it also seems to have an indirect band gap with almost identical energy ($\sim$4.8 eV) [4]. Due to its wide band gap, Ga_2O_3 has been one of the leading materials for two important applications, which are mentioned below.

Firstly, optical absorption measurements show that the cutoff wavelength of Ga_2O_3 ranges from 250 to 280 nm when the incident polarization is parallel to the **b** and **c** directions, respectively [5]. Such a wide transparency range makes Ga_2O_3 a promising material for solar-blind UV photodetectors. These detectors sense radiation with wavelength shorter than 280 nm and are at the same time insensitive to visible and infrared (IR) radiation, giving rise to a large number of applications such as flame detection, missile

guidance systems or inter-satellite communication. A wide range of deep-UV photodetector device structures based on Ga_2O_3 have been recently reported [6, 7].

Secondly, such a wide band gap results in the material withstanding very high voltages without having an electrical breakdown. The theoretical electrical breakdown field (E_b) of Ga_2O_3 is around 8 MV/cm. Experimentally, Ga_2O_3 metal-oxide-semiconductor field effect transistors (MOSFETs) have exceeded the highest E_b MOSFETs, made of SiC and GaN, reaching values up to 3.8 MV/cm [8, 9]. This has made Ga_2O_3 a strong candidate for the ultra-high power (> 1 kW) and high frequency switching (GHz) markets [6].

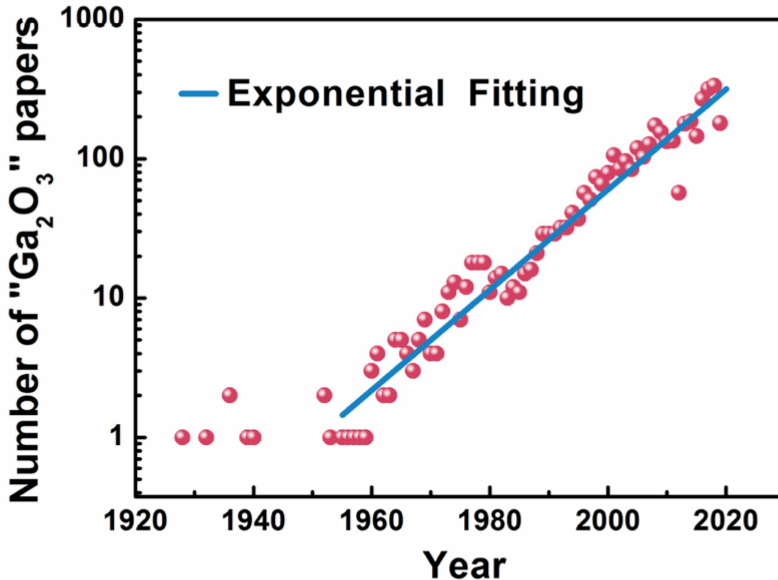

Figure 1.1: Number of publications on Ga_2O_3 as a function of time. Data from Scopus, collected and fitted by [10].

Due to these and other material capabilities and the recent availability of large bulk substrates, with an estimated three times cost advantage over SiC [11], Ga_2O_3 is becoming a material worthy of a significant research focus in parallel with a rapidly growing technological foundation. Figure (1.1) shows an exponential increase in the number of scientific publications on Ga_2O_3 in the last half century. Still, some issues for its widespread use remain, like the need to mitigate the self-heating in devices of this material due to its poor thermal conductivity (∼20 W/mK, one order of magnitude lower than SiC or GaN) and the demand for a deeper understanding of the influence

of different dopants on its fundamental material properties [6, 12].

The crystal structure of Ga_2O_3 belongs to the $C_{2/m}$ space group. It is a base-centered monoclinic Bravais lattice, where **a**⊥**b** and **b**⊥**c**, while **a** and **b** form an angle of 103.7°, and it has a two-fold rotation symmetry and a horizontal mirror plane. Ga_2O_3's conventional unit cell consists of 20 ions and is composed of two crystalographically different Ga^{3+} ions, Ga_1 coordinated tetrahedrally (4-fold coordination) and Ga_2 coordinated octahedrally (6-fold coordinated). The conventional unit cell also has three inequivalent O^{2-} ions, two threefold coordinated and one fourfold coordinated. Figure (1.2) shows the aforementioned unit cell. By inspecting this figure, we can deduce that the previously mentioned mirror symmetry of the unit cell is across the plane perpendicular to the **b** axis. Ga_2O_3's crystal structure translates into an anisotropic behaviour of several physical properties such as the electronic and thermal conductivity or the optical absorption. Ga_2O_3's unit cell parameters along with its main physical properties are displayed in table (1.1).

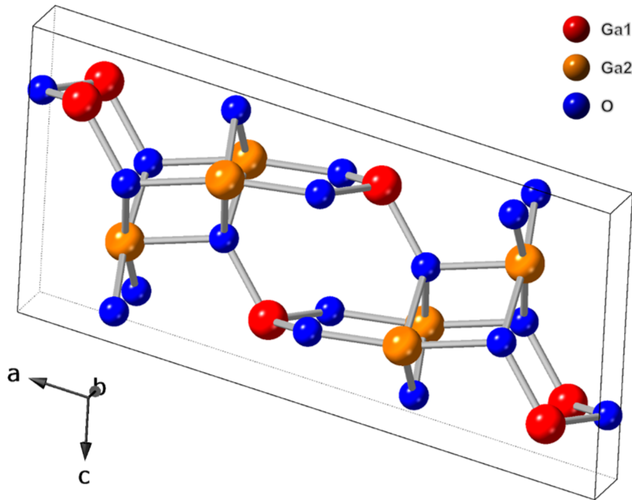

Figure 1.2: Unit cell of β-Ga_2O_3. Gallium ions are shown in red and orange to show their tetrahedral and octahedral coordination, respectively, while oxygen ions are shown in blue.

Despite possessing such a wide band gap, Ga_2O_3 is not an insulator, but an n-type semiconductor. It presents a dispersive conduction band formed predominantly by delocalized Ga 4s derived states. The native point defects with the lowest formation energies in Ga_2O_3 are Ga divacancy-interstitials

Parameter	Magnitude
a	12.23 Å
b	3.037 Å
c	5.798 Å
β	103.8°
Band gap	4.6 - 4.9 eV
Melting point	1800 °C
Refractive index (VIS)	1.90 - 2.02
Electron mobility	20 - 180 cm^2/Vs
Breakdown field	8 MV/cm
Thermal conductivity	0.1-0.3 W/cm K

Table 1.1: Lattice constant and main physical properties of β-Ga_2O_3 at RT [4, 6].

and O vacancies [13]. For many years, Ga_2O_3's electrical conductivity had been attributed to the latter, however experimental [14] and theoretical [15] works have shown that oxygen vacancies act as deep donors. Recent works tentatively attribute the n-type conductivity of Ga_2O_3 to Si and H, which are present in unintentionally doped Ga_2O_3 as shallow donor impurities [4].

Notice that the term *unintentionally doped* (UID) Ga_2O_3 is used throughout this thesis instead of *undoped* Ga_2O_3. This terminology is often used in the literature [13, 16] due to the fact that, even in high-quality grown "undoped" Ga_2O_3, the aforementioned background impurities are present in a non-negligible concentration and its concentration is expected to contribute to Ga_2O_3's physical properties. For example, the UID sample used in section 3.2 is the most "pure" Ga_2O_3 substrate sold by Tamura Corporation and its specifications state that it possesses a donor concentration equal to $9 \cdot 10^{17}$ cm^{-3} or lower.

The n-type conductivity in Ga_2O_3 can be tuned in the range of 10^{-12} to 10^2 S/cm by controlled impurity incorporation or by changes in the growth conditions [17, 18]. The three main candidates for intentional donor doping in Ga_2O_3 are the tetravalent ions of the group IV elements Si, Sn and Ge. These three donors have been used for conductive channels in, generally planar, transistors with excellent operation [6]. In this thesis, Ge and Sn incorporation in Ga_2O_3 micro- and nanostructures will be studied in chapters 3 and 4, respectively.

Analogously to other well-known TCOs such as ZnO, p-type doping in Ga_2O_3 is very challenging. The potential candidates are substitutional divalent ions such as Zn^{2+} or Mg^{2+}, but they have been found to introduce deep acceptor levels in Ga_2O_3, with ionization energies higher than 1 eV [16]. There are few reports of p-type conductivity in Ga_2O_3, and it is believed to be most likely due to ionized Ga vacancies at high temperature rather than to impurity doping [19]. Many efforts are being made to achieve p-type conductivity in order to extend Ga_2O_3's applications to bipolar devices, but the already mentioned high ionization acceptor energies and the small dispersion in Ga_2O_3's valence band indicate that it is unlikely that p-type doping will be achieved with effective hole conduction in this material [18, 20]. Nevertheless, incorporating acceptor impurities in Ga_2O_3 is useful for other purposes such as the control of electrical conductivity (e.g. to create semi-insulating material) [16]. In this thesis, the effect of Zn incorporation in Ga_2O_3 nanostructures, in particular regarding their optical properties, will be explored in chapter 3.

Moving on to its basic optical properties, as detailed previously, Ga_2O_3 has a very wide transparency range. It has a fundamental absorption ranging from 4.6 eV to 4.9 eV depending on the polarization geometries [5]. As shown in table (1.1), the phase refractive index of the material in the visible part of the spectrum is relatively high: from 2.02 (at 400 nm) to 1.90 (at 700 nm). These values were obtained by Al-Kuhaili *et al.* by fitting transmittance and reflectance curves on compact amorphous films to the Cauchy model: $n = n_\infty + B/\lambda^2 + C/\lambda^4$. Similar fits were made from ellipsometric measurements on Ga_2O_3 films of different thicknesses, giving rise to a high dielectric constant of $\epsilon_\infty = 3.57$ [21]. Additionally, Ga_2O_3 has one of the highest lasing damage thresholds among the semiconductor materials [22], which results in applications in the high power optics sector [23].

Luminescence is a non-destructive technique with a high sensitivity for the identification of native and impurity-related point defects in semiconductors. Furthermore, it is an essential property in photonics (see section 1.3), since the emission properties of the material are the basis for many optical devices. Luminescence of UID and doped Ga_2O_3, both in bulk and nanostructured form, has been studied in the past decades [24–26]. UID Ga_2O_3 features luminescence bands centered in the near-UV (NUV) and blue parts of the spectrum. As detailed before, the concentration of the impurities in the crystal structure of Ga_2O_3 and their effect on the concentration of oxygen

vacancies in the material have an effect on its physical properties, including its luminescent properties. This has given rise to controversy regarding the origin and energy positions of the emission bands of undoped Ga_2O_3 [6, 16].

Different models regarding the origin of the blue-UV emission in Ga_2O_3 have been proposed [25, 27, 28]. Currently, the most accepted model considers that the UV emission (3.2 - 3.6 eV) is originated from the recombination of free electrons and self-trapped holes (STHs), or self-trapped excitons (STEs). Recently a second recombination path involving silicon acceptors has been proposed [28]. The blue emission (2.8 - 3.0 eV) has shown universal dependency with the resistivity; its intensity decreases with decreasing ρ, and completely quenches for Ga_2O_3 single crystals heavily doped with silicon or nitrogen. It is attributed to a donor-acceptor pair (DAP) transition. As the intensity of the blue emission correlates with the oxygen vacancy concentration, the donors of this DAP transition are considered to be the oxygen vacancies.

Ga_2O_3 is not only constrained to emit in the UV-blue energy part of the spectrum. As detailed in the next section, the luminescence of Ga_2O_3 can be tailored towards higher or lower energies by the adequate introduction of optically active dopants. In particular, we will use this possibility to tailor the optical confinement of light of different energy ranges in chapter 5.

1.2 Optical properties of micro- and nanoarchitectures based on gallium oxide

Micro- and nanowires or nanobelts are nanomaterials with a high aspect ratio. Their large surface area gives rise to improved sensing properties and novel physical properties. Currently Ga_2O_3 nanostructures have been developed for applications in nanowire-based FETs [29, 30] or solar-blind photodetectors [31, 32], among others.

The first reports on the growth of β-Ga_2O_3 nanostructures date to the beginning of this century [33, 34]. In the two decades that have passed since that period, the most used micro- and nanowire synthesis methods have been thermal evaporation and (MO)CVD [35, 36]. Both methods can provide a high yield of high crystalline quality nanostructures, and many dopants can be introduced into the lattice, either in-situ or, in the case of low solubility ions, by ion implantation [37]. A wide variety of morphologies such as nanowires[35], nanorods [38], nanobelts [39] or nanoneedles [40] of

UID and doped Ga_2O_3 have been synthesized by these techniques. The well-defined facets and small surface roughness of the micro- and nanostructures make them interesting for photonics applications due to their low optical loss. Suitable geometries can be designed in order to guide and confine specific light energy ranges in certain regions, delimited by the morphology of the structure, as it will be shown in the next section and further on in this thesis.

The optical emission range of Ga_2O_3 can be tuned from the UV to the IR, depending on the optically active impurities introduced in this material [41]. Some of the main examples of the luminescence tunability by doping in Ga_2O_3 are noted below:

- The UV-blue luminescence is already present in UID Ga_2O_3, and the relative intensity of the blue and UV components depends on the resistivity of the sample, as explained in section 1.1. In addition, Ga_2O_3 bulk samples and nanowires implanted with gadolinium have been studied [42, 43]. A sharp UV peak at 3.96 eV, due to the $^6P_{7/2}$ - $^8S_{7/2}$ transitions of the Gd^{3+} ion was observed at RT. When annealing was done at low temperature (500°C) in the bulk samples, this line was very intense and was dominant in the cathodoluminescence (CL) spectrum. In nanowires, this line had a low intensity except for high annealing temperatures (900°C or 1100°C).

- Regarding green luminescence, manganese doped Ga_2O_3 nanowires with diameters of tens of nanometers displayed a broad green (559 nm) PL [44] or a yellow (590 nm) CL [45] emission band at RT due to $^4T_1$ - $^6A_1$ intraionic transitions in Mn^{2+}. Thicker microrods, of around 1 μm, showed a broad blue-green band in CL [45]. Ga_2O_3 doped with two rare earth ions, terbium [46] and erbium also presented light emission in this energy range. The latter showed intraionic lines centered in the three primary colours of the spectrum: red (660 nm), green (555 nm) and blue (420 nm), as well as in the near-infrared (NIR), at 1445 nm [41, 47].

- Regarding red luminescence, in-situ [48, 49] or implanted [42, 43] europium doped nanostructures were obtained and displayed intense red emission lines due to $^5D_0$-^7F_J transitions. In addition, chromium ions produced a broad red-NIR luminescence band at RT superimposed to two intense lines, whose origin will be explained below.

- Regarding NIR luminescence, as well as the Er^{3+} intraionic emission

mentioned above, nickel doped gallium oxide nanoparticles of a few hundred nanometers size showed a strong NIR luminescence band around 1400-1450 nm due to a characteristic Ni^{2+} intraionic transition [50]. Optical gain was observed at 1300 nm in silicate glass ceramics containing Ga_2O_3:Ni^{2+} crystals, giving rise to potential applications in broadband optical fiber amplifiers [51].

Let us focus on the red-NIR luminescence of chromium doped gallium oxide, as most of chapter 5 is based on the photonic applications of this material system. The first reports on gallium oxide were related to the optical properties of this dopant [52] due to its analogies with ruby, Cr-doped Al_2O_3, the material used to fabricate the first laser [53]. In gallium oxide, chromium incorporates in the crystal structure substitutionally in the octahedral Ga sites. Even with a very low percentage incorporation, this dopant completely modifies the luminescence of the material; the blue-UV band quenches and the dominant band is a red-NIR band ranging from 1.6 to 1.9 eV.

This emission can be described by the configurational coordinate diagram, as shown in figure (1.3). At very low temperatures, only two intense emission lines at 1.78 and 1.80 eV, known as the R-lines, are observed in the PL spectra of Ga_2O_3:Cr. Both are due to ^2E - $^4A_2$ intraionic transitions, in which the ^2E state in Cr^{3+} is split in two due to the interplay of the monoclinic crystal field and the spin-orbit interaction. Due to the intermediate crystal strength of Ga_2O_3, the energy difference between the ^2E state and a higher energy state, the $^4T_2$, is not large (around 60 meV [54]), allowing for a thermally activated emission from the $^4T_2$ level at higher temperatures (over $\sim$100 K [55]), see figure (1.3). This results in a superposition of a broad phonon-assisted band due to $^4T_2$ - $^4A_2$ transitions and the already discussed R-lines in the PL spectra of Ga_2O_3:Cr

More recently, the optical characteristics of Cr-doped Ga_2O_3 micro- and nanowires have been studied [54, 56, 57]. An intense luminescence was obtained from 4 K up to RT in Ga_2O_3:Cr microwires, following the same pattern as in the bulk form, and several parameters such as rather long decay times were obtained [54]. A very long luminescence afterglow of around 4 hours was reported in hydrothermally-grown nanowire assemblies irradiated with UV light [56]. Fabry-Pérot (FP) resonances on individual microwires due to partial reflection between the wire ends were measured by micro-PL spectroscopy [57]. This thesis, in particular chapter 5, goes a step forward and explores different photonic applications of Ga_2O_3:Cr in the micro- and nanoscale.

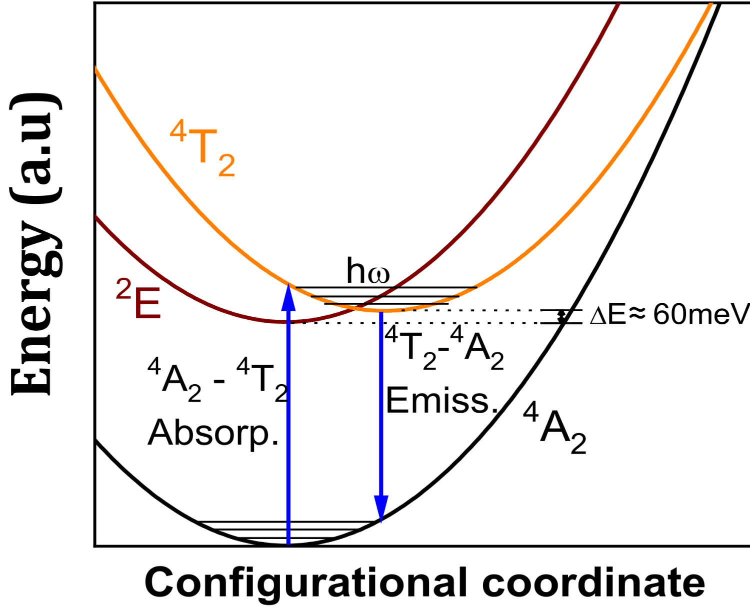

Figure 1.3: Qualitative configurational coordinate diagram of Cr^{3+} levels in Ga_2O_3, showing the thermally activated emission from the $^4T_2$ level.

Doping of Ga_2O_3 micro- and nanostructures may not only affect their physical (optical, electrical...) properties, but it can also largely modify the size and the morphology of the obtained structures. For example, Ga_2O_3 nanostructures doped with In and Sn were analyzed by I. López and co-workers [58]. They found that indium favours the formation of zig-zagged belts with a high indium concentration [59] while tin favours the formation of Ga_2O_3 branched nanowires by means of an Sn-aided secondary VLS growth on the main axis [40]. In this thesis, apart from studying certain dopants in Ga_2O_3 simple nanostructures, more complex architectures have been synthesized. In chapter 4, by selecting certain dopants and growth conditions, Ga_2O_3-SnO_2 nano-heterojunctions have been fabricated. These variations in the size, morphology and composition of the nanoarchitectures can also play a key role in tailoring their optical properties and their functionalities.

1.3 State of the art in micro- and nanowire photonics

Photonics is the area of study dedicated to the knowledge and applications of light generation, detection and manipulation. This term first appeared in the beginning of the 1960's when the first operating laser, made from ruby, was developed by Theodor Maiman [53]. The device was quickly replicated by many other scientists and soon other photonic devices like the laser diode (Robert N. Hall, 1962) or the optical fiber (Manfred Borner, 1965) were demonstrated. These well-known devices by today's society have revolutionized technology and everyday life. In present days, by virtue of the lower dissipation and higher frequencies of the optical signal compared to the electronic one, they are gradually replacing their electronic counterparts in the generation and transmission of information [60].

All these optical devices are composed of bulky components with dimensions much greater than the wavelength of visible light. Along with the size reduction of semiconductor devices for electronic applications, the last few decades have seen a progress towards micro- and nanoscale photonic devices. Semiconductor micro- and nanowires are potential building blocks of these devices and provide a special platform to tailor light-matter interactions at the nanoscale. These structures are able to not only guide the light but also generate it in virtue of their optical emission in the visible and IR energy ranges.

Most of the current semiconductor nanophotonic applications are based on the II-VI (ZnO, CdS, ...) or III-V (InP, GaN, ...) families. Optical microdevices such as optical fibers have widespread use in today's society [61], while nanowire-based photonic devices such as nanolasers, active optical switches or single nanowire spectrometers have emerged in the last years, and some are already being used commercially [62, 63]. Besides, complex nanoarchitectures such as crossed-wire junctions can improve the lasing properties of these nanodevices [64] or provide new capabilities such as optical nanoscale filters [65]. Still, the development of small-size, high-density and stable photonic devices, in particular in the UV range [66], is one of the main challenges of this sector.

As detailed in the previous section, Ga_2O_3 has a high transparency range and a rich variety of luminescence processes, ranging from the NIR to the NUV ranges. It has a high chemical stability and is able to endure high electric fields and high lasing powers. It also has a fairly large refractive

index in the NIR-NUV range. Furthermore, as we will see during this thesis, it can act as a building block for a wide range of possible nanoarchitectures. With all of this in mind, this thesis studies the fabrication and properties of Ga_2O_3-based micro- and nanowires and complex nanoarchitectures, the generation and guiding of light and the selective confinement of both red-NIR light and of violet-NUV light in these structures. It aims to present Ga_2O_3 as a viable candidate to become part of the new wave of optoelectronic and photonic materials, with potential applications in their device markets.

1.4 Basic concepts of Fabry-Pérot (FP) cavities

In this section we will focus on one of the main types of optical microcavities, which is one of the building blocks of many photonic devices: Fabry-Pérot (FP) cavities. The resonant modes present in optical cavities can be based in whispering gallery modes, due to total internal reflections in microstructures with polyhedral faces, or FP modes, due to reflections between flat wire ends, among others. Throughout this thesis, the optical resonances present in Ga_2O_3 micro- and nanostructures are found to be of the FP type. Several concepts of these cavities are introduced below.

An FP cavity is formed by an active layer of length L and index of refraction n which is situated between two mirrors of reflectivities R. In a microwire, these mirrors are directly formed by the ends of the wire due to the refractive index difference between the material and the air outside of it at the wire ends, although this reflectivity is quite low. In chapter 5, we present the fabrication of mirrors with higher and more selective reflectivity.

The resonance condition in an FP cavity can be easily obtained. It is given by the following expresesion:

$$\lambda_m = \frac{2nL}{m} \tag{1.1}$$

where λ_m are the resonant wavelengths and m is an integer. Experimentally, one will find resonant peaks which are spectrally separated by $\Delta\lambda$, also known as the Free Spectral Range (FSR). In order to check that the resonances are in fact F-P between the wire ends, we will use the following equation:

$$\Delta\lambda = \frac{\lambda^2}{Ln_g} \tag{1.2}$$

in which n_g is the group refractive index of the material. Notice that, taking into account the wide transparency range of our material, absorption losses are considered to be negligible.

Two of the most important parameters which measure the performance of an optical cavity are the quality (Q) factor and the finesse (F). In both cases, the higher the value, the better the performance of the cavity.

The Q factor is defined as the number of oscillation periods (multiplied by 2π) before the stored energy in the cavity decays to 1/e of its original value. It is obtained experimentally by [1]:

$$Q = \frac{\lambda}{\delta\lambda} \tag{1.3}$$

where $\delta\lambda$ is the Full Width Half Maximum (FWHM) linewidth of the resonant peaks. As the Q factor decreases when reducing the cavity size [67], in this thesis it will be more useful to focus on the other parameter, F, which has the following mathematical definition [1]:

$$F = \frac{\Delta\lambda}{\delta\lambda} \tag{1.4}$$

The finesse is defined as the number of round trips (multiplied by 2π) before the stored energy decays to 1/e of its original value. Assuming there are no absorption losses in the cavity, F is independent on the cavity length and can be directly related to the reflectivity of the mirrors by the following equation:

$$F = \frac{\pi\sqrt{R}}{1-R} \tag{1.5}$$

In which we have assumed that both mirror reflectivities are equal ($R_1 = R_2 \equiv R$). It must be noted that equation 1.5 is an approximation of a more complex expression and is only equivalent to this expression if the reflectivities are over 30% [68].

1.5 Objectives and organization of this PhD thesis

The main purpose of this thesis is the fabrication and characterization of complex gallium oxide architectures based on micro- and nanowires and

[1] As, for an ideal FP cavity, the FSR and the linewidth of the resonant peaks are independent of the frequency, both Q and F should be defined mathematically in the frequency space. However, for experimental reasons, we will define it mathematically in the wavelength space

the study of their optical properties for photonic applications. In order to achieve this general goal, this thesis has the following more specific objectives:

The first objective is to synthesize and study the effect of the incorporation of both n-type and (possibly) p-type dopants in gallium oxide nanostructures. The structures are grown by a thermal evaporation method with gallium oxide, gallium and the dopant of choice as source materials. The morphological, structural and luminescent properties are characterized by electron and optical microscopy techniques. With this knowledge, complex TCO nano-heterostructures which combine Ga_2O_3 and SnO_2 are synthesized and characterized

The second objective is to study the optical properties of various morphologies, in the micro- and nanoscale, of Ga_2O_3 doped with different impurities. In particular, the influence of Zn, Ge, Sn and Cr in the optical emission of the obtained structures is analyzed by luminescence-related techniques. In addition, waveguiding and confinement of their emitted light is examined in some of these structures.

The third and final objective is to study the feasibility of gallium oxide micro- and nanowires as optical microcavities in order to obtain an improved reflectivity and tunability in the NIR (for Ga_2O_3:Cr) and the blue-UV (for UID Ga_2O_3) energy ranges. To reach this objective, we perform experimental, analytical and simulated studies of the resonant optical modes present in these cavities, as a first step for the future design of photonic devices based on this material.

With these objectives in mind, this thesis is organized as follows:

- This first chapter is a brief introduction of the properties that have made Ga_2O_3 a key material for the scientific and technological community, an overview of the optical properties of doped Ga_2O_3 nanostructures, a brief summary of the state of the art in nanophotonics and some basic concepts of FP optical cavity parameters. It also includes the main objectives and organization of the thesis.

- The second chapter describes the fabrication methods used to obtain the Ga_2O_3 micro- and nanostructures and complex architectures, and the main experimental techniques used in this thesis for their study.

- The third chapter studies the influence of two key dopants on Ga_2O_3 nanostructures: zinc and germanium. Zn is one of the potential p-type

dopant candidates for Ga_2O_3 and the first half of this chapter mainly deals with the effect of this dopant on the optical properties of the material. Ge has shown to be a promising n-type dopant for Ga_2O_3 thin films and no studies had been carried out on Ge doped Ga_2O_3 nanowires prior to the content of this chapter, in which Ga_2O_3:Ge nanostructures are grown and analyzed.

- The fourth chapter focuses on Ga_2O_3-SnO_2 complex nanostructures. The study of the obtained tin oxide architectures on gallium oxide nanowires with different dimensionalities is shown in this chapter. The different types of nano-heterostructures are classified and their structural, chemical and optical properties are characterized by electronic and optical techniques.

- The fifth chapter presents the design and thorough analysis of UID and Cr-doped Ga_2O_3 patterned optical microcavities. Their photonic properties are studied experimentally, analytically and by means of simulations. The control and tunability of the generated optical resonances in the cavities is demonstrated.

- The sixth and final chapter of this thesis states the main conclusions from this work.

Chapter 2

Experimental methods

In this chapter, the experimental methods employed to achieve the objectives of the thesis are described. As well as the fabrication and the characterization methods reported here, we have also performed simulation methods for the design and analysis of optical cavities. These will be described in chapter 5.

2.1 Fabrication methods

In semiconductor oxides, there is a great variety of synthesis methods which are used to grow 1D or 2D structures in the micro- and nanometer scale. Of the myriad of available synthesis techniques, most of them make use of two growth mechanisms: vapor-liquid-solid (VLS) or vapor-solid (VS).

2.1.1 Thermal evaporation method. VLS and VS growth mechanisms

A thermal evaporation method is based on the heating of solid materials in a furnace, in this case for the nucleation and growth of micro- and nanostructures by different mechanisms. In this method, both VLS and VS mechanisms can take place.

In the VLS mechanism, nanoparticle catalyzers are used as the seed for nanowire growth. These catalyzers are generally in liquid form and are normally formed on the solid substrate by either direct deposition or by deposition and annealing of a low melting point (MP) thin film of metal. Figure (2.1) shows the main features of the VLS mechanism. The temperature is increased for the catalytic particle to melt and form a droplet. Then,

the precursor vapour is mainly adsorbed by the catalytic particles. A natural reason for this is a higher sticking coefficient (probability of adsorption) on the particle compared to elsewhere, although this is not always the main explanation. Once the saturation limit is surpassed, crystallization at the droplet-nanowire interface results in tip growth due to diffusion of adatoms across the particle. Accordingly, the particle acts as a conduit for nucleation and nanowire growth, with diameters that are set by its dimensions. More information about the VLS process can be found in refs. [69], [70].

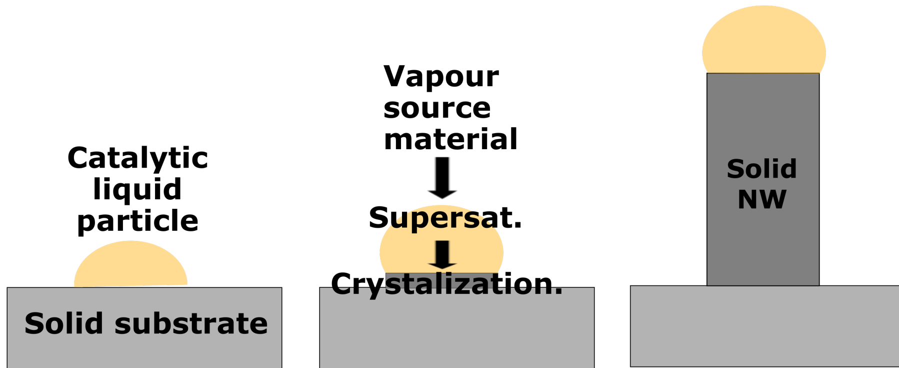

Figure 2.1: Description of VLS mechanism in a thermal evaporation synthesis method.

To avoid the use of foreign catalysts, however, it is possible to grow micro- and nanostructures by what is known as a vapor-solid (VS) mechanism. It is based on the adsorption of the vapour source material on the surface of the substrate. The adsorbed adatoms will attach directly or diffuse onto a thermodinamically favourable site or lattice plane, nucleate and begin the growth of nanowires. Figure (2.2) shows the main features of the VS mechanism for the growth of ZnO nanowires by thermal evaporation. As shown in the figure, in order to supersaturate the atmosphere and promote the nucleation of nanowires, a carrier gas and a temperature gradient are generally present in this mechanism. The complete picture of VS growth is still not completely understood by the scientific community. Different mechanisms have been proposed to explain its process. These include anisotropic growth, self-catalytic growth or growth induced by dislocations. Anisotropic growth is due to the existence of energetically favourable planes and directions in the crystalline structure of the material, while self-catalytic growth stems from the accumulation of the elements in the vapor phase along the

growth direction. In our case, we believe that the anisotropy of the unit cell of Ga_2O_3 and the choice of the source materials, as well as the temperature gradient, are the driving forces for the nanostructured growth in our furnace.

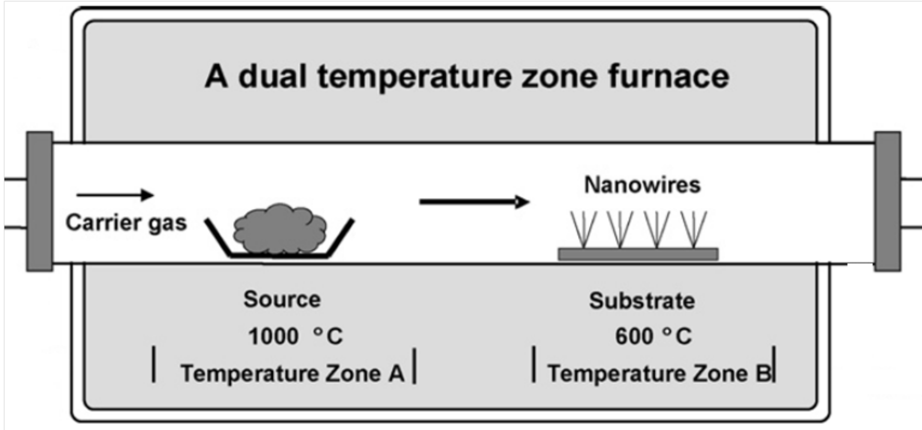

Figure 2.2: VS mechanism. In this example, it was used in ref. [71] for the growth of ZnO nanowires.

Notice that both for VLS and VS mechanisms, the solid interface in which the nanowires nucleate and grow is not always a bulk substrate as in the standard way in microelectronics; it can be the as-grown nanowire itself from which further nucleation, either catalyst-assisted or self-catalytic, occurs. This has been used for the growth of branched structures of many different materials, including TCOs [72]. For example, in ref. [40], tin doped Ga_2O_3 branched nanostructures had a tin particle at the end of the branch, which indicated a tin-aided growth of secondary Ga_2O_3 nanowires from the primary nanowire axis.

In this thesis, the micro- and nanostructures have been grown by a thermal evaporation method with no external catalysts. In our setup, nanowire growth can occur by either (or both) VLS or VS mechanisms. The furnace temperature and indicators such as the presence of a catalyzer particle at the tip can indicate what mechanism is present in each case.

2.1.2 Study of the growth conditions of the nanostructures

The micro- and nanostructures obtained in this thesis were synthesized in a horizontal tubular furnace, depicted in figure (2.3), at the Department of

Materials Physics of the Complutense University of Madrid (UCM). The thermal treatments were carried out at atmospheric pressure and under an argon flux of 0.8 l/min. The precursors were two Ga_2O_3 pellets placed symmetrically 3 cm apart from each other on top of an alumina boat, metallic gallium centered on top of the pellets and the dopants chosen in each case placed on top of the Ga_2O_3. As we will see throughout the thesis, most nanostructures grow on the pellet further away from the center of the furnace due to the carrier gas and the lower deposition temperature at this pellet, as it is depicted in figures (2.2) and (2.3). It must be noted that the synthesized Ga_2O_3 structures which appear in this thesis were found to be in the β phase; no mixed phases were detected.

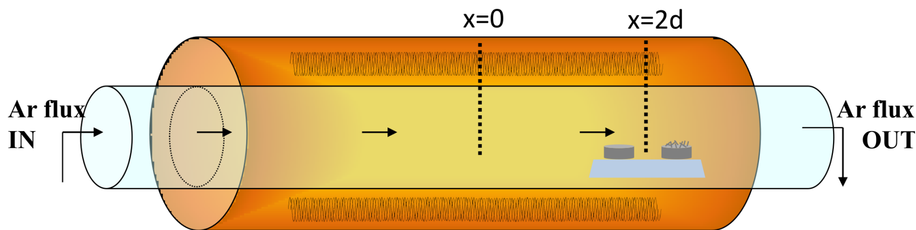

Figure 2.3: Schematic diagram of the furnace used to synthesize the samples in this thesis. The alumina boat and the pellets are shown relatively larger with respect to the furnace than the real size for clarity. In this example, the pellets are placed at position $x = 2d$.

The samples were placed in one of three possible positions defined as $x = 0$, $x = d$ and $x = 2d$, where $d = 10\,\text{cm}$ and $x = 0$ is defined as the position at the center of the furnace. Not only the temperature but also the temperature difference between both pellets was different in each position. In order to obtain these temperatures, a thermocouple was used for nominal temperatures of 1050 °C and 1250 °C. The results are summarized in table (2.1).

Two main conclusions can be extracted from these measurements. Firstly, a higher temperature difference between pellets A and B was found at $x = 2d$. This resulted in an increased number of nanostructures grown at this position. Secondly, a higher temperature difference was found with respect to the nominal temperature at 1250°C than at 1050°C. This increased the uncertainty of the temperature and the temperature gradient expected for nominal temperatures greater than 1250 °C. As an approximation, at $x = 2d$ and T >1250°C, ΔT = -400 °C can be taken. In this thesis, in the

x	ΔT [Tnom = 1050 °C] (°C)		ΔT [Tnom = 1250 °C] (°C)	
	Pellet A	Pellet B	Pellet A	Pellet B
0	-10	-10	-34	-34
d	-10	-14	-38	-60 ± 10
$2d$	-220 ± 40	-410 ± 80	-300 ± 30	-440 ± 60

Table 2.1: Temperature difference with respect to the nominal temperature for both pellets in the three used positions in the oven. The temperature uncertainty is 1 °C except at distance $2d$ for all temperatures and at distance d at 1250°C in pellet B, in which a variation of 1 cm in the thermocouple's displacement gives rise to a variation of several °C.

section where the synthesis of each type of structures is detailed, either the real temperature or the nominal temperature and the position of the alumina boat in the furnace are stated. If the nominal temperature is stated, table (2.1) can be used to obtain the temperature in each pellet.

2.1.3 Focused Ion Beam (FIB) instrument

The miniaturization of novel material systems down to the nanoscale requires additional fabrication techniques in order to further modify the architectures of the synthesized nanostructures. In this context, the Focused Ion Beam (FIB) microscope has emerged as a versatile sculpturing technique. In this thesis, this instrument was used for two main objectives:

1. Cross-section sample preparation for Transmission Electron Microscopy (TEM) analysis of Ga_2O_3/SnO_2 nanojunctions (chapter 4).
2. Fabrication of distributed Bragg reflectors (DBRs) for tunable resonant Ga_2O_3 microcavities (chapter 5).

An FIB column generates and directs a beam of high-energy ionized atoms, usually gallium, towards the sample in order to etch atoms in the selected areas. The FIB column is generally integrated as a second column in a Scanning Electron Microscope (SEM), which will be explained in the next section. The electron beam is used to locate and monitor the sample without further damaging it. Once the structure is located, it is tilted for the ions to be at normal incidence when performing the milling process. The selected structure is placed at the coincidence point of the two beams in order to be able to monitor the structure (electron beam) and mill (ion beam) in real time. A top view image mode can be formed in the FIB by detecting the

secondary electrons generated by the incident ions but, as there is some ion implantation in the lattice which causes structural damage, generally, the real-time monitoring is made by using the electron beam images.

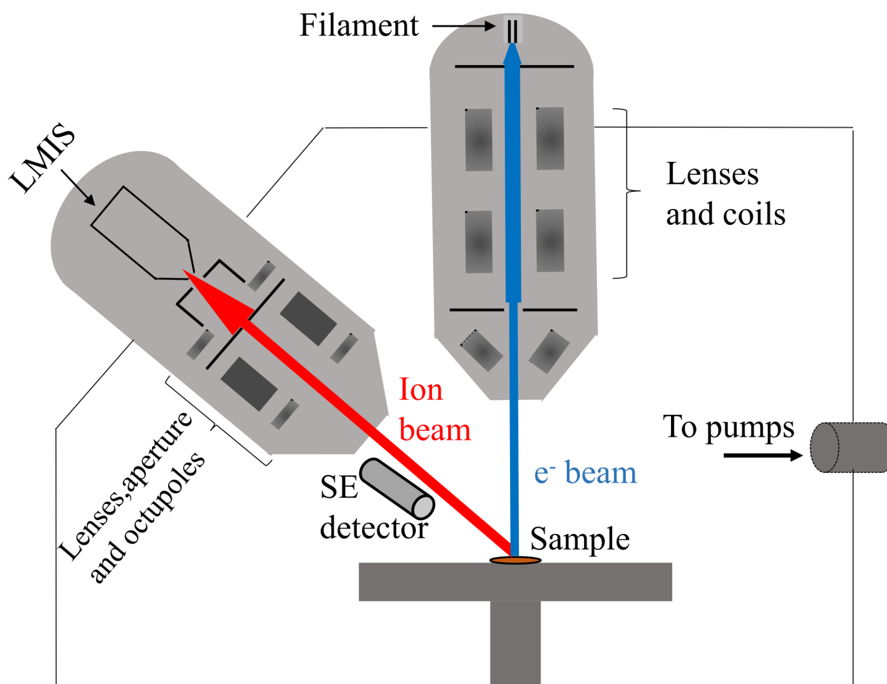

Figure 2.4: Diagram of an FIB integrated in an SEM.

How does an FIB system work? A general scheme of the FIB integrated in an SEM is shown in figure (2.4). Gallium ions are generated by a Liquid Metal Ion Source (LMIS), which consists of a metallic gallium reservoir from which ions can be drawn out by means of the extraction voltage caused by an electrode. The ions are then discriminated by a concentric aperture, accelerated up to an energy of 30 keV and collimated by a condenser lens. Then, the ions go through an aperture which determines the ion current. Different apertures with different diameters can be placed, and this is a key component in the system, as a high current will increase the milling efficiency but will also increase the irradiation damage on the nanostructures. Finally, the ions are focused by an objective lens and hit the sample, extracting the atoms of the chosen area in order to cut the structure for its cross section or to carve the desired patterns, among other applications. Both

the FIB and the SEM work at high vacuum of around 10^{-6} bar in order to avoid interaction of the electron and ion beams with the atmosphere.

Next, the physical process regarding the ion-matter interaction is explained. When an ion reaches a crystalline surface, it mainly interacts via inelastic collisions with the atomic lattice. During its trajectory, it can sputter atoms from its surface, emit electrons or photons, react chemically and break bonds, displace atoms in the crystal lattice, etc. Figure (2.5)(a) illustrates some of these events. The mass of the gallium ions is several orders of magnitude higher than the mass of the electrons and similar to the mass of the atoms, hence most of the ions' momentum is transferred to the atoms. Due to this, further collisions are generated because of the displaced atoms, which results in the extraction of material from the surface. Due to these physical and chemical processes, the interaction volume, defined as the volume in the specimen affected by the incident beam, is greater than the volume which the ions strike. This will be important for the design of nanometer-sized patterns in chapter 5.

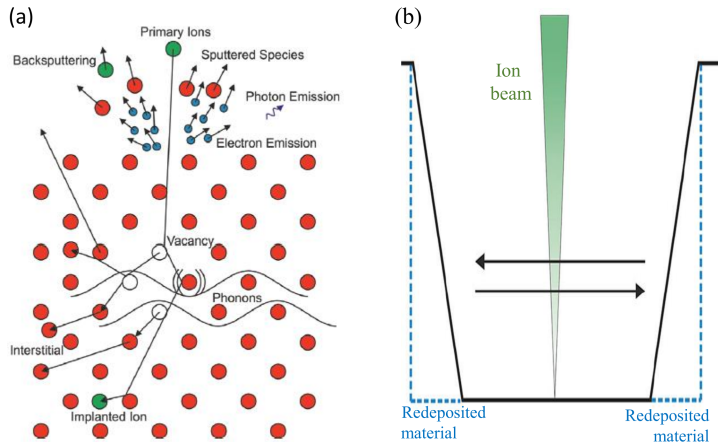

Figure 2.5: (a) Physical process of ion-matter interaction. (b) Schematics of redeposition process. Adapted from [73].

A final factor that must be taken into account when using the FIB is redeposition from the incident ions and the extracted material. Its effects are important when the escape routes of the sputtered atoms are limited, which is the case for nanopatterned gratings. The result of redeposition in these small holes is shown in figure (2.5)(b). In order to reduce redeposition effects, a cold trap is placed at the side of the chamber.

Further information of the fundamentals and applications of the FIB can be found at ref. [73].

The FIB microscopes used in this thesis were the JEOL 4500 FIB-SEM at the University of Warwick (UK) for TEM cross-section nano-heterostructure analysis and the FEI Helios Nanolab 650 at the University of the Basque Country (UPV-EHU) in Spain for distributed Bragg reflector (DBR) fabrication. For the latter, I participated in one of the fabrication batches under the supervision of José María San Juan and María Luisa Nó during a 2-week short stay at the UPV-EHU.

2.2 Characterization methods

2.2.1 Scanning Electron Microscope (SEM)

An SEM is a versatile instrument which offers complementary information to the usual morphological one by analyzing the different signals emitted by the sample after the interaction with the electron beam. The basic SEM components are shown in figure (2.6) (a). The column, which was sketched in figure (2.4), basically consists of an electron gun in which electrons are extracted from a filament by thermoionic or field effect, two or more condenser lenses which focus the beam, apertures which control the beam current, scanning coils and a final objective lens.

As high energy electrons, in the order of 5-30 keV, reach the sample, elastic and inelastic collisions occur. As the mass of an electron is much lower than the mass of an ion, there is no atom etching, and different physical processes occur with respect to the FIB. Topographic images with high spatial resolution are formed in this microscope owing to the low energy secondary electrons (SE) generated from the beam-sample interaction. Additionally, as shown in figure (2.6) (b), there are other signals emitted from the sample after its interaction with the electron beam which can give rise to very useful information such as UV-visible-IR photons (cathodoluminescence), X-ray photons and backscattered electrons. Figure (2.6) (b) presents the order of magnitude of the interaction volume of each signal, which indicates its spatial and depth resolution. This volume is very dependent on the incident energy of the electrons, increasing when the electron energy increases. The SEM characterization techniques related to these signals which have been used in this thesis are presented in the following subsections.

The SEM used in this thesis are a Leica 440 Stereoscan, a FEI Inspect, both

in the Materials Physics laboratory of the UCM. In addition, Zeiss Supra 55-VP from the Research Technology Platform (RTP) of the University of Warwick was used during a 2 months short stay at this university.

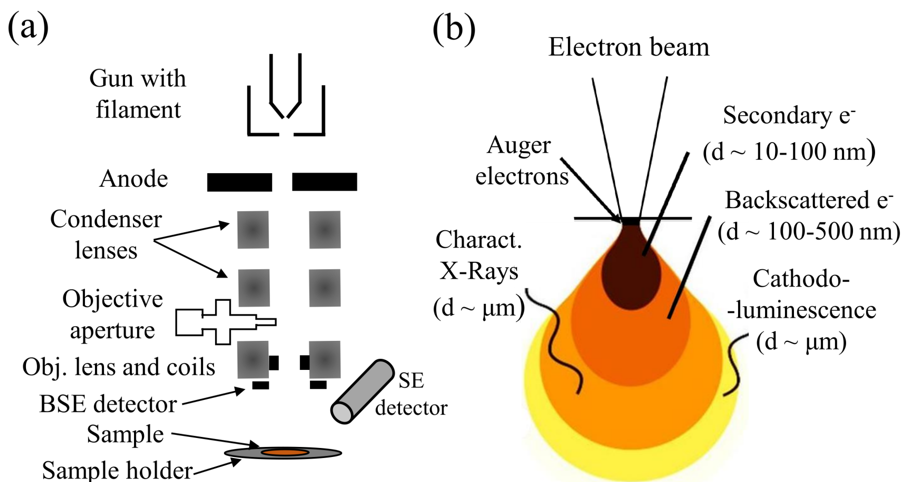

Figure 2.6: (a) Diagram displaying the main SEM components. (b) Diagram showing the main signals generated in an SEM with an approximate value of their depth (d).

2.2.1.1 Cathodoluminescence (CL)

CL is the emission of photons, ranging from the UV to the IR range, as a consequence of the desexcitation process that take place after the electron beam irradiates the material. This is a very suitable technique to investigate fundamental properties of semiconductor materials. As the incident electron energy is much higher than the material band gap, every incident electron can generate many electron-hole pairs due to several inelastic collisions. These can also be generated by secondary electrons, as they have energies up to several tens of electronvolts.

After the huge electron-hole generation, some electrons will recombine radiatively, i.e. will emit photons. Some may not encounter traps and return back to their ground state in a band to band transition (process (1) in figure (2.7)). Other electrons may form excitons, electron-hole pairs attracted to each other by the electric field which end up recombining (process (2) in figure (2.7)). Others may be temporarily trapped by intrinsic (i.e. oxygen vacancies, impurities...) or extrinsic (i.e. dopants) defects and may then

return to the ground state directly, or may encounter other traps. In these processes, they may emit a photon (radiative transition) or not; for example in process (3) figure (2.7) an electron is first trapped in a donor, then recombines with a hole in an acceptor, emitting a photon (DAP recombination). Lastly, luminescence may originate from the transitions between ionic levels of a dopant which have been split by the host crystal (process (4) in figure (2.7)). An example of such transitions was shown in figure (1.3) for Cr-doped Ga_2O_3. These are representative examples of the physical processes which lead not only to CL but also to luminescence excited by other means like photoluminescence (PL), which will be described in subsection 2.2.3.1. More detailed information about CL can be found in ref. [74].

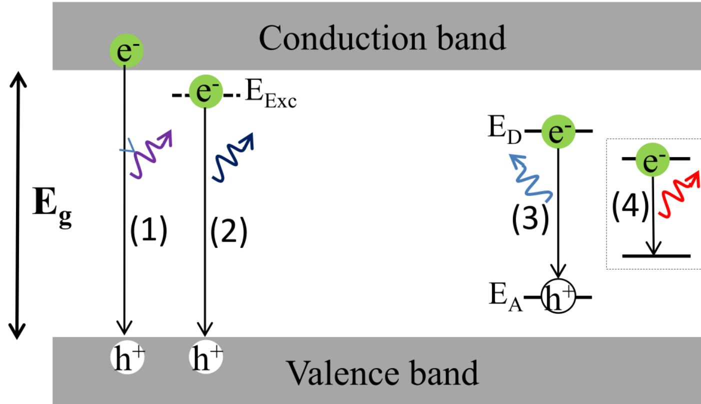

Figure 2.7: Diagram showing examples of transitions involved in luminescence. (1) Band to band transition. (2) Excitonic transition. (3) DAP recombination. (4) Intraionic transition. E_g is the band gap of the material, i.e. around 5 eV for Ga_2O_3.

In this thesis, taking advantage of the SEM, we have obtained both spatially-resolved CL spectra with wavelength resolution and spatially-resolved CL images. A very small area (a pixel) can be selected to obtain CL spectra, but the signal will originate from the interaction volume (see figure (2.6)). In order to estimate the depth of this volume both for CL spectra and images, the semi-empirical Kanaya-Okayama formula [75] is used:

$$R\,(\mu m) = \frac{0.0276 A E_b^{1.67}}{\rho Z^{0.89}} \tag{2.1}$$

where A is the atomic weight (g/mol), E_b is the beam energy (keV), ρ is the density (g/cm^3) and Z is the atomic number. For example, a value

of 0.7 µm is obtained both for Ga_2O_3 and SnO_2 if the acceleration voltage of the incident electrons is 10 kV. This value increases to 1.4 and 1.3 µm respectively if the acceleration voltage is increased to 15 kV.

As the volume has a "pear-like shape", its depth is a very important factor to keep in mind; high voltages will produce high CL signals as the energy of the incident electrons increases, but a lower signal will arise for higher voltages if the nanowire is thinner than the interaction volume. In that case, part of the signal may not come from the nanowire but from its substrate. Hence, relatively low acceleration voltages (7-10 kV) are used for CL spectra from nanowires.

Regarding the equipment used, for the CL spectra an optical fiber was placed at the Leica SEM chamber to guide the light towards a Hamamatsu PMA-11 CCD. Regarding the CL monochromatic images, an optical fiber was also used. This time, it was placed between the SEM chamber and the monochromator. The monochromator selects the wavelength reaching a photomultiplier tube (PMT), which converts the luminescence signal to an electrical one. It is connected to an amplifier which sends the signal to the computer. This system is coupled to the SE image in order to acquire the CL image of the chosen structure.

2.2.1.2 Energy-dispersive X-ray Spectroscopy (EDS)

EDS analyzes the energy of the X-rays generated by the electron beam in the sample. It can be performed both in the SEM and the STEM (see subsection 2.2.2.2 for the latter). For both cases, the physical process responsible for the X-ray generation is shown in figure (2.8). Electrons from the inner levels of the atoms are removed due to electron bombardment, creating empty states. Electrons from higher energy orbitals fill the empty states and emit photons whose energy is equal to the energy difference between the higher energy level and the empty state level. The set of these energy differences is characteristic of each element, thereby allowing for the identification such element in the sample.

The electron beam does not only produce characteristic X-rays of each element. In addition, a continuous X-ray emission covering the whole energy range, called bremsstrahlung (German for "deceleration radiation"), is detected. It is due to charged particles' (in this case, electrons) deflection by other charged particles (in this case, atomic nuclei) which result, by conservation of energy, in the emission of photons.

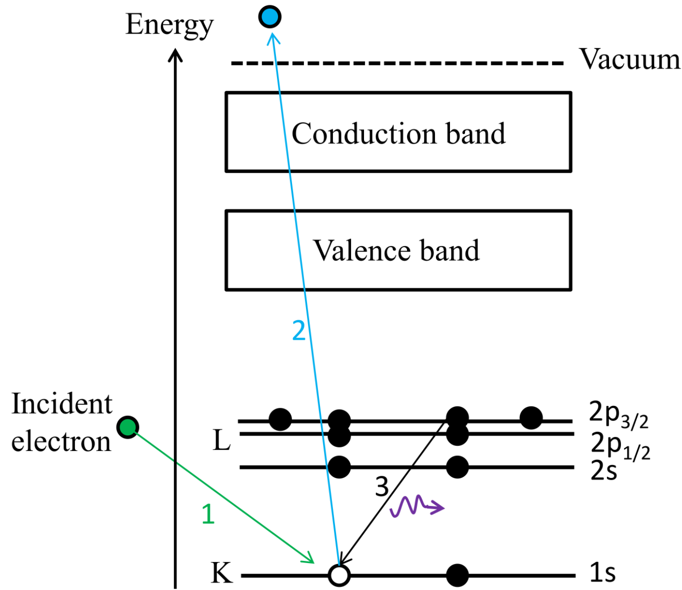

Figure 2.8: Generation of an X-ray in an atom when it is bombarded by an electron (1). In this example, an electron (2) is removed from the K shell and an electron (3) decays from the L shell, emitting an X-ray with energy = E($2p_{3/2}$)-E(1s)).

Our SEM in the Materials Physics laboratory of the UCM is equipped with an Oxford Instruments analyzer with its corresponding Bruker AXS software. This software corrects this background and, from the intensity of each X-ray line and corrections related to the atomic number and secondary fluorescence (ZAF corrections), may identify and quantify each element present in the sample as long as it has a presence of at least 0.5 to 1% at. (the technique is more precise with heavier elements) in the SEM and, for the STEM system described below in section 2.2.2.2, of at least 0.1% at. Special care must be taken in the identification and quantification of dopants in nano-heterostructures as the signal from the analyzed area may originate from other parts of the structure in which the elements are present.

The spatial resolution of this technique in the SEM is around a micron and depends on the acceleration voltage (improving for lower voltages), among other parameters. It is slightly better than the CL spatial resolution (check equation (2.1) and figure (2.6)). The EDS spatial resolution in the STEM is much better than in the SEM, reaching up to a few tens of nanometers.

2.2.1.3 Electron Backscatter Diffraction (EBSD)

As its name indicates, EBSD is based on the elastically scattered electrons which have undergone Bragg scattering (see equation (2.2)). EBSD is used to map the different material phases and their crystallographic orientations across small or large areas of a crystal with a resolution of tens of nm.

As figure (2.9) shows, the diffraction cones normal to the crystal planes, called Kossel cones, are projected into a phosphorescent screen, giving rise to Kikuchi bands. From the EBSD pattern, using the software QUANTAX CrystAlign database, it is possible to obtain the crystal phase, the orientation and the planes which give rise to each Kikuchi band. In addition, diagrams known as "pole figures" can be extracted. These figures represent the pole distributions, i.e. the crystallographic plane normals. In the case of a monocrystalline sample, the pole figure displays poles concentrated in certain orientations. The pole which passes exactly in the center of the stereographic projection corresponds to the crystalline plane parallel to the top facet of the wire. More detailed information about the basic concepts and applications on EBSD can be found in ref. [76].

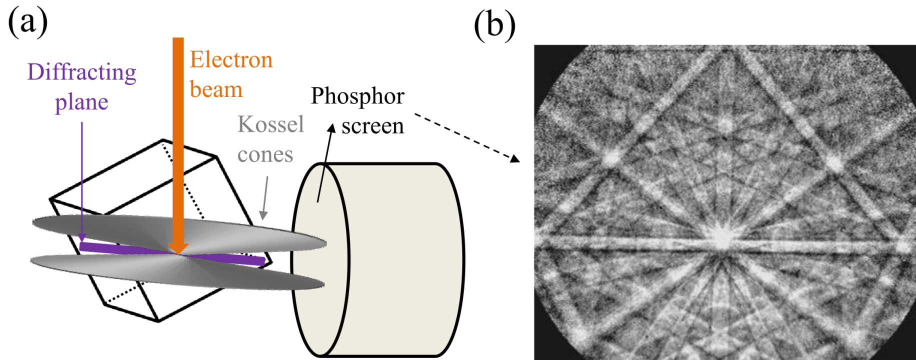

Figure 2.9: (a) Diagram showing the origin of the Kikuchi bands which form an EBSD pattern. (b) Example of an EBSD pattern, measured on a Si wafer.

2.2.2 Transmission Electron Microscopy (TEM)

A TEM is an electron microscope which forms an image from the collection the transmitted electrons through a thin sample. The fundamental parts of a TEM instrument are shown in figure (2.10).

In this thesis, two TEMs were used from the RTP of the University of War-

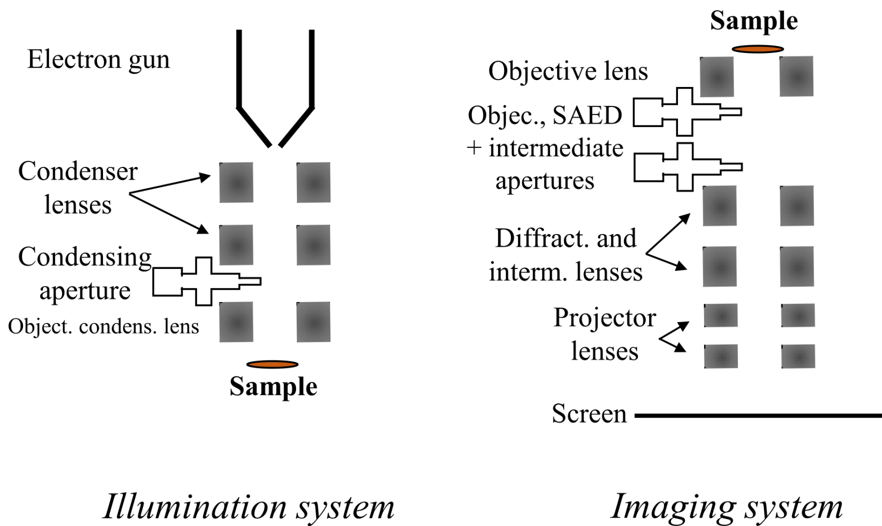

Figure 2.10: Diagram showing the main parts of a Transmission Electron Microscope.

wick (UK): a JEOL 2100 and an ARM 200 aberration-corrected Scanning TEM (STEM), both in collaboration with Prof. Ana Sánchez of the University of Warwick and co-workers. Part of the results obtained in these microscopes were acquired during a short stay of 2 months at the University of Warwick under her supervision. Besides, a TEM 3000F from the Spanish National Center for Electron Microscopy (ICTS) was used for EDS analysis of the crossed-wires in chapter 4. In all the cases, the micro- and nanostructures were gently deposited on standard TEM copper grids with carbon film.

2.2.2.1 Basics of TEM

With the TEM we can obtain images both in real space and reciprocal space, which arise from the interaction of the transmitted electrons with the sample. In the first case, different contrast mechanisms from the sample such as the mass-thickness contrast and the phase contrast give rise to different types of real space images, as it will be explained further on. Let us begin with the second case, i.e. reciprocal space information, obtained from electron diffraction patterns.

Selective Area Electron Diffraction (SAED)

In order to study the atomic structure of nanomaterials, high energy radiation must be used, as its wavelength must be equal to or smaller than the distances between atomic planes. Historically, the crystallography of the materials was deduced from X-ray diffraction techniques. The most widely used X-ray source is the Cu Kα line, with a wavelength of 0.15 nm. X-ray diffraction occurs in every crystalline material and it is based on the well-known Bragg law:

$$m\lambda = 2d_{hkl}\sin(\theta) \tag{2.2}$$

Where λ is the radiation wavelength, d_{hkl} is the interatomic distance, θ is the scattering angle and m is an integer. This law is also valid when the incident radiation are electrons with a given wavelength. In a TEM, the electron energy is typically 200 keV (one order of magnitude higher than in an SEM), which corresponds to a wavelength of $\lambda_e = 0.025$ Å, small enough to have high-resolution diffraction patterns. As the crystalline interatomic distances are of a few angstroms, which is much greater than λ_e, the electron diffraction angles tend to be very small; around 0-2 degrees. Therefore, the diffraction planes are almost parallel to the incident electron beam. The zone axis (ZA) is then defined as the crystal direction which is (almost) parallel to the electron beam.

Figure (2.11) is a schematic illustration of the geometry of electron diffraction. The distance, r, between the transmitted spot and the diffracted spot in the screen can be related to the interatomic distance by using Bragg's law. This, along with the symmetry of the diffraction pattern in the screen, allows for the indentification of the crystalline phase and the crystal orientation of the nanostructures with very high spatial resolution.

In order to obtain (SAED) patterns, the intermediate lenses are tuned in order to project the diffraction pattern into the screen. In addition, the objective aperture is removed and an aperture, called SAED aperture (see figure (2.10)), is placed in order to block most of the electron beam, thereby allowing selection of a small area of the structure. This is its main advantage of the technique over X-ray Diffraction; electron optics allow us to select single nanostructures, and even single areas within the nanostructure, and obtain their diffraction patterns.

Bright field (BF) and dark field (DF) images

Once the concept of electron diffraction has been explained, let us move to the image collection of a TEM. In essence, the concept of bright field (BF)

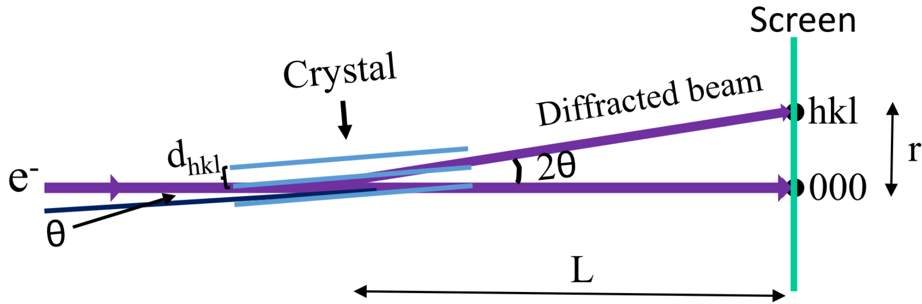

Figure 2.11: Schematic illustration of the geometry of electron diffraction. The diffracting crystal planes form a very small angle, θ, with the electron beam.

TEM image can be seen analogous to how a light slide projector works. In a slide projector, a light beam shines on a slide and only "empty" parts of the slide are seen as bright on the screen, while different contrasts made by the slide pattern are replicated on the screen with darker tones. In a similar way, electrons which are transmitted through the sample without deviating (i.e. the central spot in the diffraction pattern) form the bright field image. Areas with higher thickness or which contain atoms which are heavier will result in a lower intensity of the central diffraction spot and will therefore appear darker in this image.

A complementary image can also be formed in the TEM. If, instead of selecting the central spot in the diffraction pattern, we select one of the diffracted spots, we have a dark field (DF) image. In this case, the image contrast is inverted, and the areas with higher mass-thickness will appear brighter.

High-Resolution TEM (HRTEM) images

So far, we have focused on contrasts regarding the amplitude of the electron beam. However, is is well known from the wave-particle duality that electrons have both an amplitude and a phase. In fact, most of the dispersion mechanisms in the sample involve a phase change, but in contrast imaging the objective aperture is made small enough to make these changes unnoticeable. HRTEM images are the result of the opposite: several diffracted beams and the transmitted beam are allowed to pass through the objective aperture and the result of their interference gives rise to a high-resolution image. Therefore, HRTEM images are formed from the phase change of the electron wavefunction instead of its amplitude change.

In order to obtain an HRTEM image, the crystal must be tilted in order to have the electron beam parallel to a low index crystal direction. This way, planes parallel, or close to parallel, to the electron beam will be close to the Bragg condition, equation (2.2 and figure (2.11)), and so will diffract and form the interference pattern with the direct beam. This leads to the HRTEM image.

The resolution of HRTEM can range from 0.1 to 0.3 nm, which is enough to resolve atomic columns. However, several factors such as sample thickness changes or lens aberrations tend to limit the final resolution. Due to this, it is possible for the same sample in the same microscope to have an image in which dark spots correspond to columns of atoms, spaces between them or even a pair of atomic columns. The HRTEM image interpretation depends on the analyzed sample and sometimes further analysis is required.

2.2.2.2 Scanning Transmission Electron Microscopy (STEM)

As figure (2.12) shows, in STEM operation, the electron beam is condensed to a point and scans across the sample in a raster pattern, in a similar way to the SEM by scanning coils. Currently, many modern TEMs are equipped with scanning coils which enable both TEM and STEM mode to be used. These machines are called (S)TEMs. Many (S)TEMs have an extra prefix: ARM. This indicates that they have been aberration-corrected in the illumination and/or the imaging lens system.

One of the strengths of an (S)TEM is the ability to collect more than one signal in a highly spatially-resolved way: As well as BF and annular dark field (ADF) images, the latter which is explained in the next section, other detectors such as X-ray detectors can be placed.

Because of the large size of the detector with respect to the diffraction angles, ADF imaging is insensitive to fine details of the interference pattern and is instead very sensitive to the overall intensity. This makes ADF images more intuitive than HRTEM images: as explained in DF images, regions with higher signal correspond to atom positions whereas vacuum corresponds to a dark signal. Moreover, as the scattered intensity is approximately proportional to Z^2, where Z is the atomic number, the images show a contrast between atoms from different elements. This technique is able to reach atomic resolution, although probe aberrations and imperfections of the scanning system, where the position of the beam does not perfectly correspond to the pixel grid of the image, must be taken into account.

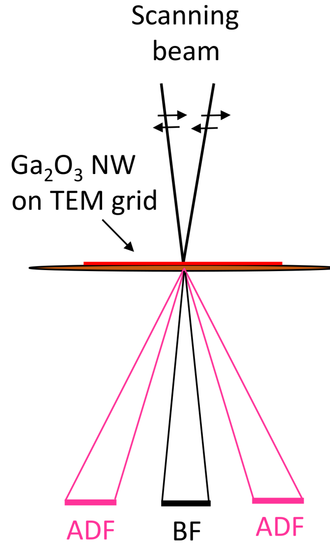

Figure 2.12: Simplified diagram of the STEM image formation.

At the same time, characteristic X-ray emission allows the measurement of EDS maps and spectra with a higher spatial and spectral resolution than at the SEM. More information on this technique is found in subsection 2.2.1.2.

More information about TEM in general and STEM in particular can be found in refs. [77], [78].

2.2.3 Fluorescence Spectroscopy

This section introduces the concept of PL in the context of the fluorescence spectrometers used in this thesis, which are an Edinburgh FLS1000 system and a Horiba Jobin-Yvon LabRam HR800 system coupled to an Olympus BXFM-ILHS microscope. They are part of the infrastructure of our research group at the UCM. In this thesis, I also used, during a 3 months short stay at the Institute of Solid State Physics (IFP) of the University of Bremen, a similar confocal microscope coupled to a Clark MXR Inc. Yb-doped fiber oscillator laser source (more details in section 2.2.4). With all of this equipment, several PL-related techniques have been performed, as described below.

2.2.3.1 Photoluminescence (PL) and PL Excitation (PLE)

PL is analogous to CL, which was explained in subsection 2.2.1.1, with the difference that the exciting particles are photons instead of electrons. These photons have a specific energy which is in the order of a few electronvolts instead of thousands of electronvolts. This allows for the selection of the electron absorption transitions which generate the photon emissions, unlike in CL. This and the different excitation density of the experimental setup can result in differences in the relative intensities of the energy bands observed in CL and PL, as it will be shown in more detail in chapter 3. More information about luminescence in general and PL and CL in particular can be found in ref. [79].

In this thesis, PL was generally measured in the above-mentioned Horiba confocal microscope (as will be detailed in 2.2.4.1) owing to its spatial resolution, however, for unintentionally doped (UID) and zinc doped Ga_2O_3, PL was also measured in the FLS1000 system for reasons explained in the next paragraph and in subsection 2.2.4.1. This system is based on a continuous Xe lamp and a monochromator which selects the excitation energy of the radiation. The emission is then collected by placing a second monochromator after the sample and varying its collection along the selected range of interest.

In order to have an intense PL signal, significant absorption must take place at the energy of the incident source. After the electrons are excited to higher energy bands or levels, they return to their equilibrium states via radiative and/or non-radiative transitions, the former results in the PL signal and the latter generally results in heating of the material. The technique showing the excitation energies which give rise to a given emission energy is known as PL Excitation (PLE). Our fluorescence spectrometer can measure PLE spectra by just switching the roles of the two monochromators with respect to a PL measurement: now the one placed after the sample for detection is fixed at a certain photon energy while the one before the sample is used to vary the excitation photon energy. This technique can be useful to get an insight of the effect of certain dopants on the band structure of the material.

2.2.3.2 Time-Resolved PL (TRPL)

Each one of the luminescent processes shown in figure (2.7) has its characteristic lifetime, which, for the materials studied, is in the range of nano- to microseconds. For TRPL in the fluorescence spectrometer, instead of the Xe

lamp, a pulsed LED with wavelength 256.8 nm was used as the excitation source. The pulse width is around 1 ns and the pulse period (time between pulses) can be changed from 50 ns to 50 µs.

Two types of measurements can be made. In the first type of measurement, the intensity of the luminescence centered at a certain energy (selected by the monochromator placed after the sample) is monitored in time and the luminescence process' decay time constants are obtained, as long as they are below the pulse period.

The second type of measurement is a time integrated PL spectrum. This spectrum presents intensity with respect to the energy of the emitted light, showing the luminescent bands in a similar way to the PL spectra obtained with a continuous laser. However, as the incident radiation is pulsed, with separation between pulses of tens of nanoseconds, luminescent processes which have different decay times will result in different relative intensities in this spectrum with respect to an analogous continuous PL spectrum.

Finally, a time-resolved emission spectroscopy (TRES) diagram can be obtained, which combines both types of measurements. In it, the intensity of the luminescence (photon counts) is shown both with respect to the emission wavelength and the time after the excitation pulse in a contour plot. This 2D contour plot allows for a complete visualization of the decay times of the different PL bands in the sample.

2.2.4 Optical spectroscopies in a confocal microscope

An optical microscope is not generally used to analyze the morphology of a nanostructure due to its low spatial resolution originated by the diffraction limit of visible light. However, once a nanostructure is located and analyzed by electron microscopy, even if the optical image does not provide additional morphological information, optical micro-spectroscopy can be performed and complementary data to the electron microscopy data can be obtained. In this thesis, the confocal instruments used provide useful optical microscopy and micro-spectroscopy measurements, as it will be shown throughout the manuscript.

A confocal microscope is an optical microscope which is based on the reduction of the image degradation and/or an improvement of the spatial resolution of the spectra by collecting, scanning point to point, only the light originated from the microscope's focal plane. This is achieved by means of a pinhole, which blocks light travelling from areas above or below this

plane. This results in the reduction of the width of the Point Spread Function (PSF), which describes the intensity distribution of a point object in the image plane. In our context, it is especially important to notice that in these microscopes the area from which the spectrum is acquired is only of some microns squared instead of the area of the whole image. A basic diagram of the confocal optics is shown in figure (2.13).

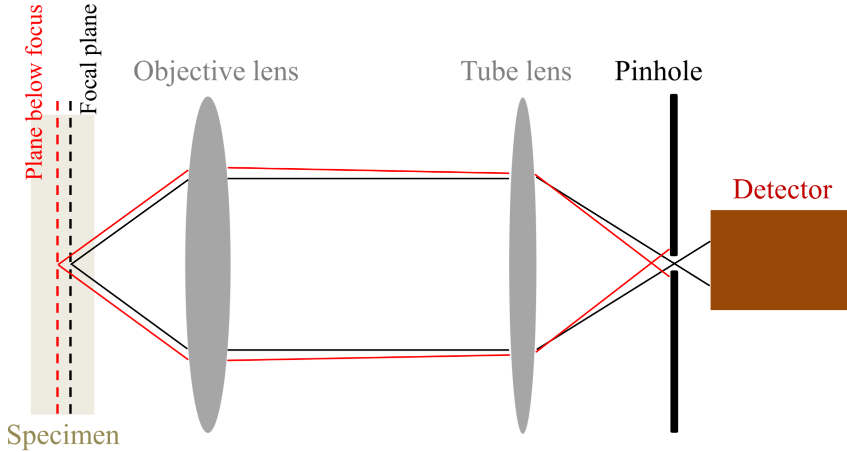

Figure 2.13: Confocal optics, showing a light ray coming from the focal plane of the sample (black rays) and from another plane (red rays). Out of focus light is blocked by the pinhole, and this improves the image and/or spatial resolution of the spectra with respect to a conventional optical microscope.

Two optical spatially-resolved micro-spectroscopies were performed with the aforementioned Horiba Jovin-YVON LabRam HR800 system: micro-PL (μ-PL) and micro-Raman (μ-Raman) spectroscopy. The experimental setup is shown in figure (2.14). As it will be shown in the next subsections, in both spectroscopies an intense monochromatic source is necessary. In the materials physics laboratory of Madrid a He-Cd ($\lambda = 325\,\mathrm{nm}$) laser which is implemented in the aforementioned system, was used as the excitation source. In addition, a similar Horiba LabRam μ-PL system was used at the IFP of the University of Bremen during my 3 months short stay. In this system, a diode-pumped Yb-doped fiber oscillator laser, frequency doubled to emit wit E = 4.82 eV ($\lambda = 256.8\,\mathrm{nm}$), was used as the excitation source.

In both optical systems, the laser light is directed by a set of mirrors and focused towards the sample by an objective lens. The optical image is

collected by the video camera. As shown in figure (2.14), the scattered and emitted light from the sample follows a different path: it is collected by the lens, spectrally divided by a spectrometer and collected by a refrigerated CCD camera. In our equipment, the pinhole is placed on the spectrometer path, hence the confocal improvement is on the spatial resolution of the spectra and not of the optical image. A polarizer can be placed before the spectrometer in order to collect the emission which is polarized vertically, horizontally or in any direction in between.

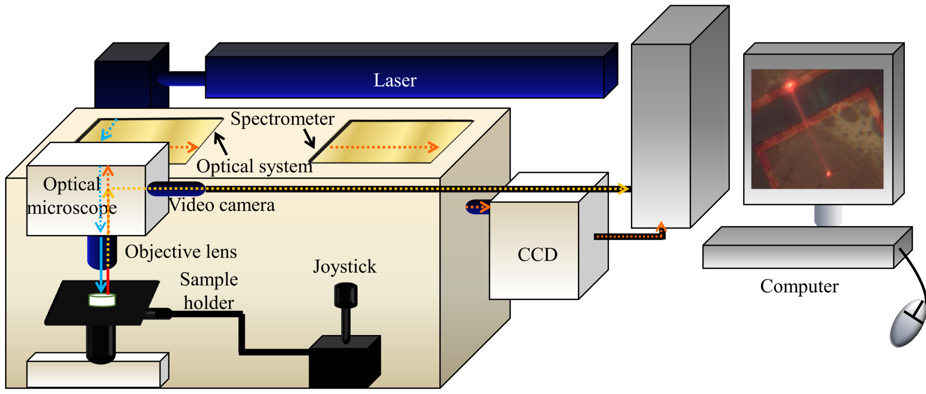

Figure 2.14: Experimental setup of the confocal microscope, used for μ-PL and μ-Raman spectroscopies, adapted from [80]. Arrows indicate the path that the incident light (in blue) and the collected light, both for images (in yellow) and spectra (in orange) follow. In the computer screen there is an example of an image collected by the confocal system. As the laser incident on the Ga_2O_3:Cr wire, it emits red light, which can be recorded both by the video camera and the CCD system.

2.2.4.1 Micro-PL

PL was explained in subsection 2.2.3.1. The main advantage of a μ-PL system is that we can select individual structures and, more importantly, areas of nanostructures, to be excited, with a resolution equal to the area of the laser spot. Furthermore, as explained in the previous subsection, light is collected only from an area around the collection point. This gives rise to two types of measurements. In the "aligned" mode, which is the usual mode, both the excitation and the collection points (more precisely, the excitation and collection areas) are virtually the same. In the "unaligned" mode, the excitation and the collection areas are separated spatially by a few microns [81]. This is achieved by slightly shifting the mirrors that guide

the laser light towards the objective lens (placed in the optical system in figure (2.14)) so that the excitation point is out of axis with the objective lens. This way, light emitted from the excitation point is effectively blocked. Figure (2.15) shows two PL images on a silicon substrate displaying these two main μ-PL measurement setups (figure (2.15) (a) and (c)), as well as a light ray diagram depicting the unaligned mode (figure (2.15) (b)).

As the available lasers in our setup at the Materials Physics laboratory of the UCM emit with energies below the band gap of gallium oxide (E_{exc} = 3.8 eV < 4.8 eV), a very low PL signal is observed with this optical system for undoped Ga_2O_3 and for Ga_2O_3 doped with most elements. Instead, the PLE spectrum of Cr-doped Ga_2O_3 [54] has an intense emission when excited with the 3.8 eV energy of the He-Cd laser, hence we can use this laser for PL measurements in Ga_2O_3:Cr wires, as we will see in chapter 5. In the other μ-PL spectra displayed in this thesis, we used the aforementioned 4.82 eV fiber oscillator laser.

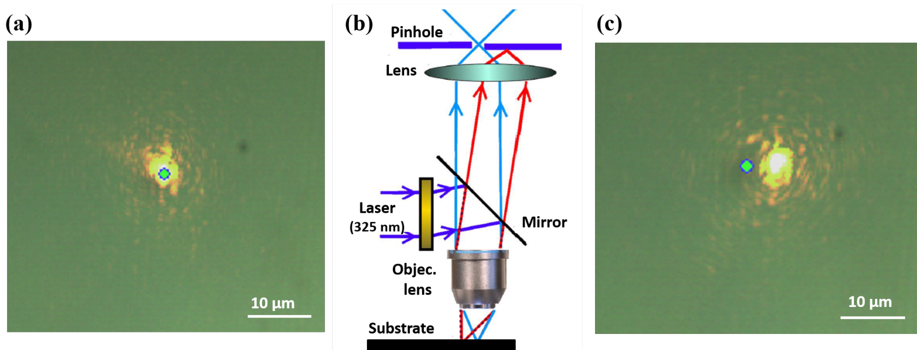

Figure 2.15: (a) PL image of a silicon wafer showing the aligned mode on the confocal microscope (b) Diagram depicting the unaligned mode in this microscope, adapted from [81]. Blue rays stem from the collection area while the red rays stem from the excitation area. (c) PL image of a silicon wafer showing the unaligned mode on the confocal microscope. In both PL images, the yellow spot shows the He-Cd laser spot and the collection point is shown in blue.

2.2.4.2 Micro-Raman Spectroscopy

When the laser radiation strikes on a material, most of the light impinging on the sample is scattered elastically, i.e. has the same energy as the incident light. However, a small percentage (under 10^{-3}%) results in a small energy change of the radiation, i.e. in inelastic scattering. This is known as Raman

scattering and its origin is the interaction of the light oscillation with the molecular or lattice vibrations, whose quanta are known as phonons, of the sample. They are characteristic of the crystal structure of the material.

A Raman spectrum displays the intensity of the Raman active phonon modes (modes which involve a polarizability change) with respect to their wavenumber, which is proportional to the energy change of the incident light. This energy change is known as the Raman shift and its standard units are cm^{-1} for historical reasons. Note that 1 cm^{-1} = 0.124 meV.

Due to the small energy change with respect to the incident energy and the small percentage of photons that are Raman scattered, an intense monochromatic light with an energy below the band gap, like our He-Cd laser light in the case of Ga_2O_3, is necessary as the incident source. As discussed in the beginning of this section for μ-PL, μ-Raman spectroscopy allows the identification of the crystal phase of not only individual micro- and nanowires, but also of areas within the microwires with a large enough size to be resolved by the laser beam. More information about Raman spectroscopy can be found in refs. [82].

2.2.5 X-ray Photoelectron Spectroscopy (XPS)

XPS, also known as ESCA (Electron Spectroscopy for Chemical Analysis) is a surface-sensitive analytical technique from which valuable chemical information of the sample can be obtained.

The XPS system used in this thesis is the ESCAmicroscopy line at Elettra Synchrotron in Trieste (Italy). The synchrotron allows for an intense and monochromatic source and the ESCAmicroscopy line has spatial resolution of around 200 nm, owing to the focusing of X-rays by means of Fresnel zone plates, which consist of radially symmetric opaque and transparent rings.

The depth of analysis in XPS can be estimated from the attenuation length λ, which expresses the depth from which 63.2% of the electrons come from. This parameter has a different value depending on the kinetic energy of the emitted photoelectrons as well as on the material analyzed, ranging from 3 to 20 Å.

Figure (2.16) is a diagram of the phenomenon of XPS. It is similar to figure (2.8) but in this case the incoming source is a soft X-ray, with an energy of hundreds of eV, and the analyzed particle is an electron removed from the core level. Its binding energy (BE) is obtained from its measured kinetic

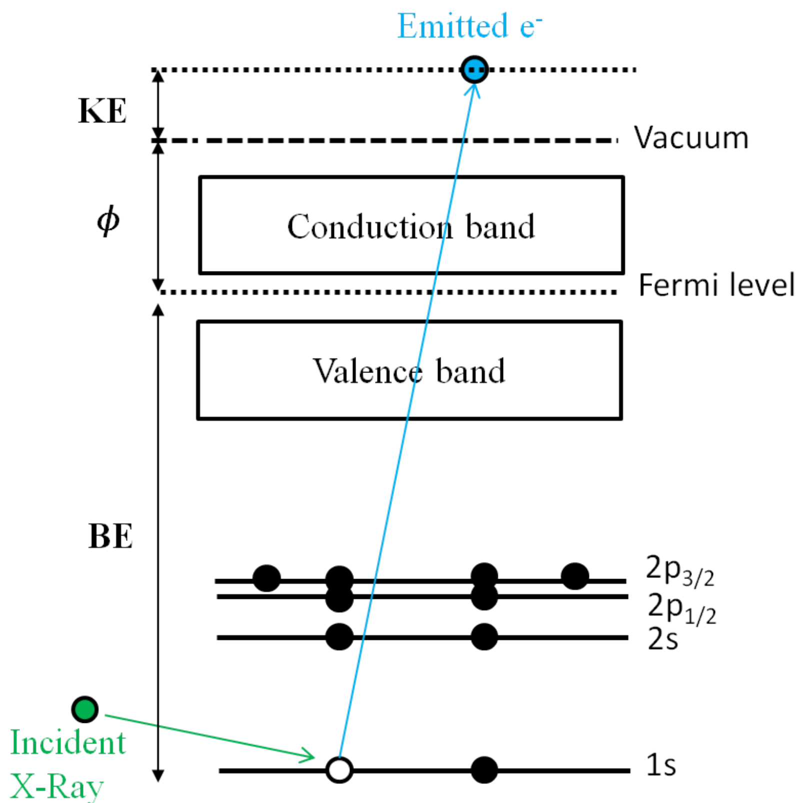

Figure 2.16: Generation of a photoelectron in an atom when it is bombarded by an X-ray photon. In this example, the electron is removed from the 1s level.

energy (KE) by applying equation 2.3:

$$KE = h\nu - BE - \phi \tag{2.3}$$

where ϕ is the work function. Similar to EDS, the value of the BE is the parameter which identifies the electron, both in terms of its parent element and its atomic level. In addition, it is sensitive to the oxidation state and the chemical environment of the atom; for instance, a higher oxidation state implies a lower screening of the valence electrons hence a higher BE. This is known as chemical shift. BE values for the elements in different oxidation states can be found in the NIST database [83]. More information about XPS can be found in ref. [84].

Chapter 3

Influence of Zn or Ge doping in Ga_2O_3 nanostructures

It is well known that very low amounts of dopants can result into severe modifications of the physical properties of Ga_2O_3 [25, 29, 85]. As commented in the Introduction of this thesis, a deeper understanding of the effects of different dopants on the properties of Ga_2O_3 is currently one of the main requirements for a more widespread development of Ga_2O_3 devices. This is especially important in the nanostructured form, in which doping may not only affect the optical and electrical properties of Ga_2O_3 but, under certain growth conditions, may also modify the morphology and dimensions of the resulting structures. In this chapter we will explore the effect of one of the few possible p-type dopants (Zn) and of one of the main n-type dopants (Ge) in the morphological, structural and optical properties of Ga_2O_3 nanostructures.

Regarding Zn, some theoretical [86] and experimental [87] reports considered this dopant one of the few good candidates for p-type doping in the Ga_2O_3 host. However, recent theoretical studies indicate that Zn acceptors have ionization energies larger than 1 eV [18]. Furthermore, p-type doping is very challenging in Ga_2O_3 due to the small dispersion in its valence band. Nonetheless, acceptor impurities in Ga_2O_3 are still important for controlling electrical conductivity [16] and, as we will see throughout the chapter, the acceptor-induced recombination levels are also interesting from the optical

point of view.

In the bibliography, successful n-type doping has been reported in Ga_2O_3 by incorporating Si, Sn or Ge among other elements, within a donor concentration range of six orders of magnitude (10^{14} to 10^{20} cm^{-3}) [4, 16]. In the nanostructured form, the incorporation of Sn in Ga_2O_3 by thermal evaporation methods has been thoroughly explored. It has been found that it influences the final morphology of the nanostructures, and its incorporation in Ga_2O_3 gives rise to luminescence bands in the visible range [40] or structures with improved gas sensing [88].

Silicon and tin has also been thermally incorporated in Ga_2O_3 nanowires, with dopant density of a 1% at. [89]. However, due to the high melting point (MP) differences between germanium and gallium oxides, the incorporation of Ge into Ga_2O_3 nanostructures had not been studied before the work displayed in this chapter, despite the promising properties exhibited by Ge doped Ga_2O_3 films [90]. In particular, bearing in mind the ionic radii of the group IV ions [14] with respect to Ga^{3+}'s, Ge impurities were proposed to be a potentially more effective dopant than Sn or Si in Ga_2O_3 due to the Ge^{4+} ion preferring the tetrahedral (4-fold coordinated) Ga (I) site instead of the octahedral one [15, 91].

3.1 Synthesis and structural analysis of Ga_2O_3:Zn structures

The first part of this chapter, related to Ga_2O_3:Zn structures, builds from preliminary work [58] regarding their synthesis and structural analysis. A brief summary of this work is presented in this section, along with our EDS and Raman measurements. Then, we will focus on our thorough luminescent analysis of Ga_2O_3:Zn, which is completely novel with respect to previous works.

The analyzed structures were synthesized in a tubular furnace at 925°C during 4 hours with an Ar flux of 0.8 l/min. The precursors were a Ga_2O_3 pellet, a metallic Ga piece and ZnO powders. After the treatment, a large amount of nanostructures were formed on top of the pellet. As the zinc oxide precursors have a much higher MP compared to the synthesis temperature and as no zinc or gallium particles were found on the structures, the growth mechanism was tentatively assigned to VS, although the coexistence of VLS mechanisms cannot be ruled out.

Figure (3.1) (a) shows a low magnification SE image of some of such structures. Instead of Ga_2O_3 nanowires, which were produced under the same conditions without Zn-related precursors, the obtained structures tend to have a belt-like morphology, i.e. one, instead of two, of the dimensions (depth) is substantially small, tens of nm, while the other two (width and length) have a micrometer-range size. The structures have lengths of 10 to 200 µm and some present width changes while others maintain their belt-like morphology throughout their length. Some of the structures were deposited on Si by grabbing them gently with tweezers and letting them fall down on top of the Si wafer. This way, individual micro- and nanobelts could be analyzed, although the majority of the structures were still in smaller agglomerated groups due to electrostatic attraction, as shown in figure (3.1) (b).

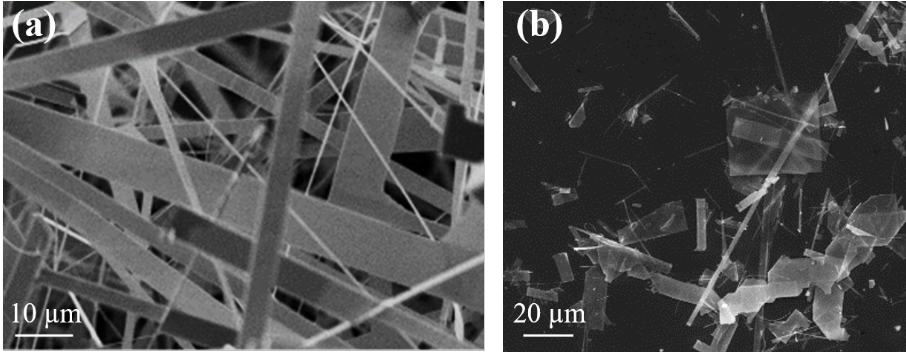

Figure 3.1: SE images of the microbelts and microwires obtained after the thermal treatment including ZnO powders. The images display structures (a) lying on top of the Ga_2O_3 pellet (b) deposited on a Si substrate.

In order to obtain information about the local atoms' environment in the lattice, we performed μ-Raman spectroscopy in several Ga_2O_3:Zn structures. A representative μ-Raman spectrum is shown in figure (3.2) (a) along with a spectrum from a reference unintentionally doped (UID) Ga_2O_3 microwire. The Raman modes obtained for both structures have a Raman shift of $169\,cm^{-1}$, $200\,cm^{-1}$, $320\,cm^{-1}$, $346\,cm^{-1}$, $416\,cm^{-1}$, $476\,cm^{-1}$, $630\,cm^{-1}$, $653\,cm^{-1}$, $658\,cm^{-1}$ and $767\,cm^{-1}$, as expected for Ga_2O_3 [92]. The peak at $520\,cm^{-1}$ is due to the first order optical phonon band of the silicon substrate in which the wires were deposited. No frequency shifts were observed, within the accuracy of the system, in any Raman mode for the Ga_2O_3:Zn belt with respect to the Ga_2O_3 reference structure.

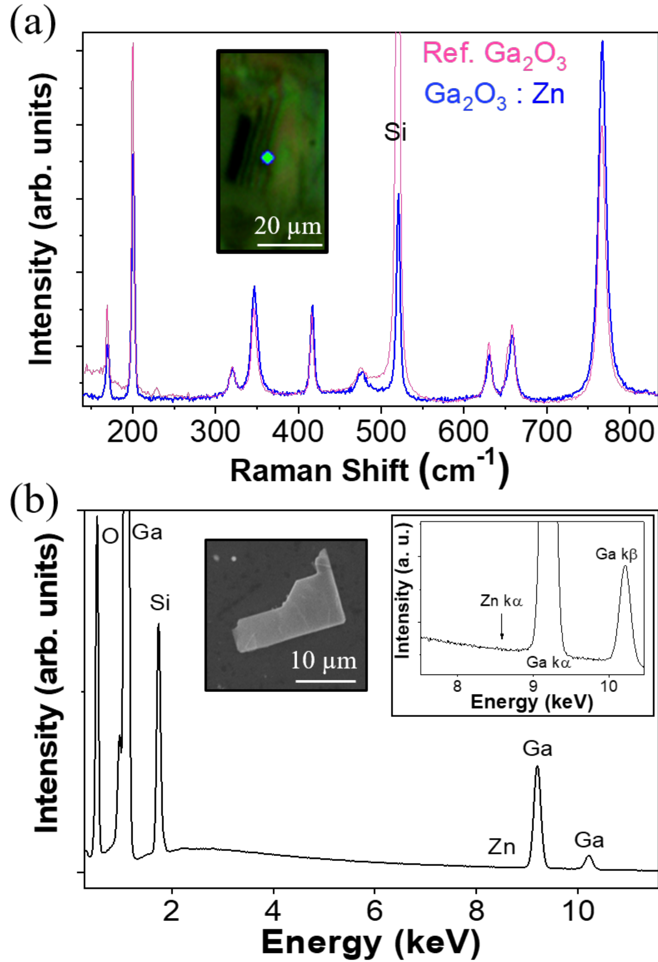

Figure 3.2: (a) Raman spectra from a reference UID Ga_2O_3 wire (pink) and from Ga_2O_3:Zn microbelts (blue). The inset shows the collection point of the latter spectrum. (b) Representative EDS spectrum of a Ga_2O_3:Zn belt. The peaks are labelled according to the emission lines of each element. The insets in (b) show an SE image of the analyzed structure and the magnified EDS spectrum in the 8-10 keV energy range.

In addition, the full width half maximum (FWHM) of the modes in the microbelts is very similar to that of the reference structure, which reveals their high crystalline quality. Some peak intensities are different in each sample. This is due to the anisotropy of the Ga_2O_3 lattice; different vibrational modes are enhanced depending on the relative orientation of these

kind of structures with respect to the incident laser polarization [93]. As the optical image shows (see inset of figure (3.2) (a)), the analyzed structure is formed by several microbelts piled on top of each other. For the spectrum shown in this figure, the structure has its long axis aligned parallel to the laser polarization, which is vertical on the image.

Elemental composition of these microbelts was determined by EDS analysis, which was performed on the SEM for several Ga_2O_3:Zn microstructures. A representative spectrum is shown in figure (3.2) (b). Both gallium and oxygen were detected with the expected proportions, while, for all the analyzed structures, the Zn content was found to be below the detection limit of the technique, i.e. below 0.5% at. It must be noted that intentional doping of semiconductor devices is generally in concentrations below 0.5% at.[62], therefore these results do not imply that the structures are not doped with Zn. Taking into account SEM analysis of the obtained structures in comparison to the same thermal treatment without Zn precursors, it can be deduced that the inclusion of Zn during the thermal growth influenced the morphology of the resulting nanostructures. In the next section we will see how the optical properties of the micro- and nanostructures have been altered with respect to undoped Ga_2O_3, and how these relate to the Zn incorporation in the Ga_2O_3 lattice.

3.2 Optical analysis of Ga_2O_3: Zn structures: CL, PL, PLE and TRPL

The optical properties of the Ga_2O_3:Zn belts were analyzed by several luminescence-related techniques such as CL, PL or time-resolved PL. These techniques often allow indirect impurity detection, below the EDS detection limit, through the radiative recombination paths among the eventual electronic states introduced in the band gap by the impurities. The luminescence of an UID Ga_2O_3 pellet grown under the same conditions is also shown in this section in order to assess the effect of Zn incorporation in the recombination levels of Ga_2O_3.

CL results

The luminescent properties of Ga_2O_3:Zn belts were first studied by means of CL in the SEM. Deconvolved CL spectra at room temperature (RT) and 100 K for both UID Ga_2O_3 and a representative Ga_2O_3:Zn belt are shown in figure (3.3). At 100 K, both the UID and the Zn doped Ga_2O_3 present

a broad UV band which can be deconvolved in two bands at 3.1 - 3.2 eV and 3.3 - 3.4 eV. As detailed in the Introduction, recent publications on the luminescence of Ga_2O_3 report the possibility of two different recombination paths in the UV, one due to electrons-STHs or to STEs and the other due to silicon (one of the main impurities in Ga_2O_3) donors and gallium-oxygen vacancy pairs or other acceptors [28]. In addition, at this temperature (100K) some contribution is expected from DAP recombinations, which tend to lie in the blue ($\sim$ 3.0 eV) range of the CL spectrum, and appear in the deconvolved RT spectra of both samples.

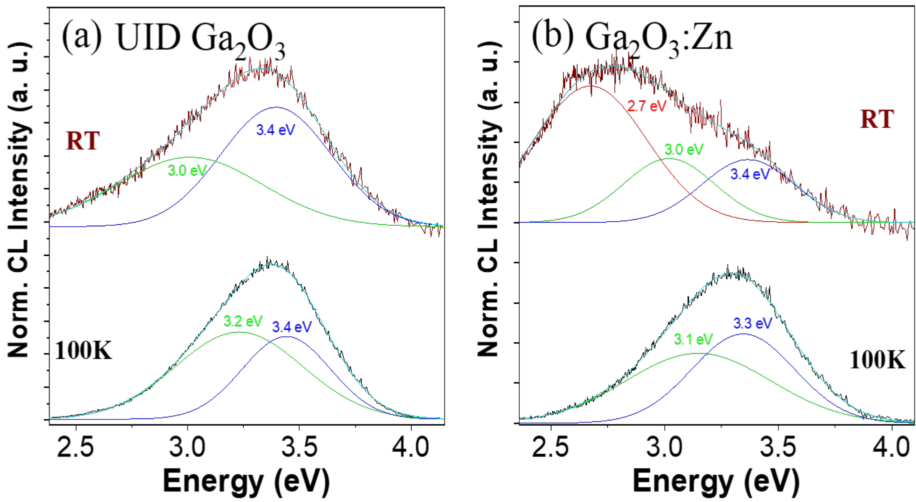

Figure 3.3: Deconvolved CL spectra at 100 K and RT of (a) Unintentionally doped (UID) Ga_2O_3 (b) a representative microbelt of the Ga_2O_3:Zn sample.

At RT, both for UID Ga_2O_3 and Ga_2O_3:Zn, our CL results show a less intense emission compared to the one at 100 K, as it is usual in most luminescence processes [79]. More importantly, a redshift is clearly visible between of our Ga_2O_3:Zn belts' RT CL spectrum and the one from the UID sample. The deconvolution of the Ga_2O_3:Zn luminescence gives rise to a novel blue-green CL band, centered at 2.7 eV, which is the most intense in the spectrum, along with the already-mentioned 3.0 eV (blue) and 3.4 eV (UV) bands.

Let us compare these results with the CL results of Ga_2O_3:Zn in the bibliography. Alema *et al.* measured CL of UID and Zn doped Ga_2O_3 thin films. The Zn doped thin films also featured a broad blue band emission at

2.7 eV, which did not appear in the UID sample. This novel blue emission was attributed to a DAP involving electrons in oxygen vacancies and holes in Zn_{Ga} defects. Furthermore, a CL band at 2.6 eV was reported to arise in other Ga_2O_3 samples allegedly containing acceptor levels [85, 94]. Hence the emergence of such band in our sample can be considered as a signature emission involving acceptor levels in Ga_2O_3. Further discussion about these emissions, and a comparison with the novel PL results of Ga_2O_3:Zn presented in the next pages, will be made in section 3.3.

PL and PLE results

In order to further study the luminescence properties of the Ga_2O_3:Zn structures, PL measurements were performed by using three different excitation sources: a Xe lamp, a pulsed LED (an EPLED) and a pulsed laser. All of them were described in section 2.2.3. In this section, we will focus on PL obtained with the first two sources. Additionally, the FLS1000 system in which the Xe lamp is mounted also allows for PLE measurements by selecting an emission wavelength and scanning different excitation wavelengths. Bearing in mind the equipment capabilities, the FLS1000 system PL-PLE results are from a group of Ga_2O_3:Zn structures deposited on Si (instead of from individual structures).

Figure (3.4) (a) shows a PL spectrum of the Zn doped microbelts. The excitation source energy was 4.96 eV, allowing for band to band excitation. This spectrum, as was the case of CL, presents the maximum luminescence intensity in the blue region (2.6 - 2.9 eV), but it contains some differences with the CL one. Its deconvolution results in the most intense PL bands centered at 2.5 eV and 2.8 eV, i.e. 0.2 eV redshifted with respect to the lower energy CL bands. The deconvolution also gives rise to a less intense UV band at 3.3 eV, comparable to the 3.4 eV CL band. These band shifts and intensity changes of PL with respect to CL are usually found [79] and can be explained with the differences in the excitation mechanisms in each technique, as it will be discussed in section 3.3. Nevertheless, the PL results can be qualitatively explained in a similar way to the previously discussed CL results.

Figure (3.4) (b) shows PLE spectra of the same Ga_2O_3:Zn sample compared to a UID Ga_2O_3 pellet for the emission wavelength of 450 nm, i.e. an energy of 2.76 eV. Quite a similar behaviour can be observed for the two samples, except for a slight broadening of the PLE curve for the UID pellet with respect to the Ga_2O_3:Zn sample. As by PLE we measure the energy

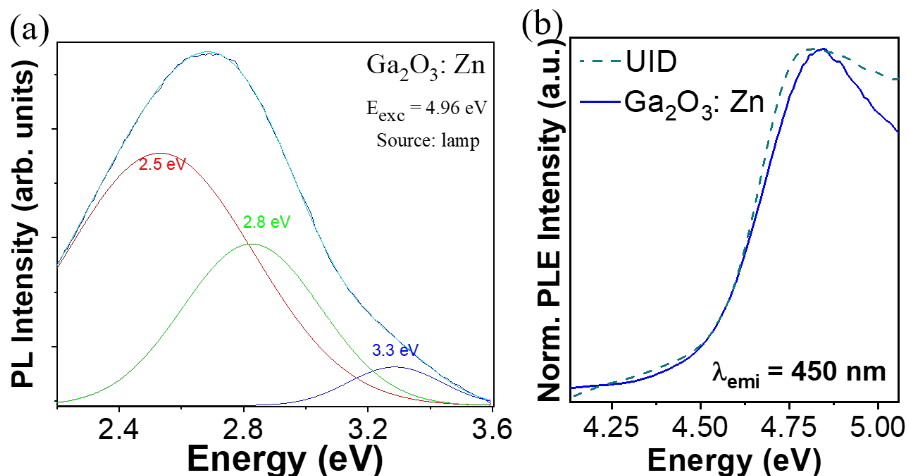

Figure 3.4: (a) Deconvolved PL spectrum from the Ga_2O_3:Zn microbelts exciting with continuous Xe monocromated lamp at E = 4.96 eV. The cyan line, which adjusts perfectly to the experimental results (in black), represents the convolution of the 2.5 eV (red), 2.8 eV (light green) and 3.3 eV (blue) bands. (b) Normalized PLE spectra obtained by setting the emission wavelength at 450 nm (2.76 eV) for Ga_2O_3:Zn (blue line) and UID Ga_2O_3 (dark cyan dashed line). All spectra from this figure to the end of the chapter were acquired at RT.

states' contribution to the visible emission in Ga_2O_3:Zn, it may indicate a modification of the density of states around the valence and conduction bands due to Zn incorporation in the Ga_2O_3 crystal lattice. The valence band in Ga_2O_3 is formed by O 2p states and, bearing in mind that there are three inequivalent oxygen positions in the monoclinic lattice [95], the PLE spectrum could be influenced due to the interaction of Zn with some of them.

Figure (3.5) shows the comparison of the normalized PL spectrum obtained when exciting with the continuous Xe lamp at 4.82 eV with the time-integrated PL spectrum obtained with a pulsed LED, with a frequency of 10MHz and the same excitation energy. In figure (3.5) (a) we can see that the UID Ga_2O_3 pellet did not exhibit any difference in the PL spectra with these two excitation sources, apart from a lower intensity when exciting with the pulsed LED. On the other hand, as shown in figure (3.5) (b), the Ga_2O_3:Zn sample shows a remarkable redshift with respect to the UID sample of around 0.4 eV when exciting with the pulsed LED, with the broad band peaking at 2.3 - 2.4 eV. A tentative explanation for these results will

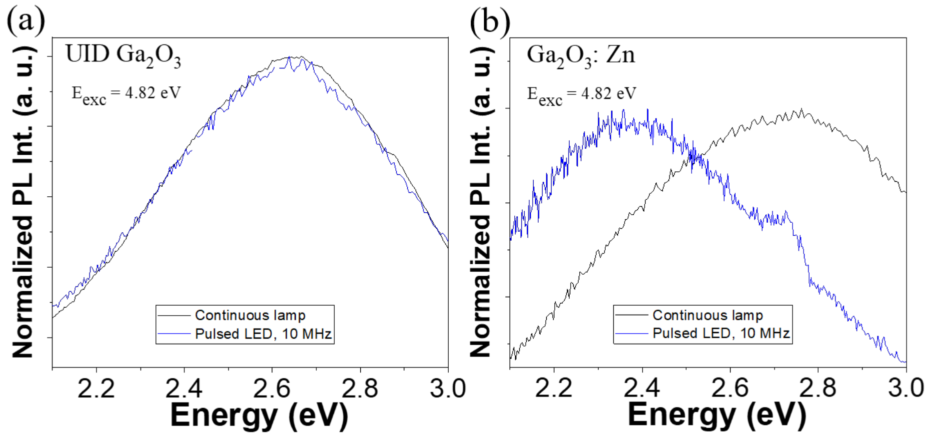

Figure 3.5: (a) Normalized PL spectra of UID Ga_2O_3 when exciting with the EPLED at 4.82 eV with a pulse frequency of 10 MHz (blue) and when exciting with the continuous Xe lamp at the same photon energy (black). (b) PL of the Zn doped Ga_2O_3 sample, again for EPLED excitation shown in blue and for continuous Xe lamp excitation shown in black.

be given in section 3.3.

Time-Resolved PL

In order to analyze the luminescence process dynamics, Time-Resolved PL (TRPL) measurements were carried out by using the pulsed LED as the excitation source. This source had already been used to obtain the time-integrated PL spectrum of figure (3.5). Like in such figure, the spectra were acquired for Ga_2O_3:Zn structures deposited on a silicon substrate.

Figure (3.6) (a) shows PL spectra taken at certain delay times, i.e. at certain times after the short-lived pulse had striked the Ga_2O_3:Zn sample. The time response of the UV emission ($>$ 3 eV) could not be measured by this system due to stray light from the EPLED in this range. The analyzed delay times were 2, 5, 10 and 30 ns, which are obviously shorter than the pulse period: 100 ns. From these spectra we can see that very shortly after the pulse, the dominant emission of Ga_2O_3:Zn arose from the blue region, i.e. around 2.8 - 3 eV. For delay times of 10 ns or higher, the relative intensity of the blue band decreased with respect to the green band centered in 2.5 eV. This suggests a higher lifetime of the green band with respect to the blue band. Remember that this band has only appeared in the PL and CL spectra of the Ga_2O_3:Zn structures.

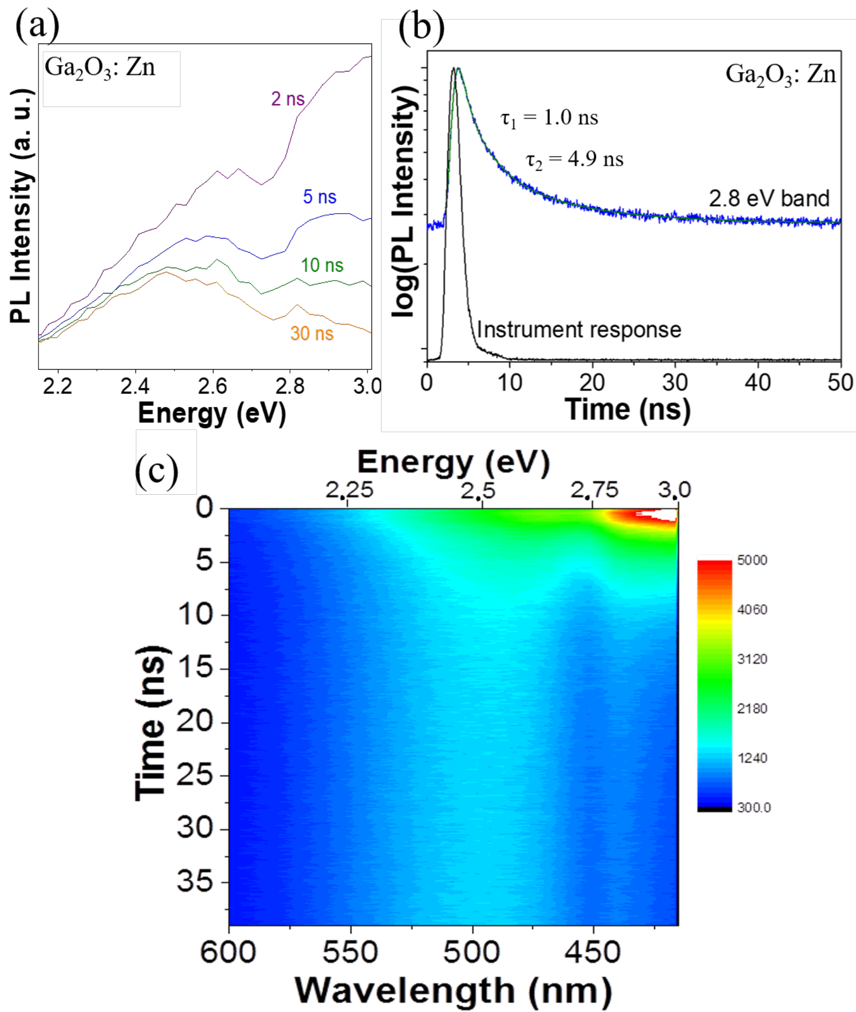

Figure 3.6: Time-resolved PL spectra for the Ga_2O_3:Zn sample with the 10 MHz (100 ns) EPLED, E = 4.83 eV, as the excitation source. (a) PL spectra obtained for different delay times (b) Decay profile for the sample at 2.8 eV emission energy, shown alongside the instrument response. (c) TRES contour map of the luminescence bands evolution. The colours indicate higher to lower photon counts for each (time-wavelength) point, as shown in the legend.

Figure (3.6) (b) shows a time profile for the 2.8 eV PL band of the Ga_2O_3:Zn sample. This time profile can be described by a sum of a constant and two decaying exponential functions:

$$a(t) = a_0 + a_1 e^{-t/\tau_1} + a_2 e^{-t/\tau_2} \tag{3.1}$$

where τ_1 and τ_2 are the time decay constants for each recombination process and a_0 is associated with a background radiative emission resulting from time decay constants much larger than the pulse period. The characteristic lifetimes were obtained by fitting the profile to this model, in which the instrument takes into account the instrument response, also shown in the figure. The obtained decay constants around 2.8 eV emission are $\tau_1 = 1.0 \pm 0.1$ ns and $\tau_2 = 4.9 \pm 0.7$ ns , which imply fast decaying recombination processes in this energy range. Due to having a decay time much longer than the EPLED pulse period, which is set at 100 ns, the time decay constant(s) for the 2.5 eV band could not be obtained with our measurement setup.

Figure (3.6) (c) shows a time-resolved emission spectroscopy (TRES) contour map, which combines the results obtained in figures (3.6) (a) and (b) and slightly extends the measurement range, both in energy and in time. In this contour map, two long decay energy bands can be observed. One is the already mentioned broad 2.5 eV green-blue band. The other one is a weaker intensity narrow band at 2.8 eV. Also, notice the faster decay in the blue range, as shown in fig. (3.6) (a). Finally, as expected, no emission is observed for energies below 2.3 eV.

Influence of the incident laser power on the PL

From the previous section, it is clear that in Zn doped Ga_2O_3 we have several competing luminescent processes with different decay times. In order to further understand such emission dynamics, we made additional PL measurements on these structures with the aid of a pulsed fiber oscillator laser (detailed in section 2.2.3) of frequency 16 MHz (pulse period = 63 ns). This laser is inserted in an confocal microscope system, therefore individual microbelts were selected for μ-PL measurements. The laser emits at 4.82 eV, allowing for band to band excitation in Ga_2O_3. The power of this laser was reduced from its operating value (around 0.4 mW) by inserting certain filters in its optical path before it striked the sample. The filters reduced the pump power to 10%, 3.2% and 1% with respect to its initial value, however a "high-medium-low-very low" label is used in figure (3.7) due to small power oscillations of the pulsed laser between the measurements.

Power-dependent PL measurements of UID and Ga_2O_3:Zn samples are displayed in figures (3.7) (a) and (b), respectively. The spectra show the UV emission of Ga_2O_3, peaking at around 3.1 and 3.6 eV, along with a lower

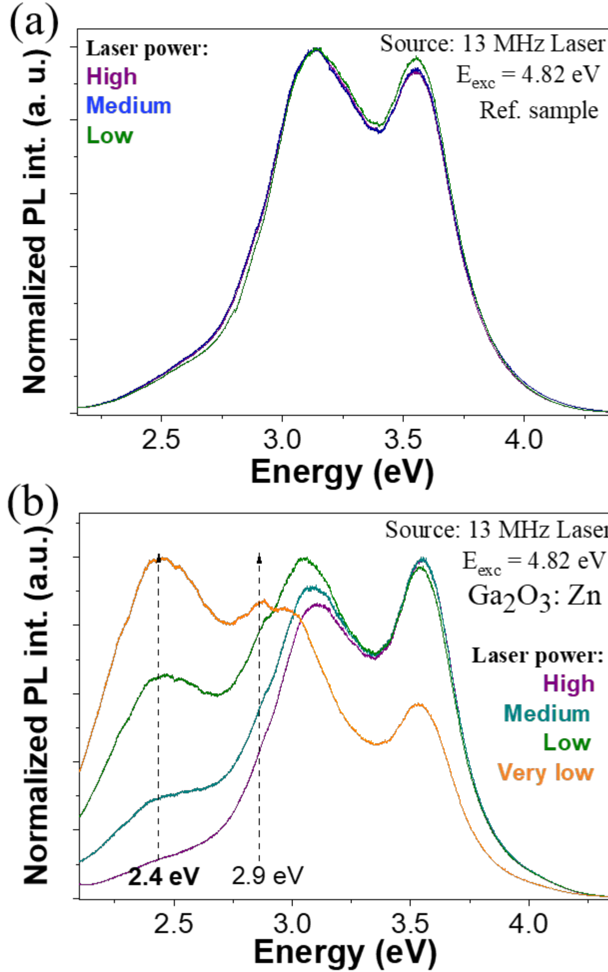

Figure 3.7: Normalized μ-PL spectra with a 4.82 eV fiber oscillator laser as excitation source. (a) for the UID Ga_2O_3 commercial sample at high (purple), medium (blue) and low (green) laser power. (b) normalized spectra for the Ga_2O_3:Zn sample at high (purple), medium (blue), low (green) and very low (orange) laser power. With respect to the "high" label (around 0.4 mW), the "medium", "low" and "very low" labels indicate the use of 10%, 3.2% and 1% power filters, although we prefer to use these labels as there were some power variations in the laser during the measurements. Dashed arrows indicate the two energy regions which increase in relative intensity with respect to the UV emission when the laser power decreases.

intensity blue band at around 2.7 eV. Both these and the Zn doped Ga_2O_3 spectra had been tentatively deconvolved. However, after analyzing these

and other samples, we believe that the CCD in this system has different (probably higher) sensitivity along the UV range which can give rise to misleading deconvolutions. Therefore, the analysis will be focused on the relative differences of both Ga_2O_3:Zn belts and UID Ga_2O_3 when the pumping power of the incident laser is reduced.

While in figure (3.7) (a) it is clear that the relative intensities of all the bands are constant for UID Ga_2O_3, figure (3.7) (b) shows a clear redshift in the Ga_2O_3:Zn sample as the laser power decreases. Arrows indicate the relative intensity increase of both in the blue (around 2.9 eV) and, especially, in the green (around 2.4 eV) part of the spectra. This important difference in the Ga_2O_3:Zn microbelts with respect to the UID reference sample is discussed along with the previous results in the next section.

3.3 Discussion on the luminescence of Ga_2O_3:Zn

As shown in the previous section, the luminescence properties of Zn doped Ga_2O_3 microbelts have been studied in order to assess the role of Zn impurities in the Ga_2O_3 host. Different energy excitation conditions have allowed for a better understanding of the luminescence mechanisms in Ga_2O_3:Zn.

Firstly, by RT CL, we obtained for Ga_2O_3:Zn microbelts a broad blue-UV spectrum which can be deconvolved into bands at 2.7, 3.0 and 3.4 eV (see figure (3.3) (b)). These results are similar to the previous CL reports [96, 97], in which the luminescence in Ga_2O_3:Zn presents a redshift with respect to the UID sample due to the emergence of a 2.7 eV band which is not present in UID Ga_2O_3. This band was attributed to a DAP recombination between electrons in oxygen vacancies and holes in Zn_{Ga} defects [97], and has also been reported in other Ga_2O_3 samples allegedly containing acceptor levels [94].

The temperature-dependent CL results also seem to indicate a faster increase of the intensity of the UV bands at lower temperatures with respect to the visible bands and/or a thermally activated transition which promotes carriers to the Zn_{Ga} related level (the latter, only in the case of Ga_2O_3:Zn). A similar temperature-dependent behaviour in CL was observed for Sn doped Ga_2O_3 structures, in which, when the temperature was reduced, the Sn-related green band gradually decreased in relative intensity with respect to the Ga_2O_3 blue-UV bands down to a complete quenching at 90 K [40].

Secondly, distinct spectra for Ga_2O_3:Zn were obtained from three different PL sources: a Xe lamp, a pulsed LED and a fiber oscillator laser. When excitation was performed over a wide area with monochromatic light from a Xe lamp, there was a redshift of around 0.2 eV with respect to CL and a further redshift was found with the EPLED as excitation source. When the excitation source was a pulsed UV laser with a period of 63 ns between pulses, the emission was in the UV range at high power but showed a strong redshift, well into the visible range, with decreasing laser power.

The dissimilarities in the spectra can be explained by the difference in the excitation mechanisms of the three sources. Specifically, the particle excitation energy is quite different for electrons in the SEM, with typical energies of thousands of electronvolts (primary electrons) with respect to photons, with an energy of some eV, similar to the band gap of Ga_2O_3. Additionally, the excitation density (ED) and the excitation frequency are very different for each source. The measured fiber oscillator laser power reaching the sample (with no filters) is around 0.4 mW. As a rough estimate, this laser spot can be considered as a circumference with diameter of around 5 microns. This results in an approximate ED of $2\,\mathrm{kW/cm^2}$ for this laser. The LED has a maximum working power of 0.04 mW and has a much broader excitation area than the laser. Therefore, its ED is orders of magnitude lower than the fiber oscillator laser ED. The laser and the LED have pulsed periods of tens of nanoseconds while the Xe lamp is a spatially broad, low intensity, continuous excitation source.

Thirdly, both the time-resolved PL spectra and the laser power dependent spectra were used to further explore the luminescence dynamics of the samples. A recent work on UID and Sn doped Ga_2O_3 films [98], showed a decay time constant of 7.8 ns for the UV (3.5 eV) PL band for UID Ga_2O_3, with 4.4 eV excitation energy, while the decay time of the blue emission was not measured. In our results, the time evolution of the blue band at 2.8 eV in Ga_2O_3:Zn gives rise to two very fast decay constants, at 1.0 ns and 4.9 ns, and a very slow decay component. By inspecting the TRES of the Ga_2O_3:Zn sample in figure (3.6) (c), most of the 2.8 eV range decays in some nanoseconds although there is some emission after 30 ns, while the broad green band centered at 2.5 eV has a decay time much longer than 100 ns. Such decay time in the green emission is much longer than the UV PL decay time reported in ref. [24] and is also longer than the fiber oscillator laser pulse period. Bearing this in mind, an explanation is found for the redshift in the PL obtained with the pulsed LED with respect to the continuous

lamp and for the redshift obtained in figure (3.7) (b) when we decreased the laser pump power.

When the ED is high, i.e. for the fiber oscillator laser at high laser power, the PL emission of the Ga_2O_3:Zn belts is found to be similar to the UID emission, with high intensity in the UV (3.0 - 3.6 eV) range. The green (2.5 eV) band seems to be saturated at such high ED. This agrees with the TRES results (figure (3.6) (c)), which show slow recombination time components, much slower than the laser pulse period, for this band.

For intermediate laser powers, the UV-blue emission still dominated, but luminescence under 2.8 eV began to appear, with a low relative intensity. As the incident power was further decreased, the emission shifted to the visible range. Visible PL bands at 2.5 eV and 2.8 eV were the most intense when the broad Xe lamp excitation source was used (see figure (3.4) (a)). Similarly, the visible bands increased in relative intensity with decreasing fiber oscillator laser power (figure (3.7) (b)). For very low ED, the main emission is centered at 2.4 eV. This can be observed both in figure (3.7) (b) (orange line) and in figure (3.5) (b). In the latter, the incident source was the very low ED EPLED PL spectrum.

All these PL results indicate that the broad blue-green luminescence of the Ga_2O_3: Zn samples can be tentatively divided into two recombination processes centered at 2.4 - 2.5 eV (green) and at 2.8 - 2.9 eV (blue). This could be tentatively related with a recent report that points out that Zn would substitute for Ga in the Ga_2O_3 crystal lattice both at tetrahedral and at octahedral positions [99]. The green recombination process has a greater relative intensity increase at low power with respect to the blue one due to its very long recombination time. It must be noted that, as well as the the 2.7 eV band, a 2.4 eV band had been detected by Wang *et al.* for high Zn nominal content (3% or higher) in Ga_2O_3 [70] although it had been attributed to a phonon replica of the 2.7 eV emission.

Considering the low incorporation of Zn in our Ga_2O_3 microbelts, the recombination processes that are responsible for the blue-green emission in Ga_2O_3:Zn have a limited number of recombination centers, which results in an expected lower intensity of such bands in this sample with respect to samples with a higher Zn incorporation such as in refs. [70, 97]. Therefore, by increasing the Zn content in the Ga_2O_3 host, the blue, and especially the green emission can be further enhanced, especially if a pulsed excitation source or a low ED excitation source are used. Our results imply that

already-grown structures with a set Zn atomic incorporation percentage can be used as live multicolour phosphors, which can emit from UV to green light depending on the excitation source.

3.4 Synthesis and electron microscopy analysis of Ga_2O_3:Ge nanostructures

Let us move to the second half of this chapter, regarding the novel growth and characterization of Ga_2O_3:Ge nanostructures.

The structures were grown in the tubular furnace by a thermal method, as it was explained in section 2.1.2. Two gallium oxide pellets were placed on top of an alumina boat, and metallic Ga and Ge powders were placed on top of the pellets. Synthesis of Ge doped Ga_2O_3 via thermal methods is challenging since the MPs of Ge (938°C) and GeO_2 (1175°C) are much lower than that of Ga_2O_3 (1900°C). Besides, GeO and GeO_2 have a high vapor pressure (close to 1 atm.) below 1900°C. This was circumvented by the use of metallic gallium. Although its MP (30°C) is much lower than that of Ge, we found out that alloying between both metals took place at 1000°C and 900°C and $x = d$ in the pellet further away from the gas flux (B). Hence, the two chosen growth temperatures were 840°C and 940°C. This Ga:Ge alloy became the seed for the nanowire growth in a self-catalyzed VLS mechanism, as it will be further discussed in the end of this section. Hereinafter, we will call the sample grown at 840°C *sample A* while the sample grown at 940°C will be called *sample B*.

After the thermal treatments, both pellets showed a small amount of UID Ga_2O_3 micro- and nanowires in their outer circumference, as shown in figure (3.8). On top of pellet B of both samples (the furthest away from the gas flux), the gallium chip had not evaporated. Instead of its natural shiny colour, it displayed a dark colour to the naked eye, while the black-coloured germanium powder was not visible anymore. It was found by EDS that the (previously) gallium metallic piece had become a GaGe alloy after the treatment, with variable proportions of both metals throughout its volume and with some nanostructures formed on top of it.

Morphological and chemical study of the obtained structures by electron microscopy

Both in sample A and sample B, on top of the GaGe alloy, several elongated nanostructures with particles at their tips were observed. Due to their

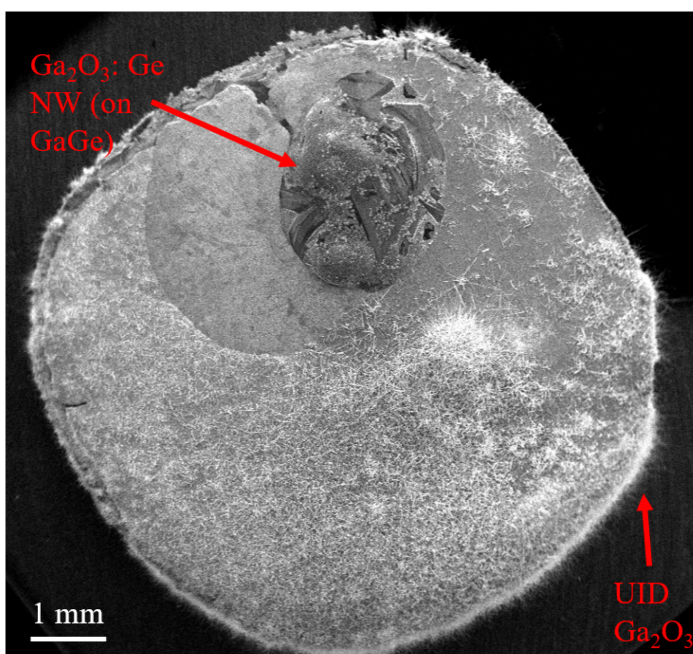

Figure 3.8: Low magnification SE image of the pellet in sample B. Both the GaGe alloy in which the Ga_2O_3:Ge micro- and nanowires grew on top of and the UID Ga_2O_3 structures which were observed in the sourth-east of the pellet are labelled accordingly. A similar picture was also observed in sample A.

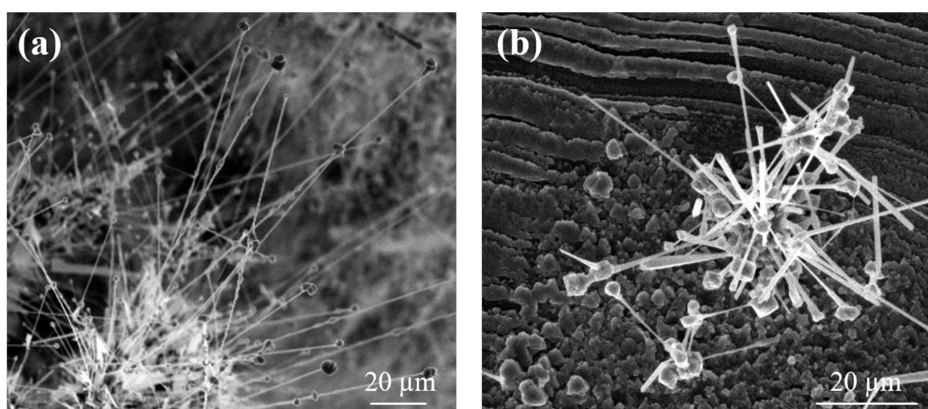

Figure 3.9: Low magnification SE images of the obtained nanowires lying on top of the metal alloy in (a) sample A and (b) sample B.

appearance, they will be hereinafter called “lollipop-like”. Figure (3.9) shows low magnification SE images of the observed structures in both samples. A fewer amount of structures was found on top of the alloy in sample B compared to sample A. Some of the nanostructures were transferred for individual characterization to silicon wafers or TEM grids by gentle contact with the GaGe alloy.

Sample A

Examples of the nanowires obtained in sample A are shown in figure (3.10). The two most usual morphologies found are lollipop nanowires (L-NW) and lollipop nanobelts (L-NB), the difference between them being that the axis is a nanowire (a few hundred nanometers width in two dimensions) or a nanobelt (a few hundred nanometers width in one dimension). Examples of an L-NW and an L-NB, are displayed in figures (3.10) (a) and (b), respectively. As shown in (b), the L-NBs often have two different widths, and the nanoparticles are always at the end of the thinner part of the L-NB axis.

A SAED pattern from the L-NW axis, from the orange box in fig. (3.10) (a) is shown in figure (3.10) (c). The diffraction spots were assigned to the monoclinic Ga_2O_3 phase along the [101] zone axis, and the GD of the nanowire was deduced to be the [010]. On the other hand, the SAED pattern from the thinner part of the L-NB, see figure (3.10) (d), showed that it is also monoclinic Ga_2O_3 and grows along the [001] direction. It must be noted that all the L-NB analyzed in this sample had a GD along the [001] direction, while L-NW were found to grow either along the [010] or along the [001] directions. The gallium germanate particles that appear in the tips seem to have a polycrystalline nature, as it can be observed in the SAED pattern in figure (3.10) (e).

These structures bear a resemblance to the self-catalytic Ga_2O_3 structures obtained by Kumar *et al.* by CVD [100]. In their study, both their Ga_2O_3 NW and NB presented the [001] GD. Taking into account that 1D nucleation is more energetically favourable than 2D nucleation and inspired by previous reports on GaN structures, they argued that the 2D growth in the NB could have been catalyst-guided by secondary nucleation sites on the surface of their NW. Based on this reasoning and considering our TEM results, we propose that the formation of Ga_2O_3 L-NB resulted from similar secondary growths from L-NW, and this process was energetically favourable for the [001]-grown L-NW with respect to the [010]-grown L-NW.

In order to assess Ge incorporation in the Ga_2O_3 lattice, EDS analysis was

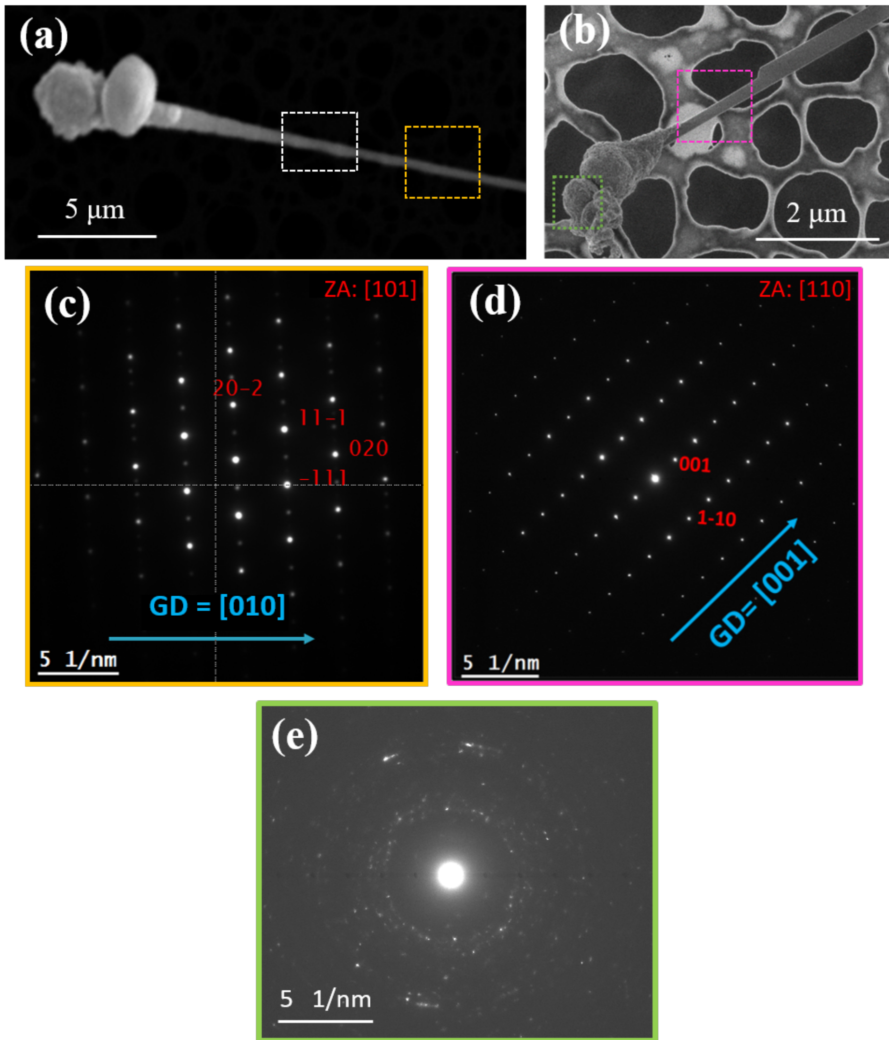

Figure 3.10: Electron microscopy analysis of nanostructures from sample A. (a) SE image of an L-NW structure. (b) SE image of an L-NB structure. (c) SAED pattern of the L-NW axis (dashed orange box in (a)), ascribed to the [101] zone axis. (d) SAED pattern of the L-NB axis (dashed pink box in (b)), ascribed to the [110] zone axis. (e) SAED pattern of the particles in the L-NB (dashed green box in (b)).

performed on the SEM and the TEM for several L-NW and L-NB structures. Figure (3.11) (a) shows an ADF-STEM image of the part of the L-NW axis from figure (3.10) (a) closer to the tip (dashed white box in fig. (3.10) (a)).

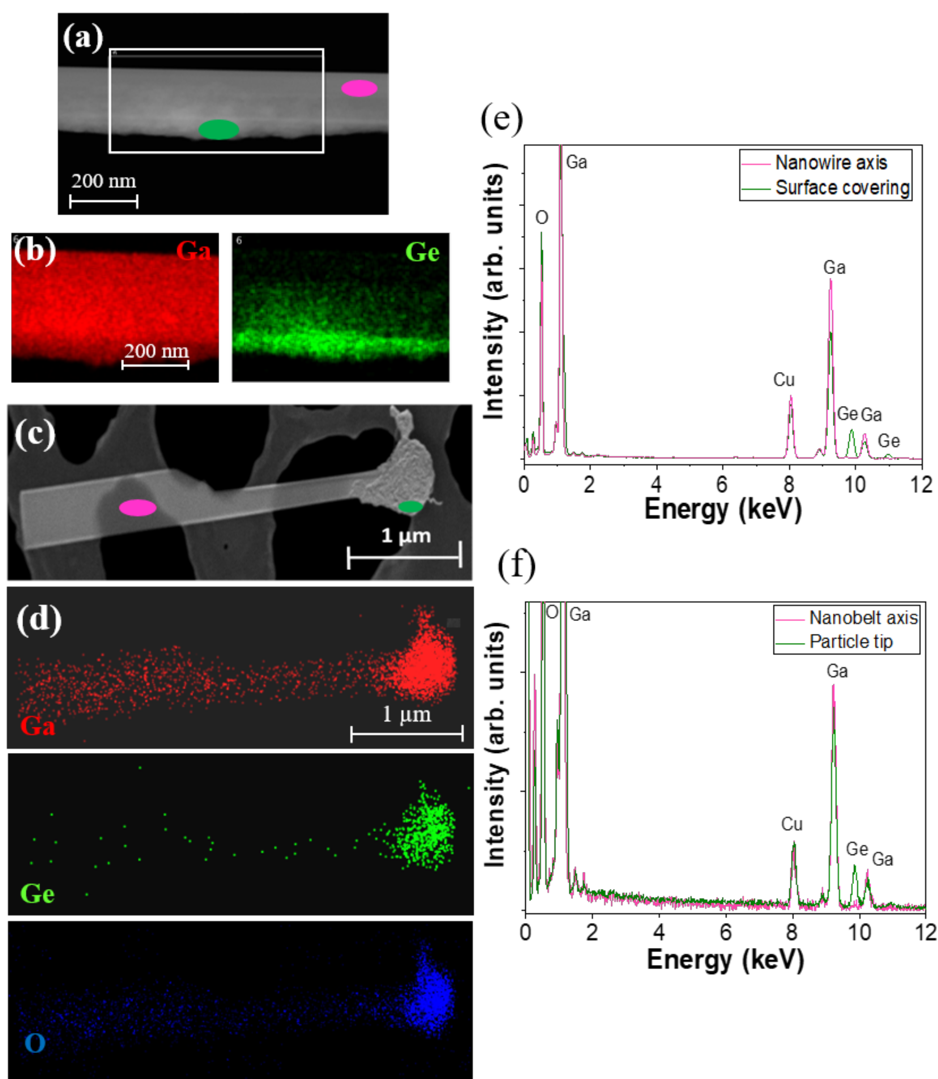

Figure 3.11: (a) ADF-STEM image of the L-NW axis in an area close to the tip (dashed white box in figure (3.10) (a)). (b) EDS-STEM Ga (left) and Ge (right) element mapping of the rectangle area indicated in (a), showing gallium germanate segregation at the nanowire surface. (c) SE image and (d) EDS elemental maps of an L-NB (Ga in red, Ge in green and O in blue). (e) EDS-TEM spectra of the L-NW axis (pink) and the Ge-rich area below the nanowire shown in (a) (green). (f) EDS-SEM spectra of the L-NB axis (pink) and particle (green) shown in (d).

Figure (3.11) (b) shows Ga (left, in red) and Ge (right, in green) map distributions of the area marked by a rectangle in fig. (3.11) (a). These figures indicate segregation at the nanowire surface of a material rich in gallium and germanium. Both in L-NW and in L-NB, EDS maps on the particles at the tip also show that they are rich both in gallium and germanium. For example, another L-NB structure is shown in figure (3.11) (c), and its EDS maps are shown in figure (3.11) (d). The EDS results indicate that this germanate material present in the tips and in some surfaces of the L-NW and L-NB is also rich in oxygen.

Figure (3.11) (e) presents local EDS-TEM spectra taken from the axis and from the Ge-rich covering of the L-NW, as indicated with pink and green ellipses respectively in fig. (3.11) (a). It can be observed that the Ge Kα line at 9.886 keV appears in the spectrum recorded at the Ge rich segregated area (green), unlike at the one recorded in the L-NW axis (pink). Quantification of the spectrum yielded a Ga/Ge ratio of 4.2 in the Ge-rich covering although it is likely to be overestimated due to the residual contribution of X-ray photons from the Ga_2O_3 axis. The Cu signal detected in the EDS spectra originated from the TEM grid in which the structures were deposited.

Figure (3.11) (f) corresponds to EDS-SEM spectra taken from the axis and from the nanoparticle at the tip of the L-NB (pink and green ellipses in fig. (3.11) (c)). The EDS quantification yielded a Ga/Ge ratio of $\sim$3 in several particles at both L-NB and L-NW tips. As a high amount of oxygen was also detected in these spectra, the results suggest the presence of gallium germanate structures in the tips such as Ga_4GeO_8 or Ga_2GeO_5 and/or some non-stoichiometric solid solution of Ga_2O_3 and GeO_2 [101]. SAED diffraction patterns from the tip (i.e. fig. (3.10) (e)) showed that the particles have some crystallinity but they did not allow a clear identification of the phase. Tips with similar properties of a GaFeO compound were obtained by Kumar *et al.* on iron-catalysed CVD growth of Ga_2O_3 nanowires [102]. Additionally, EDS analysis of several L-NB and L-NW in the TEM and SEM (e.g. spectra in pink, figs. (3.10) (e) and (f)) reveal that the amount of Ge which has incorporated in the axis is below the detection limit of the technique (below 0.1% at. or 0.5% at., depending on the technique used, see section 2.2.1.2).

Sample B

A similar structural and chemical analysis was carried out for sample B, i.e. the structures obtained for the thermal treatment at higher temperatures

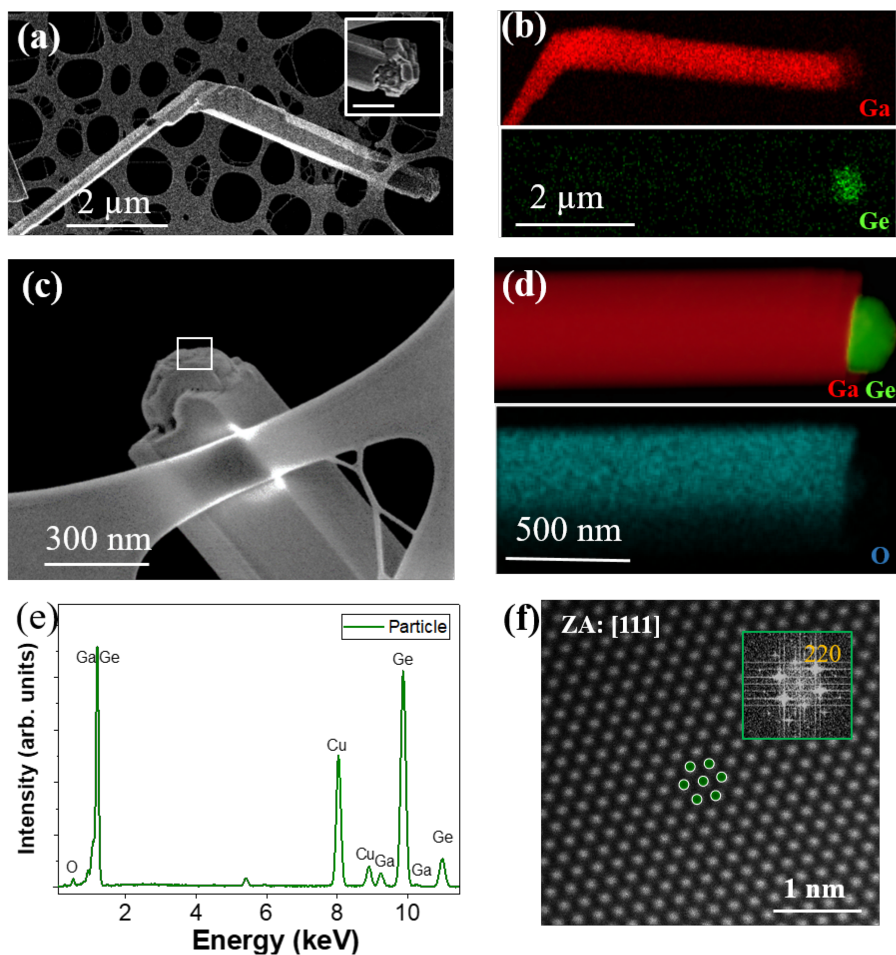

Figure 3.12: (a) SE image and (b) EDS-SEM Ga and Ge (red and green) of a structure in sample B. The inset in (a) shows a magnified image of the Ge nanocrystal in (a); scale bar = 500 nm. (c) SE image and (d) EDS-SEM Ga+Ge (red+green) and O (blue) maps of another structure in sample B. (e) EDS-TEM spectrum of the nanocrystal at the tip of second structure, from the area indicated by the white rectangle in (c). (f) STEM-ADF image of the Ge nanocrystal on the structure in (c) with the diamond-like (111) crystal structure atoms superimposed in green. Its FFT shown in the inset.

(940°C). These structures are generally wider than the structures in sample A, with widths ranging from 500 nm to 1 µm. They tend to have a well-defined nanoparticle at the end, with a diameter equal to or smaller than the

nanowire axis. Very few L-NWs, a minority compared to the aforementioned structures, were found in this sample, and there were no L-NBs.

Figures (3.12) (a) and (c) are SE images of representative structures of sample B, and figures (3.12) (b) and (d) show EDS-SEM elemental maps of the microstructures in figs. (3.12) (a) and (c), respectively. Figure (3.12) (e) is an EDS-TEM spectrum of the particle in the tip of the structure in (c). As shown in the EDS analysis of this figure, in sample B, unlike in sample A, the particles at the tip contain hardly no oxygen or gallium; they are composed mainly of Ge. Quantification of the EDS-TEM spectrum in fig. (3.12) (e) yields $\sim$5% and $\sim$1% of O and Ga, respectively, although a slight overestimation of these percentages can be expected due to emission from the Ga_2O_3 wire axis. High resolution TEM images and clear diffraction patterns were not obtained from these structures' wire axis, as they would have required a sample thinning process.

In addition, the tip particles in this sample were found to be monocrystalline. TEM analysis was carried out in the hemispherical Ge nanoparticle attached to the Ga_2O_3 wire, shown in figs. (3.12) (c) and (d). Figure (3.12) (f) is an atomically resolved STEM-ADF image of particle. Its inset shows the Fast Fourier Transform (FFT) of such image. Both correspond to the projection of diamond-structure Ge along the [111] zone axis. The tabulated interplanar distances of the $\{220\}$ planes in Ge is 0.20 nm, while the measured interplanar distances turned out to be 0.20, 0.20 and 0.23 nm. This indicates a strained or modified lattice on one of the three equivalent $\{220\}$ planes, which may be due to Ga doping in the nanoparticle and/or to strain for lattice matching with the Ga_2O_3 axis.

Discussion on the growth mechanism

In these paragraphs, the growth mechanism which has led to the structures observed in the previous sections is discussed in detail in order to obtain a deeper understanding which can be useful for future synthesis of Ge doped Ga_2O_3 structures.

First of all, notice the different morphology of the Ga_2O_3:Zn structures presented in the first half of the chapter (see Figure (3.1)) in comparison to the Ga_2O_3:Ge structures presented in section 3.4. This difference is attributed to the presence of different precursors during growth. In the former case, bearing in mind the MP of ZnO and the lack of Zn or ZnO particles in the tip, we concluded that the Ga_2O_3:Zn structures grew by a VS mechanism in which adsorbed oxide species nucleated and formed

Ga_2O_3:Zn microbelts on top of the Ga_2O_3 pellet. In the latter case, the temperatures were chosen to lie on the MP of Ge (sample B) or at a slightly lower temperature (sample A), which gave rise to a VLS mechanism for the growth of the structures on top of the metal alloy, as explained in the next two paragraphs.

By inspection of the Ga-Ge phase diagram [103], we can see that the MP of a Ga-Ge alloy lies between 29.8°C (the MP of Ga) and 938°C (the MP of Ge). In sample B, the growth temperature was 940°C. Many of the obtained Ga_2O_3 structures have a Ga doped Ge nanocrystal in its tip (see figure (3.12)), while structures grown in sample A, at T = 840°C, have instead a gallium germanate polycrystalline particle in its tip (see figure (3.11)). As mentioned above, in both samples, the structures appeared on top of GaGe alloy formed during the thermal treatment.

Having all of this in mind, we believe that, in both treatments, when the temperature rose, the Ga chip and the Ge powder formed a molten alloy which served both as the substrate and as the driving force for the Ga_2O_3:Ge nanowire growth by a VLS mechanism. In sample B, as the temperature was at the MP of Ge, the catalyzer for the 1D nanowire growth was Ge-rich, while a Ga-rich gallium germanate catalyzer sustained the 1D growth of sample A's nanostructures. As previously explained, due to secondary nucleation sites, some tapered 2D belt nanostructures were also formed in sample A. Building from by these results, controllable growth of ordered vertical Ga_2O_3:Ge nanostructures could be achieved by more complex fabrication procedures such as the one recently presented in ref. [104].

3.5 Influence of Ge doping on luminescent and structural properties

As already shown for Ga_2O_3:Zn microbelts, impurity doping below the EDS detection limit can be detected by luminescent-related techniques. In order to clarify whether some Ge has incorporated in the Ga_2O_3 crystal structure of the obtained nanostructures in samples A and B, CL was performed on several of these structures.

Figure (3.13) (a) shows an SE image of a Ga_2O_3:Ge L-NB structure obtained in sample A while figure (3.13) (b) shows an SE image of several UID Ga_2O_3 nanowires. Recall from section 3.4 and figure (3.8) that in the same thermal treatment in which Ga_2O_3:Ge structures grew on top of the metal chip,

Ga_2O_3 micro- and nanowires were observed in the outer circumference of the Ga_2O_3 pellet. Some of these were detached from the pellet, deposited on Si and used as reference Ga_2O_3 in fig. (3.13) (b). As it is usual for some Ga_2O_3 wires to grow in the pellets' circumference when no impurities are introduced in it, they are far away from the GaGe alloy and according to EDS, no Ge on or around these structures was detected, we decided to use them as the UID reference for comparison in the luminescent and Raman studies.

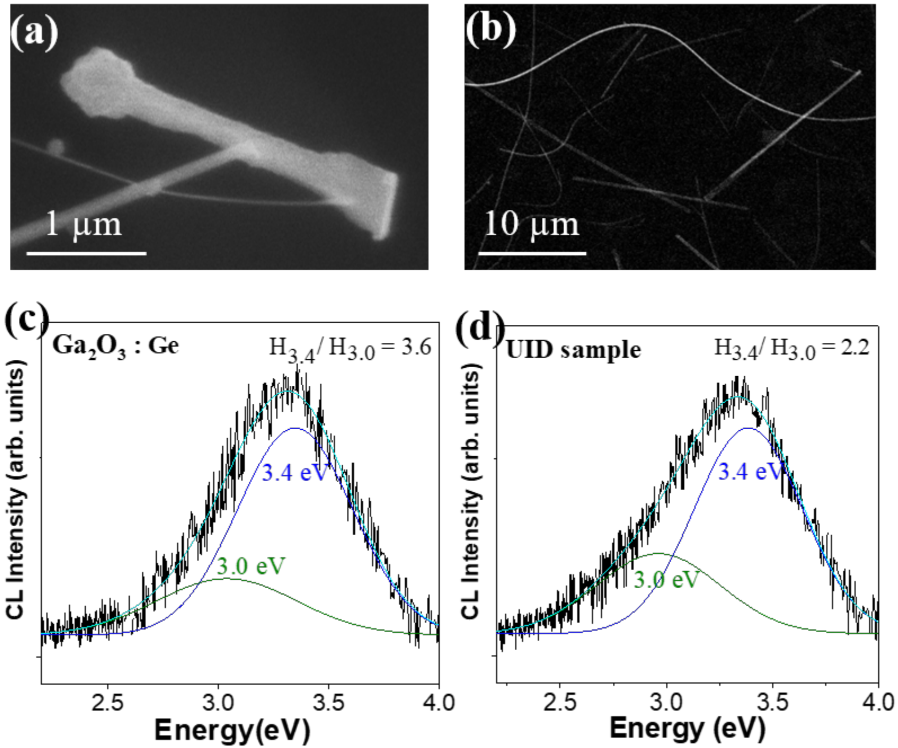

Figure 3.13: (a) SE image of the Ga_2O_3:Ge lollipop structure chosen for CL analysis. (b) SE image of UID Ga_2O_3 wires which appeared in the outside circumference of the Ga_2O_3 pellet. These wires were used as UID reference samples for CL and Raman spectroscopies. (c) Deconvolved CL spectrum of the structure in (a). (d) Deconvolved CL spectrum of the UID reference sample. The UV/blue intensity ratios are shown in the right hand corner.

Figures (3.13) (c) and (d) are CL spectra of the Ga_2O_3:Ge lollipop structure in (a) and one of the UID wires in (b), respectively. The UID sample

shows a broad blue-UV band which can be deconvolved into two components at 3.0 and 3.4 eV, like the UID sample used for the Ga_2O_3:Zn structures (figure (3.3) (a)). The 3.4 eV component can be assigned to STEs, STHs or unintentional Si impurities while the blue component is assigned to a DAP process involving O vacancies. Regarding the Ga_2O_3:Ge structure, no difference in CL was found between the area covered with gallium germanate and the uncovered area, hence the luminescence of the gallium germanate covering under the electron beam, if any, is negligible. The spectrum again shows the 3.4 and 3.0 eV bands but we can see that there is a decrease in the relative intensity of the blue part of the spectrum with respect to the UV part in the Ga_2O_3:Ge structure with respect to the UID sample.

Quantitatively, the 3.4 eV to 3.0 eV band height ratio increased in the Ga_2O_3:Ge structure with respect to the UID structure from 2.2 to 3.6, and the 3.4 eV to 3.0 eV band area ratio increased from 1.6 to 1.9. For Si doped Ga_2O_3 single crystals, Shimamura *et al.* found by PL a similar decrease of the relative intensity of the blue emission with respect to the UV one [25]. In addition, recent CL spectra obtained by Onuma *et al.* exhibit the suppression of the 2.8 to 3.0 eV emission for Si doped Ga_2O_3 single crystals [28]. As both Si and Ge are n-type dopants in Ga_2O_3, our explanation of the decrease in the blue component in the UV-blue emission in figure (3.13) (c) with respect to figure (3.13) (d) is the reduction in the concentration of the O vacancies in order to compensate the incorporation of Ge in the Ga_2O_3 lattice. This behaviour (the reduction of the blue CL intensity with respect to the UV one) was observed in several Ga_2O_3:Ge structures in both sample A and sample B. These results suggest that some Ge was incorporated in the Ga_2O_3 lattice of the obtained nanostructures on top of the metal chip in both thermal treatments.

In order to further investigate the incorporation of Ge in these nanostructures, μ-Raman spectroscopy measurements were performed and compared with UID structures' Raman spectra. Figure (3.14) shows representative μ-Raman spectrum of the axis of a lollipop structure from sample A and that of a reference Ga_2O_3 wire. Both spectra show the characteristic Ga_2O_3 Raman modes [92], along with the $520\,cm^{-1}$ Si-originated peak, as described in section 3.1 for Ga_2O_3:Zn.

The spectra show that some Ga_2O_3 vibrational modes like the $200\,cm^{-1}$ and $416\,cm^{-1}$ ones are almost identical in both the Ga_2O_3:Ge and the UID Ga_2O_3 structures, with Raman shifts and FWHM changes equal to or under $1\,cm^{-1}$, see figures (3.14) (b) and (c). However, see figures (3.14) (d) and

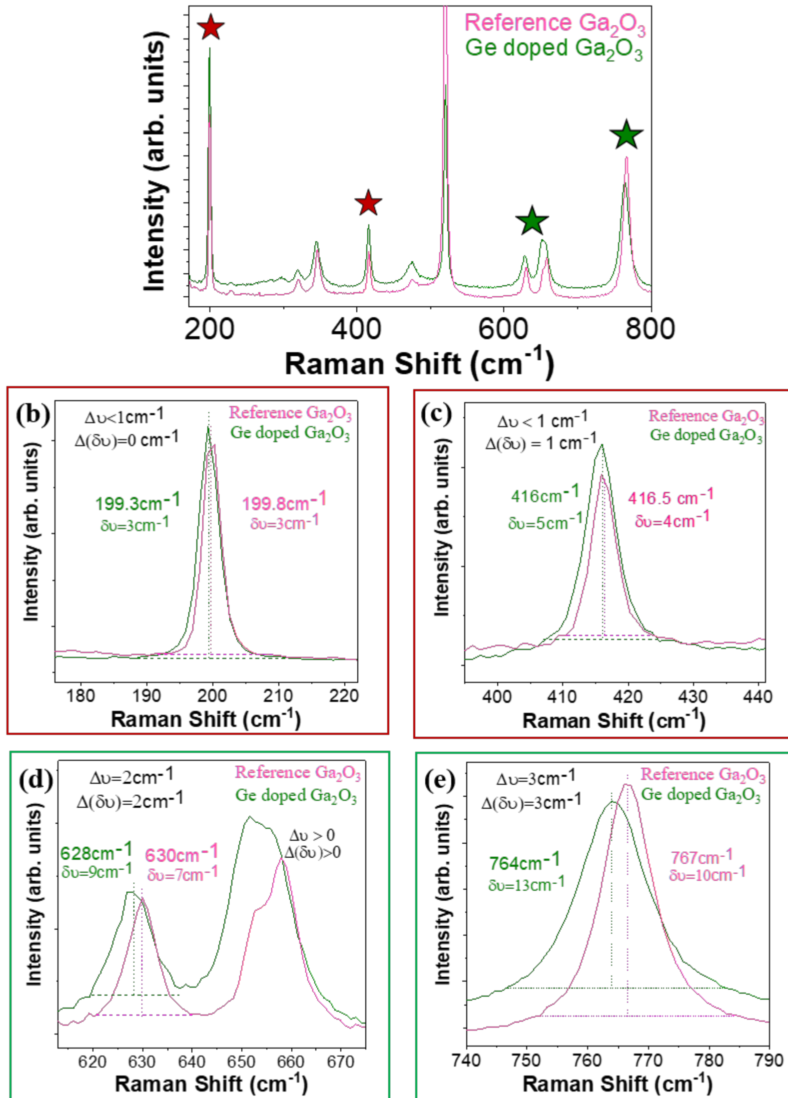

Figure 3.14: (a) Raman spectra of a Ga_2O_3:Ge structure from sample A (green) and a UID Ga_2O_3 reference (pink). (b)-(e) Detailed spectra from (a) of the peaks indicated with stars to illustrate the similarities in the 200 cm^{-1} and 416 cm^{-1} modes ((b), and (c), brown stars in (a)) compared to the Ge-induced changes of over 1 cm^{-1} in the tetrahedral modes ((d) and (e), green stars in (a)). Some spectra are slightly shifted vertically for clarity.

(e), slight differences can be seen on other Ga_2O_3 modes. In particular, the modes at 630 cm^{-1} and 766 cm^{-1} of the Ga_2O_3:Ge structure have a redshift of ~2 cm^{-1} and ~3 cm^{-1} and an increase in the FWHM of ~2 cm^{-1} and ~3 cm^{-1}, respectively. The combined 651-657 cm^{-1} modes peak also displays a similar trend. This trend was also observed in structures of sample B. The frequency values of the main Raman modes of a representative Ga_2O_3:Ge structure in both samples compared to the UID reference are shown in table (3.1).

Phonon mode	Experimental value (cm^{-1})		
	UID Ga_2O_3	Sample A	Sample B
$A_g^{(3)}$	200	199	200
$A_g^{(5)}$	346	345	345
$A_g^{(6)}$	416	416	416
$A_g^{(8)}$	630	628	628
$A_g^{(10)}$	767	764	764

Table 3.1: Spectral position of the main Raman modes for a representative structure of sample A and sample B compared to the UID reference spectrum.

The Ga_2O_3 Raman mode at 200 cm^{-1} is due to librations of chains involving octahedron stretching and the 346 cm^{-1} and 416 cm^{-1} modes are due to deformation of octahedral modes in Ga_2O_3. On the other hand, the modes at 630 cm^{-1}, 651 cm^{-1}, 657 cm^{-1} and 766 cm^{-1} are due to stretching and bending of GaO_4 tetrahedrons [105]. As Ge prefers tetrahedral positions when substituting Ga in the Ga_2O_3 lattice [15], this can result in lattice strain and an increase in the distribution of phonon states, which causes a broadening of the Raman modes, especially the tetrahedral ones. Also, Ge ions are heavier than Ga ions, resulting in a higher effective phonon mass which can give rise to a redshift in these modes [106]. This trend in the tetrahedral modes has been observed in figures (3.14) (d) and (e).

Therefore, from the μ-Raman, the CL and the EDS results displayed in this chapter we believe that, as well as having an important role in the VLS growth of the nanostructures, Ge has incorporated as a substitutional dopant in the nanowire axis of the nanostructures of both samples.

3.6 Conclusions

In this chapter, we have faced some challenges in doping Ga_2O_3 nanostructures by thermal evaporation methods. In particular, the choice of precursors and the growth temperature with respect to their melting point has been the main driving force for the thermal incorporation of two dopants, Zn and Ge, in Ga_2O_3 nanostructures by VS or VLS mechanisms. The morphological, structural and optical properties of the obtained micro- and nanostructures have been characterized by electron microscopy and optical spectroscopy techniques.

The incorporation of a very small amount of Zn in Ga_2O_3 has altered the dominant morphology of the obtained structures to a belt-like morphology. EDS and Raman spectroscopy analysis show that these Ga_2O_3 microbelts have a very low Zn content and a high crystalline quality.

Such low Zn content has greatly modified the optical properties of the microbelts. Spatially resolved CL results show an increase of the emission around 2.7 eV, which matches with the 2.7 eV CL band attributed not only to a recombination path involving substitutional Zn but, more generally, to acceptor doping in Ga_2O_3. By using three different excitation density sources (a Xe lamp, a pulsed LED and a fiber oscillator laser), the luminescence dynamics have been studied in considerable detail. Low ED sources result in a redshift of the Ga_2O_3:Zn luminescence towards the visible region, with dominant bands at 2.5 and 2.8 eV. This result agrees with the time-resolved PL spectroscopy measurements, which show a very slow decaying green band at $\sim$2.5 eV. From these results, we have claimed that the broad 2.7 eV band observed by CL due to Zn incorporation is composed of two bands with different decay times. Although the current focus of the incorporation of Zn is the possibility of p-type doping, which is regarded as very unlikely in Ga_2O_3, the optical results shown in this chapter place Ga_2O_3:Zn as an interesting material for multi-colour phosphors.

The second part of this chapter focused on the novel synthesis and characterization of Ga_2O_3:Ge nanostructures. Two main types of structures have been obtained, depending on the growth temperature. At 840°C lollipop nanowires and nanobelts with a tip made of a gallium germanate compound appear. Instead, at 940°C a Ge nanocrystal emerges at the tip of the obtained microwires. TEM results reveal the high crystalline quality of all the obtained nanostructure types. The growth dynamics of these structures has been explained by a VLS mechanism in which the catalyzer is the GaGe al-

loy or the Ge particles formed when the furnace reached the selected growth temperatures.

The incorporation of Ge as a substitutional dopant in the Ga_2O_3 axis of these structures has been studied by CL and Raman spectroscopies. The blue CL emission shows an intensity decrease with respect to the UV one, while Raman spectroscopy shows small modifications in the tetrahedral modes of Ga_2O_3 in the Ga_2O_3:Ge wire axis of the structures. As Ge has recently been proposed as one of the most promising for n-doped Ga_2O_3 devices, further control in the synthesis of these nanostructures will be necessary for their application in Ga_2O_3: Ge nanodevices or in Ga_2O_3 - GeO_2 complex architectures. The presented results in this chapter are the first milestone towards this goal.

Chapter 4

Gallium oxide - Tin oxide nano-heterostructures

After demonstrating the influence of two different dopants in the morphological, structural and optical properties of Ga_2O_3, the next step carried out in this thesis was to engineer nano-architectures with mixed dimensionalities with the aid of certain impurities: Sn and Cr.

A relevant example of these new architectures, which will be covered in this chapter, is branched nanostructures. They possess some advantages over their 1D or 0D counterparts, such as, an improved light absorption or the possibility of having complex electron and photon pathways in the same structure, which are important for optoelectronic and photonic applications, such as high pass or low pass filters, lasers or photocatalytic devices [64, 65, 72].

Regarding Sn doping, as well as affecting Ga_2O_3's electrical properties (as described in the Introduction), it has been shown to induce changes in the resulting morphology of the obtained architectures in the micro- and nanoscale. In particular, previous work [40] showed that after including a small amount of Sn in a thermal growth of Ga_2O_3 nanostructures, Sn-rich particles did not only appear at the tips of the structures, but also in some lateral surfaces. The conclusion was that these particles did not only act as the driving force for the nanowire growth, but also promoted the secondary

growths of the branched nanostructures. These architectures were formed by a single crystalline material, Ga_2O_3, i.e. no SnO_2 secondary growths appeared in them [40].

Due to the n-type character of Ga_2O_3, in order to obtain Ga_2O_3-based bipolar devices its combination with a p-type semiconductor is necessary [16]. Therefore, the inclusion of another TCO, which also has a high transparency range, and at the same time is able to have p-type carriers, would be suitable for these devices. This can be fulfilled by SnO_2, when doped with certain elements. This material, with a rutile crystal structure, has a band gap of around 3.7 eV and has shown promising applications in smart windows, transparent electrodes in photovoltaics or anodes in Li ion batteries, among others. SnO_2 can become a p-type semiconductor when Sn^{3+} ions are substituted by some tetravalent ions such as Ga^{4+} in a sufficient atomic percentage. The combination of n-type Ga_2O_3 and p-type SnO_2:Ga in a core-shell heterostructure has been used for UV detection, with a substantial increase in the on/off current contrast ratio with respect to a SnO_2 detector [107].

This chapter presents the growth and characterization of different architectures in the micro- and nanoscale involving Ga_2O_3 and SnO_2. We will also see that the incorporation of chromium to the precursors can lead to Ga_2O_3-SnO_2 nanowire heterojunctions with high crystalline quality. The goal is to understand the underlying formation mechanisms and the resulting properties of these structures for their potential device applications

4.1 Synthesis of Ga_2O_3/SnO_2 heterostructures

In a previous work, Ga_2O_3:Sn nanowires were achieved [40] by thermal evaporation methods. In this thesis, the aim was to optimize these methods to synthesize complex architectures which contained both doped Ga_2O_3 and SnO_2.

In order to achieve this, we tested several sample configurations on the tubular furnace depicted in figure (2.3) in order to find the most suitable conditions. The precursors were Ga_2O_3 pellets, SnO_2 powders and a metallic gallium piece on top. Two pellets were placed on top of the alumina boat. Separate trials with two pellets with 90% Ga_2O_3 and 10% SnO_2 but no SnO_2 powders on top resulted in the same kind of structures obtained after the thermal treatment.

In these trials, the nominal temperature ranged from 1100°C to 1500°C in steps of 100°C and the positions tested in the oven were $x = 0$, $x = d$ and $x = 2d$ (see section 2.1.2 for further details). The growth time was 8 hours. The main conclusions are summarized below:

Nom. T \Posit.	x=0	x=d	x=2d
1500°C	-	-	**HS**
1400°C	-	-	HS
1300°C	Ga_2O_3	Ga_2O_3	HS
1200°C	HS	HS	Ga_2O_3
1100°C	HS	HS	Ga_2O_3

Table 4.1: Outline of the obtained structures for different nominal temperatures and positions in the tubular furnace. A hyphen means that no structures appeared on top of the pellet, Ga_2O_3 means that only Ga_2O_3 structures appeared and HS means that heterostructures like the ones analyzed throughout the chapter appeared on top of the pellet. To know the real temperature of each pellet in each position, see table (2.1).

- No structures grew for nominal temperatures of 1400°C and above at $x = 0$ and $x = d$. Too high temperatures can result in the evaporation of the precursors before doing their role [71].
- Gallium oxide 1D structures without apparent tin incorporation were obtained for T = 1300°C at $x = 0$ and $x = d$ or for nominal temperatures of 1100°C and 1200°C at $x = 2d$.
- SnO_2-related secondary growths were obtained for the rest of nominal temperatures and positions in pellet B (the furthest away from the gas flux) and, in lower proportions, in pellet A. Similar types of complex nanostructures were obtained for each temperature-position thermal treatment in this growth window. This implies that there is a broad temperature range for the growth of Ga_2O_3-SnO_2 heterostructures.
- The chosen nominal temperature and furnace position for the in-depth analysis of this chapter, as the highest yield of complex heterostructures was found here, was 1500°C and $2d$, respectively.

It must be noted that, apart from the 8 hours growth time stated above, shorter and longer duration times (2.5 hours and 15 hours) of the thermal treatment were made, and no difference was observed in the resulting structures detailed in this chapter. In-situ images at 30 minute intervals taken at this furnace for one of these Ga_2O_3-SnO_2 growths show that most of the

nanostructures grow in the first few hours. Figure (4.1) (a) is a photo of the alumina boat after the thermal treatment, showing an enormous growth yield of micro- and nanostructures in the pellet at lowest temperature and further away from the flux (right in the image) and a small number of structures grown on the other pellet. As detailed in section 2.1.1, this is expected in the framework of a thermal growth under gas flow.

A wide range of structures with different architectures were synthesized, which can be classified in four groups. These are:

- Fin-decorated nano- and microwires.
- Polyhedral-shape decorated nanowires and branched structures.
- Skewer-like (SK) heterostructures.
- Crossed-wire (CW) heterostructures*

*These structures were obtained by adding an extra precursor, chromium oxide. More will be explained in section 4.5.

As the structures formed an agglomerated forest which prevents individual analyses, some of them were deposited on silicon substrates by gently grabbing thousands of them with tweezers and gently "brushing" on top of the silicon. As we will see throughout the chapter, the structures have very diverse sizes. Both microwires and microbelts of lengths of tens of micrometers and widths of a few micrometers were found, as well as nanostructures with similar morphologies and widths of much less than a micron. This allowed for both SEM and TEM analysis of the structures. A low magnification SE image of several micro- and nanostructures deposited on silicon is shown in figure (4.1) (b).

4.2 Polyhedral shape and fin-like decorated structures

Unlike the structures obtained in the previous chapter with Ge and Zn precursors, tin did not only incorporate into the Ga_2O_3 crystal lattice, but it also formed tin oxide nanostructures around the Ga_2O_3 nanowires. These nanostructures have either polyhedral shapes, diamonds or prisms, or produce a fuzzy covering on some lateral facets.

Figures (4.2) (a) to (d) shows SE image and EDS map examples of Ga_2O_3 micro- and nanostructures with polyhedral covering. Microwires and mi-

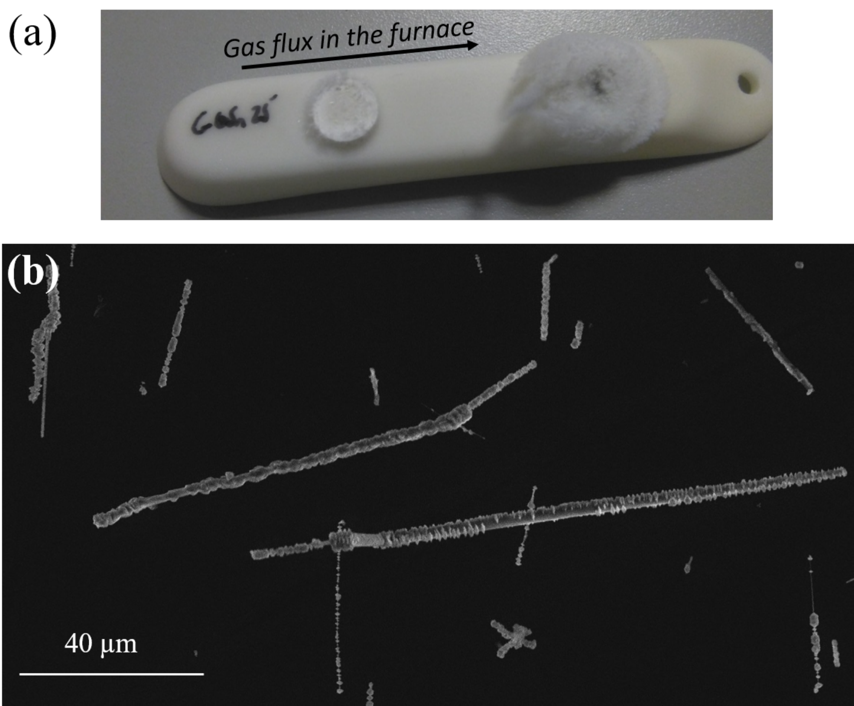

Figure 4.1: (a) Photo of the pellets after the thermal treatment, showing a very large number of micro- and nanostructures on top, especially in the pellet where the flux was pointing towards. (b) Low magnification SE image of tin oxide decorated Ga_2O_3 micro- and nanostructures.

crobelts such as the ones shown in Figure (4.2) (a) and (b) were partially covered with diamond-like crystallites. EDS maps displayed in figure (4.2) (c) to (e) show that the structures' axis is composed of gallium and oxygen while the particles are composed of tin and oxygen.

Nanowires and nanobelts (with a depth of clearly less than 1 µm) decorated with diamond-like SnO_2 nanoparticles were also found. In order to have a more microscopic view of this type of decoration, STEM and EDS mappings were performed. Figure (4.2) (f) is an ADF-STEM image and an EDS map showing that the diamonds are aligned following the nanobelt GD, with the diagonal directions parallel and perpendicular to such direction. This alignment, which is a general feature of the polyhedral covered structures, suggests some preferential structural matching. This is analyzed in the structure shown in figure (4.2) (g). This figure is a BF-TEM image of the

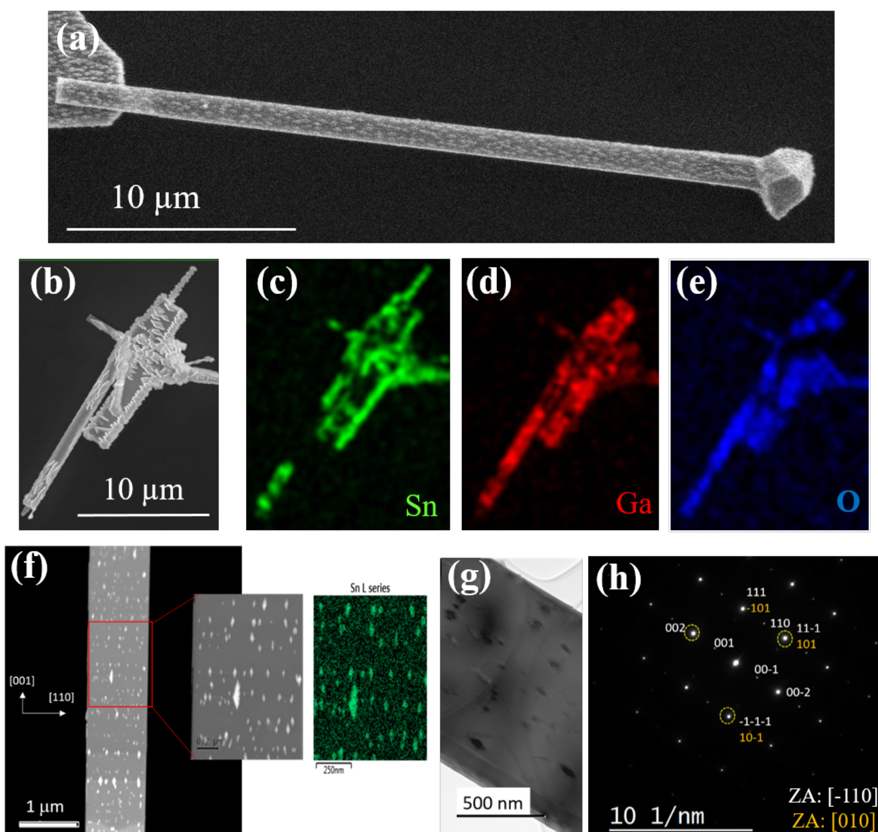

Figure 4.2: (a) SE image of a microstructure coated with nanoparticles of polygonal shape. (b) SE image and (c) to (e) EDS mapping of Sn element (green), Ga element (red) and O element (blue), respectively, of a few agglomerated structures of this type. (f) ADF-STEM image of a polygon-decorated nanobelt and EDS mapping of Sn element (gren). (g) BF-TEM image and (h) SAED pattern of the decorated nanobelt shown in (e). Diffraction spots due to Ga_2O_3 and SnO_2 have been indexed in white and orange respectively, and the zone axis is shown in the bottom right corner.

nanobelt in (e), in which the diamond shape particles have a dark contrast with respect to the wire. Figure (4.2) (h) shows its corresponding SAED pattern. The diffraction spots were assigned to the monoclinic Ga_2O_3 phase and the rutile SnO_2 phase, as the labels in white (Ga_2O_3) and orange (SnO_2) show. Hence, the diamond-shape nanoparticles are monocrystalline and all have the same orientation in the nanobelt. From the SAED pattern,

the obtained GD of the nanobelt is the [001] and lattice matching can be observed between the {111} Ga_2O_3 and the {-101} SnO_2 planes.

The other type of covering of tin oxide in Ga_2O_3 is shown below. Figures (4.3) (a) to (d) are SE images and EDS Ga + Sn maps of fin-like decorated structures. These tin oxide structures do not have polyhedral shapes, but more of a fuzzier shape, that can be compared to fins. In addition, this covering only appears in some lateral walls of the structures, instead of growing in every surface.

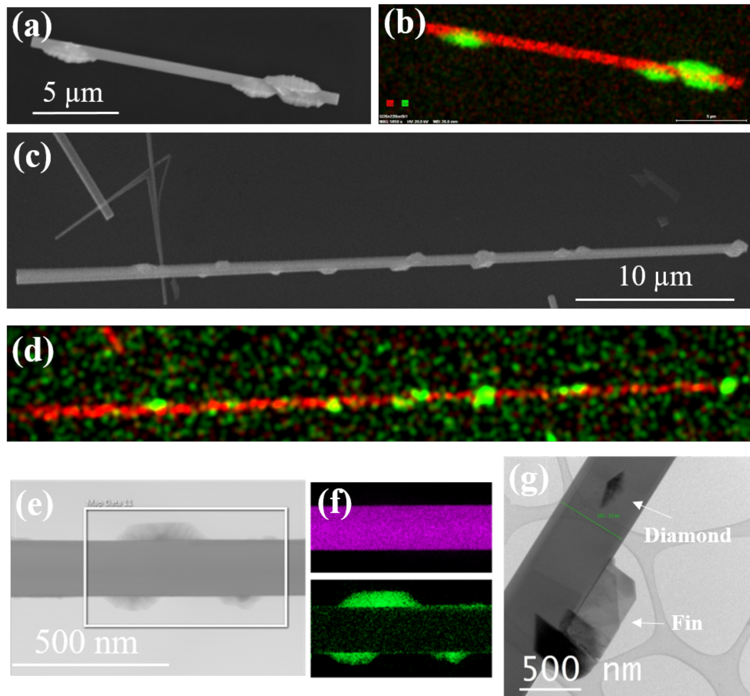

Figure 4.3: (a) SE image and (b) EDS map of a finned type microwire. (c) SE image and (d) EDS map of a longer finned type microwire. (e) BF-STEM and (f) EDS maps of a finned type nanowire, showing a tin-rich overlayer in the surface. (g) A nanowire which presents both fin covering and diamond decoration. For all the EDS maps, gallium is shown in red and tin in green except for (f), in which gallium is shown in pink.

Like with the Ga_2O_3 structures covered with SnO_2 polyhedral particles, not only Ga_2O_3 microstructures but also Ga_2O_3 nanostructures grown in this sample can have this kind fin-like decoration. Figure (4.3) (f) shows EDS-STEM maps of the fin-covered nanostructure shown in figure (4.3) (e).

From diffraction patterns (not shown), the GD for the Ga_2O_3 nanowire was found to be the [110]. From the EDS-STEM map in (f), a Sn-rich wetting layer can be observed in this fin-decorated nanowire. Like in chapter 3 for Ga_2O_3:Ge, this is another example of dopant impurities out-diffusing to the surface during growth.

Although most of the structures displayed either one type of covering or the other, some structures like the one shown in figure (4.3) (g) presented both diamond and fin covering. The image also shows that the tin oxide fuzzy covering is in some cases due to several rotated ultra-thin flakes. The formation of the Sn-rich overlayer seems to promote the 2D-growth of tin oxide on Ga_2O_3 nanowires.

4.3 Branched and decorated structures: T-shaped and L-shaped

As mentioned in the beginning of the chapter, a similar growth method but with lower amounts of Sn had resulted in branched Ga_2O_3 structures with, at most, an Sn ball at the end [40]. In this section, we will encounter similar structures but with the novelty of the decoration and covering of SnO_2 shown in the previous section with simple elongated structures. Figure (4.4) shows some examples of T-shaped and L-shaped structures. Notice the presence of Sn-rich particles in the junction of the T-shaped structure in (a) and in one of the wires with respect to its perpendicular in the L-shaped structures in (b) and (c). The main feature of these structures is the selective covering of SnO_2, showing that the deposition of tin is more energetically favourable on certain surface planes of gallium oxide with respect to others. The final decoration is, in most cases, made by polyhedral shaped particles; only in very few cases some fins appear.

The T- and L-shaped structures have similar features as the elongated structures shown in figure (4.2), however they were only found in the micrometer size, with widths of a micron or higher. This hampered the characterization of the exposed planes and GDs by TEM since it required a sample thinning process. Therefore, in order identify the crystalline phase and orientation of the tin oxide particles in these structures, Electron Back Scattered Diffraction (EBSD) in the SEM was performed. The results are presented in figure (4.5), in which a double T shaped decorated Ga_2O_3 structure (a structure with two crossed wires instead of one) is shown.

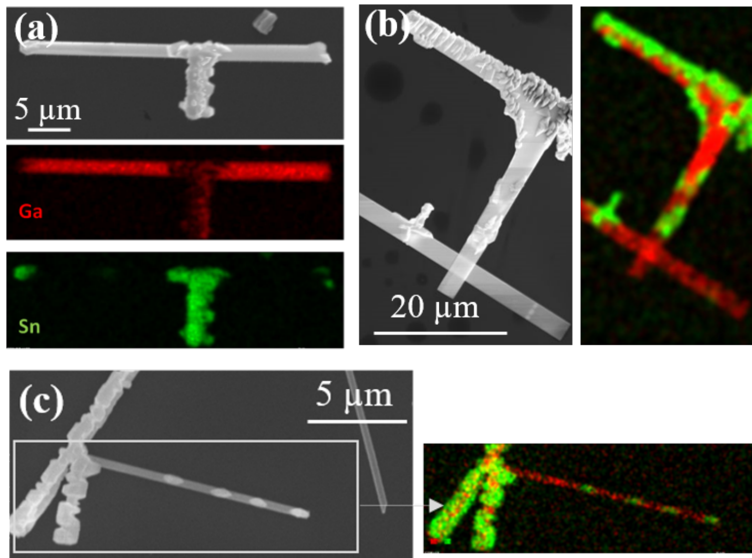

Figure 4.4: (a) SE image (top) and EDS maps (middle = Ga; bottom = Sn) of a T-shaped structure (b) SE image and EDS map of an L-shaped structure (c) SE and EDS map of another L-shaped structure. For all the EDS maps, gallium is shown in red while tin is shown in green.

As figure (4.5) (a) shows, there is a much higher density of SnO_2 particles in the vertical branches in comparison with the horizontal wire, like in the structure in figure (4.4) (a). Due to the surface roughness on the top facet of such wire, no EBSD patterns could be obtained from the Ga_2O_3 trunk. However, in the area shown in figure (4.5) (b), corresponding to the tip of one of the crossed wires, EBSD patterns were obtained. These patterns were ascribed to the rutile phase of SnO_2. The particles were found to be monocrystalline, exposing the {110} plane, as figure (4.5) (c) shows. Notice that the two studied particles are slightly tilted symmetrically with respect to the vertical axis of the silicon substrate, giving rise to a slightly tilted stereographic projection of the pole distribution with respect to the center of the pole figure, which allows to distinguish them in this figure. The EBSD pattern of one of the two particles, with the identified tetragonal SnO_2 planes is shown in figure (4.5) (d).

Theoretical studies [108] predict that the {110} rutile surface plane has the lowest energy and therefore is the most stable thermodynamically. This agrees with the particles' exposed plane found in figure (4.5). This surface

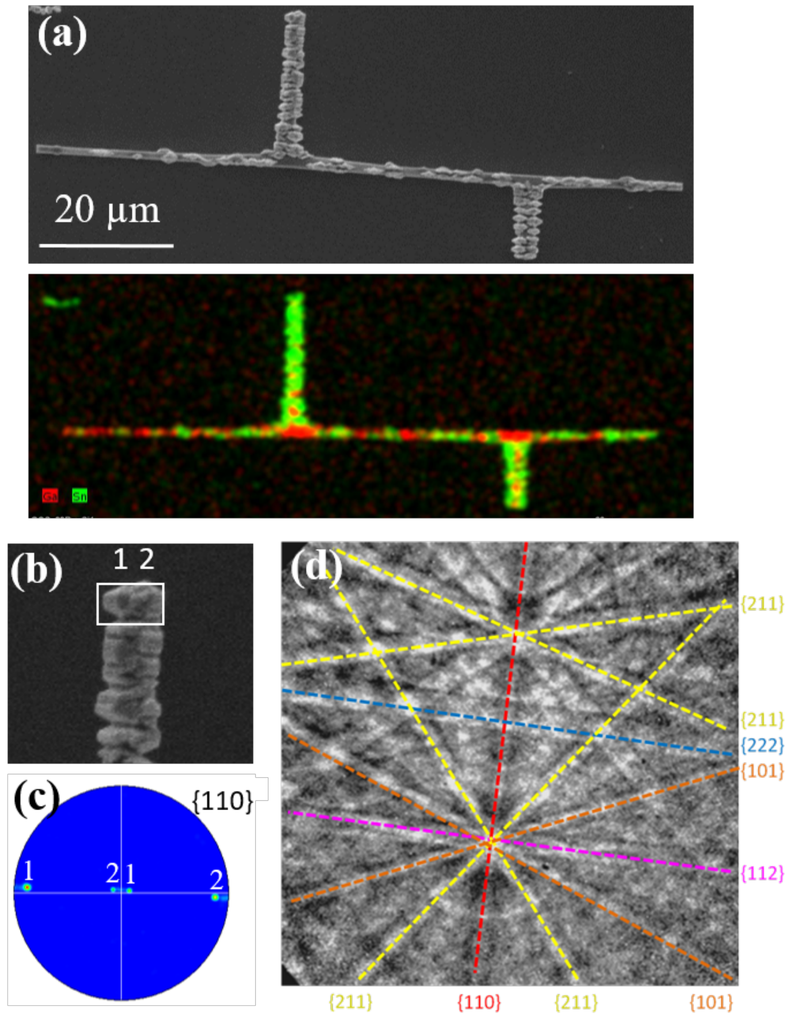

Figure 4.5: (a) SE image (top) and EDS map (bottom) of a double T type structure. (b) SE image showing the two particles (labelled 1 and 2) subject to EBSD and (c) convoluted pole figure for the [110] zone axis, indicating with white numbers the poles due to particle 1 or 2. (d) EBSD pattern of particle 2.

plane is different to the {010} plane identified by TEM on the diamond shaped nanoparticles in figure (4.2) (h). The calculated sequence for the surface stability in rutile SnO_2 is $\{110\} < \{010\} < \{101\} < \{001\}$, so it is still quite favourable energetically to form {010} SnO_2 nanoparticle covering. It could be more thermodinamically favourable than the (110) for

certain Ga_2O_3 wire facets like the one shown in fig. (4.2) (h), in which there are some lattice plane coincidences between the Ga_2O_3 wire axis and the nanoparticle covering.

To complete the microstructural characterization of the branched structures, μ-Raman spectroscopy was performed in a representative T-shaped structure. Figure (4.6) shows the μ-Raman spectra of the Ga_2O_3 wire axis (top spectrum, in pink) and the SnO_2 particles (bottom spectrum, in green). The spectra reveal a very good crystalline quality, with well-defined characteristic modes of monoclinic Ga_2O_3 and rutile SnO_2. The bottom spectrum shows the main rutile SnO_2 modes at 475, 633 and 775 cm^{-1}. In the top spectrum, the characteristic β-Ga_2O_3 Raman modes (170, 198, 320, 345, 416, 475, 629, 654 and 764 cm^{-1}) dominate, with no clear frequency shifts with respect to the reference spectra. Like in the previous chapter, the 520 cm^{-1} peak which appears in both Raman spectra corresponds to the silicon substrate.

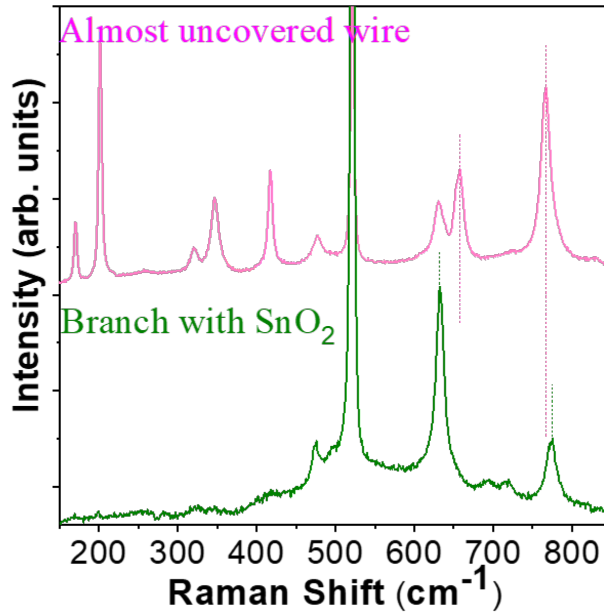

Figure 4.6: μ-Raman spectra of the uncovered part (pink) and covered part (green) of a T-shaped wire.

In order to study the luminescence of the T-shaped structure, CL was performed. The high spatial resolution of CL allowed for the acquisition of

luminescence spectra at different points in the structure. A CL spectrum of an uncovered part of a T-shaped wire is shown in figure (4.7). It presents the expected luminescence of Ga_2O_3, in the blue-UV range, with no clear emission arising due to Sn doping. CL performed on the wire covered with SnO_2 particles gave rise to a superposition of the SnO_2 and the Ga_2O_3 emissions. The luminescence of SnO_2 particles will be discussed in the next section.

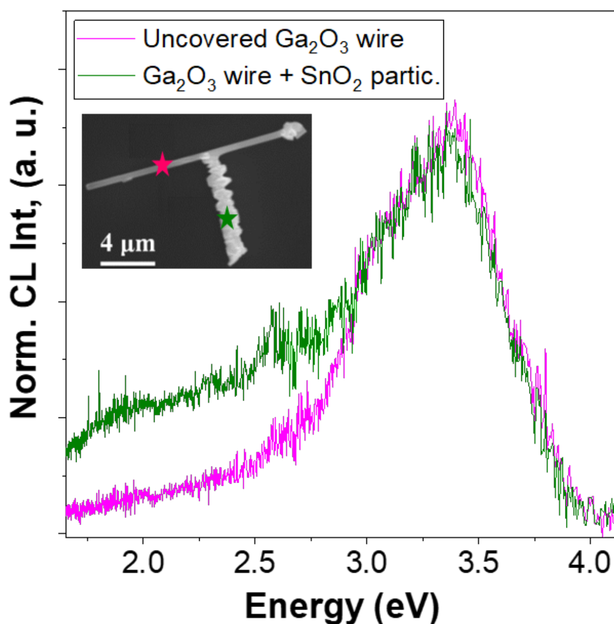

Figure 4.7: CL spectra of the uncovered part of the T-shaped structure shown in the inset with a pink star (pink line) and of the SnO_2-covered branch shown in the inset with a green star (green line).

4.4 Skewer-like (SK) heterostructures

The final main type of the obtained structures in thermal treatments involving only Ga_2O_3 and SnO_2 precursors is the skewer-like (SK) heterostructures. As it can be seen in figure (4.8) (a), these structures look like food skewers. They are composed of a main Ga_2O_3 nanowire and polyhedral-shaped SnO_2 particles. These kind of structures are not unique for the Ga_2O_3-SnO_2 system; SK structures with very similar morphology and di-

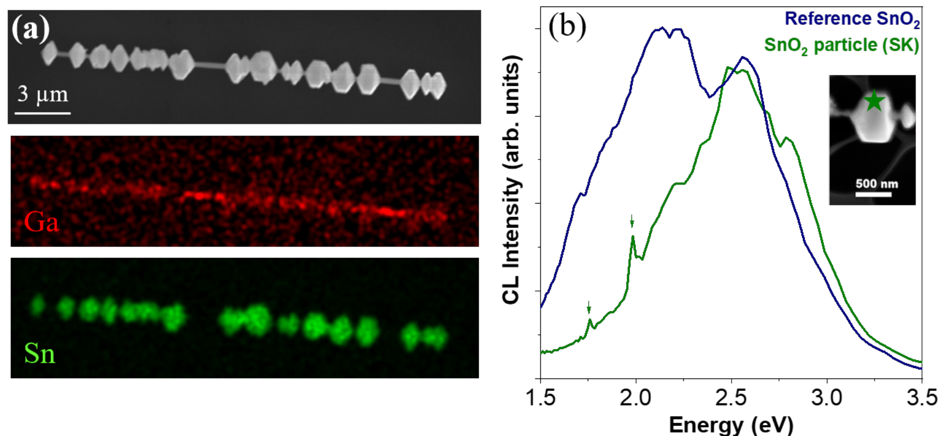

Figure 4.8: (a) SE image of a representative skewer-like structure (top) and EDS maps of this structure (middle = Ga, red; bottom = Sn, green). (b) CL spectra of a reference SnO_2 wire (blue) and a SnO_2 particle (green) from an SK heterostructure. The inset is an SE image showing the area from which the green spectrum was taken with a green star.

mensions but with a different chemistry; composed of a Zn_2GeO_4 axis and tin oxide particles with a high amount of germanium, have been recently reported [109].

In these structures, the Ga_2O_3 nanowire has a diameter of a few hundred nanometers, sometimes even less than 100 nm, and the polyhedral particles are much thicker than the nanowire, unlike the polyhedral-covered structures shown in figure (4.2). The SK structures are the most common in the whole Ga_2O_3-SnO_2 synthesized sample, see e.g. figure (4.1) (b), and are interesting for applications in nanodevices as they can be seen as a period, albeit irregular, of several nanojunctions between Ga_2O_3 and SnO_2.

Figure (4.8) (b) presents a comparison between the CL spectrum of one of the polyhedral particles which form an SK heterostructure and a reference SnO_2 microwire, synthesized under the same conditions. Both were acquired with 10 kV acceleration voltage. In the SK structure, owing to the high spatial resolution of CL and taking into account that the SnO_2 particle has a much larger volume than the Ga_2O_3 nanowire axis (around 10x), it is expected that the main signal should come from such particle, although a small contribution can be expected from the Ga_2O_3 nanowire.

Both spectra show that SnO_2 emits throughout the whole visible band, al-

though at different relative intensities depending on the dimensionality of the structure. SnO_2 has green-orange CL emission bands (centered at 1.95 eV and 2.25 eV) related to oxygen vacancies in the bulk material [110]. In addition, SnO_2 also has a CL emission in the blue part of the spectrum (centered at $\sim$2.7 eV), which is associated with oxygen-vacancy-related surface states [111]. Comparison of the CL spectra of the SnO_2 wire with the CL spectra of the SnO_2 particle shows that the blue emission has a higher relative intensity in the polyhedral particles with respect to the orange emission. We believe that this is due to the higher presence of oxygen vacancy-related surface states in these 3D nanoparticles with respect to their 2D counterparts.

In addition, a distinct feature was observed in the CL spectrum of this figure in comparison to the CL spectrum of other polyhedral particles: two narrow emissions at 1.76 and 1.98 eV (704 and 625 nm) appear (see green arrows in the spectrum in figure (4.8) (b)). One possible explanation for these peaks would be some kind of optical resonances in this particle. The peak separation is too small for Fabry-Pérot (FP) resonance modes between both sides of the particle. It could fit with whispering gallery modes between the different faces of the irregular hexagonal prism. However, a set with a higher number of peaks is usually expected for WGM. The explanation for the main narrow emission, at 1.98 eV, will be given further on in this section.

In order to determine the crystallographic relationship between the Ga_2O_3 axis and the SnO_2 particles in the SK structures, TEM analysis was carried out. Figure (4.9) (a) is a low-magnification TEM image of an SK heterostructure. For this structure, high-resolution TEM images and their corresponding Fourier transform (FT) pattern were carried out both in the axis, figure (4.9) (b), and the particle, figure (4.9) (c). The monoclinic Ga_2O_3 and rutile SnO_2 phases were identified for the trunk and particle, respectively. The Ga_2O_3 trunk was found to grow along the [110] direction. The SnO_2 particle is monocrystalline, with well defined facets with characteristic (101) and (100) planes, although the main facet exposed is the one perpendicular to the electron beam, i.e. the $\{010\}$. As explained before, this surface is the theoretically second most favourable energetically. It must be noted that TEM analyses on other SK heterostructures showed these same facets.

Notice the presence of moiré fringes in figure (4.9) (a), in the superposition of the SnO_2 particles and the Ga_2O_3 axis. Moiré fringes are produced by the superposition of two lattices with very similar spacing and/or orienta-

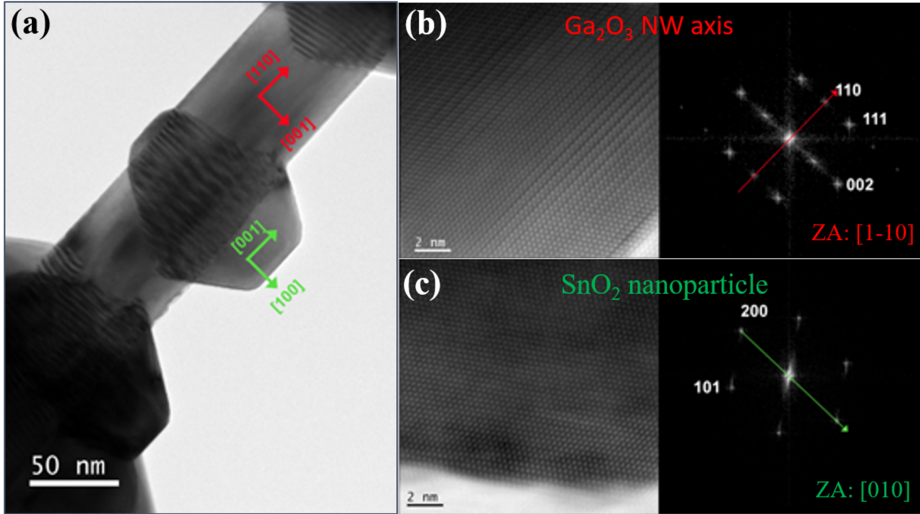

Figure 4.9: (a) BF-TEM image of a skewer-like nanostructure. (b) HRTEM analysis of the nanowire axis of the structure and its corresponding FFT. (c) HRTEM analysis of the nanoparticle on the structure and its corresponding FFT.

tion. A higher magnification image of such pattern is shown in figure (4.10) (a). In our SK structures, we observed traslational fringes in the direction parallel to the Ga_2O_3 GD, the [110]. Figure (4.10) (b) corresponds to the FFT pattern of the area indicated with a dashed rectangle in figure (4.10) (a). The experimental analysis of this pattern gave a value of a periodicity of d_M (exp.) $= 4.1\,\text{nm}$. On the other hand, the theoretically expected value for the periodicity of a traslational moiré pattern can be calculated by equation (4.1):

$$d_M = \frac{d_A * d_B}{|d_A - d_B|} \tag{4.1}$$

Where d_A and d_B are the interplanar distances of the two planes involved in forming the moiré pattern. In this case, see figure (4.9), they are the (110) plane of Ga_2O_3 and the (001) plane of SnO_2. The theoretical-expected value for the above mentioned planes is d_M (theo.) $= 3.9\,\text{nm}$, which is close to the measured periodicity. This suggests that SnO_2 is relaxed at the very early stage of the particle growth, with minimal strain. Figure (4.10) (c) is a ball and stick model showing the lattice matching of the (110) plane of Ga_2O_3 (d= 2.95 Å) and the (001) plane of SnO_2 (3.19 Å). Notice that in

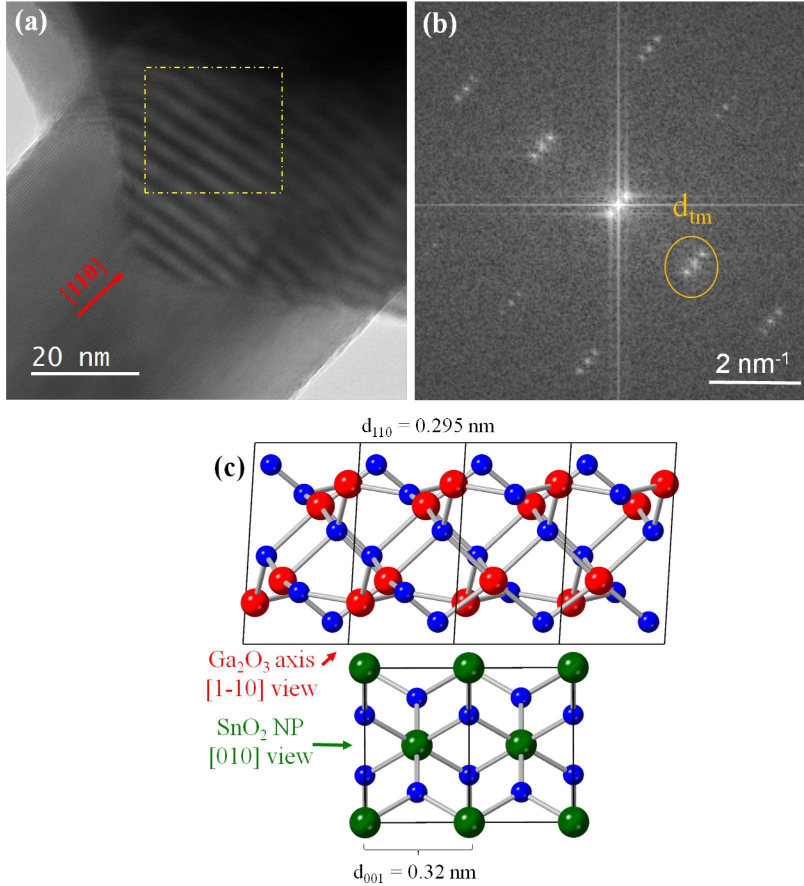

Figure 4.10: (a) BF-TEM image of the moiré fringes in the SK heterostructure. (b) FFT of the dashed rectangle. Some diffraction spots originated from the moiré fringes are highlighted by an orange circle. (c) Ball and stick model of the lattice matching between the Ga_2O_3 nanowire axis (top) and the SnO_2 particle (bottom), in the same orientation as the TEM view in figures (4.9) (b) and (c). Ga ions are shown in red, O ions in blue and Sn ions in green. The interplanar distances of the (110) Ga_2O_3 and the (001) SnO_2 planes are also labelled.

this diagram the zone axis of both materials is chosen to be the same as the TEM zone axes in figures (4.9) (b) and (c).

XPS analysis with high spatial resolution was performed at the ESCAmicroscopy line of the Elettra synchrotron in order to obtain information about the surface of the nanowire axis of the SK heterostructure. The incident photon energy was 648 eV. This translates into a mean free path of the

excited photoelectrons of the outer shells of around 10 Å, and a few Å less for core level electrons [84]. The energy axis was calibrated by fixing the C 1s level to its well-known value of 248.8 eV [112]. Figure (4.11) (a) shows an XPS map of the chosen SK structure, representing the intensity of the Ga 3d line. Figure (4.11) (b) shows the XPS spectrum of the nanowire axis in the valence band - Ga 3d - Sn 4d energy window. This window allows for the recording of both Ga 3d and Sn 4d levels in the same measurement. The results show that the main peak is the Ga 3d one, which lies at 20.6 eV. In addition, the Sn 4d peak is also present in the spectrum. This implies that the nanowire surface is Sn-rich, which was also the case for the nanostructure in figures (4.3) (e) and (f).

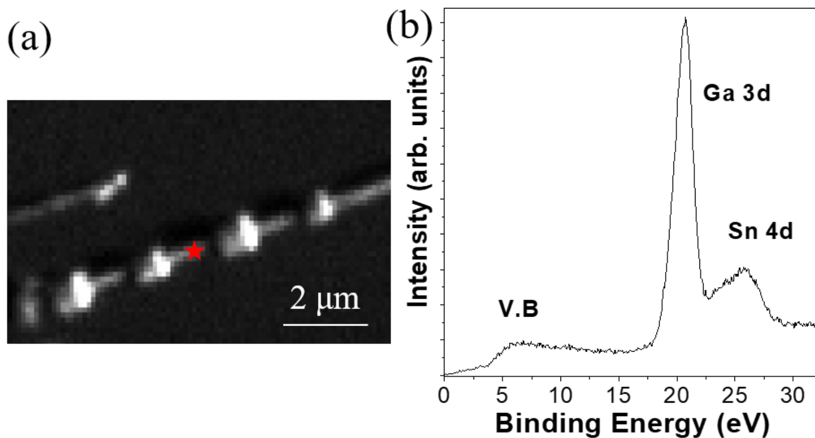

Figure 4.11: (a) XPS map of the SK structure at the Ga 3d energy. (b) XPS spectrum of the valence band, Ga 3d and Sn 4d lines, measured from the nanowire axis of the SK heterostructure (red star in (a)).

Finally, a Focused Ion Beam (FIB) cross-section perpendicular to the Ga_2O_3 wire GD and containing one of the SnO_2 polyhedral particles, see figure (4.12) (a), was fabricated from an SK heterostructure to further characterize the nanowire-particle heterojunction. A low magnification ADF-STEM image of this section is displayed in figure (4.12) (b), showing the Ga_2O_3 nanowire surrounded by the SnO_2 particle.

The crystallographic relationship of Ga_2O_3 and SnO_2 in this structure was determined from ADF-STEM images such as the one shown in figure (4.12) (c). The GD of the Ga_2O_3 axis in this SK structure is the [010], which in the TEM projection is parallel to the [001] axis of SnO_2. This direction is

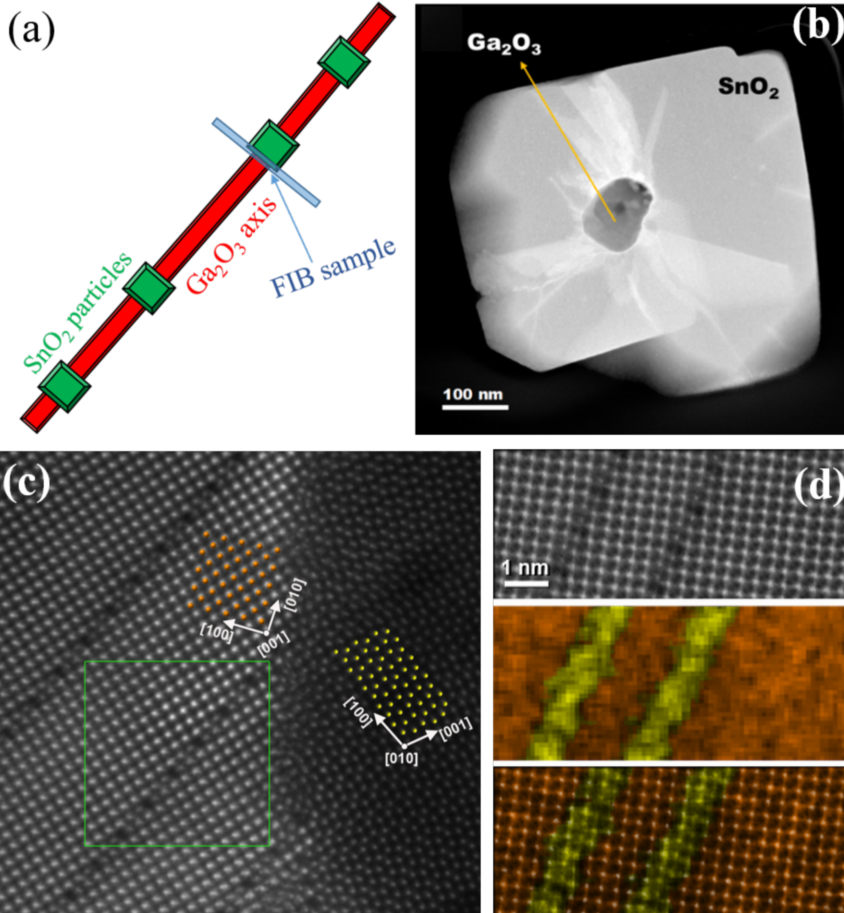

Figure 4.12: (a) Diagram depicting the cross-section of the Ga_2O_3-SnO_2 junction prepared by FIB on an SK heterostructure. (b) Low magnification ADF-STEM cross-section image of the SK structure prepared by FIB. (c) Atomic resolution ADF image of the heterojunction between the Ga_2O_3 axis (right in fig. (c)) and the SnO_2 particle (left in fig. (c)), overlapped with the cation balls model for Ga_2O_3, yellow, and SnO_2, orange. (d) ADF image (top), EDS-TEM map (middle) and both superposed (bottom) of part of the SnO_2 nanoparticle, showing Ga intergrowth.

different to the [110] direction obtained in the structure of figure (4.9) (b), although the interplanar distance of both planes in Ga_2O_3 is very similar (3.04 Å in the {010} planes versus 2.95 Å in the {110} planes). In both cases, they are very similar to the 3.19 Å interplanar distance of SnO_2. Therefore, lattice matching with the {001} planes of SnO_2 with minimal

strain is possible in both [110]- and [010]-grown SK structures. Dark lines marking boundaries along {210} planes of the SnO_2, like the one marked with a green rectangle in figure (4.12) (c), were observed. Figure (4.12) (d) is a combination of an atomic resolution ADF-STEM image and EDS elemental mapping recorded in two of these boundaries. It reveals that a sheet of gallium rich material is clearly present in both boundaries. In addition, the ADF images show hexagonal tunnels with a diameter of less than 3 Å and a period of approximately 1 nm in the boundaries. Such intergrowth and formation of hexagonal tunnels has been reported between Ga_2O_3 and other rutile structures such as TiO_2 [113], with potential applications for ionic conductivity. From these observations, it is not clear whether the intergrowths formed concurrently with growth of the SnO_2 particles around the Ga_2O_3 axis or they were formed after SnO_2 growth by condensation of Ga interstitials (during cooling or otherwise). Further work will be needed in order to determine whether these intergrowths are present in all the particles and in all the SK heterostructures or only in some of them, e.g. in the [010]-grown SKs but not in the [110]-grown SKs.

This Ga_2O_3 intergrowth can be the cause for the already mentioned localized CL emission at 2.0 eV (see figure (4.8) (b)). As deep level point defects (such as oxygen vacancies in SnO_2) create localized wave functions, the modification of the electronic states structure, in this case due to Ga_2O_3 intergrowth, could result in the narrowing of the 2.0 eV orange emission in SnO_2 due to broken bonds or strain. In addition, the 1.8 eV peak can be tentatively attributed to a phonon replica of the 2.0 eV emission, although new trapped states originating from the Ga_2O_3 intergrowth cannot be ruled out for any of the two observed peaks.

4.5 Ga_2O_3-SnO_2 crossed-wire (CW) heterostructures

Let us move to the crossed-wire (CW) heterostructures. These structures were formed when an additional compound, chromium oxide, was added to the precursors (metallic Ga, Ga_2O_3 pellet and SnO_2 powders) in the thermal treatment. This addition, along with a longer growth time of 15 hours, was the only difference in the synthesis method: the rest of the parameters such as the furnace used, the gas flux and the growth temperature were kept the same with respect to the growth parameters given in section 4.1. It must be noted that none of the previously mentioned decorated structures appeared

in this thermal treatment. Therefore, the inclusion of chromium oxide as a precursor profoundly altered the types of nano-heterostructures obtained.

Figures (4.13) (a) and (b) are an SE image and an EDS map of a representative CW structure. These structures are composed of a gallium oxide axis and several tin oxide crossed wires. The Ga_2O_3 central wires have a width of a hundred to several hundred nanometers, depending on the CW structure. The crossed wires are generally wider than the central nanowire, and form approximately 90° with it. Some larger structures also have crossed wires with different angles, as shown in [114], where the CW structures were analyzed by X-Ray Fluorescence (XRF). The obtained atomic percentage of chromium incorporated on the Ga_2O_3 axis was 0.7% at. while gallium and tin maps displayed no remarkable interdiffusion along the junction and no agglomeration effects.

Figure (4.13) (c) shows μ-Raman spectra of the axis (pink) and perpendicular wires (green) of the crossed-wire structure. Bearing in mind the diameter of the laser spot (see figure (2.15)), some contribution of the other material to the signal, i.e. the SnO_2 crossed wires to the signal obtained from the axis, cannot be avoided. For example, the 633 cm^{-1} Raman mode of SnO_2 can be observed in superimposed to the 629 cm^{-1} mode of Ga_2O_3 in both spectra. Still, the main modes of each material (the 200 cm^{-1} mode of Ga_2O_3 and the 633 cm^{-1} of SnO_2) are the most intense in its corresponding spectrum. More importantly, none of the mode frequencies show clear shifts or have a substantial increase in FWHM with respect to the reference materials, which implies a high crystalline quality of the CW nanostructures.

In order to obtain the percentage of tin in the Ga_2O_3 nanowire, special care had to be taken in order to avoid any contribution from the SnO_2 crossed wires. Several EDS spectra were taken on the SEM from different nanowire axis of CW structures, and the Sn cation percentage was found to be 4% - 6% depending on the structure. However, bearing in mind the generation volume in an SEM, crossed wire contribution to the Sn signal was identified as an overestimating factor in these percentages. In order to eliminate this factor, EDS spectra were obtained in the TEM, in an area where no crossed wire could interfere. A representative example is shown in figure (4.13) (d) in pink; the Sn cation percentage in Ga_2O_3 was found to be (2.6 ± 0.5)% at. Such percentage of tin in the host is expected to considerably increase the n-type character of the Ga_2O_3 axis while not altering its monoclinic crystal structure.

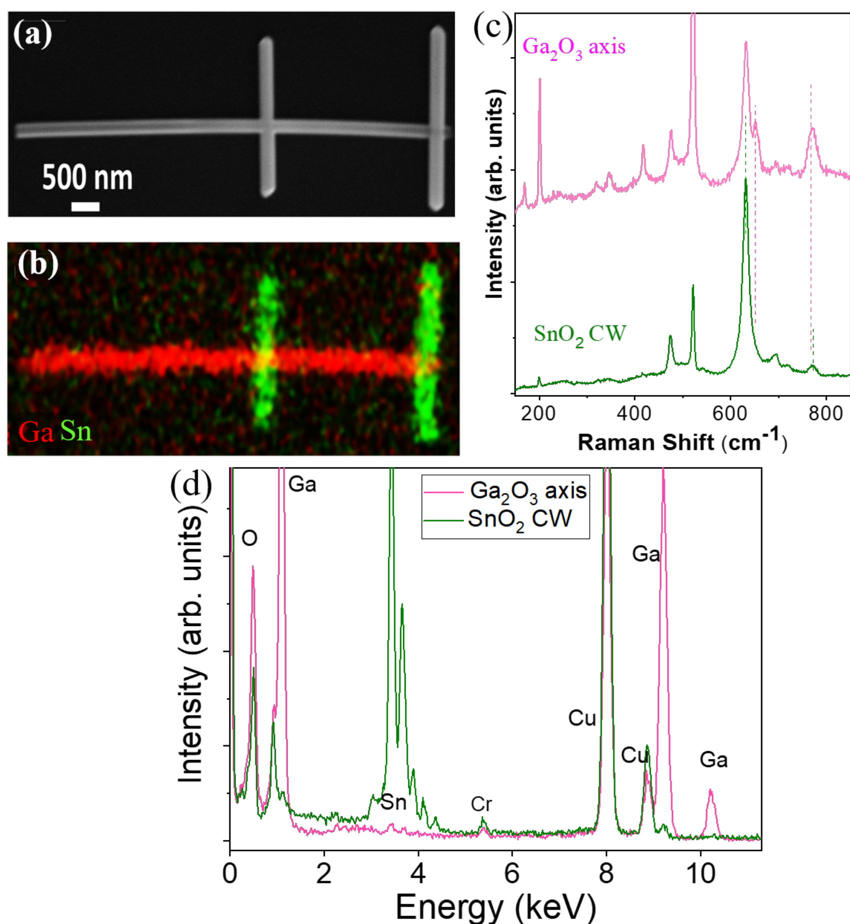

Figure 4.13: (a) SE image and (b) EDS map of a crossed-wire (CW) structure. (c) μ-Raman spectra in which the excitation laser spot was mainly centered in the axis (pink) or in crossed wires (green) of a CW structure. (d) EDS-TEM spectra of a CW structure. Analogously to (c), the spectrum from the Ga_2O_3 axis is shown in pink while the spectrum for a SnO_2 crossed wire is shown in green. The peaks are labelled with the corresponding element.

On the other hand, from the EDS-TEM spectrum shown in green in figure (4.13) (d), the SnO_2 crossed wires have a Ga cation concentration of around 3.6% at. SnO_2:Ga thin films were reported to require Ga concentrations above 5% to present p-type conductivity [115]. However, the Ga percentage obtained in this work could be enough for SnO_2 nanowires to be p-type, according to ref. [107]. This opens the applicability range of

these heterostructures for bipolar devices containing Ga_2O_3 such as improved transparent UV detectors [107], which is one of the main aims for this material [16]. In addition, Ga doping in SnO_2 nanostructures have been recently reported to show improved gas sensing properties [116].

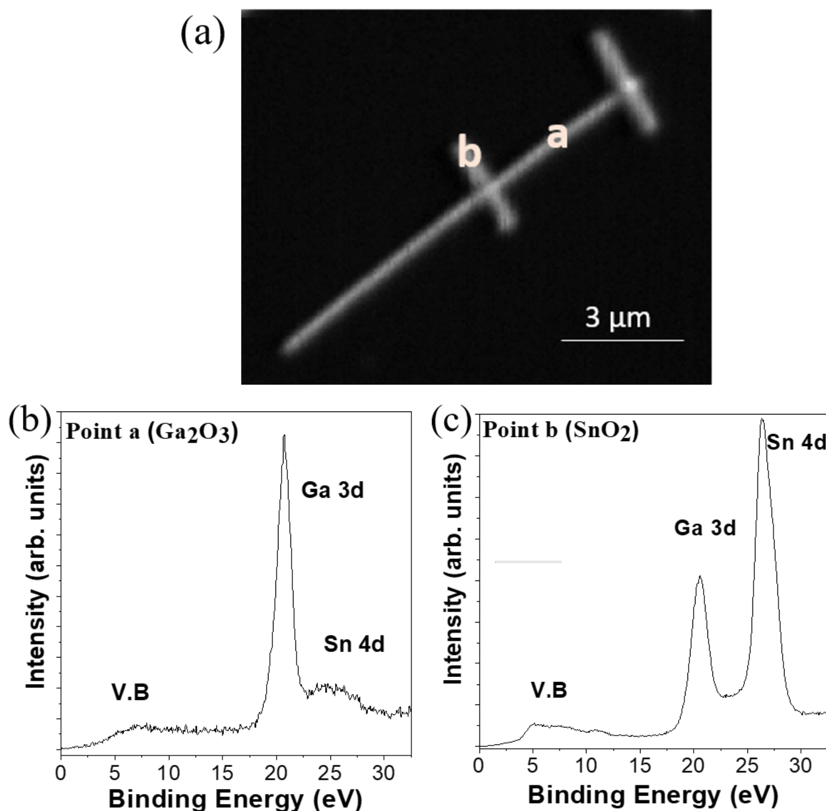

Figure 4.14: (a) XPS map of the CW structure at the Ga 3d energy. (b) XPS spectrum of the valence band, Ga 3d and Sn 4d lines, obtained from the axis of the CW heterostructure (point a in (a)). (c) XPS spectrum of the valence band, Ga 3d and Sn 4d lines, obtained from one of the crossed wires of the CW structure (point b in (a)).

In order to get a deeper insight into the surface electronic structure of the CW structures, XPS with high spatial resolution was performed in one of these structures. Figure (4.14) (a) is an XPS map of the structure at the Ga 3d energy and figure (4.14) (b) shows the spectrum of the nanowire axis in the Ga 3d - Sn 4d energy window. The results show that the main peak is the Ga 3d peak at 20.7 eV, while an almost negligible Sn 4d peak, with an

intensity much lower than for the SK heterostructure (see figure (4.11) (b)), can be observed. This implies that the surface of the CW heterostructures is not Sn-rich, unlike in the SK heterostructures. Figure (4.14) (c) is an analogous XPS spectrum of one of the crossed wires. Apart from the Sn 4d peak, a high intensity Ga 3d peak at 20.5 eV can be observed, which reveals a high gallium content in the surface of the Ga doped SnO_2 crossed wires.

TEM analysis

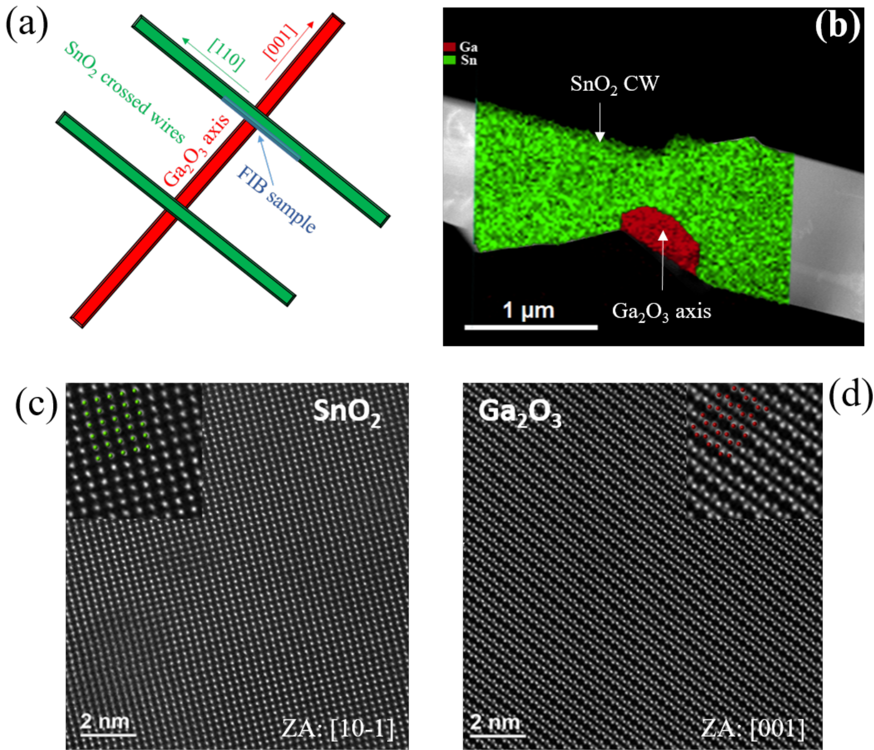

Figure 4.15: (a) Diagram depicting the cross-section of the Ga_2O_3-SnO_2 junction prepared by FIB on a CW structure. It also displays the obtained growth directions by TEM. (b) STEM analysis of the junction cross-section prepared by FIB: ADF-STEM image overlapped with the compositional map provided by EDS (Ga in red, Sn in green). (c) ADF-STEM image of the SnO_2 crossed wire. (d) ADF-STEM image of Ga_2O_3 nanowire axis. Insets in (c) and (d) display atomic resolved ADF images overlapped with model crystal structures in both cases.

In order to elucidate the crystallographic properties of the Ga_2O_3-SnO_2 heterojunction, a FIB section, perpendicular to the Ga_2O_3 nanowire axis GD

and containing a SnO_2 crossed wire, see figure (4.15) (a), was prepared. Figure (4.15) (b) is a low magnification ADF image with EDS elemental map superimposed of the heterojunction, revealing the Ga_2O_3 nanowire axis and the SnO_2 crossed wire in the FIB specimen. High magnification ADF images of an area in each material are shown in figures (4.15) (c) and (d). The atomic structures indicate that the projections are the [10-1] for the rutile SnO_2 crossed wire and the [001] for the monoclinic Ga_2O_3 nanowire. As the FIB cut had been taken perpendicular to the nanowire longitudinal direction, this implies that the Ga_2O_3 nanowire grows along the [001] direction. This result reveals the different GD of the CW heterostructures with respect to the SK heterostructures and the other nanowires analyzed so far. This point is discussed in the next section.

Figure (4.16) (a) shows an atomically-resolved ADF image of the Ga_2O_3-SnO_2 CW heterojunction prepared by FIB, projected into the (001) and (10-1) planes of Ga_2O_3 and SnO_2, respectively. Brighter atomic columns observed in the top of the image correspond to tin ions ($Z = 50$) forming an ordered SnO_2 lattice while darker atomic columns observed in the bottom of the image correspond to gallium ($Z = 31$) ions forming an ordered Ga_2O_3 lattice. The image was obtained from the top part of the Ga_2O_3 axis and bottom part of SnO_2 crossed wire shown in figure (4.15) (b).

The FFT of figure (4.16) (a) is shown in figure (4.16) (b). As there are two ordered lattices in the ADF image, there are two sets of diffraction spots in the FT, which come from one or the other lattice. In this figure, indexed diffraction spots associated with Ga_2O_3 are labelled in red and those corresponding to SnO_2 are labelled in green. From the ADF analysis, the GD of the SnO_2 crossed wire is the [101]. The image shows that both nanowires are joined by an interface which is not edge-on under these STEM conditions. No linear or planar defects and no disorder was observed in the interface region on these heterojunctions, as it had been anticipated by XANES measurements [114].

Notice the overlap of certain diffraction spots. They show the lattice coincidence between {310} planes in Ga_2O_3 and {020} planes in SnO_2. Figure (4.16) (c) is a ball and stick model of the lattice matching of these planes, showing views of SnO_2 and Ga_2O_3 which are perpendicular to the STEM view in (a) and (b). It can be noticed that the {310} plane connects the octahedral atoms in Ga_2O_3, which are shown in orange in the ball and stick diagram. The interatomic distance of both planes is 0.24 nm.

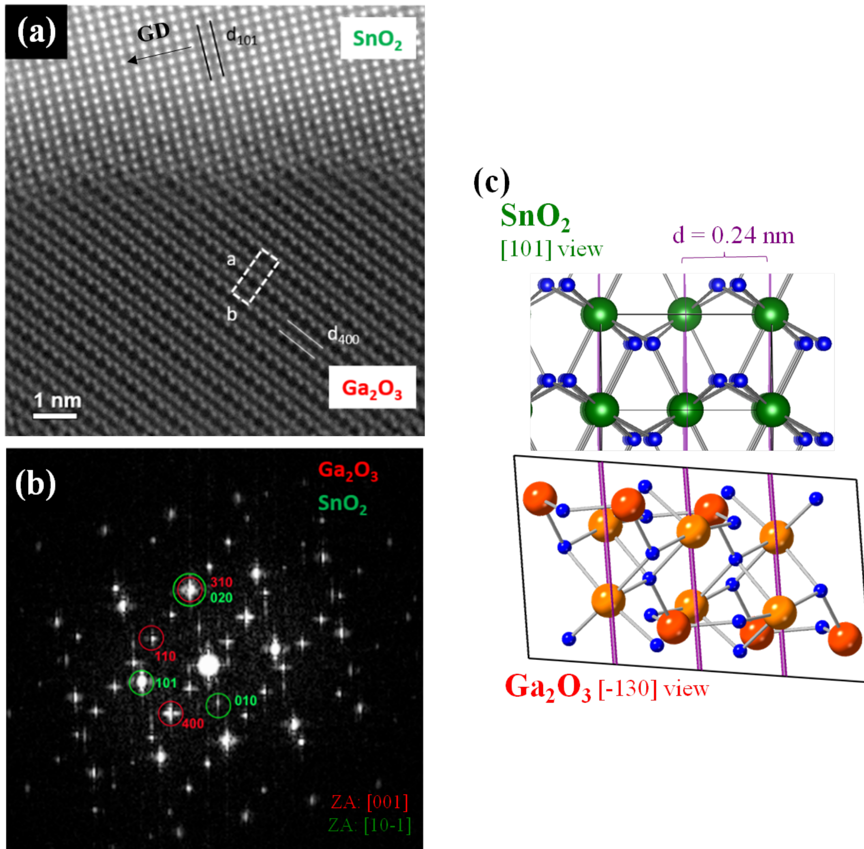

Figure 4.16: (a) Atomically-resolved ADF image of the crossed-wire heterojunction projected onto the (001) and (10-1) planes of Ga_2O_3 and SnO_2 respectively. The GD of the SnO_2 CW is [101], perpendicular to the (101) plane indicated in the image. The a and b planes of Ga_2O_3 are also shown for clarity. (b) FFT of (a) that reveals lattice coincidence between {020} planes in SnO_2 and {310} planes in Ga_2O_3. (c) Ball and stick model of the (020) plane of SnO_2 (top) and of the (310) plane of Ga_2O_3 (bottom), both shown in purple. Gallium tetrahedral and octahedral atoms in Ga_2O_3 are shown in red and orange, respectively. The structures are viewed from the [101] direction (SnO_2) and the [-130] direction (Ga_2O_3) to show the lattice matching of these planes. Both have an interplanar distance of 0.24 nm.

Luminescence analysis of CW heterostructures

Branched semiconductor nanostructures have been found to present interesting applications in photonics, such as optical filters or a lasers, due to the reduction of the laser threshold with respect to individual wires [64,

65]. Therefore, it is very interesting to explore the luminescence of our CW heterostructures. Both CL and PL were performed in several CW structures. CL allowed for the excitation of the Ga_2O_3 and SnO_2 luminescence with a high spatial resolution while PL allowed for the selective excitation of SnO_2 luminescence. The results are displayed below for a representative CW structure.

Figure (4.17) (a) is an SE image of a CW heterostructure whose luminescence is studied. Figure (4.17) (b) shows CL spectra of the Ga_2O_3 nanowire (pink) and the SnO_2 crossed wires (green). The latter presents the expected luminescence from SnO_2, with the main emission in the orange-green part of the spectrum due to oxygen vacancies in the bulk material [110]. It must be noted that the blue band at 2.7 eV has a very low intensity, in contrast to the CL of the SnO_2 nanoparticles of the SK structures (see figure (4.8) (b)). Therefore, the luminescence from these SnO_2 crossed wires is more similar to the bulk material, with low emission arising from surface states.

Additionally, apart from the orange-green emission, there seems to be contribution from lower energies (around 1.8 eV). It had been found that substitutional chromium incorporation in SnO_2 reinforces the orange-red emission with respect to the green-blue one [117] although care must be taken as SnO_2 sintered at different temperatures and under different conditions has very different luminescent spectra in this range due to the presence or absence of different oxygen vacancy states [110].

Regarding the Ga_2O_3 horizontal wire in figure (4.17) (a), its CL spectrum in figure (4.17) (b) presents its characteristic UV-blue emission (see chapter 3) along with a non negligible band in the orange-red (1.8-2.1 eV) region. We believe that this emission is partly due to guided light from the crossed wires; notice that the Ga_2O_3 central nanowire has SnO_2 crossed-wires nearby which can be partly excited both by the electron beam and by the UV emission of Ga_2O_3. However, the red (1.8 eV) contribution is slightly larger in the horizontal wire compared to the crossed wires. This can be tentatively ascribed to the emission of chromium ions in Ga_2O_3. Even with very low amounts of Cr^{3+} in Ga_2O_3, the characteristic red luminescent emission is intense (see [54] and the next chapter).

The CL spectra in figure (4.17) (b) show that the emission in the Ga_2O_3 nanowire is complementary energy-wise to the emission in the crossed wires in the CW heterostructures, and the combination of both covers the whole of the visible - near UV spectrum. Monochromatic CL images of the charac-

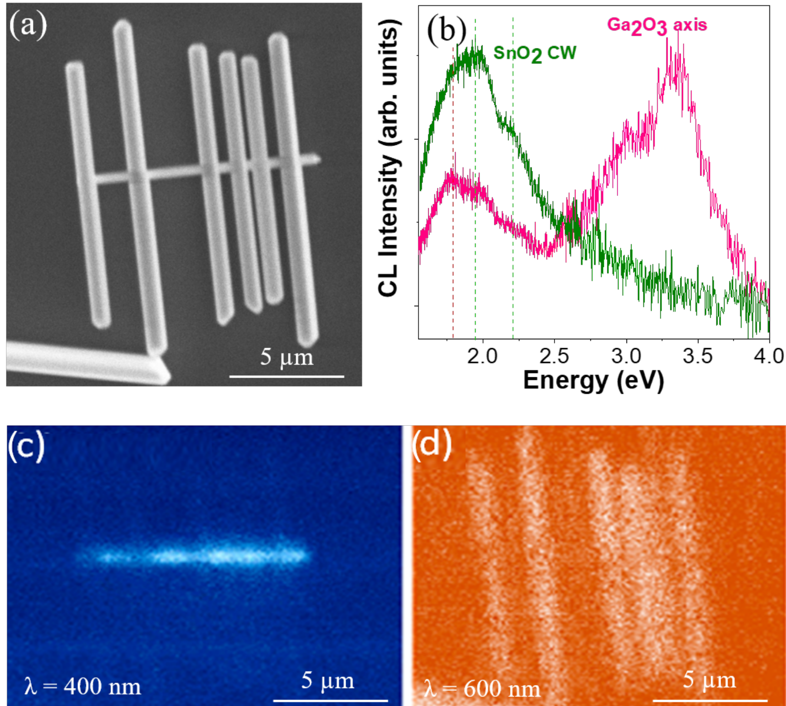

Figure 4.17: (a) SE image of a CW structure. (b) CL spectra of Ga_2O_3 axis (pink) and SnO_2 crossed wires (green). Red and green dashed lines indicate identified emission bands for SnO_2. (c) Monochromatic CL image at 400 nm of the structure shown in (a). (d) Monochromatic CL image at 600 nm of the structure shown in (a).

teristic emission of Ga_2O_3 and SnO_2 in this heterostructure were performed and are displayed in figures (4.17) (c) and (d), respectively. In these figures, it can be seen that the main 400 nm (3.1 eV) emission comes from the axis, while crossing wires emit in the 600 nm (2.1 eV) range.

Let us continue the luminescence analysis of the CW structures with PL. Figure (4.18) (a) shows the μ-PL spectrum of the SnO_2 crossed wires (black line) from the same structure as in the previous figure. It also shows a μ-PL spectrum of SnO_2 polyhedral-shaped particles (light green line). The spectra display similar features to the CL spectra in figure (4.17) (b), namely:

1. The green-blue emission, assigned to oxygen vacancy-related surface states, is strongly enhanced in the polyhedral-shaped particles.

2. The orange-red emission, tentatively assigned to chromium incorporation, is enhanced in the in SnO_2 crossed wires.

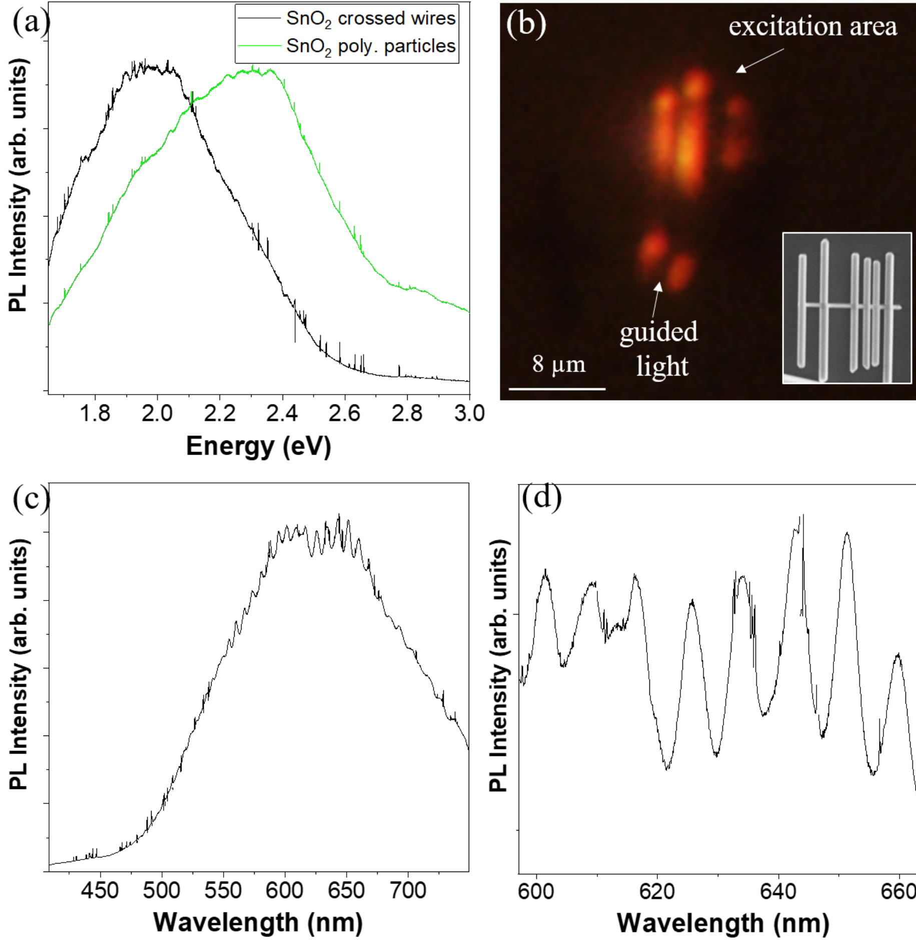

Figure 4.18: (a) μ-PL spectrum of the SnO_2 crossed wires of a CW heterostructure (black) compared to a PL spectrum of polyhedral shaped SnO_2 particles (light green). (b) PL image of such structure in real colour, showing their orange-red emission and light guiding. λ_{exc} = 325 nm. The inset shows an SE image of the structure, the same as in figure (4.17) (a). (c) PL spectrum analogous to (a) but with the collection point placed on one side of the wires, showing optical resonances. (d) Zoom of the spectrum in (c) in the 600-670 nm range.

Figure (4.18) (b) is a PL image of the CW structure under excitation of the UV (325 nm) laser, with a similar orientation to Figure (4.17) (a). As

already underlined throughout the thesis, due to its ultra-wide band gap, a very weak emission is observed from Ga_2O_3 with most dopants when exciting with 3.8 eV (i.e. our He-Cd laser), and Sn doped Ga_2O_3 is no exception to this. This was used in our favour to obtain the luminescence of the SnO_2 crossed wires with almost no contribution from the central Ga_2O_3 wire. SnO_2, with a band gap of 3.7 eV, showed a high luminescent intensity for excitation with our 3.8 eV laser. This emission is in the orange-red range, as discussed in the previous paragraph for CL. The image shows that the PL emission can be guided from one end to the other of the SnO_2 wire.

When the collection point was placed at one end of the SnO_2 wires, the PL spectrum presents resonant peaks, see figures (4.18) (c) and (d). The value of the measured group refractive index of SnO_2, both undoped and Cr doped, is 2.0 [118]. By inserting several wavelength differences between peaks ($\Delta\lambda$), a value of (12.5±0.2) µm was obtained for the optical length in the 620-660 nm wavelength range when using equation (1.2) for FP resonances. The two crossed wires in which the laser spot was centered are the ones in the left of the inset of figure (4.18) (b). Their measured lengths by SEM are 9.5 and 13.6 µm, although their end facets are not sharp so the optical path from side to side of the wire is not well defined. By comparing the wire lengths and the optical path obtained by the FP equation, it seems that the longest wire (the second from the left in the inset) is the main contributor to the resonant peaks observed in figure (4.18) (d). Finally, the finesse of the crossed-wire cavity was retrieved from the peak separation and FWHM of the resonant modes by using equation (1.4). Values up to 2.8 were obtained. This is similar to the values obtained in ref. [118] for SnO_2:Cr microtubes, microplates and microrods.

4.6 Discussion on the nanostructures' formation mechanisms

From the results exposed in this chapter, the formation mechanism for the structures is discussed. As commented in section 3.1, nanowires with very different GDs have been reported, depending on the synthesis method and metal catalyst used [119, 120]. In our synthesis conditions, the choice and amount of tin oxide or the use of chromium firstly affected the GD of the Ga_2O_3 nanowires. In both thermal growths, the temperature at the pellets is around 1100°C-1200°C (see section 4.1 and table (2.1)). With only tin oxide impurities, the [110] or the [010] GDs have been found for the Ga_2O_3

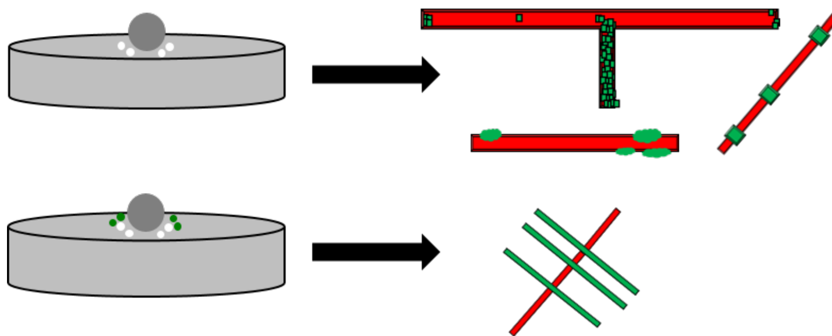

Figure 4.19: Sketch describing the main types of nanostructure formations depending on the precursors used. When the precursors are Ga_2O_3, Ga (grey) and SnO_2 powder (white), structures from sections 4.2 to 4.4 grow, while if Cr_2O_3 powder (green) is added to the precursors, CW heterostructures (section 4.5) grow.

nanowires which end up forming SK structures, while codoping with Cr favours the [001] GD. The existence of a certain GD results in a characteristic faceting of the final nanostructure, which is a key factor for the secondary growths which give rise to the different type of architectures obtained.

For thermal treatments including tin oxide and no chromium oxide, the surface facets of the elongated Ga_2O_3 nanowires favoured an epitaxial growth of 3D SnO_2 particles along the nanowire with a crystal orientation resulting in low surface energies and very low lattice mismatch with the Ga_2O_3 wire axis (see sections 4.2 and 4.4). In other structures, certain surface facets are decorated with SnO_2 ultrathin flakes (see section 4.2). In both cases, the nucleation arises from out-diffusion of Sn impurities in the Ga_2O_3 nanowires, which was deduced from the observed tin-rich surface in these structures (see figures (4.3) (f) and (4.11)).

Additionally, the presence of SnO_2 among the precursors promoted the formation of branched Ga_2O_3 nanowires, as it had been previously reported [40]. In this thesis, a greater amount of SnO_2 had been included and, as a result, SnO_2 was not only responsible for this secondary growth but also decorated the structures in a similar way to the 1D elongated structures explained in the previous paragraph. As figure (4.4) shows, the decoration is not homogeneous but preferably along certain facets, as well as in the intersections between the L-shaped and T-shaped structures. Size dependency can also be inferred: microwires and mirobelts generally form branched structures (see figures (4.2) (g) and (4.4)) while nanowires are decorated either by 2D flakes which form fins (see figure (4.3)) or by 3D polyhedral

particles. Many of the latter form SK structures (see figure (4.8)). A sketch with some examples of this kind of structures which have been encountered throughout the chapter is shown in figure (4.19) (top).

Finally, the addition of chromium oxide resulted in the growth of Ga_2O_3 - SnO_2 CW structures, as sketched in figure (4.19) (bottom). As noted before, the presence of Cr_2O_3 precursor promoted a certain GD of the Ga_2O_3 nanowires. This can be due to a modification of the mobility and diffusion of the adsorbed species due to the presence of chromium. A different GD implies other lateral surface planes of the nanowire and therefore different lattice matching conditions between Ga_2O_3 and SnO_2, as shown in the (S)TEM analysis throughout the chapter. Therefore, the choice and amount of the precursors allowed for shape engineering of the obtained TCO nano-heterostructures, enabling for 2D or 3D growth of SnO_2 on Ga_2O_3 (figure (4.19), top) or for 1D growth of SnO_2 on Ga_2O_3 (figure (4.19), bottom).

4.7 Conclusions

In this chapter, gallium oxide - tin oxide nano-heterostructures have been synthesized and morphologically, crystalographically, chemically and optically characterized.

With Ga_2O_3, SnO_2 and metallic gallium precursors, a wide growth window (both in temperature and temperature gradient) has been found. Elongated longitudinal and branched Ga_2O_3 micro- and nanostructures, which are partially covered by SnO_2 2D or 3D nanostructures, have been obtained. Electron microscopy studies suggest that the formation of a SnO_2 wetting layer on the [110] or [010]-grown Ga_2O_3 nanowire is responsible for the secondary growths of SnO_2 particles. The most common type of heterostructure is a Ga_2O_3 nanowire covered with larger-sized 3D SnO_2 polyhedral nanocrystals, whose exposed facets are the ones with minimum energy. By FIB-prepared cross-section STEM-ADF imaging of the heterojunction, it was found that some of these particles show gallium-rich intergrowth along {210} SnO_2 planes with periodic hexagonal tunnels, with possibile applications in ionic conductivity.

The addition of chromium oxide has resulted in a new dimensionality of the heterostructures: CW heterostructures composed of a [001]-grown Ga_2O_3 nanowire and several SnO_2 crossed wires. EDS-TEM spectra show a 2.6% incorporation of Sn in Ga_2O_3, making the trunk further n-type and a 3.6% incorporation of Ga in the crossed wires, tentatively making them p-type.

The Ga_2O_3 - SnO_2 nanojunction has been analyzed by ADF-STEM after FIB preparation, showing lattice matching and no disorder in the interface junction. We also observed partial lattice matching in the SK structures, hence both of the SK and the CW TCO heterostructures have potential application in bipolar nanodevices.

The luminescence of the heterostructures has been studied by CL and PL. The Ga_2O_3 nanowires emit in the expected UV-blue range while the SnO_2 particles have a luminescence composed of the orange-green bands due to oxygen vacancies and a blue band due to oxygen vacancy-related surface states. The luminescence in the SnO_2 crossed wires is in the orange-red region, with almost no intensity in the blue-UV region. Therefore, the heterostructures display a complementary luminescence which covers the whole visible spectrum. Furthermore, some of the CW structures guide the orange-red emission between their ends, displaying optical resonances. These results point out their possible use for photonic wave-guiding applications.

In conclusion, by controlling certain growth parameters, shape engineering in the nanoscale has been achieved in the Ga_2O_3 - SnO_2 system. This strategy is a useful approach to capitalize the large amount of possibilities of TCO assemblies such as the ones presented in this thesis. Novel designs should allow the tailoring of physical properties, such as optical guiding or electronic transport, which depend on the architecture, crystalline structure and chemical composition of the complex nano-heterostructures.

Chapter 5

Ga_2O_3 distributed Bragg reflector optical microcavities

5.1 Introduction

As described in chapter 1, Ga_2O_3 is a suitable material for photonic applications by virtue of its wide transparency range (up to 4.9 eV) and its rather high refractive index in the visible range (1.9 - 2.0). In the previous chapters, we have shown that different elongated Ga_2O_3 and SnO_2 morphologies with transversal dimensions in the range of microns or hundreds of nanometers are able to guide light and even show some optical resonances, albeit with low quality. In this chapter, we will study in depth the possibility of obtaining optical cavities based on Ga_2O_3 micro- and nanowires with a controlled and improved performance to emit and confine light from the red-NIR to the violet-NUV energies.

Most of the cavities studied in this chapter are based on Cr-doped Ga_2O_3. This optically active ion is a good choice for Ga_2O_3-based photonics for two reasons. Firstly, as we will see throughout the chapter, the red-NIR Ga_2O_3:Cr emission is very intense and can be excited with photon energies below the absorption edge of the material. Secondly, its red-NIR emission shows an homogeneous broadening, which is needed for optical tunability, i.e. control of the resonant wavelengths, from a single material optical cavity [121]. This is especially important for many of the current device applica-

tions of these cavities such as optical sensors or optical active switches [122]. As detailed in the introduction, chromium fulfills this requisite in Ga_2O_3 due to its phonon-assisted $^4T_2$ - $^4A_2$ transition.

This chapter focuses on the thorough study and optimization of Ga_2O_3 optical microcavities doped with this transition element, which have a largely improved performance after FIB patterning of distributed Bragg reflectors (DBRs). Furthermore, we will also study the feasibility of extending our work to the broad UV-blue band of UID Ga_2O_3, which results in shorter wavelength emitting cavities that are important for applications in areas such as optical computing or information storage [123]. In both cases, the structures are deposited on TEM grids, which were used as a substrate to avoid optical losses that would arise on bulk substrates. Hence, the analyzed optical cavities throughout the chapter are based on structures that are suspended in air, except for the carbon "mesh".

The Ga_2O_3:Cr microwires studied in this chapter were grown by a two-step thermal evaporation method in which Ga_2O_3 pellets were first annealed at 1500°C for 8 hours to form the wires and were then annealed in an alumina boat containing Cr_2O_3 powders in order to incorporate chromium by thermal diffusion into the crystal lattice of the wires. Cr cation atomic concentration was found to be in the range of 0.5% at. or lower by EDS [54]. After the thermal treatments, the Ga_2O_3:Cr micro- and nanowires had grown and formed a skein on top of the pellet.

5.2 State of the art in Ga_2O_3 resonant cavities. Design of the DBR mirrors

In section 4.5 of the previous chapter, we found that the elongated SnO_2 structures forming the CW structures were able to guide light and show weak FP resonances. We did not only observe this behaviour in these particular structures. For example, figure (5.1) (a) shows the SE image of a Ga_2O_3:Zn microbelt, which is part of the same sample studied in chapter 3. From tilted SE images (not shown) its thickness is estimated to be around 500-600 nm. This value is clearly higher than the wavelength of visible light in Ga_2O_3, therefore, this kind of long belts can guide their luminescence throughout their volume.

Figure (5.1) (b) is an optical image of the same microbelt. Apart from the visible lamp, in this image, as the 4.82 eV UV laser was also turned on, the

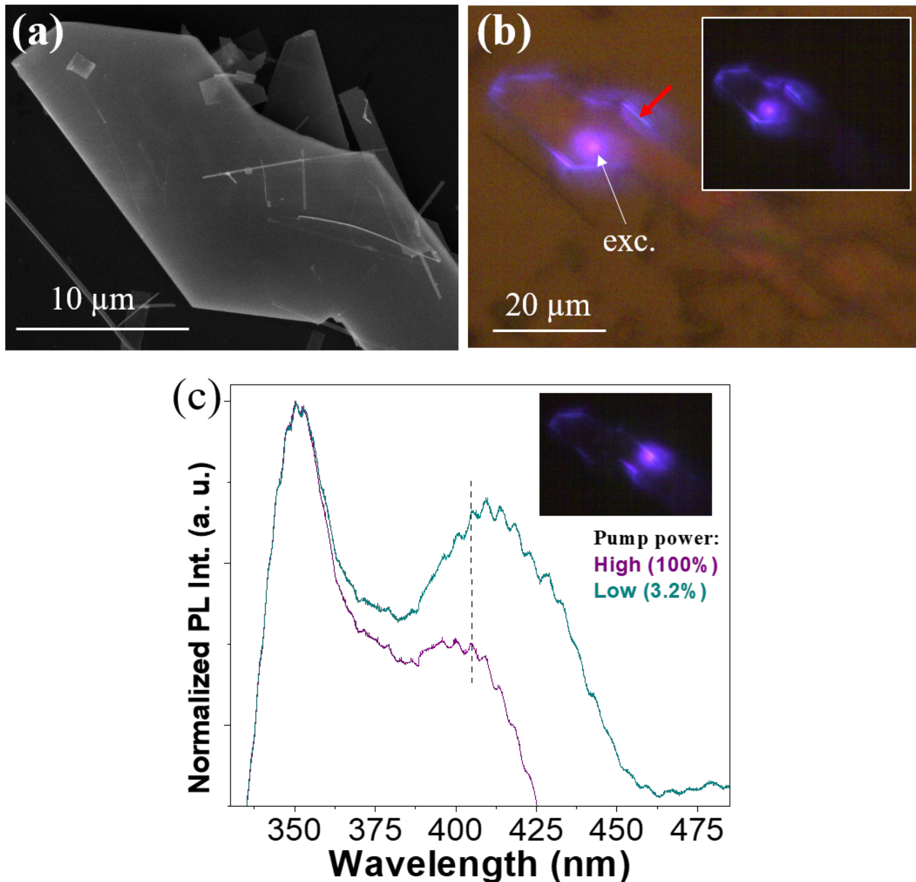

Figure 5.1: (a) SE image of a Ga_2O_3:Zn microbelt deposited on Si substrate. (b) True colour $\mu - PL$ image of the Ga_2O_3:Zn belt, in which the visible lamp light is superimposed with the structure's luminescent emission (excited with a 4.82 eV laser). The excitation area is indicated with a white arrow. The same structure shown with the lamp light off, hence with only its PL emission, is shown in the inset. (c) Normalized PL spectra acquired at one of the lateral walls of the structure, at the point marked with a red arrow in (b), both for high (purple, no filter) and low (green, 3.2% filter) excitation powers.

visible part of the PL emission from the structure was also recorded on the video camera detector. The inset shows the same PL emission with the lamp light turned off. The images reveal that the intense emission of the belt, excited by the laser on the point labelled "exc.", was guided throughout the structure and scattered on the lateral walls of the belt. Spectra recorded

in an arbitrary point of the structure presented no resonances, while PL spectra collected in one of such lateral walls (red arrow in (b)), is shown in figure (5.1) (c). They present faint optical resonances modulating the UV-blue emission of Ga_2O_3:Zn.

By using equation (1.2), the optical path of the resonances was found to be 8 µm. This agrees for the resonances to originate from reflections between the sidewall indicated with a red arrow in fig. (5.1) (b) and the opposite sidewall. As figure (5.1) (c) indicates, these resonances were also observed for lower incident laser powers and present no clear shifts with changing pump power, indicating that the pulsed laser did not heat the Ga_2O_3:Zn microstructures. The observed relative increase of the visible emission with respect to the UV one in these Ga_2O_3:Zn flakes with decreasing pump power was already explained in chapter 3.

These kind of optical resonances were also observed in as-grown Ga_2O_3:Cr wires. Figure (5.2) (a) is a low magnification image of some of the deposited wires on a TEM grid. Micro-PL (μ-PL) spectra of these wires were performed and showed the characteristic Ga_2O_3:Cr intense red-NIR emission; i.e. a superposition of the two sharp R-lines and the broad phonon-related band which arises from intraionic Cr^{3+} transitions (see figure (1.3) and ref. [54]). Owing to their smooth lateral wall surfaces, these wires were able to guide such light and display weak FP resonances due to weak reflectivity at the wire ends caused by the refractive index change between the material and the air. An example of an unpatterned wire with weak FP resonances is shown in figure (5.2) (b).

For device applications such as nanolasers or optical sensors, it is necessary to significantly improve the confinement factor in the structures, i.e. to reduce the sum of all the losses per round trip of the excited light. These losses can arise from scattering due to low reflectivity in the cavity walls, absorption effects inside the cavity, etc. As our fabricated micro- and nanostructures have smooth lateral walls and Ga_2O_3 is non-absorbent in the visible range (up to the NUV), cavity wall refractive-index-change-induced reflectivity losses are the main limiting factor in the unpatterned structures. This reflectivity can be straightforwardly estimated by use of the Fresnel equation. Assuming negligible absorption and normal incidence:

$$R = \left(\frac{n_1 - n_2}{n_1 + n_2}\right)^2 \tag{5.1}$$

For Ga_2O_3:Cr, we can estimate the refractive index in the red-NIR region

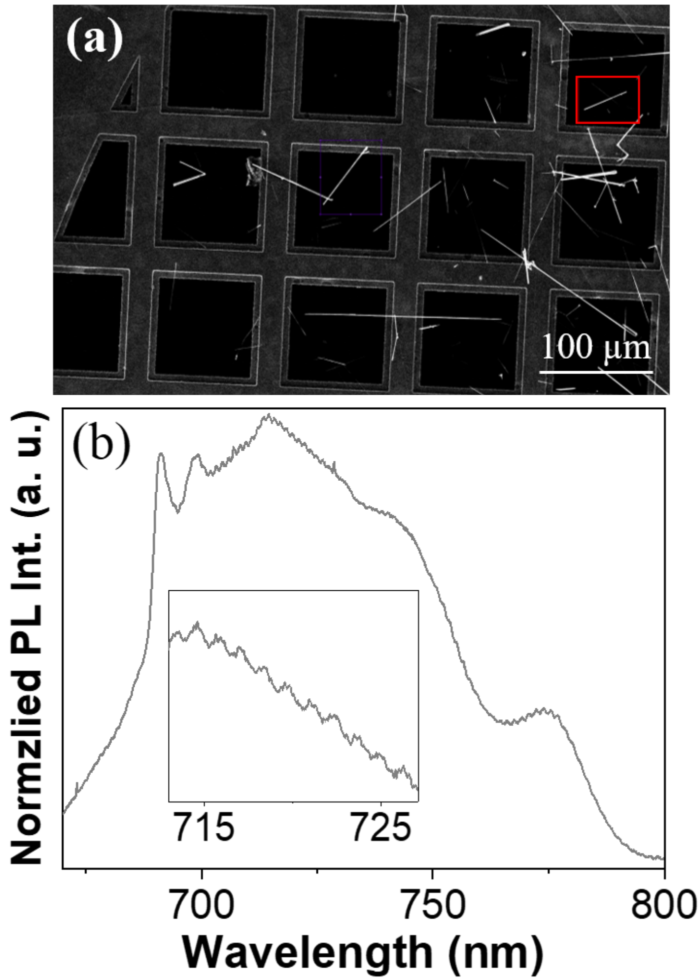

Figure 5.2: (a) SE image of a TEM grid on which several microwires were deposited. Some were chosen for FIB patterning. The red square shows a good candidate for an optical cavity, as the wire is isolated and freestanding on the carbon "mesh". (b) μ-PL spectrum of a Ga_2O_3:Cr microwire. The inset shows a magnified view of the 713-727 nm range, in which weak resonances which were ascribed to the FP-type can be observed

to be around 1.9 [124]. This gives rise to R $\approx$ 10% due to refractive index contrast in the wire ends, resulting in a low confinement of the light inside the as-grown microwire cavities.

In this context, optical microcavities based on DBRs are a very good option

for high reflectivity cavities. They avoid the use of metal mirrors and provide additional capabilities such as a wide wavelength tunability, as it will be shown in this chapter. A DBR is a periodic structure formed by alternating refractive indices, which enhances the reflectivity of certain wavelength ranges by virtue of interference phenomena. These high reflectivity wavelength ranges are known as stop bands (SBs). Not only are they used for this purpose in semiconductor micro- and nanowires [125, 126], but they are also a basic component of commercial photonic devices such as Vertical-Cavity Surface-Emitting Lasers [127].

The position of the DBR SB is very dependent on the DBR periodicity (a), also known as DBR lattice parameter. For the wavelength in the midpoint of such SB, λ_B, this dependence follows the following equation:

$$m\lambda_B = 2n_{eff}a\cos\theta \tag{5.2}$$

where m is an integer, n_{eff} is the effective refractive index of the DBR, θ is the incident angle and λ_B is known as the Bragg wavelength. It can be proven analytically that both the SB width and the peak reflectivity (R) strongly depend on the refractive index contrast of the two materials which form the DBR, increasing with increasing refractive index contrast for a set number of periods [127, 128]. R can reach up to 100% on a certain wavelength range for an ideal, planar infinite DBR for sufficient number of periods, although in the next section we will see that this value is much more difficult to achieve for FIB-patterned DBR-based cavities in micro- or nanowires.

As there would be many leakage points in the Ga_2O_3:Zn microbelts, we decided to pattern the DBRs in the longitudinal direction of the elongated Ga_2O_3:Cr structures, which have the additional advantage of having high luminescence intensity when exciting with energies under 4 eV (in particular, with the He-Cd laser). Further on, we also attempted elongated structures of UID Ga_2O_3.

Hence, in this thesis we propose the use of DBR mirrors in order to enhance the confinement factor of the Ga_2O_3 optical cavities. Additionally, tunability of both the reflected wavelength range (see equation (5.2)) and the separation between resonant peaks (see equation (1.2)) is possible by modifying the DBR periodicity (a) and the distance between the DBRs that form the cavity (L), respectively.

The standard design and notation of the DBR cavities presented in this thesis is shown in figure (5.3). The wire has a width defined as w_t and

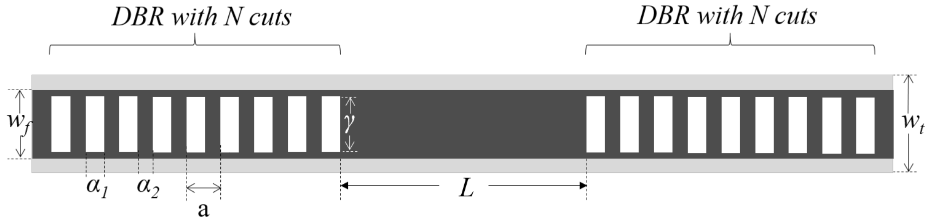

Figure 5.3: Schematic of the DBR cavity parameters.

a top facet defined as w_f. If the wire has a rectangular shape, $w_t = w_f$, but generally we will find microwires with $w_f < w_t$. We have designed the DBR cavities by patterning two DBRs, each formed by N rectangular holes. Their separation, of length L, is the length of the active region of the cavity, where the luminescence is excited. The holes completely cross the depth of the wire in order to increase the refractive index contrast and therefore have a higher reflectivity for low N. The hole length is α_1 and each hole is separated from the next by material of length α_2. The periodicity of the DBR is defined as a, hence $\alpha_1 + \alpha_2 = a$.

5.3 FDTD simulations on DBR reflectors

Once the objective has been set, it was convenient to examine computationally whether this kind of design could work in Ga_2O_3 elongated structures before beginning the whole experimental fabrication and characterization process. Therefore, in order to discern the utility of the DBRs in our material system and to tailor the position of the SB with respect to the Ga_2O_3:Cr luminescence band, several finite-difference time-domain (FDTD) simulations were performed with the OptiFDTD commercial software. In this software, 3D models of a microwire with set dimensions and a set refractive index can be designed. The wire dimensions were experimentally determined from each specific wire from SEM analysis. Regarding the modelled refractive index, Ga_2O_3 is considered a dispersive medium since there is significant variation of the refractive index in the energy ranges we are considering. In our FDTD-designed Ga_2O_3 structures, we used the Sellmeier dispersion relation:

$$\epsilon = A + \frac{B\lambda^2}{\lambda^2 - C^2} \tag{5.3}$$

where A, B and C are fitting constants. For Ga_2O_3 in this wavelength range, by fitting data from Al-Kuhaili *et al* [124], the following values were obtained: $A = 2.31$, $B = 1.14$ and $C = 0.24\,\mu m$, giving rise to a value of $n = \sqrt{\epsilon} = 1.88$ - 1.91 in the Ga_2O_3: Cr (650-850 nm) emission range, with a discrepancy of 0.18% or lower between our fit and Al-Kuhaili *et al*'s. It must be noted that in [124] the measurements were performed on UID Ga_2O_3 thin films. The presence of chromium in our structures could slightly modify the refractive index of Ga_2O_3 but taking into account the low percentage ionic incorporation of Cr, its effect on n can be considered negligible for our simulation purposes.

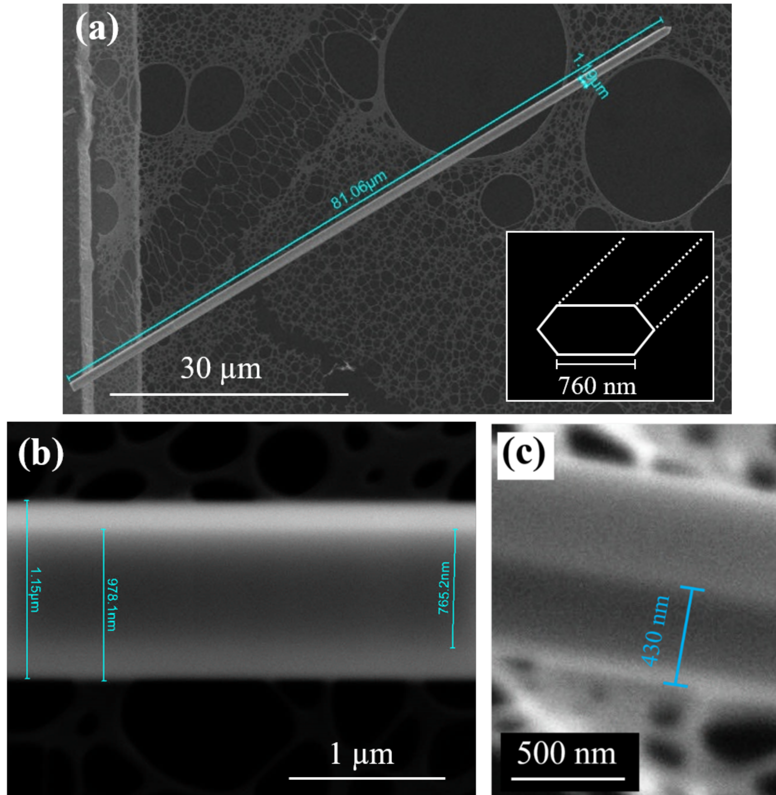

Figure 5.4: SEM images of microwire 1 before FIB patterning. (a) Top view of the wire before FIB patterning. (b) Detail of the wire, showing its 1.15 µm width and its 760 nm top facet. (c) 57° tilted image from which the depth of the wire is obtained. From the contrasts in images like (b) and (c), we suggest that the cross-section of the Ga_2O_3:Cr wires is an irregular hexagon, as sketched in the inset of (a).

Figure (5.4) (a) shows an SEM image of the microwire which gave rise to two of the first successfully fabricated Ga_2O_3: Cr DBR cavity. It will be named throughout the chapter as *microwire 1* for reference. From top view SEM measurement, see figures (5.4) (a) and (b), the length of the wire is 81 µm and the transversal width of the wire is $w = 1.15$ µm. Notice in (b) the slight brightness changes in both sides of the wire. This indicates that the cross-section of the wire is not rectangular. From this image, $w_f =$ 760 nm was obtained. The non-rectangular cross-section of the wire was confirmed by tilted images such as the 57° image shown in figure (5.4) (c). From these images, the depth of this wire was calculated: $d = \frac{430\,\text{nm}}{\sin(57)} =$ 510 nm. As sketched in the inset of fig. (5.4) (a), the cross-section shape of microwire 1, which is representative of the shape of the majority of the Ga_2O_3:Cr wires, was modelled as an irregular hexagon in which the longest side is the top facet, w_f.

The final parameters which must be selected in the FDTD simulations are the DBR dimensions. As explained before, the parameter which most affects the position of the SB is the periodicity, a, of the DBR. The optimum a cannot be calculated straightforwardly from equation (5.2) since our DBRs are not planar and their transversal directions are not much higher than the wavelength of light. In addition, the periodic holes are not milled for the whole width of the microwire. Hence, it is the FDTD simulations which give us the best approximation for the DBR's SB.

For every selected wire and DBR parameter dimensions, including the wire's non-rectangular cross-section, designs for the FDTD software were made. Figures (5.5) (a) and (b) show a top view and a side view, respectively, of the 3D simulated design of microwire 1, with the obtained dimensions by SEM, along with a test DBR. The spatial mesh dimensions in these simulations were 30 nm in x, y and 20 nm in z, which meet the FDTD requirement that the largest mesh should not be bigger than a tenth of the analyzed light wavelengths.

In all the simulations for Ga_2O_3:Cr wires, a Gaussian modulated continuous wave centered at 740 nm with half width 3.33×10^{14} Hz was generated (in red colour in figure (5.5) (a)). This incident Gaussian wave was implemented in a position to the left of the DBR. Once the simulation starts, the wave propagates for 15000 steps with step size 1.66×10^{-17} s. This step size is short enough to follow the Courant-Friedrichs-Lewy (CFL) condition [129] and the total time is long enough for the Gaussian wave to encounter the DBR and be detected in the positions mentioned further on. The prop-

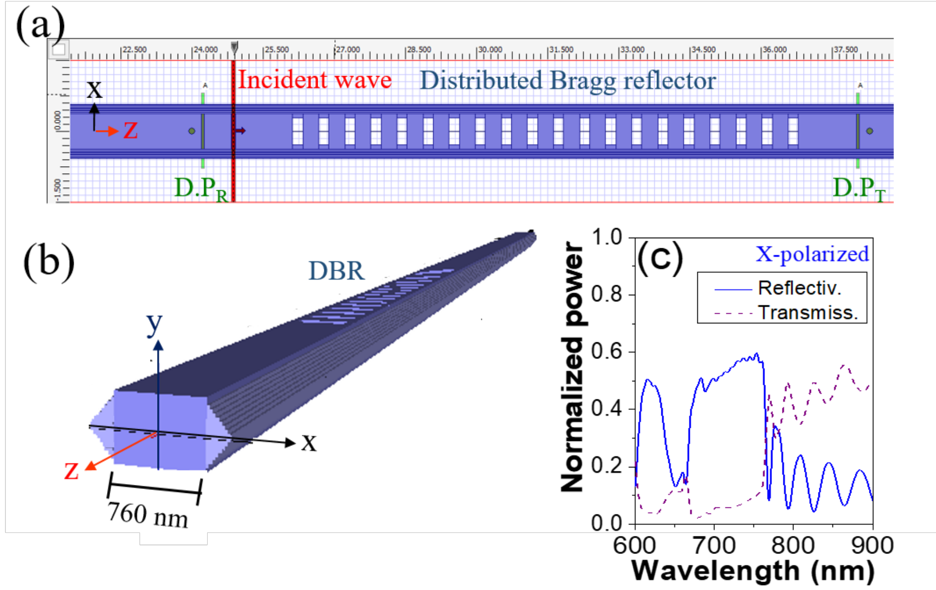

Figure 5.5: FDTD design and simulation of microwire 1. (a) Top view (ZX plane) showing the designed microwire, the DBR, the excitation Gaussian wave (red) and the two detection planes (green). D.P$_R$ indicates the reflected detection plane while D.P$_T$ indicates the transmitted detection plane. (b) Side view, in which the DBR was placed closer to z = 0 compared to its real position in the simulation (shown in (a)) in order to allow it to be seen in this image. In both images, axes are defined: z is the propagation direction (longitudinal axis), x is parallel to the width of the microwire and y is the optical axis, which is parallel to the depth of the microwire. (c) Simulated reflectivity (blue) and transmission (dashed purple) through the DBR, normalized with respect to the incident light wavelength. In this example, the expected R would only be, at most, of 58%. Further trials were made in order to improve the simulated DBR performance.

agation of the electromagnetic field through the designed structure can be monitored live during the duration of the simulation, which is several hours. Part of the incident power reflects due to the DBR. Detection planes placed at the left and right of the DBR were used to detect the reflected (R) and transmitted (T) power, as shown in figure (5.5) (a) in green, as a function of time. Subsequent Fourier transform yielded R and T for each frequency (i.e. wavelength). An example of simulated R and T spectra is shown in figure (5.5) (c). For each wavelength, we have the following equality:

$$1 = R + S + T \tag{5.4}$$

which indicates that, for a given incident power, a certain percentage of photons are reflected (R) by the DBR, others are scattered (S) by it and the rest are transmitted (T). $S(\lambda)$ can be deduced by applying equation (5.4).

Axes definition in figure (5.5) will be followed throughout the chapter. The z-axis is the propagation direction, parallel to the longitudinal axis of the microcavity. The transversal axis which is vertical in figure (5.5) (a), and is parallel to the width of the wire, is the x-axis. The y-axis, shown in figure (5.5) (b), is parallel to the depth of the microwire.

5.4 FIB patterning and SEM characterization of the microcavities

Tens of simulations were performed following the procedure described in the previous section for different wire and DBR dimensions. With the acquired information, the DBR microcavities were patterned by using a FIB microscope in collaboration with the UPV-EHU. The selected ion beam parameters were the following: 30 kV and 8-25 pA. The value of the current was lower than for usual FIB operation in order to increase the resolution of the drilled holes and to reduce ion damage on the structures.

With the aid of a FIB microscope software, periodic rectangles of set dimensions can be defined. However, the real hole length (α_1) and width (γ) obtained after milling is higher than the programmed ones due to the ion interaction volume (which in turn depends on the programmed depth, the ion beam current, etc.). Also, some redeposition effects are expected which slightly reduces the length and width of the hole in the deepest part of the wire. This can be observed in the brightness changes of the hole perimeter, see e.g. figure (5.6) (c). More details about these points were given in section 2.1.3. In order to minimize these effects, preliminary trials were made in spare microwires in order to finely adjust the defined parameter dimension of the DBRs so they resulted in the desired parameters. Monitorization of such parameters was done by in-situ SEM measurements after these trials.

After these adjustments, DBRs of the desired α_1, γ and a were carved by FIB. By considering the FIB resolution, as well as the SEM image resolution and observed slight thermal drifts during milling, in our case we can take the FIB uncertainty for the obtained α_1 and γ of the holes with respect to the planned ones to be ± 20 nm and for a of the DBR to be ± 10 nm.

Figures (5.6) (a) and (b) show the SEM images of the two patterned DBR

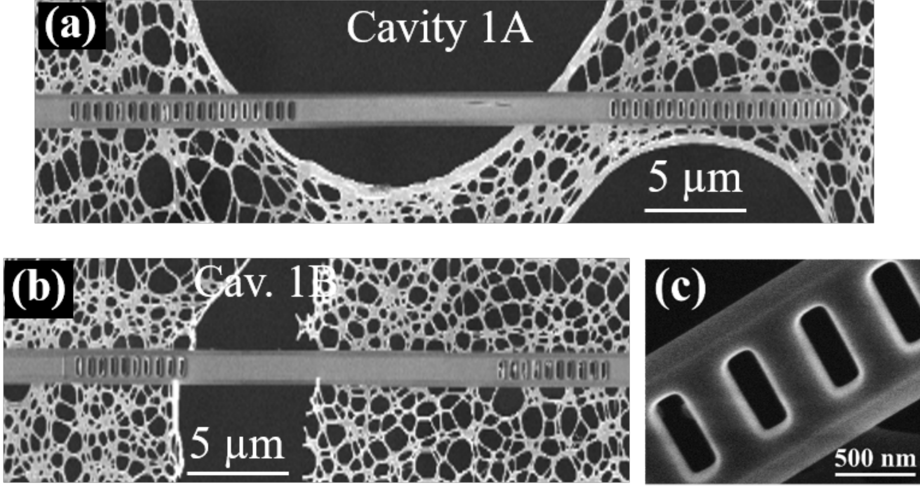

Figure 5.6: SEM images of the cavities of microwire 1 after FIB patterning. (a) Image of cavity 1A. (b) Image of cavity 1B. (c) Detail of some FIB drilled holes which form one of the DBRs.

cavities in microwire 1, labelled as cavity 1A and cavity 1B, respectively. As shown in figure (5.3), each cavity is formed by two nominally identical sets of N rectangular holes drilled by FIB which are separated by a distance L. In this case, $N_{1A} = 20$ and $L_{1A} = 15.2\,\mu\text{m}$ in cavity 1A while $N_{1B} = 10$ and $L_{1B} = 15\,\mu\text{m}$ in cavity 1B. The periodicity of the DBRs was chosen to be $a = 520\,\text{nm}$, while $\alpha_1 = 210\,\text{nm}$ and $\gamma = 570\,\text{nm}$. All the parameters of microwire 1 and its cavities compared to other cavities will be displayed in table (5.2), in section 5.8.

5.5 Polarized μ-PL characterization of the cavities

The μ-PL analysis for all the cavities fabricated in this thesis was carried out at RT in the confocal microscope and compared with results on the same structures before patterning. All the μ-PL spectra were performed by excitation with the 325 nm line of a He-Cd laser except for the spectra shown in section 5.10. Unlike Ga_2O_3 doped with most other elements, Ga_2O_3:Cr presents a high luminescence yield when exciting with the He-Cd laser due to absorption between the $^4A_2$ and the $^4T_1$ intraionic Cr^{3+} levels [54].

In the confocal microscopes used, a custom design module allows for the deviation of the excitation laser spot with respect to the collection point, as

described in section 2.2.4. The excitation point was placed inside the cavity while the detection point was placed at one of the DBRs, as schematized in figure (5.7) (a). Wave-guiding of the photoluminescent light and scattering at the DBRs can be observed experimentally in μ-PL images such as the one obtained in cavity 1A, see figure (5.7) (b). As expected, although resonant cavity modes can be seen in the μ-PL spectra in any measurement configuration in which the active region is excited, a higher relative signal with respect to the background Ga_2O_3:Cr luminescence always occurs for the aforementioned measurement configuration.

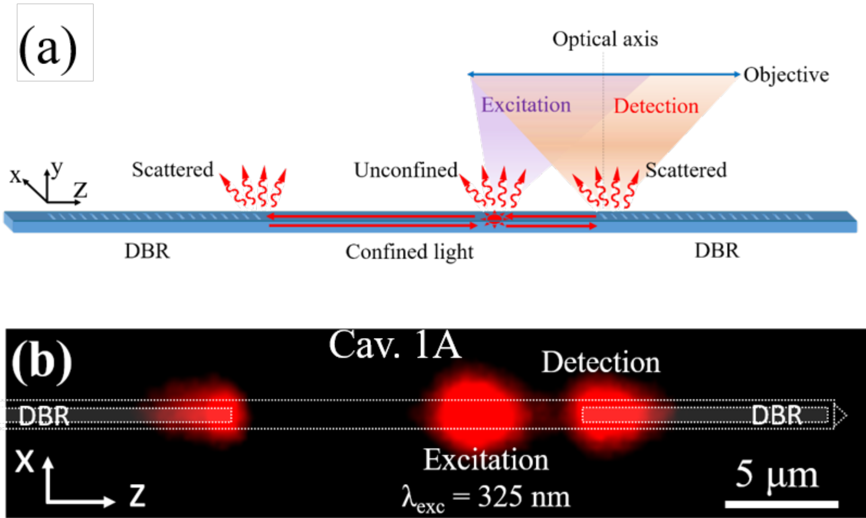

Figure 5.7: (a) Diagram of the DBR cavity excitation and detection configuration in the confocal system for the acquisition of μ-PL spectra. (b) True colour μ-PL image of microwire 1, cavity 1A, under excitation of the $\lambda = 325\,\mathrm{nm}$ laser. The figure indicates the excitation and detection points. White dotted lines are a guide to the eye to represent the wire and the patterned DBRs in both sides.

μ-PL spectra from the unpatterned wire and cavities 1A and 1B are presented in figure (5.8). The unpatterned wire showed weak modulation of the Ga_2O_3:Cr band, which was ascribed to FP-type resonances along the wire. By applying equation (1.2), $L = 87\,\mu\mathrm{m}$ was obtained, which fits with the total length of the microwire. SEM images (see figure (5.4)) showed that the lateral walls of this microwire are smooth, resulting in an expected low surface-scattering loss. Therefore, the most relevant losses of the unpatterned wire were due to the low reflectivity of the wire ends (around 10%, see section 5.2); this explains the low quality of the resonances of the

unpatterned wire FP cavity.

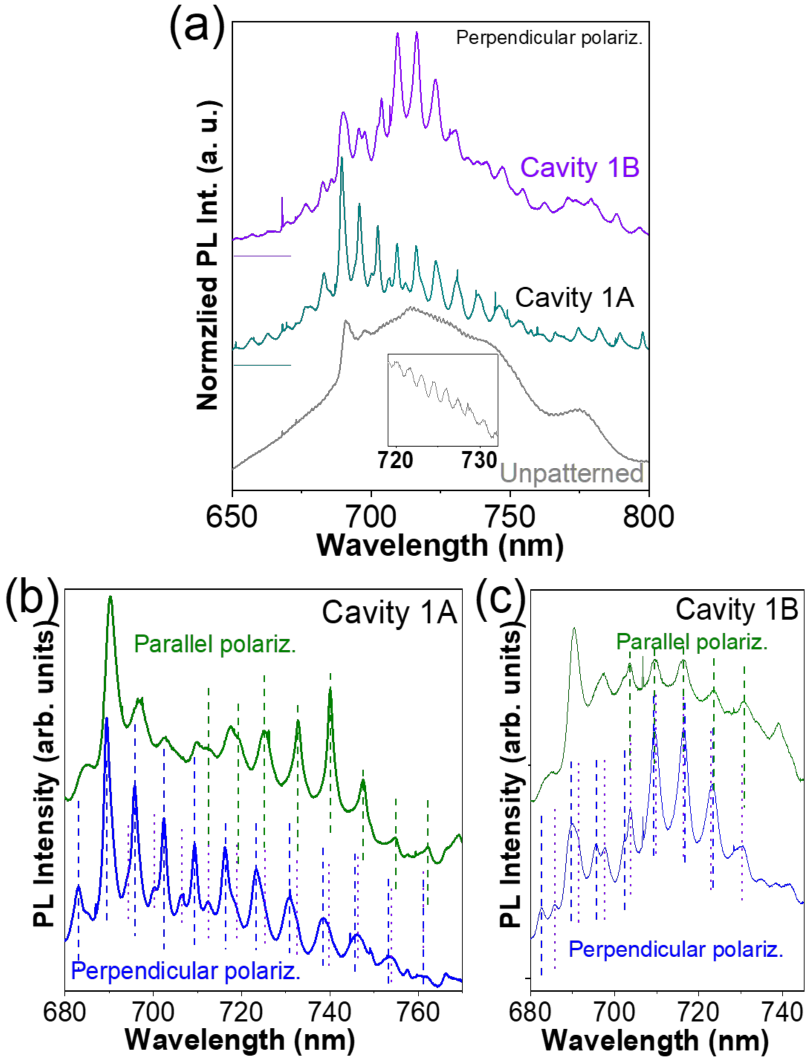

Figure 5.8: (a) Normalized μ-PL spectra from unpatterned wire (gray) and cavities 1A (dark cyan) and 1B (purple), taken at perpendicular polarization configuration measurements. The inset shows a detail of the weak resonances observed in the unpatterned wire. (b) μ-PL spectra from cavity 1A acquired with parallel (green) and perpendicular (blue) polarizations. (c) Similar spectra as (b) from cavity 1B. In (b) and (c) vertical dashed lines show calculated peak positions, as detailed further in the chapter, for E_x^{11} (dashed blue), E_x^{12} (purple) and E_y^{11} (green) modes. In all the cases, the spectra are vertically shifted for the sake of clarity.

A strong enhancement of the modulations was observed in the spectra of the FIB-patterned microcavity (figure (5.8) (a)). These resonances can be ascribed to FP modes at each of the cavities, in which the DBRs act as mirrors within specific wavelength ranges, i.e. their SBs. In addition, a strong polarization dependence of the acquired luminescence can be observed in figures (5.8) (b) and (c). Blue solid lines show spectra with the perpendicular polarization, meaning that the polarizer transmission axis was parallel to the x-axis (see figure (5.5)) while green solid lines show spectra with the parallel polarization, i.e. with the polarizer transmission axis parallel to the z-axis (i.e. longitudinally).

Besides, notice that not only the main peaks have different wavelength positions for each polarization, but also a more complex peak structure can be seen for each polarization configuration due to less intense peaks being also present, for example see the dotted purple lines in the perpendicular polarization spectra. This multimode structure is expected bearing in mind the lateral dimensions of the microwire with respect to the guided wavelength range. It is usual for a semiconductor nanowire to operate in a single mode only when its diameter is equal to or lower than the guided wavelength inside the wire [130]. In Ga_2O_3:Cr wires, $\lambda_{in} = \lambda/n =$ 350-400 nm, which is lower than both w_t and d, although they are in the same order of magnitude. A thorough analysis of the resonant cavity modes present in this wire is displayed in the next section.

5.6 Analytical study: Marcatili and Goell models, longitudinal resonance condition

In order to understand the polarization dependence of the resonances and the multimode structure observed in microwire 1 and in other microwires, an analytical procedure based on the models developed by Marcatili [131] and Goell [132] was used. In these models, modes are considered taking into account the geometry of the wire and the peaks observed in the μ-PL spectra.

In a dielectric waveguide (WG) with a rectangular shape, the propagating modes can be analyzed following the above-mentioned models. In both cases, the solutions, i.e. the wave-guided modes, can be divided polarization-wise into two, named E^x_{pq} and E^y_{pq}. The E^x_{pq} mode is defined by having H_x = 0, while the dominant electric and magnetic polarizations are E_x and H_y. Its electric field can be considered essentially x-polarized. On the other

hand, the E^y_{pq} mode has $H_y = 0$, and E_y and H_x dominate. Its electric field can be considered essentially y-polarized. The two mode numbers, p and q, count the number of antinodes of the electric and magnetic fields in the x and y axes, respectively.

For example, the fundamental mode has p=q=1, meaning that both the transversal electric and magnetic fields have one antinode which is placed in the midpoint of the cross-section, analogously to the fundamental mode in a 1D vibrating string. These fundamental guided modes, in both polarizations (E^x_{11} and E^y_{11}), are expected to be the dominant ones in our cavities [133], and will be confined longitudinally by the DBRs, giving rise to resonant peaks in our μ-PL spectra.

For microwire 1, a sketch of its cross-section was shown in figure (5.4) (a). In a first approximation, it can be considered as approximately rectangular, with $w_t = 2d$. An almost-rectangular shape of the wire cross-section was found in all the patterned Ga_2O_3:Cr wires. In order to check the validity of this approximation in microwire 1, the Poynting vector of the fundamental mode assuming a rectangular waveguide was calculated and compared it to the simulated field in the wire. Figure (5.9) (a) represents the Poynting vector amplitude as obtained for Marcatili's model for the E^x_{11} mode, which obeys the following equation:

$$S_z = \frac{1}{2}Re(E_x H_y^*) = \frac{A^2}{2k_z}\left(\mu_0\omega - \frac{k_x^2}{\omega\epsilon_0 n^2}\right)\cos^2(k_x x)\cos^2(k_y y) \qquad (5.5)$$

where A is the amplitude of the magnetic field and ω is the frequency of the wave. Notice that we have used that in E^x modes $H_x = 0$. Figure (5.9) (b) shows the power intensity obtained with FDTD simulations for the fundamental mode of an x-polarized wave with 709-nm vacuum wavelength propagating along microwire 1. Dashed white lines in both figures indicate the real cross-section, while dashed orange lines in figure (5.9) (a) indicate the rectangular cross-section approximation. Very good agreement between both figures can be seen, and in both cases the Poynting vector amplitude is negligible in the WG boundaries, especially in the rectangle's corners. Therefore, we used the approximation of considering elongated structures such as microwire 1 as rectangular WGs for the analytical analysis of their guided modes.

By considering the polarization of the electric field of each mode, spectra acquired with the perpendicular polarization configuration in the DBR cavities, i.e. with the polarizer in the x direction, were expected to essentially

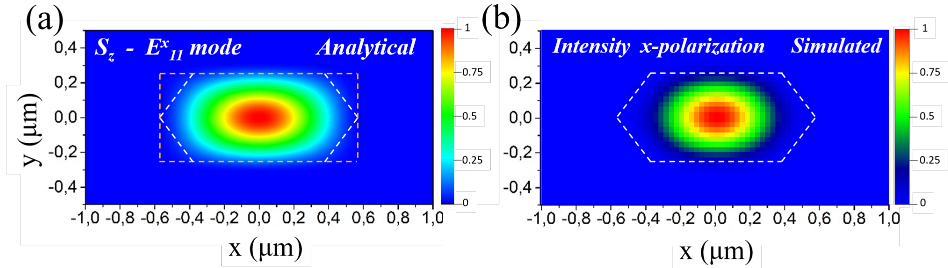

Figure 5.9: Comparison between the Poynting vector amplitude along the WG cross-section for (a) the Marcatili E^x_{11} mode calculated analytically and (b) the FDTD-simulated x-polarized wave.

show guided E^x_{pq} modes which have been confined in the longitudinal direction. In parallel polarization setup, the polarizer is parallel to the z-axis. As E_z is non-zero for both E^x and E^y modes, a combination of both modes should be detected for this setup.

By using this model, the components of the $\vec{k}$-vector and the dispersion relation $w(k_z)$ were calculated by solving the following simultaneous equations for the E^x_{pq} modes:

$$\begin{aligned} k_x \frac{w_t}{2} &= (p-1)\frac{\pi}{2} + \arctan\left(\frac{n^2\sqrt{k_0^2(n^2-1)-k_x^2}}{k_x}\right) \\ k_y \frac{d}{2} &= (q-1)\frac{\pi}{2} + \arctan\left(\frac{\sqrt{k_0^2(n^2-1)-k_x^2}}{k_x}\right) \\ k_z^2 &= k_0^2 n^2 - k_x^2 - k_y^2 \end{aligned} \tag{5.6}$$

where w_t and d are the transversal dimensions of the wire, $k_0 = \frac{2\pi}{\lambda}$ is the vacuum wavenumber of the detected wavelength (λ_0) and n is the refractive index of the WG. From these equations, k_x and k_y were calculated numerically and, from them, k_z was obtained. More information about these equations, including the analogous equations to 5.6 for the E^y_{pq} modes, is found in appendix A.

However, we must bear in mind that Marcatili's model contains two important approximations: grazing incidence and low refractive index contrast between the WG and its surroundings (more details are given in appendix A). The latter approximation is not valid for our Ga_2O_3:Cr microwires. On

the other hand, Goell's model is valid for the general case. It uses the same mode nomenclature as Marcatili but does not require this low refractive index contrast assumption, at the cost of losing some insight of the modes and requiring computational methods to solve the equations.

In microwire 1, by inspecting the results in refs. [132, 134], for the case of $w_t = 2d$, we checked that Marcatili's results for our identified E^x modes were virtually equal to those by Goell. Therefore, we used Marcatili's model for these modes, i.e. the ones obtained for perpendicular polarization, while a correction to Goell's model was used from plots in ref. [134] for the identification of the parallel polarization fundamental mode E^y_{11}.

Once this analysis was performed and the k_x, k_y and k_z values of the guided modes were obtained for each identified peak, the set of peaks had to follow the longitudinal resonance condition along the wire length:

$$k_z = m\frac{\pi}{L_{eff}} \tag{5.7}$$

where m is an integer and L_{eff} is the effective length of the cavity. Notice that equation (1.1), which is generally used in FP resonant microwire cavities, is in fact an approximation of equation (5.7) with $k \approx k_z$. By imposing equation (5.7), the obtained k_z values by Marcatili's or Goell's model were used to know whether the set of peaks could be ascribed to consecutive integer (m) longitudinal resonant modes of the chosen guided mode (i.e. E^x_{11}) for a certain L_{eff}. Additionally, this L_{eff} had to make sense compared to the physical length of the cavity and had to be virtually the same in all the identified modes for each cavity.

Excellent fits were obtained in both DBR cavities of microwire 1 for the identified sets of peaks when they were ascribed to these modes and we imposed the longitudinal resonance condition. Every assigned resonant peak (see appendix A for cavity 1A) is labelled in figure (5.8) with the following colour code: E_x^{11} modes are labelled in dashed blue lines, E_x^{12} modes are labelled in dashed purple lines and E_y^{11} modes are labelled in dashed green lines. It should be noted that, although parallel polarization configuration detects E_z components, which are non-zero for both E^x and E^y mode resonances, the identified resonant peaks agreed better with E^y_{11} mode than with the E^x ones. Besides, it can be seen in figure (5.8) that they do not share most of the wavelength positions with the identified E^x resonant modes in perpendicular polarization. Therefore, some of the most intense resonances for parallel polarization were assigned to the E^y_{11} mode while

the less intense resonances in parallel polarization could not be assigned to an individual mode and can be considered a combination of E^x and higher order E^y modes.

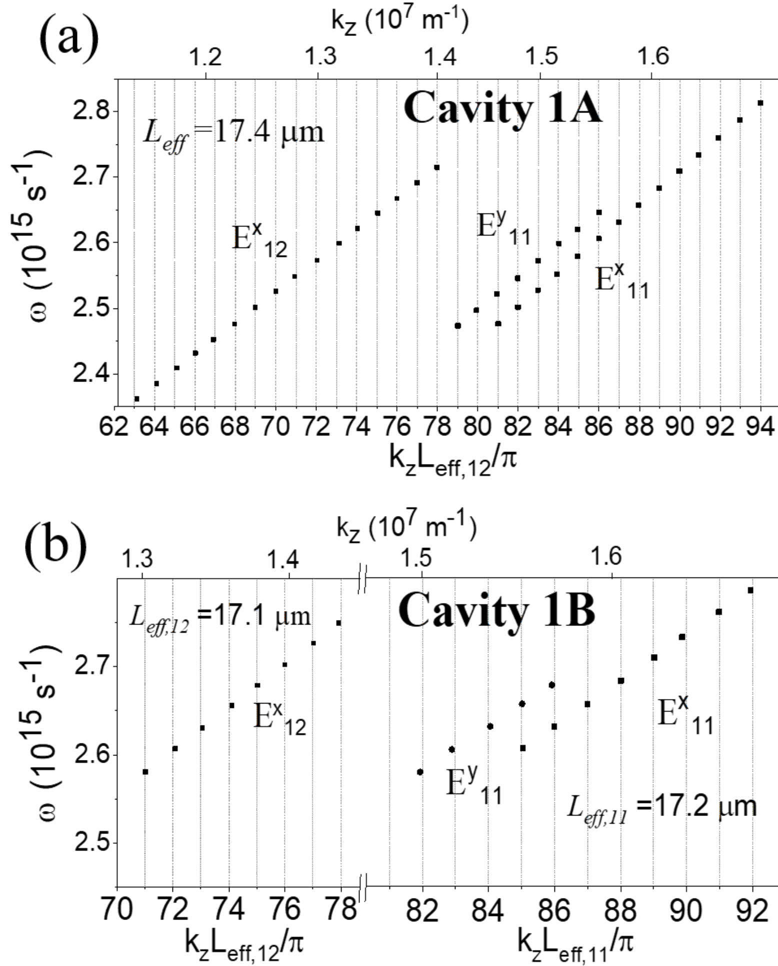

Figure 5.10: Dispersion relations (a) in cavity 1A and (b) in cavity 1B obtained from the μ-PL peak positions in microwire 1 for E^x_{11}, E^x_{12} and E^y_{11} modes from figure (5.8). L_{eff} values are calculated by imposing k_z to be proportional to consecutive integer numbers, m, for several consecutive peaks. k_z values shown in the upper axis correspond to those from Marcatili's model. The k-component and m values for cavity 1A are shown in appendix A.

Figure (5.10) shows the dispersion relations for the sets of resonant peaks of both DBR cavities in microwire 1, which were assigned to E^x_{11}, E^x_{12} and E^y_{11}

modes by using Marcatili's model for the E^x modes and Goell's model for the E^y_{11} mode, as detailed in the previous paragraphs and in appendix A. The obtained effective length value that satisfies the longitudinal resonance condition was $L_{eff} = 17.4\,\mu m$ for all the modes in cavity 1A and $L_{eff} = 17.2\,\mu m$ for all modes (except the E^x_{12} mode, with 17.1 µm) in cavity 1B. Notice that cavity 1B has an SEM-measured L which is 0.2 µm lower than cavity 1A, which fits with the difference in the obtained L_{eff} between the two cavities. However, both cavities have a measured L between the DBRs which is 2.2 µm smaller than the obtained L_{eff} of the confined modes. This can be explained by an effective penetration depth of the confined light in the DBRs, which is defined as the distance from the start of the DBRs to the position where an ideal metallic mirror would be positioned. For an ideal, planar, infinite DBR the penetration depth can be obtained by applying the following equation [135]:

$$\delta_{eff} = \frac{\bar{n}\lambda_B}{4n\Delta n} + \frac{\lambda_B \Delta n}{2\pi^2 n\bar{n}} \tag{5.8}$$

where $\bar{n}$ is the average refractive index, Δn the refractive index contrast and λ_B the Bragg wavelength. The patterned DBRs in the microwire are not ideal, planar nor infinite so applying equation (5.8) is a very rough estimation. A value of around $\delta_{eff} = 0.9\,\mu m$ is obtained, which is quite close to the obtained experimental penetration depth in both cavities of $\delta_{exp} = \frac{L_{eff}-L}{2} = 1.1\,\mu m$ in each DBR.

5.7 DBR reflectivities. Comparison with simulations

In order to examine the performance of the patterned cavities, the finesse (F) of the resonances and the reflectivity (R) values of the DBRs were obtained from the experimental resonant peaks and compared to the FDTD simulations. As the DBRs have the same parameters in both sides of the cavity, R can be assumed to be the same in both DBRs which form each cavity. Therefore, once F of each peak was obtained experimentally by using equation (1.4), we calculated the DBR reflectivity for that wavelength by applying equation (1.5).

As well as F values, quality factor (Q) values can also be obtained by using equation (1.3). For example, for one of the sharper peaks in cavity 1A, at 798 nm, a value of $Q = 750$ was calculated. This value is slightly lower than the unpatterned wires' Q factor [57] due to the significantly smaller length of

the DBR cavities compared to the unpatterned wires, which directly reduces the Q factor for shorter optical cavities [67]. Therefore, in our analysis we focused on the effect of DBR patterning on the F values, as they are the optimal parameter to have an insight of the performance of the optical cavities, independently of the difference in their lengths [136].

As an example, figure (5.11) shows the experimental data for the F calculation from the 798 nm peak. As displayed in this figure, $F = 7.5$, which corresponds to $R = 66\%$. This value is around three times higher than F values from unpatterned wires [57], which implies a significant improvement of the stored energy per round trip in the optical cavities due to DBR patterning.

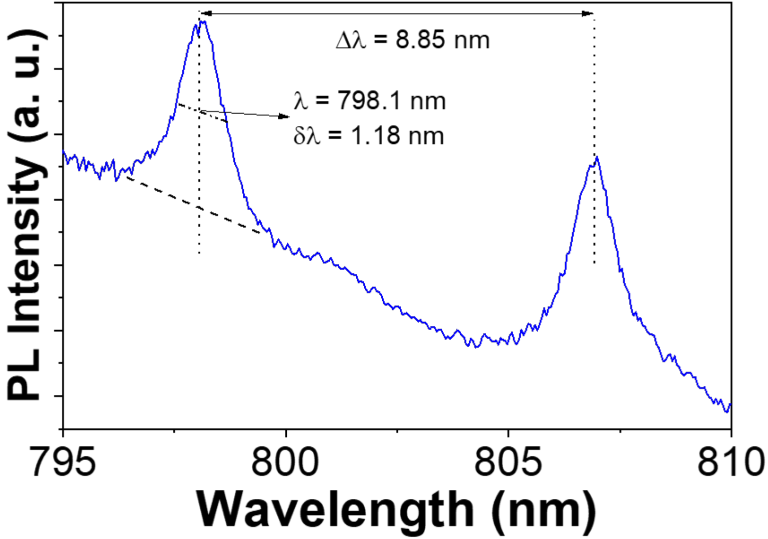

Figure 5.11: Finesse calculation in the 800 nm range for cavity 1A for perpendicular polarization. $F = 7.5$ is calculated for the 798 nm peak from the ratio of the FSR of this peak and the next consecutive peak from the E^x_{11} mode and the FWHM ($\delta\lambda$) of the peak, see equation (1.4).

Table (5.1) displays representative F and R values of microwire 1, cavity 1A, obtained from experimental μ-PL results shown in figures (5.8) and (5.11). It must be noted that some F values in cavity 1A could not be obtained due to multimode resonances lying in very similar wavelength positions or to a convolution between a resonant peak and one of the intraionic R-lines. These convolutions result in an increase in the apparent FWHM of

such peaks. Cavity 1B's μ-PL spectra have broader peaks, which prevented accurate F calculations in most of the cases.

Polarization	λ_p [nm]	F	R
Perpendicular	696	4.0	0.46
	702	4.8	0.52
	709	5.1	0.55
	716	4.0	0.47
	798	7.5	0.66
	806	7.9	0.67
	816	6.7	0.63
Parallel	732	4.3	0.49
	740	4.8	0.53
	747	5.1	0.54

Table 5.1: F and R values obtained for several peaks and polarizations from experimental μ-PL results of cavity 1A (see figures (5.8)) and (5.11)).

As shown in table (5.1), for cavity 1A there are two wavelength ranges in perpendicular polarization with high F; around 700-720 nm and around 800-820 nm, in which the highest obtained DBR reflectivity (R) is 55% and 67%, respectively. In cavity 1B, which has 10 DBR periods instead of 20, approximate R values of around 40% were obtained in the 700 nm range, i.e. around 15% less than cavity 1A. In parallel polarization, there is one high-reflectivity wavelength range in cavity 1A, which lies around 730-750 nm, with R around 50%. These results indicate the possibility of in-situ tunability, polarization-wise, of the high reflectivity range in the fabricated microcavities. The obtained R values are notably higher than in the unpatterned wire and in the range of those experimentally demonstrated in DBR micro- or nanowire structures fabricated in other material systems [125, 137].

These R values can be compared to the expected DBR reflectivities which had been obtained by FDTD simulations (see section 5.3). The wavelength dependence of the simulated reflected power for cavity 1A is shown in figures (5.12) (a) and (b). As discussed in section 5.6, x-polarization corresponds to E^x_{pq} modes while y-polarization corresponds to E^y_{pq} modes. For x-polarization (figure (5.12) (a)), within the Ga_2O_3:Cr emission range (650-850 nm), two high DBR reflectivity regions can be noticed in the FDTD reflected power spectra: one around 720 nm and the other around 820 nm, both reaching around 80% maximum expected reflectivity. A local mini-

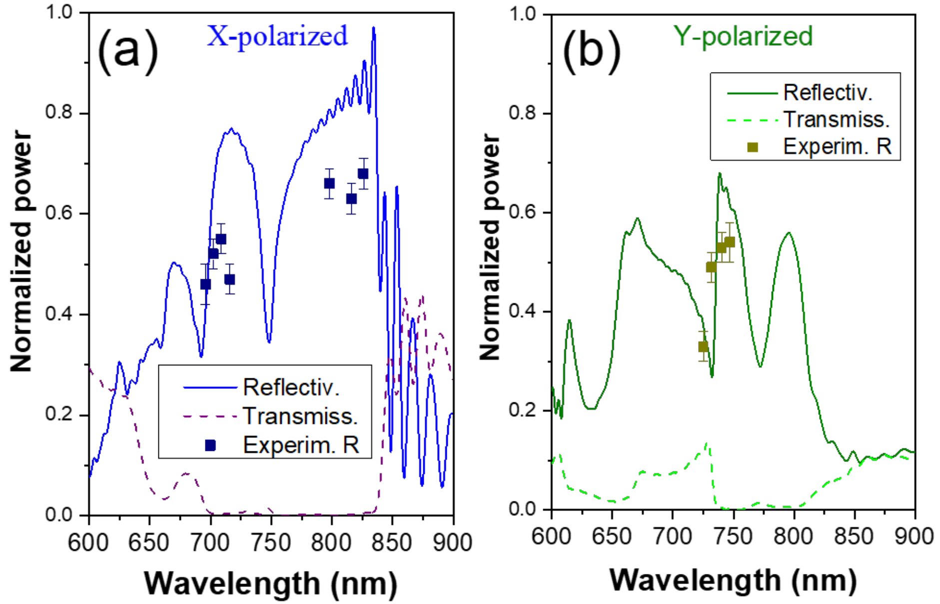

Figure 5.12: Simulated FDTD reflected and transmitted power spectrum of the modelled DBR of cavity 1A for (a) x-polarization (blue and dashed purple, respectively) and (b) y polarization (dark green and dashed light green, respectively). Squares show experimental R values of cavity 1A obtained from F results, using equations (1.4) and (1.5).

mum of DBR reflectivity can be seen between the two maxima, at around 750 nm. On the other hand, for y-polarization (figure (5.12) (b)), a lower expected DBR reflectivity was found in the simulations, reaching values slightly over 60% at 750 nm and with two reflectivity minima at around 730 and 770 nm.

These features are in accordance with cavity 1A's experimental μ-PL parallel and perpendicular polarization spectra (see figures (5.8) (b) and (5.11)): the perpendicular polarization spectra (which measures confined E^x_{pq} modes) has the best resolved peaks at around 700-720 nm and at around 800-820 nm, while the parallel polarization spectra (in which confined E^y_{11} modes were identified) presents fine peaks around 740 nm. Quantitatively, we compared the obtained experimental R values decuded from F values, shown in table (5.1), with the simulated reflectivity spectra. Experimental R values, shown in dark blue and dark yellow squares in figures (5.12) (a) and

(b) respectively, are in good agreement with the simulated values, except that experimental values are systematically lower than the simulated ones. This is expected due to experimental dispersion of the α_1, γ and a in the FIB-fabricated DBR, as discussed in section 5.3. In addition, the multi-mode structure observed in these cavities can cause an artificial broadening of some of the main resonant peaks due to contributions from secondary peaks, which reduces the experimentally-measured F and therefore reduces the calculated experimental R.

FDTD-simulated transmission spectra are also shown in figure (5.12), in dashed purple and dashed light green for (a) and (b) respectively. The SB for x-polarization essentially covers the whole emission of Ga_2O_3:Cr. For y-polarization, the SB covers the 740-800 nm region, while a ~10% transmission is observed for the rest of the Ga_2O_3:Cr range. From this analysis, we conclude that via FDTD simulations, the DBRs can be designed with the desired parameters in order to substantially increase the reflectivity at the wire ends in the selected wavelength range. In addition, the results show that the most important power loss in microwire 1, which prevented from reaching even higher reflectivity values in the cavity, was scattering at the DBRs.

5.8 Tailoring the Ga_2O_3:Cr cavity designs

After the thorough analysis carried out in the DBR cavities of microwire 1, fabrication of improved Ga_2O_3:Cr DBR cavities following a similar procedure as described up to this point was envisaged. If we revisit figures (5.12) and (5.8) (a), it is clear that the highest reflectivity range in the DBRs was not in the highest PL intensity range, which would be convenient to increase the percentage of confined photons. The highest theoretical and experimental reflectivities were around 800 nm while the highest emission intensity of the microwires was around 720 nm. As we checked that the simulations are quite accurate in predicting the SB wavelength positions, our aim was to tune the highest reflectivity range towards the 720 nm wavelength range by reducing the DBR periodicity, a, with respect to microwire 1's DBRs. Additionally, two other goals were introduced in this second round of designed Ga_2O_3:Cr DBR microcavities:

- To pattern cavities with smaller length, in order to have a higher FSR, which increases the separation of the fundamental and higher order WG-resonant modes.

- To pattern wires with smaller lateral dimensions in order to reduce the contribution of higher order WG propagation modes in the μ-PL spectra.

Both goals involve size reduction, which is by itself an important factor in the development of more efficient photonic devices [138]. However, size reduction of the DBR cavities complicates the characterization in our μ-PL optical system. Regarding the first aim, on cavities with lengths smaller than around 7 µm, the excitation and the collection areas in the confocal microscope start to overlap, which results in a higher contribution of the primary PL with respect to the confined modes. As for the second aim, cavities with smaller lateral dimensions require more care in the laser spot position and focusing, and they are expected to have a lower PL emission. Therefore, a trade-off had to be found between size reduction and optimum PL measurements when selecting the most convenient wires for FIB patterning. A clear improvement on the results of microwire 1 was achieved on two samples, which will hereinafter be named *microwire 2* and *microwire 3*.

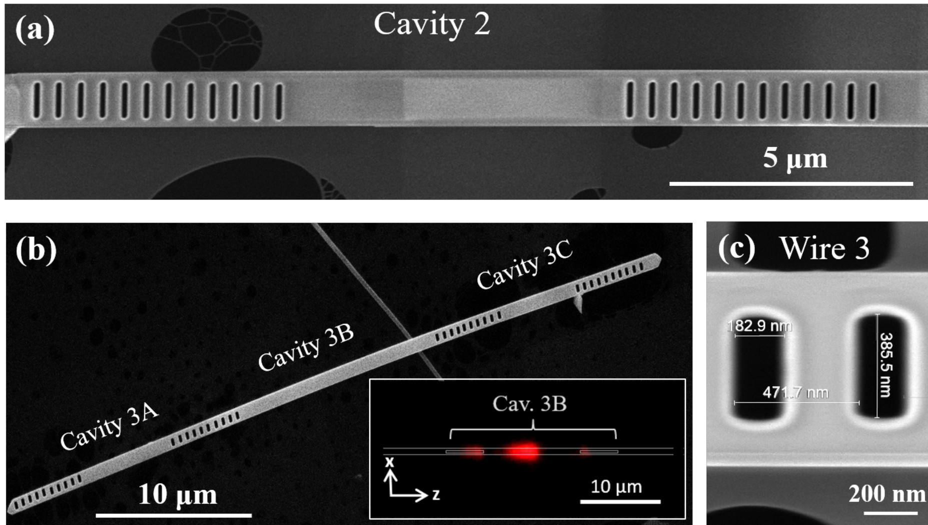

Figure 5.13: SE image of (a) cavity 2, (b) cavities 3A to 3C and (c) two holes which are part of one of the DBRs in wire 3. The inset in (b) corresponds to a μ-PL image of cavity 3B when excited with the $\lambda = 325$ nm laser, showing light guiding and some scattering at the DBRs. The DBRs and the wire sidewalls are indicated with white dotted lines as a guide to the eye.

SE images of the patterned cavities in microwires 2 and 3 are shown in

Wire	w_t(nm)	w_f(nm)	d(nm)	L(**μm**)	α_1(nm)	a(**nm**)	γ(nm)
1	1150	760	510	**15;15**	210	**520**	570
2	1100	890	480	**7**	130	**450**	700
3	730	600	620	**6;13;5**	190	**470**	370

Table 5.2: Comparison of the cavities' parameters. The length of each cavity is separated in semicolons and is rounded up to the nearest micron. For example, $L_{3A} = 6\,\mu\text{m}$, $L_{3B} = 13\,\mu\text{m}$ and $L_{3C} = 5\,\mu\text{m}$.

figure (5.13). A real μ-PL image of cavity 3B is shown in the inset of in figure (5.13) (b), showing analogous behaviour to figure (5.7) (b). The dimensions and DBR parameters of both microwires, compared to microwire 1's, are presented in table (5.2). Firstly, notice that in both wires a was reduced from 520 nm to 450 or 470 nm. In addition, in wire 2's DBR cavity, $\alpha_2 = a - \alpha_1$ was kept constant to wire 1's at 310 nm, resulting in a reduction of α_1, while in wire 3's DBR cavities, α_1 was kept similar to wire 1's and α_2 was reduced. In these cavities, the value of a was selected in order to place the DBR SB in the maximum PL intensity range, and two different values of α_1 and α_2 were attempted in order to check its influence on the maximum experimental DBR reflectivity. As we will see further on, similar reflectivities were obtained in both cases, hence the influence of the ratio α_1:α_2 in our case was found to be mostly negligible.

Secondly, notice in table (5.2) that wire 2 has similar lateral dimensions to wire 1 but a lower L, of 7 µm, was selected, while wire 3 has a smaller width (w_t and w_f) and presents three different DBR cavities of lengths ranging from 5 to 13 µm. This resulted in optical microcavities with different (higher) FSRs. Finally, a lower number DBR periods, N, was selected in the cavities: in wire 1 the best working DBR cavity (1A) had 20 periodic holes in each DBR, while 12 holes in wire 2's DBRs and 10 in the DBRs of wire 3's cavities proved to be enough to obtain high reflectivity in the desired wavelength range.

Figure (5.14) (a) shows μ-PL spectra of cavity 2, both in parallel (blue) and perpendicular (green) polarization measurement setups. Figure (5.14) (b) presents the simulated reflected power in x- and y-polarizations (blue solid and green dashed lines, respectively), the FDTD-simulated transmitted power in x-polarization (purple dashed line) and the experimental reflectivity of the identified peaks in perpendicular polarization (dark blue squares).

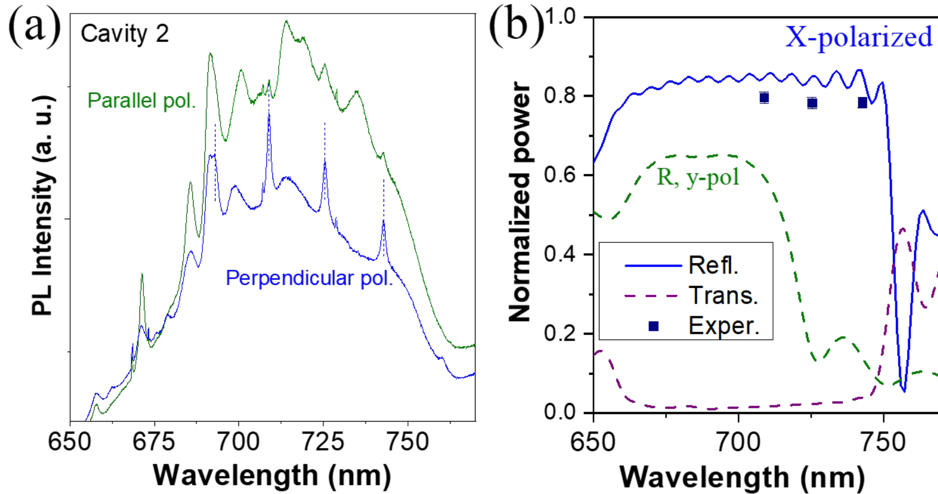

Figure 5.14: (a) μ-PL spectra from the DBR cavity patterned in wire 2, acquired with parallel (green) and perpendicular (blue) polarizations. (b) simulated FDTD reflected power spectrum of one DBR of cavity 2 for x-polarization (solid blue) and y polarization (dashed green). The simulated transmitted power in x-polarization is shown in dashed purple. Dark blue squares show experimental perpendicular polarization R values obtained from F results, using equation (1.5).

A quantitative analytical approach, similar to the procedure detailed for microwire 1, was carried out for the resonant peaks of cavity 2 in perpendicular polarization. The identified Marcatili E_{11}^{x} mode resonances are shown in vertical dashed lines in the blue spectrum in figure (5.14) (a). They lie at 693.0, 708.9, 725.4 and 742.8 nm. The resonant peaks display a low FWHM and a high intensity with respect to the broad Ga_2O_3:Cr PL band. They were successfully ascribed to the E_{11}^{x} mode with an L_{eff} = 7.6 µm which follows the longitudinal resonance condition (equation (5.7)) for consecutive integer numbers. Notice that this L_{eff} is only 0.6 µm higher than L, which implies a penetration of only 0.3 µm of the confined waves in these DBRs. Apart from these four peaks and intraionic Cr^{3+} R-lines at 692 and 696 nm, hardly no other resonant peaks can be seen in the highest intensity Ga_2O_3:Cr PL wavelength range. Notice that at 693 nm the resonant peak is superimposed to the lower wavelength R-line, increasing the apparent FWHM of this R-line in perpendicular polarization with respect to parallel polarization.

Regarding parallel polarization, a series of broad peaks can be noticed in

the 690-740 nm range. As discussed in section 5.6, this measurement configuration allows both x- and y-polarization modes to be present. In microwire 1, due to the higher reflectivity in y-polarization compared to x-polarization in the 740-750 nm range (see figure (5.12)), E_{11}^{y} modes could be identified in this range of the parallel polarization μ-PL spectrum. However, figure (5.14) (b) shows that in microwire 2 we were able to design DBRs in order to have high reflectivity in x-polarized guided modes, clearly higher than the y-polarized guided modes, throughout the Ga_2O_3:Cr emission range. This results in E_{pq}^{x} modes faintly appearing in the whole range of the parallel polarization spectrum, as it can be seen in figure (5.14) (a). However, notice in this figure the low FWHM high intensity peaks in parallel polarization at 671 and 685 nm. These two peaks, with an FSR of 15 nm which fits with consecutive modes of an $L \approx 7\,\mu m$ cavity, are in the highest reflectivity range in the simulated y-polarization spectra, with an expected R of over 60%, and can therefore be (mainly) attributed to E_{pq}^{y} modes.

Experimental F and R values of the identified E_{x}^{11} mode peaks were obtained and are displayed as blue squares in figure (5.14) (b). The comparison with the simulated peaks yields an excellent agreement both in the wavelength position and the reflectivity values. R values of 78% to 80%, related to F values of 12.8 to 13.8, were experimentally obtained. These experimental values are notably better than the highest F and R values of cavity 1A (see Table (5.1)) with a lower number of required DBR periods (20 vs 12). Apart from the reduction of scattering losses at the DBRs, which is evident when comparing the FDTD R and T spectra of this cavity with cavity 1A's, the fact that experimental R values resemble more the simulated R values implies an improvement in the smoothness of the FIB-patterned periodic holes. Furthermore, the selected DBR periodicity allowed for the high reflectivity resonances to be placed around the PL band peak position.

Let us move to microwire 3. As already detailed, three cavities were patterned in this wire, and their parameters are displayed in table (5.2). Figure (5.15) (a) to (c) show μ-PL spectra of cavities 3A, 3B and 3C in perpendicular polarization. The three cavities exhibit well-resolved resonant peaks. As $L_{3A} = 4.9\,\mu m$ and $L_{3C} = 5.9\,\mu m$, cavities 3A and 3C are the shortest working cavities achieved in this thesis, resulting in only 4 and 3 resonant peaks in the Ga_2O_3:Cr emission range, respectively. Recall that by this fabrication method we have been able to modify the number of resonant peaks in the PL range and their FSR by placing the DBRs that form each cavity closer or further away from each other. Parallel polarization spectra

of these cavities are not shown as they display a mode mix similar to wire 2's cavity (see figure (5.14) (a)).

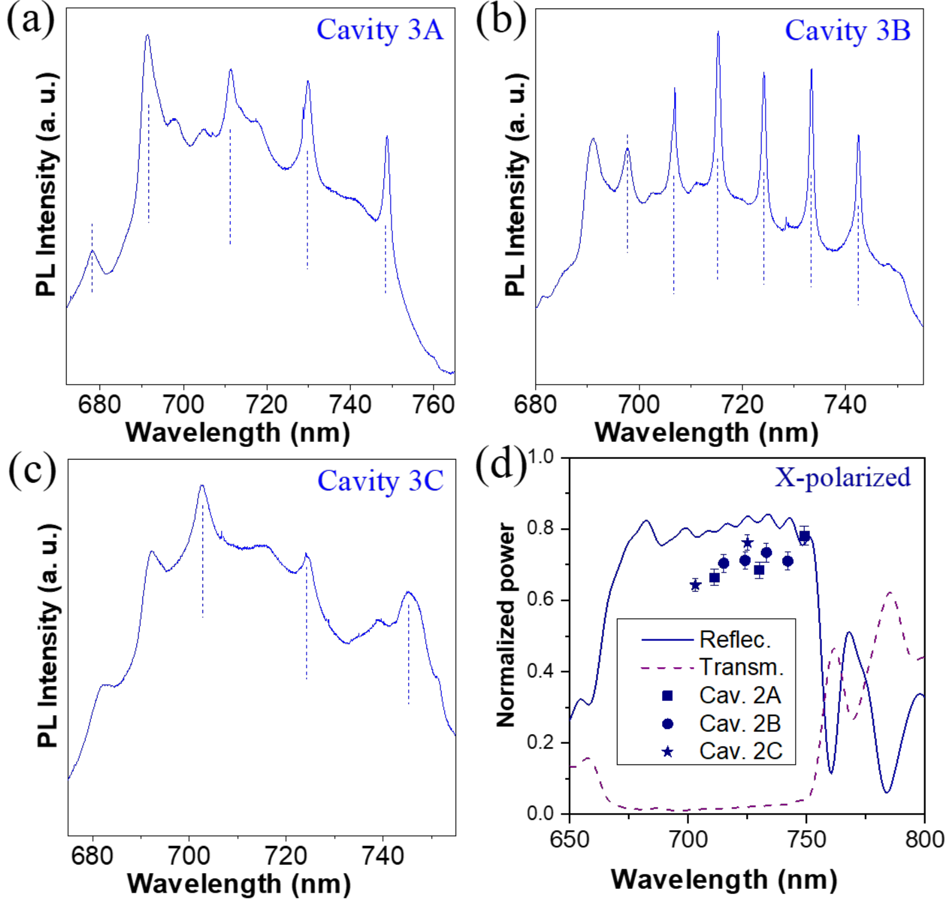

Figure 5.15: μ-PL spectra acquired in perpendicular polarization from (a) cavity 3A, (b) cavity 3B and (c) cavity 3C. The identified resonant peaks ascribed to the E^x_{11} mode are labelled with dashed vertical lines. (d) Simulated FDTD reflected power spectrum of one DBR of the cavities in wire 3 for x-polarization (dark blue). The simulated transmitted power in x-polarization is shown in dashed purple. Experimental perpendicular polarization R values obtained from F values by using equation (1.5) are shown in blue squares, circles and stars for cavities 3A, 3B and 3C, respectively.

The main resonant peaks in cavities 3A to 3C were studied by using the Marcatili model and the longitudinal resonance condition, analogously to previous cavities. Excellent fits to the E^x_{11} mode were obtained for all the

main peaks of the three cavities, with consecutive integers obtained for effective lengths of 6.78, 13.85 and 5.51 µm. Consequently, the DBR penetration depths obtained in the three cases lie between 0.3 and 0.4 µm. It is reasonable to expect them to have an almost identical value in the three cavities, as they belong to the same wire and the DBR parameters are the same for the three DBR cavities. The slight penetration depth variations between the cavities are in the expected range bearing in mind the approximations used by the Marcatili model (see appendix A) and the FIB patterning uncertainties. Therefore, the results indicate that cavities 3A to 3C present well defined resonances with the expected FSR for the fundamental E^x mode.

Figure (5.15) (d) shows the FDTD-simulated reflected and transmitted powers in x-polarization, as well as the experimental R of the identified peaks of the three cavities in perpendicular polarization. As the three cavities were patterned in the same wire and have the same DBR parameters, they were all compared to the same FDTD-simulated reflectivity spectrum. Experimental R values from 64% to 78% were obtained for the three cavities in microwire 3 in the highest intensity μ-PL range, i.e. in the 700 to 750 nm wavelength range. It must be noted that two other E^x_{11} resonant mode peaks around 690 nm were identified (one in cavity 3A, one in cavity 3B) but their associated R could not be obtained due to convolution with the intraionic R-lines. In addition, no high R resonances were obtained below 690 nm despite the expected large R for the 675-690 nm range according to the simulations. This discrepancy may arise from a slight blueshift and/or broadening of ~10 nm of the simulated SB with respect to the experimental SB. Anyhow, the excellent agreement between simulations and experiments for both the magnitude of R and the width and position of the SB has been proven for the three microwires, which implies the possibility to successfully tailor the optical resonances in these kind of photonic devices.

5.9 Influence of the laser power on the resonances

An optical cavity switches from spontaneous to stimulated emission (i.e. reaches the lasing condition) when, for a certain wavelength, the round trip gain surpasses the sum of all the losses. This occurs when the pump power reaches a certain value for a certain wavelength range, this range known as the gain envelope. If the mode wavelength spacing is smaller than the gain envelope, multiple, simultaneously present laser modes would appear, which can be the case in nanowire Fabry-Pérot lasers [138, 139]. In order to elucidate whether our DBR cavities have reached the lasing condition, we

have analyzed the intensity and FWHM of one of the main μ-PL resonant peaks in one of the best-working cavities, cavity 3B, with respect to the pump power of the He-Cd incident laser.

Figure (5.16) (a) shows normalized spectra of cavity 3B with perpendicular polarization setup for 100% laser pump power (i.e. equivalent to Figure (5.15) (b)) and 10% laser pump power. For this analysis, it is useful to know the ED which corresponds to these incident powers. By measuring the power of the He-Cd laser spot just before reaching the sample with a Kimmon KPM-1000 power meter, a value of 1.5 mW was obtained. By approximating the laser spot to a circumference with diameter 3 µm (see figure (2.15)), this implies an estimated value of 20 kW/cm^2 ED for 100% pump power of this laser. The pump power was reduced to 10% of this value by inserting a filter of optical density 1 in the path of the incident laser light.

Both spectra show the expected resonances for the DBR cavity, as discussed in the previous section. However, two interesting differences can be observed in the 10% pump power spectrum with respect to the 100% one. Firstly, the R-lines (at 692 and 696 nm) have a higher intensity with respect to the broad phonon-assisted band of Cr^{3+}. Secondly, a blueshift of ~1 nm can be observed. Both phenomena can be explained with a local temperature increase in the cavity caused by the pumping laser, with a lower magnitude at 10% pump with respect to at 100%. As explained in the Introduction, the Cr^{3+} intraionic phonon-assisted band is a thermally-activated transition which increases in intensity with respect to the R-line-related transitions when the temperature increases [54]. A lower ED implies a lower local temperature increase of the cavity, hence a lower relative intensity of the broad band with respect to the R-lines. As for the observed blueshift for lower pump power, it is well known that when the temperature changes in an optical cavity, both the refractive index and the cavity length change proportionally, which results in resonant mode peak shifts. This can be expressed by the following equation [140]:

$$\frac{d\lambda_m}{dT} = \lambda_m(\delta' + \alpha') \tag{5.9}$$

where δ' and α' are the thermo-optic and thermal expansion coefficients of the material (in this case Ga_2O_3), respectively. As δ' and α' are positive constants, a lower local temperature in the optical cavity implies a blueshift of the resonant modes.

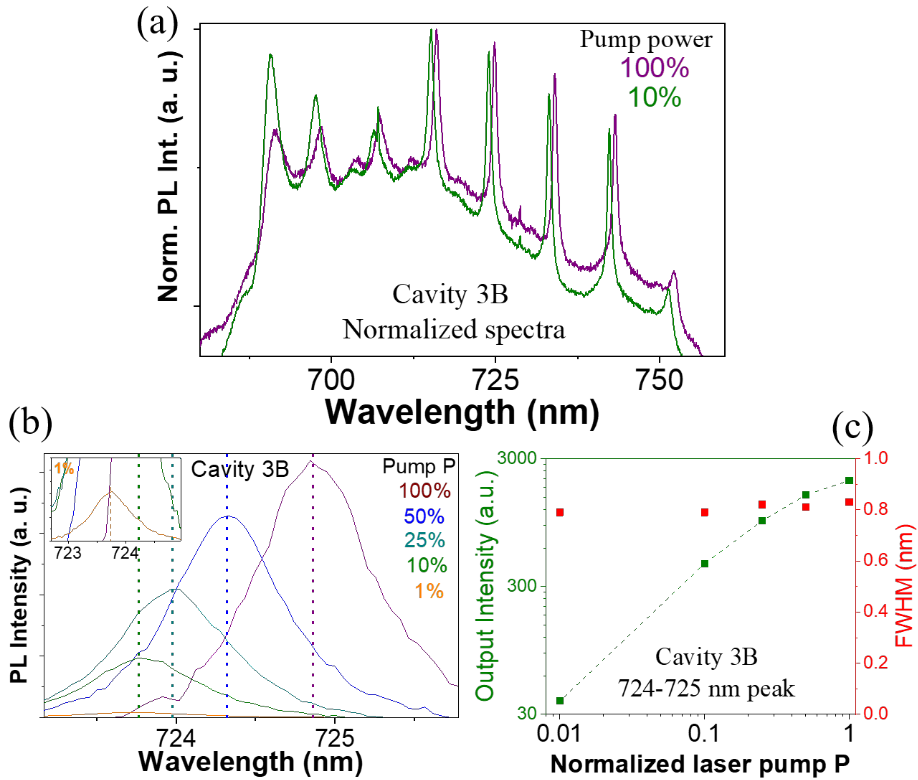

Figure 5.16: (a) Normalized μ-PL spectra acquired from cavity 3B in perpendicular polarization with 100% laser power (purple) and 10% laser power (green). (b) 724-725 nm peak of the μ-PL spectra in (a) before normalization with different laser pump powers: 100% (purple), 50% (blue), 25% (cyan), 10% (green) and 1% (orange). Vertical dashed lines are used as a guide to the eye to show the peak blueshift with decreasing laser power. The 1% spectrum is amplified in the top left corner inset. (c) Emission intensity (green, logarithmic) and peak FWHM (red) as a function of the He-Cd laser pump power in logarithmic scale, normalized to the maximum pump power (100%).

Figure (5.16) (b) shows the as-obtained μ-PL perpendicular polarized spectra (before normalization) equivalent to fig. (5.16) (a) but only for the resonant peak centered in 724-725 nm, in which a subtraction of a linearly decaying baseline has been made in order to eliminate the contribution of the broad phonon band. In addition to 100% (purple) and 10% (green) pump power, 50% (blue), 25% (cyan) and 1% (orange) pump power spectra for this peak range are shown in this figure, which were acquired by insert-

ing different optical density filters in the optical path of the He-Cd laser. Notice the monotonic blueshift of the resonant peak with decreasing pump power due to lower heating of the DBR cavity by the incident laser. This behaviour was reversible, i.e. the different spectra could be obtained in any order and after the measurements the DBR cavity continues operating as usual.

For the 724-725 nm resonant peak shown in fig. (5.16) (b), the total output peak intensity as a function of pump power was obtained and is represented in double logarithmic scale in figure (5.16) (c). If we compare this graph with a typical nanowire lasing intensity vs pump power graph (e.g. see fig. 2(d) in [138]), we can conclude that stimulated emission has not been reached in our DBR cavities. Another effect of reaching stimulated emission, which can be more clearly detected than the previous condition in certain systems, is the abrupt linewidth narrowing in the resonant peak(s) [141]. In our DBR cavities, as also shown in figure (5.16) (c) in red squares, the FWHM of the peak remains almost constant for all pump powers. Hence, the results show that by pumping with our He-Cd laser, the obtained Ga_2O_3:Cr DBR cavities are in the spontaneous emission regime. In this regime, however, interesting photonic applications remain for these cavities. For example, the in-situ peak shifts due to local temperature variations in the cavities suggests their use as temperature sensors, in analogy to similar developed systems [140].

Comparison and future of Ga_2O_3:Cr optical cavities

Table (5.3) presents a comparison of the highest experimental reflectivities obtained in the Ga_2O_3:Cr emission range for the DBR cavities analyzed so far in this chapter. After the successful patterning of cavities 1A and 1B, cavities 2 and 3A to 3C were able to further improve the maximum R in the DBRs up to 80% and, at the same time, reduce the number of DBR periods down to 10-12 and slightly reduce the transversal dimensions of the wires for which these cavities work. Despite this large reflectivity, in the previous section it was concluded that the DBR cavities do not show lasing for the He-Cd laser pump power range. This may be due to the fact that, although the obtained μ-PL is very intense, it is originated from individual Cr ions in Ga_2O_3, which are present in an atomic concentration of 0.5% at. or lower. This limits the number of recombination centers excited by the laser spot. By attempting other excitation sources, such as high intensity and broad excitation area light sources or electrical contacts, further work can be made to elucidate whether the lasing threshold can be reached in

these high reflectivity Ga_2O_3:Cr DBR cavities.

Cav. 1A		Cav. 2		Cav. 3A		Cav. 3B		Cav. 3C	
λ[nm]	R	λ[nm]	R	λ[nm]	R	λ[nm]	R	λ[nm]	R
798	0.66	709	0.80	749	0.78	733	0.73	725	0.76
709	0.55	749	0.78	730	0.69	742	0.71	703	0.64

Table 5.3: Comparison of the highest experimental reflectivities in the 700-800 nm range for the DBR-patterned microcavities analyzed in this chapter.

Besides, notice that size reduction of the Ga_2O_3:Cr optical microcavities is reaching an important lower threshold. In other semiconductor nanowire systems such as ZnO it is found out that, independently of the optical cavity length, wire diameters which are lower than the resonant wavelengths inside the semiconductor do not lase due the optical field extending considerably outside the nanowire [142]. As λ_{in} is 350-400 nm, the lateral dimensions d and w_t have a lower threshold of around 400 nm. Notice that we have achieved excellent working DBR cavities with $d_{min} = 520$ nm, which is close to this threshold. We checked this lower threshold experimentally; two wires of lateral sizes between 200 and 400 nm were DBR-patterned by FIB and we found no resonant peaks in the μ-PL spectra. Therefore, in order to obtain semiconductor nanowire optical cavities based on Ga_2O_3 with similar size to the so-far working ZnO nanowire lasers and in order to attempt to reach the lasing threshold, the PL emission of the optical cavities was translated to lower wavelengths, as described in the next section of this chapter.

5.10 Undoped Ga_2O_3 DBR cavities

After the thorough work on Cr-doped Ga_2O_3 DBR microcavities of the previous sections, the next logical step was to use the same simulation, fabrication and characterization methods with UID Ga_2O_3 micro- and nanowires. DBR cavities of UID Ga_2O_3 have two main advantages over Ga_2O_3:Cr cavities:

- Short-wavelength DBR-based optical devices are not that technologically mature in comparison to devices in the red-NIR emission range [127]. As the intrinsic emission of UID Ga_2O_3 is in the blue-UV energy range, it is one of the natural candidates in this sector.
- As the confined luminescence in UID Ga_2O_3 nanowires is in a shorter wavelength range (approximately half of the Ga_2O_3:Cr ones), further

size reduction of the DBR cavities is possible, as lower wire transversal dimensions are able to guide these λ.

However, new challenges arise. Firstly, an excitation source with high energy is required for band-to-band excitation in UID Ga_2O_3. For this purpose, we used the fiber oscillator laser (4.82 eV) at Bremen University. Secondly, the DBR SB needs to be shifted towards the blue-UV range. FDTD simulations were performed and we concluded that a trade-off had to be found between the lower DBR periodicity required (see equation (5.2)) and the resolution of the FIB instrument.

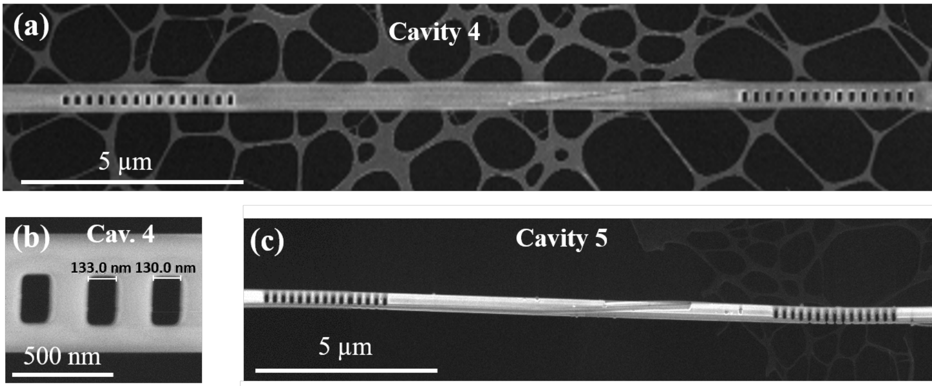

Figure 5.17: (a) SE image of cavity 4. (b) Higher magnification image of one of the two DBRs in this cavity, showing the small value of α in the holes. (c) SE image of cavity 5.

Figure (5.17) shows SEM images of the UID Ga_2O_3-fabricated nanocavities. The nanowires were grown on the tubular furnace at 900°C with Ga_2O_3 and Ga precursors under Ar flow. Once they were deposited in the TEM grid, analogously to Ga_2O_3:Cr wires, some of them were selected for FIB patterning. Two DBR cavities are shown in figures (5.17) (a), cavity 4, and (5.17) (c), cavity 5. As explained before, the DBRs in these cavities must considerably reflect light in the blue-UV wavelength range, which is where the UID Ga_2O_3 structures emit. A value of $a = 280\,\text{nm}$ with $N = 15$ DBR repetitions was selected for both nanocavities, bearing in mind FDTD simulations and FIB possibilities, as discussed further on.

The dimensions and DBR parameters of the patterned UID Ga_2O_3 wires, compared to the most successful Ga_2O_3:Cr wire (3) are presented in table (5.4). The UID Ga_2O_3 nanocavities have a smaller width and, due to the smaller a, a smaller total length of the DBRs. The length of cav-

Wire	w_t(nm)	w_f(nm)	d(nm)	L (μm)	α_1(nm)	a(nm)	γ(nm)
3	730	600	620	5-13	190	470	370
4	500	220	640	12	130	280	200
5	500	380	460	12	150	280	290

Table 5.4: Comparison of the UID DBR cavities (4 and 5, blue) with Ga_2O_3:Cr DBR cavity 3 (red). All values are given with uncertainty ±10 nm, and L is rounded up to the nearest µm for the sake of clarity.

ities 4 and 5 is larger than most of the designed Ga_2O_3:Cr cavities: 12.0 and 12.4 µm. Shorter UID DBR cavities were also attempted but did not show clear resonances when measured with the fiber oscillator laser confocal setup.

Figures (5.18) (a) and (b) show μ-PL spectra from cavities 4 and 5, respectively. Analogously to previous measurements, in order to increase the signal from the resonances with respect to the broadband emission, the collection point was placed in one of the DBRs while the excitation area was placed inside the active region of the cavity, as shown in the inset of fig. (5.18) (b). This inset shows a μ-PL image of cavity 5, whose emission was rendered by the camera as blue. As shown in the spectra, the emission range of these UID cavities is in the NUV-violet range (340 to 420 nm) instead of the Ga_2O_3:Cr red-NIR range.

Not only the emission wavelength but also the DBR reflectivity has been partially translated to this range, as it can be observed in the spectra and will be further analyzed at the end of this section. In cavity 4, fig. (5.18) (a), the highest intensity and finest peaks are around 400 nm, as shown in the inset. In cavity 5, fig. (5.18) (b), very intense resonances can be seen in the 370-400 nm wavelength range, and further resonant peaks can be observed for $\lambda < 360$ nm. It must be noted that the unpolarized spectrum is shown instead of the perpendicular polarization spectrum in the latter cavity because the wire is tilted with respect to its longitudinal axis.

The resonant modes in cavity 5 were examined analytically, analogously to section 5.6. As the wire has an almost-rectangular cross-section (see table (5.4)), the E^x_{pq} and E^y_{pq} modes should be centered around the same wavelength positions. The 9 main consecutive resonant peaks shown in figure (5.18) (b), which lie in the 375 to 395 nm wavelength range, were ascribed to the fundamental E^x_{11} mode by using the Marcatili model. An effective length of $L_{eff} = 13.3$ µm was obtained. As this value is 0.9 µm

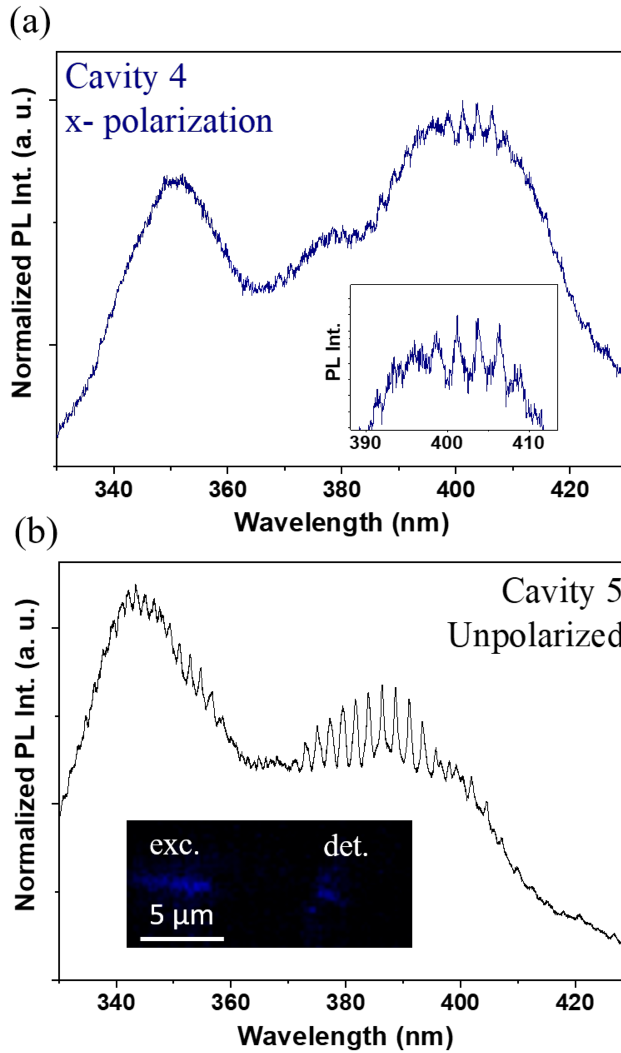

Figure 5.18: (a) Normalized μ-PL spectrum from cavity 4, obtained with the polarizer placed in the x-axis. The inset shows the same spectrum magnified in the emission range around 400 nm. (b) Normalized μ-PL spectrum from cavity 5, without polarization filter. The inset shows a μ-PL image of the same cavity, indicating the excitation and detection points for the μ-PL spectrum.

higher than the measured length of the cavity by SEM, this implies a penetration depth of 0.4-0.5 µm, which is similar to the obtained penetration depths in FIB-fabricated DBRs for the red-NIR range. It must be noted

that, as the wavelength is substantially lower in these wires, the condition of grazing incidence is met despite the smaller lateral dimensions of the WGs (see the inequalities shown in appendix A for more details).

The reflectivity of the DBRs was obtained from the finesse of the peaks by using equation (1.5). Moderate R values were obtained, ranging from 38% to 44% in cavity 4 and from 41% to 49% in cavity 5. These values are presented in figure (5.19) along with the FDTD-simulated R and T values for both cavities. In both cavities, very good agreement is found between the simulated and the experimental R values. In cavity 4, both μ-PL and simulations show a reflectivity maximum of 44% in the violet wavelength range. However, a redshift of around 10 nm can be deduced between the simulated and the experimental results of this nanocavity. Similar possible SB shifts of $\sim$10 nm were also observed in some Ga_2O_3:Cr microcavities (e.g. see figure (5.14) (b)) and can be considered as our experimental-simulated uncertainty. In cavity 5, the simulations successfully predicted reflectivities from 40% to 50% in the 350-410 nm emission range. Some experimental reflectivities match the FDTD-predicted values, while the lower obtained experimental R with respect to the simulations can be explained by artificial broadening from more than one resonant mode being present in a similar wavelength value.

The results also show room for improvement. Firstly, the simulations indicate that the reflectivity and the transmission of the DBRs add up to 50% or lower both in cavity 4 and 5 in the violet-NUV range. Hence, it is clear that most of the light is currently being lost due to scattering at the DBRs. Secondly, figure (5.19) indicates that a further blueshift in the DBR SB would be necessary in order to have projected reflectivities of almost 80% (cavity 5) to almost 100% (cavity 4) coinciding with the luminescence band maxima of UID Ga_2O_3, but this would require even thinner hole carving at the FIB instrument.

Bearing in mind the generation volume of the ions (see section 2.1.3) and the slight thermal drifts observed, a further reduction of the DBR periodicity in combination with having completely carved holes with sufficient resolution would probably be too demanding for the FIB instrument. One interesting alternative would be to make shallow periodic indentations in the wire. This would not only reduce the ion generation volume, hence allowing for a smaller DBR periodicity, but it should also limit the scattering loss at the DBRs [137]. However, this indentation depth must be controlled very precisely when carving with the FIB. Furthermore, the refractive index

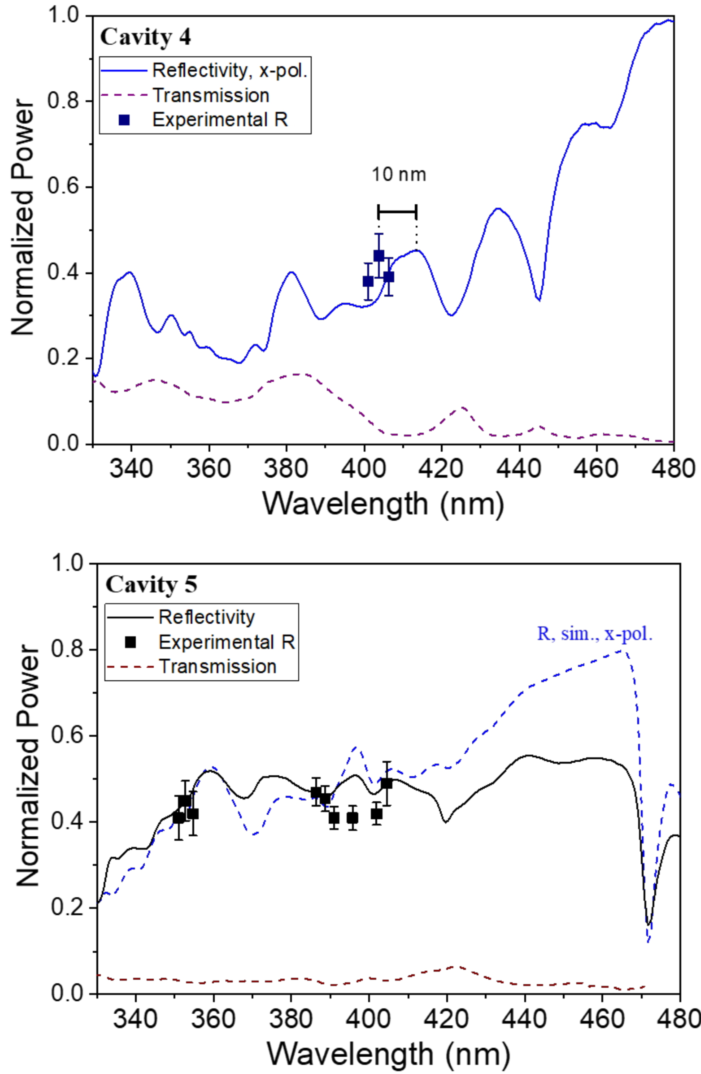

Figure 5.19: (a) Comparison of the FDTD-simulated reflected power spectrum in x-polarization (blue line) and experimental R results (blue squares) obtained using equation (1.5) for cavity 4. (b) Comparison of the FDTD-simulated reflected power spectrum (black line) with the experimental R results analogously obtained (black squares) for cavity 5. Blue dashed lines show the simulated spectra in the x-polarization for cavity 5. In both spectra, transmitted power through both DBR cavities is shown in dashed purple lines.

contrast between the indentations and the material would be much lower than the current cavities, which would involve a higher number of necessary periods (N) in the DBRs to reach similar low DBR T values like the ones presented here (see section 5.2). Other alternatives such as tapered designs [143] would limit the scattering which is currently present in our $a = 280\,\text{nm}$ UID DBR cavities. However, very precise values of α are required for them to work. We are currently exploring these approaches, taking into account both the simulations and the necessary experimental conditions in order to obtain feasible novel optimized designs of tunable Ga_2O_3 DBR nanocavities.

5.11 Conclusions

In this chapter, we have designed, fabricated and analyzed gallium-oxide-based optical micro- and nanocavities with DBRs as the end-mirrors for the first time in gallium oxide and in most metal oxides. By use of FDTD simulations, we have tuned the DBR parameters for each microwire geometry in order to obtain an improved optical confinement in their luminescent range. A thorough analysis of their performance has been made by polarized μ-PL measurements, analytical methods and FDTD simulations, all of which have allowed to further understand and optimize the operation of the DBR cavities.

Strongly modulated room temperature red-NIR and violet-NUV μ-PL spectra have been achieved in the patterned cavities, and they have a stable operation under the laser beam. The observed resonant mode structure and the dependence of the resonant peak positions on the polarization of the measurement setup have been explained by E^x_{pq} and E^y_{pq} rectangular waveguide propagating modes, with longitudinal resonance condition in the z-component of the k-vector. Successful fits to these modes have been carried out, which have allowed for the retrieval of their dispersion relations and the effective longitudinal lengths of the DBR cavities.

The optical resonances are located in the expected wavelength range and their experimental finesse and reflectivity was found to be similar to what was anticipated from the FDTD simulations, reaching up to 80% in the red-NIR and up to 50% in the violet-NUV range. Therefore, the DBRs have proven to effectively confine light within the cavity and our simulated results have shown very good agreement with our experimental results. Additionally, DBRs with different parameters have given rise to different polarization-dependent stop band ranges, which we spectrally shifted de-

pending on the desired working range of the cavities. Besides, successful DBR cavities with different lengths, from 5 to 15 µm, have been experimentally achieved, resulting in the tunability of the number of resonant peaks and their FSR within the emission range. Furthermore, the wavelength position of the resonances can be reversibly modified in-situ by changing the incident laser power due to local heating in the cavities.

Therefore, these novel Ga_2O_3 optical cavities have proven to be useful in tunable nano- and microscale photonics for device applications such as temperature sensors or light detectors. Furthermore, these DBR cavities still have room for improvement; from our current results, new designs have been proposed. This work paves the way for Ga_2O_3 to be considered as a good candidate for novel nanophotonic devices both in the long- and short-wavelength ranges.

Chapter 6

Conclusions

The last chapter of this PhD thesis summarizes the main conclusions of this work. Along with the review of the main results, a critical analysis is made, exploring the limitations and opportunities of our work.

1. A large quantity and wide variety of Ga_2O_3 micro- and nanostructured morphologies have been achieved by a thermal evaporation method, all showing high crystalline quality. By this high-yield cost-effective method, we have obtained Ga_2O_3 elongated structures doped with Zn, Ge, Sn or Cr. As well as the choice of the precursors, other factors such as the growth temperature have been demonstrated to play a role in their morphology and microstructure:

- Ga_2O_3 powders, Ga metal and ZnO precursors has resulted in large Ga_2O_3 microstructures with belt-like morphology, i.e. with one of its dimensions of a few hundred nanometers. Zn has incorporated in a low concentration, under the EDS detection limit, resulting in no visible modification in the Ga_2O_3 crystal structure, as shown by Raman spectroscopy. As well as the important morphological changes attributed to the inclusion of Zn in the precursors, the luminescence results explained further on are a good guide to understand the substitutional incorporation of Zn in Ga_2O_3.

- The inclusion of Ge powders in the thermal treatment has resulted in the formation of a GaGe alloy which acts as a catalyst for the vapor-liquid-solid (VLS) growth of Ga_2O_3:Ge nanowires. The Ga_2O_3 monocrystalline nanowires and nanobelts grew along the [010] or [001] directions, the nanobelts resulting from secondary nucleation sites in the [001]-grown nanowires. These growths occur when the growth temperature is slightly lower than the Ge melting point (840ºC),

and gallium germanate covers the tip of the nanowires or nanobelts. Growth at the Ge melting point (940°C) generates thicker wires with a Ge nanocrystal in their tip. These novel results are a first step towards the realization of more complex structures such as the ones presented in the next bullet point.

- Shape engineering of Ga_2O_3 - SnO_2 nano-heterostructures has been achieved by exploring the optimum temperature and precursors (Ga, Ga_2O_3 and SnO_2). We have obtained a high yield of Ga_2O_3 elongated structures, both 1D and L- or T-shaped, with SnO_2 partial covering, either fuzzy or by polyhedral particles. By XPS and TEM, we have observed an Sn-rich wetting layer in the nanostructures' wire axis, which provides material for the 3D SnO_2 particle growth. Especially interesting are the heterojunctions formed by 1D Ga_2O_3 nanowires and 3D polyhedral SnO_2 particles, called skewer-like (SK) structures, which grow in the [110] or [010] directions, show partial lattice matching between Ga_2O_3 and SnO_2 and present ionic tunnels in some of the SnO_2 particles.

- The inclusion of Cr_2O_3 as a source material in the Ga_2O_3-SnO_2 system modifies the preferential growth direction of the Ga_2O_3 nanowires towards the [001] and favours the formation of SnO_2 crossed-wires attached to the Ga_2O_3 nanowires, that grow perpendicular to the Ga_2O_3 nanowire. The Ga_2O_3 trunk has $\sim$2.6% Sn atomic incorporation while the SnO_2 crossed wires have $\sim$3.6% Ga atomic incorporation, resulting in a potential development of a p-n heterojunction in the nanoscale. ADF-STEM characterization in this junction reveals that it has a high crystalline quality, resulting from the lattice matching between the {020} Ga_2O_3 and the {310} SnO_2 atomic planes.

Therefore, as a first conclusion, in this thesis we have studied the influence of different growth parameters and mechanisms in the synthesis of doped Ga_2O_3 micro- and nanoarchitectures by thermal treatments. The obtained nanostructures are a first step to understand the role of key n- and potential p-type dopants in Ga_2O_3. Furthermore, Ga_2O_3 - SnO_2 heterostructures have been synthesized and thoroughly analyzed up to the atomic level, which has provided important results on the lattice matching of both materials, pointing out for their use in TCO nanodevices. Although the synthesis method does not provide total control over the size, microstructure and morphology of the resulting structures, in this thesis we have demonstrated the possibility to shape engineer doped nanoarchitectures with certain growth-

dependent preferential characteristics and a high crystalline quality. Further work could lead to ascertain our tentative achievement of p-n nanojunctions of Sn doped Ga_2O_3 and Ga doped SnO_2, as well as to combine Ga_2O_3 with p-type TCOs such as NiO in the nanoscale.

2. The optical properties of the synthesized Ga_2O_3 (and SnO_2) micro- and nanostructures have been analyzed by cathodoluminescence (CL), photoluminescence (PL) and related techniques. The role of the different dopants in their luminescence properties has been discussed. In particular:

- Zn doping in Ga_2O_3 results in luminescence bands in the visible region. A broad 2.7 eV band has been measured by CL at room temperature, which does not appear in unintentionally doped (UID) Ga_2O_3. For the first time, this band has been studied in depth by PL. We have made PL measurements with three different light sources: a Xe lamp, a pulsed LED and a fiber oscillator laser, the pulsed LED also used for time-resolved PL spectroscopy. The broad visible emission in the Ga_2O_3:Zn samples has been concluded to be composed of a blue (2.8 eV) and a green (2.5) band with different luminescent dinamics. Low excitation density (ED) PL sources result in the increase of the relative intensity of the blue emission and, especially, the green emission, due to a longer decay time of the latter (>100 ns) with respect to the more energetic bands. The results make Ga_2O_3:Zn structures attractive for multi-color emission devices. Furthermore, their luminescence is guided throughout their volume, and weak optical resonances have been identified due to partial reflections in the lateral faces of the Ga_2O_3:Zn microbelts.
- By CL, we have found that Ge incorporation in Ga_2O_3 nanostructures reduces the intensity of their visible (3.0 eV) emission with respect to their UV (3.4 eV) one. Further work on the PL of Ga_2O_3:Ge, similar to the one carried out in this thesis on Ga_2O_3:Zn, should improve the understanding of the effect of Ge doping on the energy levels of Ga_2O_3, a topic which would shed new light on the use of this so-far mostly unexplored dopant for optoelectronics applications.
- The Ga_2O_3 - SnO_2 heterostructures present a complementary luminescence, both in CL and in PL, which cover the whole visible range. Ga_2O_3 emits in the UV-blue energy range and SnO_2 has a luminescence from the green to the red energy ranges. These SnO_2 emissions are very dependent on their dimensionality: in crossed-wire (CW)

1D structures, the orange-red emission is dominant, while the blue-green emission is the most intense in the 3D particles. This allows for dimensionality-dependent tuning of the SnO_2 luminescence. Moreover, the CW structures present light guiding and Fabry-Pérot (FP) optical resonances, which allow for their use in photonic applications.

- Chromium doping in Ga_2O_3 profoundly alters the luminescence of the elongated structures; switching it towards the red-NIR range due to intraionic Cr^{3+} transitions. This emission can be guided through the wires and, in unmodified wires with smooth lateral walls and end facets, weak FP resonances appear in the μ-PL spectra.

Therefore, as a second conclusion, in this thesis we have made a thorough optical analysis of the doped Ga_2O_3 structures, linked to their chemical and morphological characterization. The study of their optical properties has allowed for a further understanding of the effect of the introduction of different impurities in the recombination paths of Ga_2O_3. The promising results presented in this thesis allow Ga_2O_3 to be considered as a good candidate for optoelectronic and photonic devices, especially if approaches are used to improve the optical confinement in these structures such as the ones presented in the next and final point of the conclusions.

3. This thesis presents an innovative approach to improve the optical performance of semiconductor micro- and nanowire cavities. It is based on three main stages, which result in the successful design and characterization of Focused Ion Beam (FIB)-etched distributed Bragg reflector (DBR) optical microcavities:

- We have simulated different Ga_2O_3 structures and DBR parameters before FIB fabrication by finite-difference time-domain (FDTD) methods. 3D models of the selected Ga_2O_3 candidate microwires with their possible DBR parameters have been designed. After the propagation of the Gaussian wave in the wire and DBR, its reflection, transmission and scattering as a function of the vacuum wavelength can be obtained from these simulations. As the FIB is able to reproduce the optimum DBR parameters according to the simulations with high precision, this allows to tune the DBR design in order to have its maximum reflectivity in the emission range. In this thesis, we have explored both the red-NIR (Ga_2O_3:Cr) and the violet-NUV (UID Ga_2O_3) energy ranges.

- We have optically characterized the performance of the DBR cavities. Strongly modulated red-NIR and blue-NUV μ-PL spectra have been

measured on several successful Cr-doped and UID Ga_2O_3 nanopatterned cavities, respectively. As well as the possibility to tune the highly confined wavelength ranges and peak separations (FSR) with the FIB, the DBR cavities show in-situ tunability by using different polarization setups or by varying the laser power.

- We have modelled analytically the experimentally-obtained guided-confined modes. The wavelength position and polarization dependence of these modes has been modelled by the use of Marcatili and Goell waveguide models and the FP longitudinal resonance condition. In particular, perpendicular polarization measurements present the most intense resonant peaks, which have been modelled by the longitudinal confinement of the E_{11}^x waveguide modes. The FSR of the resonant modes in every cavity matches with the optical length (L_{op}) of the cavities, with a slightly increased L_{op} with respect to the selected distance between the DBRs due to the penetration depth of the electromagnetic waves in the DBRs. Both simulated and experimental reflectivities have shown very good agreement in all the cavities, reaching values up to 80% and 50% in Ga_2O_3:Cr and UID Ga_2O_3 DBR cavities, respectively.

Therefore, as a third and final conclusion, novel DBR cavities based on Ga_2O_3 micro- and nanowires have been designed, fabricated and characterized by experimental, analytical and simulated procedures. The results shed light on the possibility of upgrading the optical performance of the synthesized architectures, in particular the percentage of confined light, by FIB DBR patterning. The innovative work carried out in this thesis has allowed to improve and further understand FP DBR cavities in the nanoscale, and can be beneficial not only for Ga_2O_3 but also for other semiconductor oxide systems, like the CW structures that were previously detailed. The results presented in this thesis are an important step towards the micro- and nanofabrication of novel transparent oxide photonic devices such as optical detectors, temperature sensors or tunable lasers.

Appendix A

Marcatili and Goell mode calculations

This appendix contains information on how, in chapter 5, the Marcatili and Goell models were applied in order to assign the different peak positions of the μ-PL spectra of the optical cavities to dielectric waveguide (WG) modes, E^x_{pq} and E^y_{pq}, which are confined in the z direction by the DBRs. The notation used is the same as in that chapter, unless stated otherwise. It contains the following:

1. Discussion on the approximations used by the Marcatili model.
2. Basic equations of the Marcatili and Goell models.
3. An example of the procedure used for the mode assignment: cavity 1A.

More detailed information about planar optical waveguides in general and the deduction the WG modes explained here can be found in refs. [131, 134, 144].

Discussion on the approximations of the Marcatili model

In dielectric rectangular WGs, an exact analytical solution of its propagating modes is not possible due to the difficulty in matching boundary conditions [133]. However, analytical and computational solutions result in very good approximate mode solutions. Let us begin by the main approximations used by the analytical Marcatili method. They are shown below

- Grazing incidence of the plane wavelet associated with the guided

mode, which can be expressed by the following inequalities:

$\frac{p\lambda_{in}}{4d} << 1$; $\frac{q\lambda_{in}}{4w_t} << 1$

Note that the wavelength to be considered is the one inside the cavity. These inequalities gain importance when considering dielectric WGs in the micro- and nanoscale. In Ga_2O_3: Cr wires, $\lambda_{in} \approx 400\,\text{nm}$ and, for example, in microwire 1, $d = 520\,\text{nm}$. This results in an approximate value on the left of the first inequality of 0.2 for E^x_{1q} modes, which can be considered good enough bearing in mind the approximate nature of our procedure. Notice that in undoped Ga_2O_3, $\lambda \approx 200\,\text{nm}$, which allows for WGs with smaller cross section to follow this condition.

- The difference between the refractive index of the WG and of its surrounding medium is not over 50% [131]. This results in certain areas outside the WG having negligible electromagnetic energy, as indicated in figure (A.1) in red. This condition is not true in Ga_2O_3 wires surrounded by air (n = 1), as n ≈ 2 in the red-NIR range. However, plots in [134] indicate that we can still use the Marcatili method for E^x_{11} and E^x_{12} modes in our Ga_2O_3: Cr microwires as the mode solutions are virtually the same as for the more exact Goell's method in the measured wavelength range.

Basic equations of the Marcatili and Goell models

Figure (A.1) shows a schematic of the cross section of a 3D rectangular WG of refractive index n surrounded by air. Bearing in mind the approximations used in Marcatili's method, the boundary conditions for the electromagnetic field (continuity of electric and magnetic fields in the interfaces) need only to be imposed in $x \pm w_t/2$ and $y \pm d/2$.

By solving the Maxwell equations on a rectangular dielectric WG, one can group the solutions into two groups according to the polarization of the electric and magnetic fields. If we consider E_x and H_y as predominant fields and set $H_x = 0$, we obtain the equation for the magnetic field in an E^x_{pq} mode:

$$H_y = A\cos(k_x x - \phi)cos(k_y y - \Phi) \quad (x \leq w_t/2, y \leq d/2) \tag{A.1}$$

where $\phi = (p-1)\frac{\pi}{2}$ and $\Phi = (q-1)\frac{\pi}{2}$. By applying the boundary conditions, the following simultaneous equations are obtained:

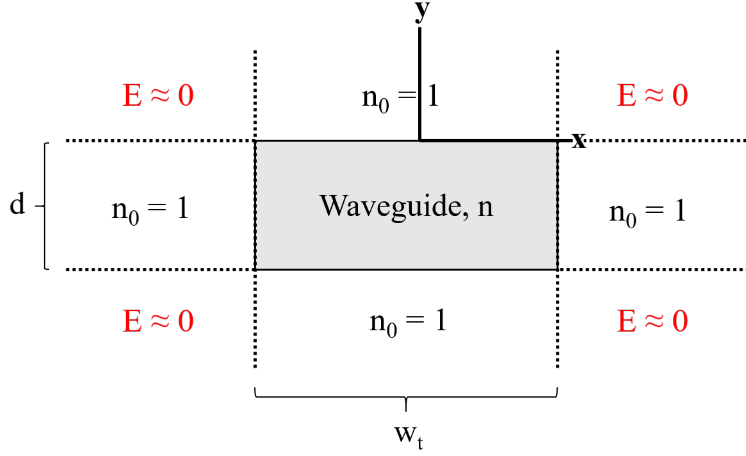

Figure A.1: (a) Schematic of the cross section of a 3D rectangular WG of refractive index n surrounded by air ($n_0 = 1$). Marcatili's approximation assumes that the electromagnetic field in the areas indicated by "E $\approx$ 0" in red is negligible, unlike Goell's. In addition, the WG parameters d and w_t, analogous to the parameters used in chapter 5, and the x and y axis (vertically shifted $d/2$ for clarity) are shown.

$$
\begin{aligned}
k_x \frac{w_t}{2} &= \phi + \arctan\left(\frac{n^2\sqrt{k_0^2(n^2-1)-k_x^2}}{k_x}\right) \\
k_y \frac{d}{2} &= \Phi + \arctan\left(\frac{\sqrt{k_0^2(n^2-1)-k_x^2}}{k_x}\right) \\
k_z^2 &= k_0^2 n^2 - k_x^2 - k_y^2
\end{aligned}
\tag{A.2}
$$

Similar equations are obtained for the E^y_{pq} modes, in which E_y and H_x are

considered as the predominant fields and H_y is set to 0:

$$\begin{aligned} H_x &= A\cos(k_x x - \phi)\cos(ky_y - \Phi) \quad (x \leq w_t/2, y \leq d/2) \\ k_x \frac{w_t}{2} &= \phi + \arctan\left(\frac{\sqrt{k_0^2(n^2-1) - k_x^2}}{k_x}\right) \\ k_y \frac{d}{2} &= \Phi + \arctan\left(\frac{n^2\sqrt{k_0^2(n^2-1) - k_x^2}}{k_x}\right) \\ k_z^2 &= k_0^2 n^2 - k_x^2 - k_y^2 \end{aligned} \tag{A.3}$$

Note that when the guided wavelets are confined in the z-direction, k_z must also follow the longitudinal resonance condition (equation (5.7)), as explained further on.

On the other hand, the computational Goell model provides accurate solutions for the dielectric WG modes. It does consider the electromagnetic field in areas indicated in red in figure (A.1). The equations are solved by using cylindrical coordinates, resulting in computerized solutions in the form of Bessel functions and modified Bessel functions multiplied by trigonometric functions. The solutions obtained for both models can be compared by representing the so-called propagation curves. In them, the normalized propagation constant P^2 is represented in the y axis. This parameter depends on k_z:

$$P^2 = \frac{(k_z/k_0)^2 - 1}{n_r^2 - 1} \tag{A.4}$$

In the x axis of the propagation curves, $B = \frac{2d}{\lambda}\sqrt{n_r^2 - 1}$ is represented. For a given value of B, which depends on the wire transversal length d and the PL wavelength in air λ, P^2 and therefore k_z obtained for both methods can be compared from plots in ref. [134]. If P^2 is the same, the analytical Marcatili model is used in order to have a better insight of the modes. If there are non-negligible differences between the value of P^2 in both models, a correction must be applied in order to obtain a more accurate k_z value.

Example: cavity 1A

Tables (A.1) to (A.3) show the calculated k_x, k_y k_z and m values for the identified E_x^{11}, E_x^{12} and E_y^{11} modes, respectively, of microwire 1, cavity 1A. From the results shown in these tables, the peaks in the μ-PL spectra (see

figure (5.8)) are mode-identified and the dispersion relation (see figure (5.10) (a)) is obtained.

After this information, let us briefly explain how the tables are obtained. In microwire 1, B lies between 2.1 and 2.4. It is found that P^2 is virtually the same for E^x_{11} and E^x_{12} from both methods, therefore the analytical Marcatili model is used for these modes (tables (A.1) and (A.2)). The procedure in both cases is as follows: for every identified peak we believe belongs to that mode, the first two equations in eq. (A.2) are solved; k_x and k_y are obtained. Then, k_z is obtained by using the third equation in eq. (A.2). Finally, by applying the longitudinal resonance condition (equation (5.7)), it is possible to know whether the set of peaks can be ascribed to consecutive integer (m) longitudinal resonant modes of the chosen wave-guided mode (i.e. E^x_{11}), for a certain L_{eff}. This effective length must be slightly higher than the length of the active region of the cavity and its value must be virtually the same in all the wave-guided modes for each cavity. For this L_{eff}, the values of m are obtained; if all of them are consecutive integers (with >90% confidence interval), the fit is successful.

For E^y_{11} modes shown in table (A.3), the Marcatili method overestimates the value of P^2 (k_z) and a correction must be applied. The procedure then is as follows: first, k_z is calculated as if Marcatili's model was valid, analogously to what was explained in the previous paragraph. Then, by use of the corrections in P^2, the value of k_z from the Goell method is obtained. Finally, the longitudinal resonance condition is applied in order to obtain the m values for a certain L_{eff}. In the analyzed cavities, the obtained L_{eff} is virtually the same in all the guided-confined modes. For example in tables (A.1) to (A.3), the obtained L_{eff} is 17.4 µm.

Mode	λ_p [nm]	k$_x$ [μm^{-1}]	k$_y$ [μm^{-1}]	k$_z$ [μm^{-1}]	m
E_x^{11}	670.1	2.65	4.88	17.0	94.0
	676.4	2.65	4.87	16.8	93.0
	683.0	2.65	4.86	16.6	91.9
	689.4	2.64	4.85	16.4	90.9
	695.8	2.64	4.83	16.2	90.0
	702.4	2.64	4.82	16.1	89.0
	709.3	2.64	4.81	15.9	88.0
	716.2	2.64	4.80	15.7	87.0
	723.3	2.64	4.79	15.5	86.0
	730.8	2.64	4.78	15.3	85.0
	738.5	2.64	4.76	15.2	83.9
	745.7	2.64	4.75	15.0	83.0
	753.4	2.63	4.74	14.8	82.0
	761.1	2.63	4.73	14.6	81.0

Table A.1: k_x, k_y k_z and m values obtained for peaks corresponding to E_x^{11} modes for microwire 1, cavity 1A. k-vector components were calculated by using Marcatili's model, as detailed in the text. For this set of fitted peaks, L_{eff} = 17.4 µm was obtained to match the longitudinal resonant condition for consecutive integer numbers m, which coincides with the L_{eff} value of the other peaks assigned to other modes. Trials of fitting these peaks to other modes imposing a constant L_{eff} result in sensitively worse fits than the obtained ones.

Mode	λ_p [nm]	k$_x$ [μm^{-1}]	k$_y$ [μm^{-1}]	k$_z$ [μm^{-1}]	m
E_x^{12}	694.3	2.64	9.53	14.1	78.0
	700.3	2.64	9.51	13.9	77.0
	706.6	2.64	9.48	13.7	76.0
	712.6	2.64	9.46	13.5	75.0
	719.0	2.64	9.44	13.4	74.0
	725.2	2.64	9.41	13.2	73.1
	732.8	2.64	9.38	13.0	72.0
	739.6	2.64	9.36	12.8	70.9
	746.2	2.64	9.33	12.6	70.0
	753.6	2.63	9.30	12.4	69.0
	761.1	2.63	9.27	12.3	68.0
	768.6	2.63	9.25	12.1	66.9
	775.2	2.63	9.22	11.9	66.0
	782.4	2.63	9.19	11.8	65.1
	790.2	2.63	9.16	11.6	64.1
	798.0	2.63	9.13	11.4	63.1

Table A.2: k_x, k_y k_z and m values obtained for peaks corresponding to E_x^{12} modes for microwire 1, cavity 1A. k-vector components were calculated by using Marcatili's model, as detailed in the text. For this set of fitted peaks, L_{eff} = 17.4 µm was obtained to match the longitudinal resonant condition for consecutive integer numbers m, which coincides with the L_{eff} value of the other peaks assigned to other modes. Trials of fitting these peaks to other modes imposing a constant L_{eff} result in sensitively worse fits than the obtained ones.

Mode	λ_p [nm]	kx [μm^{-1}]	ky [μm^{-1}]	kz [μm^{-1}]	m
E_y^{11}	712.4	-	-	15.5	86.0
	719.3	-	-	15.3	84.9
	725.3	-	-	15.1	84.0
	732.9	-	-	14.9	83.0
	740.3	-	-	14.8	82.0
	747.4	-	-	14.6	81.0
	754.9	-	-	14.4	79.9
	762.2	-	-	14.2	79.0

Table A.3: k_z and m values obtained for peaks corresponding to E_y^{11} modes for microwire 1, cavity 1A. k_z values were calculated by applying a correction to Marcatili's model in order to fit to Goell's model, as detailed in the text. For this set of fitted peaks, $L_{eff} = 17.4\,\mu\text{m}$ was obtained to match the longitudinal resonant condition for consecutive integer numbers m, which coincides with the L_{eff} value of the other peaks assigned to other modes. Better fits are obtained compared to trying to fit to E_y^{11} modes by using the Marcatili model. Trials of fitting these peaks to other modes imposing a constant L_{eff} result in sensitively worse fits than the obtained ones.

Bibliography

[1] R. Kumar, O. Al-Dossary, G. Kumar, and A. Umar. *Zinc oxide nanostructures for NO_2 gas–sensor applications: A review.* Nano-Micro Letters **7**.2 (2015) 97–120.

[2] S. Manandhar, A. K. Battu, A. Devaraj, V. Shutthanandan, S. Thevuthasan, and C. V. Ramana. *Rapid Response High Temperature Oxygen Sensor Based on Titanium Doped Gallium Oxide.* Scientific Reports **10**.1 (2020) 1–9.

[3] E. H. Anaraki, A. Kermanpur, L. Steier, K. Domanski, T. Matsui, W. Tress, M. Saliba, A. Abate, M. Grätzel, A. Hagfeldt, et al. *Highly efficient and stable planar perovskite solar cells by solution-processed tin oxide.* Energy & Environmental Science **9**.10 (2016) 3128–3134.

[4] J. Zhang, J. Shi, D-C. Qi, L. Chen, and K. H. L. Zhang. *Recent progress on the electronic structure, defect, and doping properties of Ga_2O_3.* APL Materials **8**.2 (2020) 020906.

[5] N. Ueda, H. Hosono, R. Waseda, and H. Kawazoe. *Anisotropy of electrical and optical properties in β-Ga_2O_3 single crystals.* Applied Physics Letters **71**.7 (1997) 933–935.

[6] S. J. Pearton, J. Yang, P. H. Cary IV, F. Ren, J. Kim, M. J. Tadjer, and M. A. Mastro. *A review of Ga_2O_3 materials, processing, and devices.* Applied Physics Reviews **5**.1 (2018) 011301.

[7] X. Chen, F. Ren, S. Gu, and J. Ye. *Review of gallium-oxide-based solar-blind ultraviolet photodetectors.* Photonics Research **7**.4 (2019) 381–415.

[8] A. J. Green, K. D. Chabak, E. R. Heller, R. C. Fitch, M. Baldini, A. Fiedler, K. Irmscher, G. Wagner, Z. Galazka, S. E. Tetlak, A. Crespo, J. Leedy, and G. H. Jessen. *3.8-MV/cm Breakdown Strength of MOVPE-Grown Sn-Doped beta-Ga_2O_3 MOSFETs.* IEEE Electron Device Letters **37**.7 (2016) 902–905.

[9] M. D. McCluskey. *Point defects in Ga_2O_3*. Journal of Applied Physics **127**.10 (2020) 101101.
[10] D. Guo, Q. Guo, Z. Chen, Z. Wu, P. Li, and W. Tang. *Review of Ga_2O_3 based optoelectronic devices.* Materials Today Physics **11**.100157 (2019).
[11] S. B. Reese, T. Remo, J. Green, and A. Zakutayev. *How much will gallium oxide power electronics cost?* Joule **3**.4 (2019) 903–907.
[12] Y. Zhang, Q. Su, J. Zhu, S. Koirala, S. J. Koester, and X. Wang. *Thickness-dependent thermal conductivity of mechanically exfoliated β-Ga2O3 thin films.* Applied Physics Letters **116**.20 (2020) 202101.
[13] J. M. Johnson, Z. Chen, J. B. Varley, C. M. Jackson, E. Farzana, Z. Zhang, A. R. Arehart, H-L. Huang, A. Genc, S. A. Ringel, C. G. Van de Walle, D. A. Muller, and J. Hwang. *Unusual Formation of Point-Defect Complexes in the Ultrawide-Band-Gap Semiconductor β-Ga_2O_3*. Physical Review X **9**.4 (2019) 041027.
[14] E. G. Víllora, K. Shimamura, Y. Yoshikawa, T. Ujiie, and K. Aoki. *Electrical conductivity and carrier concentration control in β-Ga_2O_3 by Si doping.* Applied Physics Letters **92**.20 (2008) 202120.
[15] J. B. Varley, J. R. Weber, A. Janotti, and C. G. Van de Walle. *Oxygen vacancies and donor impurities in β-Ga_2O_3*. Applied Physics Letters **97**.14 (2010) 142106.
[16] M. J. Tadjer, J. L. Lyons, N. Nepal, J. A. Freitas, A. D. Koehler, and G. M. Foster. *Review—Theory and Characterization of Doping and Defects in β-Ga_2O_3*. ECS Journal of Solid State Science and Technology **8**.7 (2019) Q3187–Q3194.
[17] N. Ueda, H. Hosono, R. Waseda, and H. Kawazoe. *Synthesis and control of conductivity of ultraviolet transmitting β-Ga_2O_3 single crystals.* Applied Physics Letters **70**.26 (1997) 3561–3563.
[18] A. Kyrtsos, M. Matsubara, and E. Bellotti. *On the feasibility of p-type Ga_2O_3*. Applied Physics Letters **112**.3 (2018) 032108.
[19] Stephen Pearton, Fan Ren, and Michael Mastro. *Gallium Oxide. Technology, devices and applications.* 1st edition. Elsevier, Oct. 2018.
[20] M. Higashiwaki and G. H. Jessen. *Guest Editorial: The dawn of gallium oxide microelectronics.* Applied Physics Letters **112**.6 (2018) 060401.
[21] M. Rebien, W. Henrion, M. Hong, J. P. Mannaerts, and M. Fleischer. *Optical properties of gallium oxide thin films.* Applied Physics Letters **81**.2 (2002) 250–252.

[22] J-H. Yoo, S. Rafique, A. Lange, H. Zhao, and S. Elhadj. *Lifetime laser damage performance of β-Ga_2O_3 for high power applications.* APL Materials **6**.3 (2018) 036105.

[23] H. Deng, K. J. Leedle, Y. Miao, D. S. Black, K. E. Urbanek, J. McNeur, M. Kozák, A. Ceballos, P. Hommelhoff, O. Solgaard, R. L. Byer, and J. S. Harris. *Gallium Oxide for High-Power Optical Applications.* Advanced Optical Materials (2020) 1901522.

[24] L. Binet and D. Gourier. *Origin of the blue luminescence of β-Ga_2O_3.* Journal of Physics and Chemistry of Solids **59**.8 (1998) 1241–1249.

[25] K. Shimamura, E. G. Víllora, T. Ujiie, and K. Aoki. *Excitation and photoluminescence of pure and Si-doped β-Ga_2O_3 single crystals.* Applied Physics Letters **92**.20 (2008) 201914.

[26] T. Onuma, S. Fujioka, T. Yamaguchi, M. Higashiwaki, K. Sasaki, T. Masui, and T. Honda. *Correlation between blue luminescence intensity and resistivity in β-Ga_2O_3 single crystals.* Applied Physics Letters **103**.4 (2013) 041910.

[27] R. Jangir, S. Porwal, P. Tiwari, P. Mondal, S. K. Rai, T. Ganguli, S. M. Oak, and S. K. Deb. *Photoluminescence study of β-Ga_2O_3 nanostructures annealed in different environments.* Journal of Applied Physics **112**.3 (2012) 034307.

[28] T. Onuma, Y. Nakata, K. Sasaki, T. Masui, T. Yamaguchi, T. Honda, A. Kuramata, S. Yamakoshi, and M. Higashiwaki. *Modeling and interpretation of UV and blue luminescence intensity in β-Ga_2O_3 by silicon and nitrogen doping.* Journal of Applied Physics **124**.7 (2018) 075103.

[29] P-C. Chang, Z. Fan, W-Y. Tseng, A. Rajagopal, and J. G. Lu. *β-Ga_2O_3 nanowires: synthesis, characterization, and p-channel field-effect transistor.* Applied Physics Letters **87**.22 (2005) 222102.

[30] S. Ahn, F. Ren, J. Kim, S. Oh, J. Kim, M. A. Mastro, and S. J. Pearton. *Effect of front and back gates on β-Ga_2O_3 nano-belt field-effect transistors.* Applied Physics Letters **109**.6 (2016) 062102.

[31] Y. Li, T. Tokizono, M. Liao, M. Zhong, Y. Koide, I. Yamada, and J-J. Delaunay. *Efficient assembly of bridged β-Ga_2O_3 nanowires for solar-blind photodetection.* Advanced Functional Materials **20**.22 (2010) 3972–3978.

[32] T. He, Y. Zhao, X. Zhang, W. Lin, K. Fu, C. Sun, F. Shi, X. Ding, G. Yu, K. Zhang, S. Lu, X. Zhang, and B. Zhang. *Solar-blind ultraviolet photodetector based on graphene/vertical Ga_2O_3 nanowire array heterojunction.* Nanophotonics **7**.9 (2018) 1557–1562.

[33] Y. C. Choi, W. S. Kim, Y. S. Park, S. M. Lee, D. J. Bae, Y. H. Lee, G. S. Park, W. B. Choi, N. S. Lee, and J. M. Kim. *Catalytic growth of β-Ga_2O_3 nanowires by arc discharge.* Advanced Materials **12**.10 (2000) 746–750.

[34] J. Li, X. Chen, Z. Qiao, M. He, and H. Li. *Large-scale synthesis of single-crystalline β-Ga_2O_3 nanoribbons, nanosheets and nanowires.* Journal of Physics: Condensed Matter **13**.48 (2001) L937.

[35] S. Kumar and R. Singh. *Nanofunctional gallium oxide nanowires - nanostructures and their applications in nanodevices.* physica status solidi (RRL)–Rapid Research Letters **7**.10 (2013) 781–792.

[36] Z. Galazka. *β-Ga_2O_3 for wide-bandgap electronics and optoelectronics.* Semiconductor Science and Technology **33**.11 (2018) 113001.

[37] K. Lorenz, M. Peres, M. Felizardo, J. G. Correia, L. C. Alves, E. Alves, I. López, E. Nogales, B. Méndez, J. Piqueras, M. B. Barbosa, J. P. Araújo, J. N. Gonçalves, J. Rodrigues, L. Rino, T. Monteiro, E. G. Víllora, and K. Shimamura. *Doping of Ga_2O_3 bulk crystals and NWs by ion implantation.* Proceedings of SPIE **8987** (2014) 89870M.

[38] S. C. Vanithakumari and K. K. Nanda. *A One-Step Method for the Growth of Ga_2O_3-Nanorod-Based White-Light-Emitting Phosphors.* Advanced Materials **21**.35 (2009) 3581–3584.

[39] L-C. Tien and C-H. Chen W-T.and Ho. *Enhanced Photocatalytic Activity in β-Ga_2O_3 Nanobelts.* Journal of the American Ceramic Society **94**.9 (2011) 3117–3122.

[40] I. López, E. Nogales, B. Méndez, J. Piqueras, A. Peche, J. Ramírez-Castellanos, and J. M. González-Calbet. *Influence of Sn and Cr doping on morphology and luminescence of thermally grown Ga_2O_3 nanowires.* The Journal of Physical Chemistry C **117**.6 (2013) 3036–3045.

[41] E. Nogales, I. López, B. Méndez, J. Piqueras, K. Lorenz, E. Alves, and J. A. García. *Doped gallium oxide nanowires for photonics.* Proceedings of SPIE **8263** (2012) 82630B.

[42] E. Nogales, P. Hidalgo, K. Lorenz, B. Méndez, J. Piqueras, and E. Alves. *Cathodoluminescence of rare earth implanted Ga_2O_3 and GeO_2 nanostructures.* Nanotechnology **22**.28 (2011) 285706.

[43] I. López, K. Lorenz, E. Nogales, B. Méndez, J. Piqueras, E. Alves, and J. A. García. *Study of the relationship between crystal structure and luminescence in rare-earth-implanted Ga_2O_3 nanowires during annealing treatments.* Journal of materials science **49**.3 (2014) 1279–1285.

[44] Y. P. Song, P. W. Wang, X. Y. Xu, Z. Wang, G. H. Li, and D. P. Yu. *Magnetism and photoluminescence in manganese–gallium oxide nanowires with monoclinic and spinel structures.* Physica E: Low-dimensional Systems and Nanostructures **31**.1 (2006) 67–71.
[45] A. Gonzalo, E. Nogales, K. Lorenz, E. G. Víllora, K. Shimamura, J. Piqueras, and B. Méndez. *Raman and cathodoluminescence analysis of transition metal ion implanted Ga2O3 nanowires.* Journal of Luminescence **191** (2017) 56–60.
[46] J. Zhao, W. Zhang, E. Xie, Z. Liu, J. Feng, and Z. Liu. *Photoluminescence properties of β-Ga_2O_3: Tb3+ nanofibers prepared by electrospinning.* Materials Science and Engineering: B **176**.12 (2011) 932–936.
[47] E. Nogales, B. Méndez, and J. Piqueras. *Visible cathodoluminescence of Er ions in β-Ga_2O_3 nanowires and microwires.* Nanotechnology **19**.3 (2007) 035713.
[48] E. Nogales, B. Méndez, J. Piqueras, and J. A. García. *Europium doped gallium oxide nanostructures for room temperature luminescent photonic devices.* Nanotechnology **20**.11 (2009) 115201.
[49] J. Zhao, W. Zhang, E. Xie, Z. Ma, A. Zhao, and Z. Liu. *Structure and photoluminescence of β-Ga_2O_3: Eu3+ nanofibers prepared by electrospinning.* Applied Surface Science **257**.11 (2011) 4968–4972.
[50] S. Ye, Y. Zhang, H. He, J. Qiu, and G. Dong. *Simultaneous broadband near-infrared emission and magnetic properties of single phase Ni 2+-doped β-Ga_2O_3 nanocrystals via mediated phase-controlled synthesis.* Journal of Materials Chemistry C **3**.12 (2015) 2886–2896.
[51] S. Zhou, G. Feng, B. Wu, N. Jiang, S. Xu, and J. Qiu. *Intense infrared luminescence in transparent glass-ceramics containing β-Ga_2O_3: Ni2+ nanocrystals.* The Journal of Physical Chemistry C **111**.20 (2007) 7335–7338.
[52] H. H. Tippins. *Optical and microwave properties of trivalent chromium in β-Ga_2O_3*. Physical Review **137**.3A (1965) A865.
[53] Theodore H Maiman. *Stimulated optical radiation in ruby.* nature **187**.4736 (1960) 493–494.
[54] E. Nogales, J. A. García, B. Méndez, and J. Piqueras. *Red luminescence of Cr in β-Ga_2O_3 nanowires.* Journal of applied physics **101**.3 (2007) 033517.
[55] Y. Tokida and S. Adachi. *Photoluminescence spectroscopy and energy-level analysis of metal-organic-deposited Ga_2O_3: Cr3+ films.* Journal of Applied Physics **112**.6 (2012) 063522.

[56] Y-Y. Lu, F. Liu, Z. Gu, and Z. Pan. *Long-lasting near-infrared persistent luminescence from β-Ga2O3: Cr3+ nanowire assemblies.* Journal of Luminescence **131**.12 (2011) 2784–2787.

[57] I. López, E. Nogales, B. Méndez, and J. Piqueras. *Resonant cavity modes in gallium oxide microwires.* Applied Physics Letters **100**.26 (2012) 261910.

[58] Iñaki López García. "Propiedades físicas y dopado de nanoestructuras de óxido de galio". PhD thesis. 2015.

[59] I. López, A. D. Utrilla, E. Nogales, B. Méndez, J. Piqueras, A. Peche, J. Ramírez-Castellanos, and J. M. González-Calbet. *In-doped gallium oxide micro-and nanostructures: morphology, structure, and luminescence properties.* The Journal of Physical Chemistry C **116**.6 (2012) 3935–3943.

[60] M. Girtan. *Is photonics the new electronics? Mihaela Girtan discusses electronics and the rise of photonics, and asks what the future has in store for technology.* Materials Today **17** (2014) 100–101.

[61] G. Brambilla, F. Xu, P. Horak, Y. Jung, F. Koizumi, N. P. Sessions, E. Koukharenko, X. Feng, G. S. Murugan, J. S. Wilkinson, and D. J. Richardson. *Optical fiber nanowires and microwires: fabrication and applications.* Advances in Optics and Photonics **1**.1 (2009) 107–161.

[62] Jordi Arbiol and Qihua Xiong. *Semiconductor nanowires: materials, synthesis, characterization and applications.* 1st edition. Elsevier, Apr. 2015.

[63] Z. Yang, T. Albrow-Owen, H. Cui, J. Alexander-Webber, F. Gu, X. Wang, T-C. Wu, M. Zhuge, C. Williams, P. Wang, et al. *Single-nanowire spectrometers.* Science **365**.6457 (2019) 1017–1020.

[64] C. Cheng, B. Liu, H. Yang, W. Zhou, L. Sun, R. Chen, S. F. Yu, J. Zhang, H. Gong, H. Sun, and J. J. Fan. *Hierarchical assembly of ZnO nanostructures on SnO_2 backbone nanowires: low-temperature hydrothermal preparation and optical properties.* ACS nano **3**.10 (2009) 3069–3076.

[65] J. Ye, C. Zhang, C-L. Zou, Y. Yan, J. Gu, Y. S. Zhao, and J. Yao. *Optical wavelength filters based on photonic confinement in semiconductor nanowire homojunctions.* Advanced Materials **26**.4 (2014) 620–624.

[66] M. Kneissl, T-Y. Seong, J. Han, and H. Amano. *The emergence and prospects of deep-ultraviolet light-emitting diode technologies.* Nature Photonics **13**.4 (2019) 233–244.

[67] C.-Z. Ning. *Semiconductor nanolasers and the size-energy-efficiency challenge: a review*. Advanced Photonics **1**.1 (2019) 014002.

[68] M. Suter and P. Dietiker. *Calculation of the finesse of an ideal Fabry–Perot resonator*. Applied optics **53**.30 (2014) 7004–7010.

[69] K. W. Kolasinski. *Catalytic growth of nanowires: vapor–liquid–solid, vapor–solid–solid, solution–liquid–solid and solid–liquid–solid growth*. Current Opinion in Solid State and Materials Science **10**.3-4 (2006) 182–191.

[70] H. Wang, L. A. Zepeda-Ruiz, G. H. Gilmer, and M. Upmanyu. *Atomistics of vapour–liquid–solid nanowire growth*. Nature communications **4** (2013) 1956.

[71] N. Wang, Y Cai, and R. Q. Zhang. *Growth of nanowires*. Materials Science and Engineering: R: Reports **60**.1-6 (2008) 1–51.

[72] C. Cheng and H. J. Fan. *Branched nanowires: synthesis and energy applications*. Nano Today **7**.4 (2012) 327–343.

[73] Kahraman Keskinbora. *Prototyping micro- and nano-Optics with Focused Ion Beam lithography*. SPIE, Apr. 2019.

[74] Ben G. Yacobi and David B. Holt. *Cathodoluminescence Microscopy of Inorganic Solids*. Springer, 1990.

[75] K. A. Kanaya and S. Okayama. *Penetration and energy-loss theory of electrons in solid targets*. Journal of Physics D: Applied Physics **5**.1 (1972) 43.

[76] K. Z. Baba-Kishi. *Review Electron backscatter Kikuchi diffraction in the scanning electron microscope for crystallographic analysis*. Journal of materials science **37**.9 (2002) 1715–1746.

[77] Barry Carter and David B. Williams. *Transmission Electron Microscopy: Diffraction, imaging and spectrometry*. Springer, 2016.

[78] Peter J. Goodhew and John Humphreys. *Electron microscopy and analysis*. CRC Press, 2000.

[79] Miroslav Dramićanin. *Luminescence thermometry: methods, materials, and applications*. Woodhead Publishing, 2018.

[80] Belén Sotillo Buzarra. "Síntesis y caracterización de micro-y nanoestructuras de ZnS: X (X= Al, Ga, In)". PhD thesis. 2014.

[81] R-M. Ma, X-L. Wei, L. Dai, S-F. Liu, T. Chen, S. Yue, Z. Li, Q. Chen, and G. G. Qin. *Light Coupling and Modulation in Coupled Nanowire Ring- Fabry-Pérot Cavity*. Nano letters **9**.7 (2009) 2697–2703.

[82] Jürgen Popp and Thomas Mayerhöfer. *Micro-Raman Spectroscopy: Theory and Application*. Walter de Gruyter GmbH & Co KG, 2020.

[83] A. V. Naumkin, A. Kraut-Vass, S. W. Gaarenstroom, and C. J. Powell. *NIST X-ray Photoelectron Spectroscopy Database. Measurement Services Division of the National Institute of Standards and Technology (NIST).* 2018.

[84] John F Watts and John Wolstenholme. *An introduction to surface analysis by XPS and AES* (2003).

[85] A. Gonzalo, E. Nogales, B. Méndez, and J. Piqueras. *Influence of growth temperature on the morphology and luminescence of Ga_2O_3: Mn nanowires.* physica status solidi (a) **211**.2 (2014) 494–497.

[86] L. Chao, Y. Jin-Liang, Z. Li-Ying, and Z. Gang. *Electronic structures and optical properties of Zn-doped β-Ga_2O_3 with different doping sites.* Chinese Physics B **21**.12 (2012) 127104.

[87] Q. Feng, J. Liu, Y. Yang, D. Pan, Y. Xing, X. Shi, X. Xia, and H. Liang. *Catalytic growth and characterization of single crystalline Zn doped p-type β-Ga_2O_3 nanowires.* Journal of Alloys and Compounds **687** (2016) 964–968.

[88] L. Mazeina, Y. N. Picard, S. I. Maximenko, F. K. Perkins, E. R. Glaser, M. E. Twigg, J. A. Freitas Jr, and S. M. Prokes. *Growth of Sn-Doped β-Ga_2O_3 Nanowires and Ga_2O_3- SnO_2 Heterostructures for Gas Sensing Applications.* Crystal growth & design **9**.10 (2009) 4471–4479.

[89] J. Díaz, I. López, E. Nogales, B. Méndez, and J. Piqueras. *Synthesis and characterization of silicon-doped gallium oxide nanowires for optoelectronic UV applications.* Journal of Nanoparticle Research **13**.5 (2011) 1833.

[90] E. Farzana, E. Ahmadi, J. S. Speck, A. R. Arehart, and S. A. Ringel. *Deep level defects in Ge-doped (010) β-Ga_2O_3 layers grown by plasma-assisted molecular beam epitaxy.* Journal of Applied Physics **123**.16 (2018) 161410.

[91] N. Moser, J. McCandless, A. Crespo, K. Leedy, A. Green, A. Neal, S. Mou, E. Ahmadi, J. Speck, K. Chabak, N. Peixoto, and G. Jessen. *Ge-Doped β-Ga_2O_3 MOSFETs.* IEEE Electron Device Letters **38**.6 (2017) 775–778.

[92] C. Kranert, C. Sturm, R. Schmidt-Grund, and M. Grundmann. *Raman tensor elements of β-Ga_2O_3.* Scientific reports **6** (2016) 35964.

[93] Z. Sun, L. Yang, X. Shen, and Z. Chen. *Anisotropic Raman spectroscopy of a single β-Ga_2O_3 nanobelt.* Chinese Science Bulletin **57**.6 (2012) 565–568.

[94] E. Chikoidze, A. Fellous, A. Perez-Tomas, G. Sauthier, T. Tchelidze, C. Ton-That, T. T. Huynh, M. Phillips, S. Russell, M. R. Jennings, B. Berini, F. Jomard, and Y. Dumont. *P-type β-Ga_2O_3: a new perspective for power and optoelectronic devices.* Materials Today Physics **3** (2017) 118–126.
[95] H. He, R. Orlando, M. A. Blanco, R. Pandey, E. Amzallag, I. Baraille, and M. Rérat. *First-principles study of the structural, electronic, and optical properties of Ga_2O_3 in its monoclinic and hexagonal phases.* Physical Review B **74**.19 (2006) 195123.
[96] X. H. Wang, F. B. Zhang, K. Saito, T. Tanaka, M. Nishio, and Q. X. Guo. *Electrical properties and emission mechanisms of Zn-doped β-Ga_2O_3 films.* Journal of Physics and Chemistry of Solids **75**.11 (2014) 1201–1204.
[97] F. Alema, B. Hertog, O. Ledyaev, D. Volovik, G. Thoma, R. Miller, A. Osinsky, P. Mukhopadhyay, S. Bakhshi, H. Ali, and W. V. Schoenfeld. *Solar blind photodetector based on epitaxial zinc doped Ga_2O_3 thin film.* physica status solidi (a) **214**.5 (2017) 1600688.
[98] Y. Usui, D. Nakauchi, N. Kawano, G. Okada, N. Kawaguchi, and T. Yanagida. *Scintillation and optical properties of Sn-doped Ga_2O_3 single crystals.* Journal of Physics and Chemistry of Solids **117** (2018) 36–41.
[99] N. Isomura, T. Nagaoka, Y. Watanabe, K. Kutsuki, H. Nishinaka, and M. Yoshimoto. *Determination of Zn-containing sites in β-Ga_2O_3 film grown through mist chemical vapor deposition via X-ray absorption spectroscopy.* Japanese Journal of Applied Physics (2020).
[100] S. Kumar, C. Tessarek, G. Sarau, S. Christiansen, and R. Singh. *Self-Catalytic Growth of β-Ga_2O_3 Nanostructures by Chemical Vapor Deposition.* Advanced Engineering Materials **17**.5 (2014) 709–715.
[101] V. Agafonov, D. Michel, A. Kahn, and M. P. Y. Jorba. *Crystal growth by chemical vapour transport in the GeO_2-Ga_2O_3 system.* Journal of crystal growth **71**.1 (1985) 12–16.
[102] S. Kumar, G. Sarau, C. Tessarek, M. Y. Bashouti, A. Hähnel, S. Christiansen, and R. Singh. *Study of iron-catalysed growth of β-Ga_2O_3 nanowires and their detailed characterization using TEM, Raman and cathodoluminescence techniques.* Journal of Physics D: Applied Physics **47**.43 (2014) 435101.
[103] R. W. Olesinski and G. J. Abbaschian. *The Ga- Ge system.* Bulletin of Alloy Phase Diagrams **6**.3 (1985) 258–262.

[104] X. Cao, J-S Li, X-D. Zhang, T. He, L. Zhang, Y. Ma, K. Xu, J. Zhao, W. Tang, and B. Zhang. *Controllable Ga Catalyst Deposition on GaN Template and Fabrication of Ordered Vertical β-Ga 2 O 3 Nanowire Array*. Journal of Physics D: Applied Physics (2020).

[105] D. Dohy, G. Lucazeau, and A. Revcolevschi. *Raman spectra and valence force field of single-crystalline β Ga_2O_3*. Journal of Solid State Chemistry **45**.2 (1982) 180–192.

[106] D. Tuschel. *Effect of Dopants or Impurities on the Raman Spectrum of the Host Crystal*. Spectroscopy **32** (2017) 13–18.

[107] C-L. Hsu and Y-C. Lu. *Fabrication of a transparent ultraviolet detector by using n-type Ga_2O_3 and p-type Ga-doped SnO_2 core-shell nanowires*. Nanoscale **4**.18 (2012) 5710–5717.

[108] J. Oviedo and M. J. Gillan. *Energetics and structure of stoichiometric SnO_2 surfaces studied by first-principles calculations*. Surface Science **463**.2 (2000) 93–101.

[109] J. Dolado, K. L. Renforth, J. E. Nunn, S. A. Hindsmarsh, P. Hidalgo, A. M. Sánchez, and Méndez B. *Zn_2GeO_4/SnO_2 Nanowire Heterostructures Driven by Plateau–Rayleigh Instability*. Crystal Growth & Design **20**.1 (2019) 506–513.

[110] D. Maestre, A. Cremades, and J. Piqueras. *Cathodoluminescence of defects in sintered tin oxide*. Journal of applied physics **95**.6 (2004) 3027–3030.

[111] X. T. Zhou, F. Heigl, M. W. Murphy, T. K. Sham, T. Regier, I. Coulthard, and R. I. R. Blyth. *Time-resolved x-ray excited optical luminescence from Sn O 2 nanoribbons: Direct evidence for the origin of the blue luminescence and the role of surface states*. Applied physics letters **89**.21 (2006) 213109.

[112] F. J. Flores-Ruiz, C. I. Enriquez-Flores, F. C-C, and F. J. E-B. *Nanotribological performance of fullerene-like carbon nitride films*. Applied surface science **314** (2014) 193–198.

[113] J. García-Fernández, M. García-Carrión, A. Torres-Pardo, R. Martínez-Casado, J. Ramírez-Castellanos, E. Nogales, J. M. González-Calbet, and B. Méndez. *New insights into the luminescent properties of Na stabilized Ga–Ti oxides homologous series*. Journal of Materials Chemistry C **8**.8 (2020) 2725–2731.

[114] G. Martínez-Criado, J. Segura-Ruiz, M-H. Chu, R. Tucoulou, I. López, E. Nogales, B. Méndez, and J. Piqueras. *Crossed Ga_2O_3/SnO_2 multiwire architecture: a local structure study with nanometer resolution*. Nano letters **14**.10 (2014) 5479–5487.

[115] C-Y. Tsay and S-C. Liang. *Fabrication of p-type conductivity in SnO_2 thin films through Ga doping.* Journal of Alloys and Compounds **622** (2015) 644–650.
[116] G. Singh and R. C. Singh. *Synthesis, Characterization and Gas Sensing Properties of Ga-Doped SnO_2 Nanostructures.* Journal of Electronic Materials **48**.7 (2019) 4478–4490.
[117] M. García-Tecedor, D. Maestre, A. Cremades, and J. Piqueras. *Influence of Cr doping on the morphology and luminescence of SnO_2 nanostructures.* The Journal of Physical Chemistry C **120**.38 (2016) 22028–22034.
[118] M. García-Tecedor, D. Maestre, A. Cremades, and J. Piqueras. *Tailoring optical resonant cavity modes in SnO_2 microstructures through doping and shape engineering.* Journal of Physics D: Applied Physics **50**.41 (2017) 415104.
[119] H. J. Chun, Young S. C., S. Y. Bae, H. .n Seo, S. J. Hong, J. Park, and H. Yang. *Controlled structure of gallium oxide nanowires.* The Journal of Physical Chemistry B **107**.34 (2003) 9042–9046.
[120] I. D. Hosein, M. Hegde, P. D. Jones, V. Chirmanov, and P. V. Radovanovic. *Evolution of the faceting, morphology and aspect ratio of gallium oxide nanowires grown by vapor–solid deposition.* Journal of crystal growth **396** (2014) 24–32.
[121] Brian Henderson and G. Frank Imbusch. *Optical spectroscopy of inorganic solids.* Volume 44. Oxford University Press, 2006.
[122] M. Zapf, R. Röder, K. Winkler, L. Kaden, J. Greil, M. Wille, M. Grundmann, R. Schmidt-Grund, A. Lugstein, and C. Ronning. *Dynamical tuning of nanowire lasing spectra.* Nano letters **17**.11 (2017) 6637–6643.
[123] M. H. Huang, S. Mao, H. Feick, H. Yan, Y. Wu, H. Kind, E. Weber, R. Russo, and P. Yang. *Room-temperature ultraviolet nanowire nanolasers.* science **292**.5523 (2001) 1897–1899.
[124] M. F. Al-Kuhaili, S. M. A. Durrani, and E. E. Khawaja. *Optical properties of gallium oxide films deposited by electron-beam evaporation.* Applied Physics Letters **83**.22 (2003) 4533–4535.
[125] J. Kong, S. Chu, J. Huang, M. Olmedo, W. Zhou, L. Zhang, Z. Chen, and J. Liu. *Use of distributed Bragg reflectors to enhance Fabry–Pérot lasing in vertically aligned ZnO nanowires.* Applied Physics A **110**.1 (2013) 23–28.

[126] Y. Yang, T. Wei, R. Zhu, H. Zong, J. Lu, J. Li, H. Liao, G. Yu, C. Pan, and X. Hu. *Tunable single-mode lasing in a single semiconductor microrod.* Optics express **26**.23 (2018) 30021–30029.

[127] C. Zhang, R. ElAfandy, and J. Han. *Distributed Bragg Reflectors for GaN-Based Vertical-Cavity Surface-Emitting Lasers.* Applied Sciences **9**.8 (2019) 1593.

[128] Steven G. Johnson Robert D. Meade Joshua N. Winn and John D. Joannopoulos. *Photonic crystals: Molding the flow of light.* Princeton University Press Princeton, NJ, 2007.

[129] R. Courant, K. Friedrichs, and H. Lewy. *On the partial difference equations of mathematical physics.* IBM journal of Research and Development **11**.2 (1967) 215–234.

[130] Y. Ma, X. Guo, X. Wu, L. Dai, and L. Tong. *Semiconductor nanowire lasers.* Advances in optics and photonics **5**.3 (2013) 216–273.

[131] E. A. J. Marcatili. *Dielectric rectangular waveguide and directional coupler for integrated optics.* Bell System Technical Journal **48**.7 (1969) 2071–2102.

[132] J. E. Goell. *A circular-harmonic computer analysis of rectangular dielectric waveguides.* Bell System Technical Journal **48**.7 (1969) 2133–2160.

[133] K. D. Laakmann and W. H. Steier. *Waveguides: characteristic modes of hollow rectangular dielectric waveguides.* Applied optics **15**.5 (1976) 1334–1340.

[134] J. E. Goell. “Rectangular dielectric waveguides”. *Introduction to Integrated Optics.* Springer, 1974 pages 73–103.

[135] L. R. Brovelli and U. Keller. *Simple analytical expressions for the reflectivity and the penetration depth of a Bragg mirror between arbitrary media.* Optics communications **116**.4-6 (1995) 343–350.

[136] Richard S. Quimby. *Photonics and lasers: an introduction.* John Wiley & Sons, 2006.

[137] A. Fu, H. Gao, P. Petrov, and P. Yang. *Widely tunable distributed Bragg reflectors integrated into nanowire waveguides.* Nano letters **15**.10 (2015) 6909–6913.

[138] R. Röder and C. Ronning. *Review on the dynamics of semiconductor nanowire lasers.* Semiconductor Science and Technology **33**.3 (2018) 033001.

[139] David J. Klotzkin. *Introduction to semiconductor lasers for optical communications.* Springer, 2013.

[140] Z. Chen, S. Xiong, S. Gao, H. Zhang, L. Wan, X. Huang, B. Huang, Y. Feng, W. Liu, and Z. Li. *High-temperature sensor based on fabry-perot interferometer in microfiber tip.* Sensors **18**.1 (2018) 202.

[141] W-Z. Xu, F-F. Ren, D. Jevtics, A. Hurtado, L. Li, Q. Gao, J. Ye, F. Wang, B. Guilhabert, L. Fu, H. Lu, R. Zhang, H. H. Tan, M. D. Dawson, and C. Jagadish. *Vertically emitting indium phosphide nanowire lasers.* Nano letters **18**.6 (2018) 3414–3420.

[142] M. A. Zimmler, F. Capasso, S. Müller, and C. Ronning. *Optically pumped nanowire lasers: invited review.* Semiconductor Science and Technology **25**.2 (2010) 024001.

[143] A. R. M. Zain, N. P. Johnson, M. Sorel, and M. Richard. *Ultra high quality factor one dimensional photonic crystal/photonic wire micro-cavities in silicon-on-insulator (SOI).* Optics express **16**.16 (2008) 12084–12089.

[144] Katsunari Okamoto. *Fundamentals of optical waveguides.* Academic press, 2006.

Appendix B

List of publications related to this PhD thesis

Publications derived from this thesis

1. Shape engineering driven by selective growth of SnO_2 on doped Ga_2O_3 nanowires.
   M. Alonso-Orts, A. M. Sánchez, I. López, E. Nogales, J. Piqueras, B. Méndez.
   Nano letters 17(1), 515-522 (2017).

2. Tailoring the shape of oxide complex nanostructures.
   B. Méndez, I. López, **M. Alonso-Orts**, A. Sanz, E. Nogales, P. Hidalgo, J. Piqueras.
   Proceedings of SPIE 10248, 1024805 (2017).

3. 3D and 2D growth of SnO_2 nanostructures on Ga_2O_3 nanowires: Synthesis and structural characterization.
   M. Alonso-Orts, A. M. Sánchez, I. López, E. Nogales, J. Piqueras, B. Méndez.
   CrystEngComm 19(41), 6127-6132 (2017).

4. Modal analysis of β-Ga_2O_3:Cr widely tunable luminescent optical microcadvities.
M. Alonso-Orts, E. Nogales, J. M. San Juan, M. L. Nó, J. Piqueras, B. Méndez.
Physical Review Applied 9(6), 064004 (2018).

5. Structural and luminescence properties of Ga_2O_3:Zn micro- and nanostructures.
I. López, **M. Alonso-Orts**, E. Nogales, B. Méndez.
physica status solidi (a) 215(19), 1800217 (2018).

6. Direct observation of tunnelled intergrowth in SnO_2/Ga_2O_3 complex nanowires.
O. M. Rigby, A. V Stamp, S. A. Hindmarsh, **M. Alonso-Orts**, E. Nogales, B. Méndez, A. M. Sánchez.
Nanotechnology 30(5), 054003 (2019).

7. Exciting and confining light in Cr doped gallium oxide.
M. Alonso-Orts, E. Nogales, J. M. San Juan, M. L. Nó, J. Piqueras, B. Méndez.
Proceedings of SPIE 10919, 109191S (2019).

8. Ge incorporation in gallium oxide nanostructures grown by thermal treatment.
M. Alonso-Orts, A. M. Sánchez, E. Nogales, B. Méndez.
Journal of Materials Science 55, 11431-11438 (2020).

9. Optical properties of Ga_2O_3 nanostructures.
M. Alonso-Orts, E. Nogales, B. Méndez.
Book Chapter to be published in the *IoP Editorial*, in printing process (expected by the end of 2020).

10. Near-UV optical cavities in Ga_2O_3 nanowires.
M. Alonso-Orts, G. Chilla, R. Hötzel, E. Nogales, J. M. San Juan, M. L. Nó, M. Eickhoff, B. Méndez.
Under Review.

Other related publications

1. Influence of Li doping on the morphology and luminescence of Ga_2O_3 microrods grown by a vapor-solid method.
   I. López, **M. Alonso-Orts**, E. Nogales, B. Méndez, J. Piqueras.
   Semconductor Science and Technology 31 (11), 115003 (2016).

2. Micro-opto-electro-mechanical device based on flexible β-Ga_2O_3 micro-lamellas.
   M. Peres, A. J. S. Fernandes, F. J. Oliveira, L. C. Alves, E. Alves, T. S. Monteiro, S. Cardoso, **M. Alonso-Orts**, E. Nogales, B. Méndez, E. G. Villora, K. Shimamura, K. Lorenz.
   ECS Journal of Solid State Science and Technology 8(7), Q3235 (2019).